Prediction of the Swelling Properties of Expansive Soils Using Machine Learning Methods

Aolin Zhang

Thesis submitted to the University of Ottawa
in partial Fulfillment of the requirements for the
Doctorate in Philosophy degree in Civil Engineering

Department of Civil Engineering
Faculty of Engineering
University of Ottawa

© Aolin Zhang, Ottawa, Canada, 2025

ABSTRACT

Expansive soils swell significantly when they absorb water and exhibit high swelling pressures if their volume changes are restrained. This characteristic behavior of all expansive soils is mainly attributed to the presence of hydrophilic clay minerals such as montmorillonite and illite. Geotechnical engineers worldwide face considerable challenges in providing reliable approaches for construction and design of geo-infrastructures constructed with or within expansive soils. Common engineering problems caused by these soils include cracked and uneven pavements, uplifted and tilted foundations, slope failures, and the sliding of retaining walls. Over the past several decades, annual global economic losses associated with the damage and repair costs of geotechnical infrastructures built within or with expansive soils have been estimated at several billion US dollars.

To better understand and address these challenges, researchers have developed various experimental methods over the past five decades to determine key swelling properties of expansive soils that include: swelling and compression indices, swelling pressure, and swelling potential. These laboratory methods, particularly oedometer tests, are reliable and reproducible. However, they require extensive equipment and trained personnel, and the testing process often takes several weeks to complete, making them both time-consuming and expensive. As a result, they are not always practical for use in routine geotechnical investigations. Although several empirical and semi-empirical equations have been proposed to predict the swelling behavior of expansive soils, their applications are often limited due to regional differences in expansive soil characteristics and a lack of general applicability. Therefore, there is a need for more simple, economical, reproducible and reliable prediction methods that can be used universally for different types of expansive soils based on basic soil properties that can be obtained from conventional laboratory tests.

In this study, to achieve this key objective, simple models / equations are developed for key geotechnical properties related to the swelling and compressibility behavior of expansive soils with the aid of advanced Machine Learning (ML) techniques.

Comprehensive databases were compiled from published literature, covering a wide range of soil types and geological conditions around the world. Three comprehensive ML algorithms—Multilayer Perceptron (MLP), Support Vector Machine (SVM), and Extreme Learning Machine (ELM)—were applied, along with regression analysis, to predict the swelling index and swelling pressure based on fundamental soil properties; namely, liquid limit, plasticity index, dry density, and initial suction. The proposed models demonstrated reliable predictive capabilities across diverse datasets.

Additionally, Multivariate Adaptive Regression Splines (MARS) and MLP algorithms were employed to develop prediction models for estimating the swelling potential of expansive soils. An extensive dataset was used to support model training and validation. Sensitivity analysis was applied to refine the input variables, ensuring an efficient and accurate model structure. Simplified equations were derived from the optimized models to facilitate their application in practice. The validation of these models was conducted through comprehensive comparative analyses, including evaluations between different ML models and against traditional empirical equations. The results demonstrated significant improvements in prediction accuracy and generalization, offering a practical approach for assessing swelling potential.

Furthermore, in this study ML-based models are presented for predicting the compression index of expansive soils, a critical parameter for evaluating compressibility and settlement behavior in foundation design. A database of 238 expansive soil samples gathered from different countries of the world was established, representing diverse geotechnical conditions. Sensitivity and correlation analyses identified liquid limit, plasticity index, initial void ratio, and dry density as the most influential input factors. Two primary ML algorithms, Newton-Raphson-Based Optimizer Enhanced Extreme Gradient Boosting (NRBO-XGBoost) and MLP, were used to develop reliable prediction models. While the NRBO-XGBoost model exhibited superior performance in terms of accuracy and generalization, the MLP model was further simplified into an empirical equation, making it more convenient for preliminary design applications.

To further evaluate the accuracy and reliability of the proposed models and equations, extensive validation studies were carried out. Published case studies results from the literature were used to assess the prediction accuracy of the models for four key expansive soil parameters: swelling index, swelling pressure, swelling potential, and compression index. The results of these analyses showed strong agreement between the predicted and measured values across different soil types and geographical regions. These case studies confirmed the applicability of the models for capturing the behavior of expansive soils under varying conditions.

In addition, this study integrates the proposed models to jointly simulate the volume change behavior of expansive soils under constant-volume and consolidation-swell conditions. By applying the swelling index, swelling pressure, swelling potential, and compression index models together, the overall volume change behavior was predicted and validated using laboratory data from multiple expansive soils. The results demonstrate the consistency and compatibility of the models when applied in combination, reinforcing their practical value in engineering practice applications.

In summary, this study presents a valuable framework that integrates conventional soil mechanics principles with advanced ML algorithms to improve the prediction of key volumetric parameters of expansive soils. The proposed models and simplified equations enable reliable estimation of swelling and compressibility characteristics based on basic soil properties. Their consistency and compatibility, demonstrated through extensive validations on extensive laboratory test results and case studies, highlight their practical value in conventional design and geotechnical engineering applications across various regions around the world affected by expansive soils.

ACKNOWLEDGMENTS

The research presented in this Ph.D. thesis was conducted at the Department of Civil Engineering, University of Ottawa, under the supervision of Professor Sai K. Vanapalli. I am sincerely grateful for his guidance and support throughout my studies. His valuable advice on my research, mentorship in developing my teaching skills, and encouragement beyond academics have all been instrumental to my growth. His support was particularly touching during the challenging period of the COVID-19 pandemic, and I deeply appreciate the time and effort he devoted to helping me complete this work.

I would also like to acknowledge the financial assistance provided by the China Scholarship Council (CSC), in partnership with the University of Ottawa, as well as funding from the Natural Sciences and Engineering Research Council of Canada (NSERC).

My sincere thanks extend to the members of my thesis committee, Prof. Bhaskar Chittoori, Prof. Elena Zabolotnii, Prof. Mamadou Fall, and Prof. Zhong Han, for their time, constructive feedback, and thoughtful insights throughout this process.

In addition, I am especially thankful to the University of Ottawa for offering me the opportunity to pursue my graduate studies here. Over the past seven years, I have completed both my master's and Ph.D. degrees. This has been a rewarding and transformative journey, and I am grateful for the experiences that have shaped both my academic development and personal growth.

I would also like to express my appreciation to the faculty officer, Luc, for his kind assistance over the years. My thanks go as well to my colleagues and friends in our research group—Xiuhan, Mengxi, Mingshu, Yao, Hongyu, Maha, Ziwen, Xinye, Pan, Hao, and Zhiyuan—for their support, collaboration, and friendship throughout this journey.

I would also like to thank Junjie Wang for his consistent support throughout my academic journey. His encouragement during challenging times was truly appreciated. Additionally,

I would like to express my sincere gratitude to Xinting Cheng, whose insights and assistance greatly contributed to the smooth progress of my research.

A special thanks goes to my cherished little companions—Dami, Mizhuai, Mimi, Laodongxi, Zhongqiu, and Jiuer—whose quiet presence and gentle company brought me comfort and joy along the way.

Most importantly, I am deeply thankful to my family. My sincere gratitude goes to my parents for their unwavering support and encouragement throughout my studies. I am also thankful to my grandmother for her kindness, her constant encouragement, and the care she has always shown me.

TABLE OF CONTENTS

ABSTRACT ..... **II**

ACKNOWLEDGMENTS ..... **V**

TABLE OF CONTENTS ..... **VII**

LIST OF FIGURES ..... **XIV**

LIST OF TABLES ..... **XX**

Chapter 1 ..... **1**

Introduction **1**

1.1 Research background **1**

1.2 Objectives, novelty and methodology **5**

1.2.1 To propose a method for predicting swelling index and swelling pressure 5

1.2.2 To propose a method for predicting swelling potential 6

1.2.3 To propose a method for predicting compression index 7

1.2.4 To validate the proposed models independently 8

1.2.5 To validate the proposed models through integrated application 9

1.3 Layout **10**

References **13**

Chapter 2 ..... **16**

Literature review **16**

2.1 Introduction **16**

2.2 Expansive minerals **16**

2.3 Swelling mechanism **20**

2.4 Factors affecting soil movement 22

2.4.1. Soil type 23

2.4.2. Soil structure 23

2.4.3. Initial water content 24

2.4.4. Plasticity index 24

2.4.5. Dry density 24

2.4.6. Soil salinity 25

2.4.7. Loading 26

2.4.8. Permeability 26

2.5 Unsaturated soils 27

2.5.1 Matric suction 29

2.5.2 Osmotic suction 32

2.6 Volumetric behavior in unsaturated soils 33

2.6.1 Stress state variables 33

2.7 Volume change constitutive relationship 39

2.8 Prediction methods for swelling properties 45

2.8.1 Oedometer test methods 46

2.8.2 Empirical methods 52

2.8.3 Suction-based methods 57

2.8.4 Artificial intelligence-based methods 63

2.9 Compression behavior and compression index of expansive soils 65

2.10 Summary 66

References 68

Chapter 3 79

Predicting swelling index and swelling pressure of expansive soils using multiple artificial intelligence techniques 79

3.1 Introduction 79

3.2 Background 81

3.2.1. Swelling index 81

3.2.2. Swelling pressure 84

3.2.3. AI technology in the study of expansive soils 88

3.3 Methodology 89

3.3.1 Multilayer perceptron (MLP) 89

3.3.2 Support Vector Machine (SVM) 91

3.3.3 Extreme Learning Machine (ELM) 93

3.3.4 Evaluation indexes 94

3.3.5 Database establishment and preprocessing 95

3.4 AI modeling and results 100

3.4.1 Prediction of swelling index 100

3.4.2 Prediction of swelling pressure 105

3.5 Summary 116

References 118

Chapter 4 127

A practical machine learning-based approach for predicting 1-D vertical swelling potential of expansive soils 127

4.1 Introduction 127

4.2 Methodology 131

4.2.1. MLP algorithm 133

4.2.2 MARS algorithm 134

4.2.3 Evaluation indexes 135

4.3 Database establishment 137

4.3.1 Selection of input parameters 137

4.3.2 Correlation between selected inputs 139

4.3.3 Outlier detection 141

4.4 Modelling results and analysis 143

4.4.1 Multivariate Adaptive Regression Splines (MARS) 143

4.4.2 Multilayer Perceptron (MLP) 147

4.4.3 Error analysis 150

4.4.4 Sensitivity analysis 151

4.4.5 Model optimization 155

4.4.6 Model comparisons 158

4.5 Limitations 160

4.6 Summary 160

References 162

Chapter 5 170

Predicting the compression index of expansive soils with hybrid machine learning approaches 170

5.1 Introduction 170

5.2 Database establishment 175

5.2.1 Selection of input parameters 175

5.2.2 Outlier detection 178

5.2.3 Correlation analysis of input soil properties 180

5.2.4 Data splitting 182

5.3 Methodology 182

5.3.1 Newton-Raphson-Based Optimizer Enhanced Extreme Gradient Boosting 183

5.3.2 Multilayer Perceptron 189

5.3.3 Other conventional algorithms 192

5.3.4 Evaluation indexes 193

5.4 Modelling results and analysis 194

5.4.1 NRBO-XGBoost models 195

5.4.2 MLP models 197

5.4.3 Other conventional machine learning models 199

5.4.4 Error analysis and model comparisons 201

5.4.5 Sensitivity analysis 206

5.4.6 Simplified MLP-based equation for predicting compression index 208

5.5 Limitations and future works 209

5.6 Summary 210

References 212

Chapter 6 219

Validation and application of the proposed methods in this study on published case studies 219

6.1 Case studies of the proposed methods for estimating swelling index 220

6.2 Case studies of the proposed methods for estimating swelling pressure 226

6.3 Case studies of the proposed methods for estimating swelling potential 233

6.3.1 Natural heave in open ground due to rainfall 233

6.3.2 Pipeline leakage-induced heave under building concrete slab 236

6.3.3 Heave of excavated slope with rooted vegetation 240

6.3.4 Ground heave under spread footing 244

6.3.5 Ground heave induced by excavation and artificial rainfall 248

6.3.6 Discussion and summary of case study results 250

6.4 Case studies of the proposed methods for estimating compression index 255

6.4.1 Case study A: Consolidation settlement of an untreated expansive soil site 255

6.4.2 Case study B: Settlement behavior of expansive soil under a square footing 256

6.4.3 Case study C: Settlement prediction for expansive soil under embankment loading 258

6.5 Summary 260

References 262

Chapter 7 264

Integrated application of models for predicting constant volume and consolidation-swell oedometer test curves 264

7.1 Introduction 264

7.2 Integrated validation of the proposed models using constant-volume test curves 265

7.3 Integrated validation of the proposed models using consolidation-swell test curves 271

7.4 Summary 276

References 278

Chapter 8 279

Conclusions and suggestions for future research 279

8.1 Major conclusions 279

8.1.1 Predicting swelling index and swelling pressure of expansive soils using multiple artificial intelligence techniques 279

8.1.2 A practical machine learning-based approach for predicting 1-D vertical swelling potential of expansive soils 280

8.1.3 Advanced machine learning models for predicting the compression index of expansive soils 280

8.1.4 Validation and application: Case studies of the proposed methods in this study 281

8.1.5 Integrated application of models for predicting constant volume and consolidation-swell oedometer test curves 281

8.2 Recommendation for future research studies 282

LIST OF FIGURES

Fig. 1.1 Countries affected by expansive soils around the world..... 2

Fig. 1.2 Research framework and layout of the thesis..... 12

Fig. 2.1 A single silica tetrahedron and the sheet structure of silica tetrahedrons arranged in a hexagonal network (modified after Mitchell and Soga (2005)) .. 17

Fig. 2.2 A single octahedral unit and the sheet structure of the octahedral units (modified after Mitchell and Soga (2005)) 18

Fig. 2.3 Schematic diagrams of the structures of (a) 1:1 unit lattice, (b) 2:1 unit lattice (modified after Mitchell and Soga (2005)) 18

Fig. 2.4 Schematic diagrams of the structures of (a) montmorillonite, (b) illite (modified after Mitchell and Soga (2005)) 19

Fig. 2.5 (a) Schematic diagrams of the interlayer expansion of the clay mineral montmorillonite (b) Schematic diagrams of diffuse double layers..... 22

Fig. 2.6 Variation of suction with respect to depth 28

Fig. 2.7 Capillarity and negative water pressure (modified after Fredlund and Rahardjo (1993)) 30

Fig. 2.8 The relationship among pore radius, matric suction, and capillary height (modified after Fredlund and Raharjio (1993)) 31

Fig. 2.9 Microscopic soil-water-air interaction in unsaturated soils (modified after Mitchell and Soga (2005))..... 32

Fig. 2.10 Three-dimensional constitutive surfaces for unsaturated soil: (a) soil structure constitutive surface, (b) water phase constitutive surface (modified after Fredlund and Rahardjo (1993)) 43

Fig. 2.11 Three-dimensional constitutive surfaces for unsaturated soil expressed using soil mechanics terminology: (a) void ratio constitutive surface, (b) water content constitutive surface (modified after Fredlund and Rahardjo (1993))..... 45

Fig. 2.12 (a) procedure for correcting swelling pressure (from Fredlund and Rahardjo, 1993) (b) Schematic of heave estimation using Fredlund (1983) method (from Tu and Vanapalli, 2016) 49

Fig. 2.13 Hypothetical oedometer test results (modified after Nelson et al. (2006)) . 50

Fig. 2.14 Strain-based "equivalence" of reduction of suction from $(u_a - u_w)_i$ to zero (path HB) to reduction in net normal stress from σ_{ocv} to σ_{ob} (along path G'B, the SP) (from Singhal et al. (2011))..... 52

Fig. 3.1. Prediction performance of the proposed equation for predicting swelling index. 84

Fig. 3.2 The principle of the MLP algorithm..... 89

Fig. 3.3 Flow chart for MLP modelling..... 90

Fig. 3.4 The principle of the SVM algorithm..... 92

Fig. 3.5 The principle of the SVM algorithm..... 93

Fig. 3.6 The computation architecture of the ELM algorithm. 94

Fig. 3.7 Swelling index prediction results of MLP (a) training and (b) testing sets; SVM (c) training and (d) testing sets; ELM (e) training and (f) testing sets.. 102

Fig. 3.8 Comparison of the two proposed equations for predicting swelling index. 103

Fig. 3.9 Influence of hidden layer numbers on the prediction accuracy..... 106

Fig. 3.10 Maximum constant volume swelling pressure (P_{scv}) predicted by Model 1 and Model 3 using MLP algorithm. 110

Fig. 3.11 Maximum consolidation-swell swelling pressure (P_{scs}) predicted by Model 5 and Model 9 using MLP algorithm. 111

Fig. 4.1. Typical free-swell oedometer test..... 129

Fig. 4.2 The principle of the MLP algorithm..... 133

Fig. 4.3 The principle of the MARS algorithm..... 135

Fig. 4.5. Summary of results related to outlier detection 142

Fig. 4.6 The influence of Maxfunction on the performance of models..... 144

Fig. 4.7. Prediction results of the MARS model with 9 inputs (Model 1) 146

Fig. 4.8 Influence of hidden layer numbers on the prediction accuracy..... 148

Fig. 4.9. Prediction results of the MLP model with 9 inputs (Model 2) 149

Fig. 4.10 Error distribution of the a) MARS and b) MLP model..... 150

Fig. 4.11 Relative importance factors given by a) Model 1 and b) Model 2 155

Fig. 4.12 Prediction results of the MLP model with 6 inputs (Model 3) 156

Fig. 4.13 Comparison of swelling potential prediction among experimental, AI, and empirical methods..... 159

Fig. 5.1 Cloud-rain plot for outlier detection (a) Liquid limit (LL), clay content (C), plasticity index (I_p), and water content (w); (b) Specific gravity (G_s), dry density (ρ_d), initial void ratio (e_o), and compression index (C_c) 179

Fig. 5.2 Correlation matrix and pairwise scatter plots among soil variables and compression index..... 181

Fig. 5.3 Flowchart of NRBO-XGBoost modelling process 189

Fig. 5.4 The principle and flowchart of MLP algorithm 191

Fig. 5.5 Prediction results of NRBO-XGBoost model with 7 inputs (Model 1)..... 195

Fig. 5.6 Prediction results of NRBO-XGBoost model with 4 inputs (Model 2)..... 196

Fig. 5.7 Prediction results of MLP model with 7 inputs (Model 3) 197

Fig. 5.8 Prediction results of MLP model with 4 inputs (Model 4) 198

Fig. 5.9 Prediction results of SVM (Model 5), ELM (Model 6), and MARS (Model 7) models with 4 inputs 200

Fig. 5.10 (a) Predicted compression index C_c versus I_p using NRBO-XGBoost and MLP models; (b) Residuals of predicted versus measured C_c across I_p for NRBO-XGBoost and MLP models. 203

Fig. 5.11 (a) Predicted compression index C_c versus I_p using SVR, ELM and MARS models; (b) Residuals of predicted versus measured C_c across I_p for SVR, ELM and MARS models. 204

Fig. 5.12 (a) Predicted compression index C_c versus I_p using the NRBO-XGBoost model and Terzaghi and Peck (1967) equation; (b) Residuals of predicted versus measured C_c across I_p for the NRBO-XGBoost model and Terzaghi and Peck (1967) equation. 205

Fig. 5.13. Normalized SHAP feature importance of the input soil properties for the best-performing NRBO-XGBoost model (Model 2). 207

Fig. 6.1 Comparison among Eq. (3.16), (3.17) and measured P_{scv}: (a) French clay; (b) Guabirotuba Formation-1; (c) Oklahoma clay; (d) Regina clay. 227

Fig. 6.2 Comparison among Eq. (3.18), (3.19) and measured P_{scs}: (a) Burleson clay; (b) Colorado clay; (c) Grayson clay; (d) San Diego clay. 229

Fig. 6.3 Geotechnical properties of the Maryland clay site (Modified after Fityus et al., 2004) 234

Fig. 6.4 Floor plan of study site and contours of measured heave (Modified after Yoshida et al., 1983) 237

Fig. 6.5 Seepage analysis boundary setup (Modified after Vu and Fredlund 2004) 238

Fig. 6.6 Soil-water characteristic curve of Regina clay (Modified after Vu and Fredlund 2004) 238

Fig. 6.7 Measured vs predicted displacements reported by Vu and Fredlund (2004) 239

Fig. 6.8 Cross-section of the instrumented slope at Zaoyang site (modified after Ng et al. (2003)) 241

Fig. 6.9 Gravimetric water content profiles during artificial rainfall infiltration (modified after Ng et al. (2003)) 242

Fig. 6.10 Swelling of Zaoyang expansive soil at different depths (modified after Ng et al. (2003)) 243

Fig. 6.11 Layout of spread footing if RF1 area and boring program (modified after Briaud et al. (2003)) 245

Fig. 6.12 Soil stratigraphy and geotechnical properties in RF1 (modified after Briaud et al. (2003)) 246

Fig. 6.13 Measured vertical displacement at the footing in RF1 (modified after Briaud et al. (2003)) 247

Fig. 6.14 Ground heave, moisture variation, and Atterberg limits of Al-Ghatt shale (modified after Briaud et al. (2003)) 249

Figure 6.15 Comparative evaluation of swelling potential across scales 253

Fig. 6.16 Consolidation settlement of footing on Black Cotton Soil (Case study A) 256

Fig. 6.17 Consolidation settlement of a square footing on Ouarzazate expansive soil (Case study B)..... 257

Fig. 6.18 Consolidation settlement of Yunnan expansive soil under embankment (Case study C) 259

Fig. 6.19 Comparison of field and predicted consolidation settlements for the three case studies..... 260

Fig. 7.1 Framework for model development, validation, and integrated application 265

Fig. 7.2 Integrated model validation using CVT results for Regina Clay 266

Fig. 7.3 Integrated model validation using CVT results for Al-Qatif Clay 267

Fig. 7.4 Integrated model validation using CVT results for Dallas Soil 268

Fig. 7.5 Integrated model validation using CST results for Regina Clay 271

Fig. 7.6 Integrated model validation using CST results for Medinah White Clay . 272

Fig. 7.7 Integrated model validation using CST results for Black Cotton Soil 273

LIST OF TABLES

Table 1.1 The annual costs dealing with the damage to infrastructures built on expansive soils for different regions in the world (modified after Adem and Vanapalli (2013)). 4

Table 2.1 Effective stress equations for unsaturated soils modified after (Vanapalli, 1994; Lu, 2010) 34

Table 2.2 The oedometer test-based heave prediction methods modified after (Singhal, 2010; Vanapalli and Lu, 2012) 46

Table 2.3 Summary of the empirical methods modified after (Nelson and Miller, 1997; Rao et al., 2004; Çimen et al., 2012; Vanapalli et al., 2012; Adem, 2015) 52

Table 2.4 Suction-based methods for predicting ground heave (modified after Adem (2015)) 57

Table 2.5 Summary of the comparison among methods 67

Table 3.1 Empirical equations for predicting swelling index 82

Table 3.2 Empirical equations for predicting swelling pressure 86

Table 3.3 Information of soils used to predict swelling index 96

Table 3.4 Information of soils used to predict swelling pressure 98

Table 3.5 Statistical analysis for the established swelling index prediction models 102

Table 3.6 Parameters of MLP, SVM and ELM swelling index prediction models. 102

Table 3.7 Sensitivity analysis of the MLP models 107

Table 3.8 Inputs combinations of the MLP models 108

Table 3.9 Statistical analysis for the established swelling pressure prediction models 112

Table 3.10 Parameters of MLP, SVM and ELM swelling pressure prediction models 113

Table 3.11 Weights and biases of the MLP swelling pressure prediction models... 115

Table 4.1 Annual cost associated with expansive soils worldwide..... 128

Table 4.2 Summary of soil properties used for predicting the swelling potential of expansive soils..... 138

Table 4.3 Weights and biases derived from the Model 2..... 152

Table 4.4 Coefficients of basis functions derived from the Model 1 152

Table 4.5 Weights for each input variables in the Model 1..... 153

Table 4.6 Statistical analysis for the established swelling potential prediction models 156

Table 4.7 Weights and biases derived from the Model 3..... 157

Table 5.1 Global annual expenditures related to expansive soils 171

Table 5.2 Summary of soil properties used for predicting the compression index of expansive soils..... 177

Table 5.3 Summary of the advantages and limitations of the employed machine learning algorithms..... 193

Table 5.4 Main parameters of the NRBO-XGBoost models established in this study. 197

Table 5.5 Summary of prediction performance (R^2, RMSE, and NRMSE) of the employed models 206

Table 6.1 Detailed comparisons of three methods for estimating swelling index and swelling potential. 224

Table 6.2 Validation results of swelling pressure prediction equations (P_{scv}) based on Eqs. (3.16) and (3.17) 231

Table 6.3 Validation results of swelling pressure prediction equations (P_{scs}) based on Eqs. (3.18) and (3.19) 232

Table 6.4 Summary of case study results for swelling potential 254

Table 7.1 Summary of integrated model validation using CVT results 270

Table 7.2 Summary of integrated model validation using CST results 275

CHAPTER 1

INTRODUCTION

1.1 Research background

There has been an increase in the arid and semi-arid regions of the world due to global warming in various regions that include East Asia, South Africa, and East Australia. The semi-arid and arid regions of the world now account for approximately 13% and 15% of the Earth's land area, or 1.9 million km² and 2.3 million km², respectively (Huang et al., 2016). As a result of reduced rainfall, coupled with natural evaporation and plant transpiration, the natural groundwater levels in these areas are often far below the ground surface, leaving the surface soils in a persistently unsaturated state.

Conventional soil mechanics are typically used for the interpretation of soils assuming saturated conditions. However, unsaturated soil is a multiphase medium consisting of a solid phase (soil particles), a liquid phase (water), and a gas phase (air). Unlike in saturated soils, the interaction between the liquid and gas phases in unsaturated soils forms an air-water interface, which generates surface tension that is closely associated with capillary suction. This suction contributes to an increase in shear strength and significantly influences other hydro-mechanical properties, including permeability, compressibility, and volume change behavior (Fredlund and Rahardjo, 1993). Over the past seven decades, numerous researchers have proposed rational frameworks for interpreting the hydraulic and mechanical behavior of unsaturated soils while accounting for the role of suction (Bishop, 1959; Fredlund and Morgenstern, 1977; Vanapalli et al., 1996; Leong and Rahardjo, 1997; Alonso et al., 1999; Lu and Likos, 2006; Puppala et al., 2006; Sheng et al., 2011; Gao et al., 2020).

Expansive soils are a typical example of unsaturated soils and are widely distributed across arid and semi-arid regions of the world (Nelson et al., 2015), as illustrated in Fig. 1.1. These

soils are highly sensitive to fluctuations in moisture content and are characterized by significant swelling behavior upon wetting. The extreme droughts and intense rainfall associated with global climate change have exacerbated the susceptibility of expansive soils to swelling-related hazards (Jones and Jefferson, 2012).

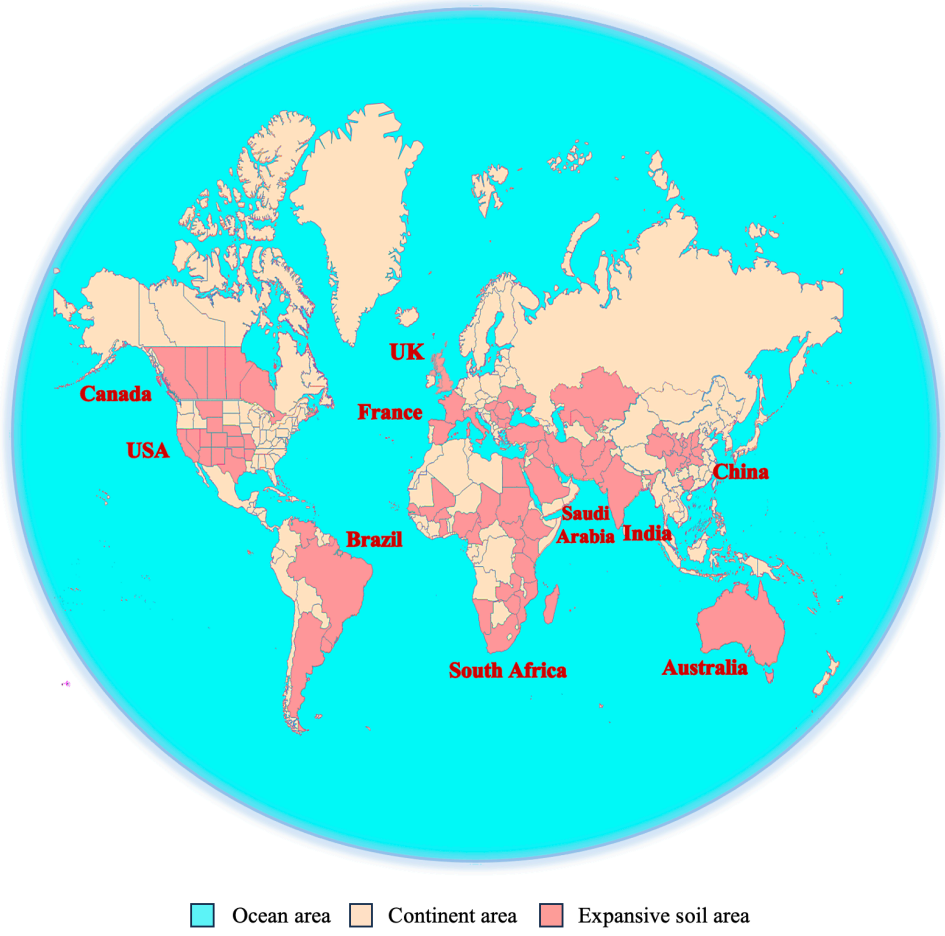


Fig. 1.1 Countries affected by expansive soils around the world

The formation of expansive soils is primarily linked to the weathering of igneous and sedimentary rocks, resulting in the development of highly active clay minerals, such as montmorillonite, which exhibit a strong affinity for water (Mitchell and Soga, 2005; Chen, 2012). During periods of rainfall or increased moisture availability, these minerals absorb

substantial amounts of water, causing an increase in volume and the generation of swelling pressures.

In addition to their well-documented swelling potential (ε%) and swelling pressure (P_s), expansive soils also exhibit significant compressibility. The compression index (C_c), which characterizes the primary consolidation behavior of soils under loading, plays a crucial role in evaluating the long-term settlement of structures founded on expansive soil deposits. Expansive soils are prone to considerable settlement when subjected to external loads. Therefore, the reliable prediction of both swelling behavior and compression index is critical for the safe and efficient design of foundations and earth structures in areas underlain by expansive soils.

More than 50% of the world's population lives in regions where expansive soils are present, leading to significant geotechnical challenges in infrastructure development. The hydro-mechanical behavior of expansive soils, including their swelling and compressibility, poses substantial risks to the serviceability and safety of civil infrastructure. Common engineering issues include differential heave, excessive foundation settlement, cracking of retaining walls, pavement distortion, and pipeline damage. These challenges often lead to high maintenance costs and safety concerns (Mokhtari and Dehghani, 2012; Zumrawi, 2013; Mohamed et al., 2014; Djellali et al., 2017; Tu and Vanapalli, 2016; Adem and Vanapalli, 2015; Liu and Vanapalli, 2017; Li et al., 2021; Venkatesan et al., 2021). Many countries invest significant resources annually to mitigate these issues. For example, in the United States alone, the annual cost of damage related to expansive soils exceeds $13 billion, with one-third of this damage occurring in residential and commercial structures (Puppala and Cerato, 2009), with approximately one-third of this damage occurring in residential and commercial buildings (Wray and Meyer, 2004). Similar economic impacts are reported worldwide, as summarized in Table 1.1 (Johnson, 1973; Ruwaih, 1987; Ng et al., 2003; Osman et al., 2005; Puppala and Cerato, 2009; Jones and Jefferson, 2012). As such, expansive soils represent one of the most problematic soil types in geotechnical engineering practice, necessitating reliable methods for predicting their swelling and compressibility behavior.

Table 1.1 The annual costs dealing with the damage to infrastructures built on expansive soils for different regions in the world (modified after Adem and Vanapalli (2013)).

Region	Annual Damage Costs	Reference
France	€ 3.3 billion	Johnson (1973)
Saudi Arabia	$ 300 million	Ruwaih (1987)
UK	£ 400 million	Driscoll and Crilly (2000)
China	¥ 100 million	Ng et al. (2003)
Australia	$ 150 million	Osman et al. (2005)
USA	$ 13 billion	Puppala and Cerato (2009)

Given the widespread distribution of expansive soils and their potential to cause severe damage to infrastructure, reliable prediction of their deformation behavior is essential. Accurate forecasting plays a key role in improving design safety and minimizing economic losses associated with ground movements. In response to these challenges, significant research efforts have been directed toward developing methods to predict the volumetric behavior of expansive soils. These methods include oedometer test procedures, empirical correlations, and suction-based approaches (Vanapalli and Lu, 2012). However, each of these methods has inherent limitations. Oedometer tests are limited to fully saturated conditions and are both time-consuming and costly. Empirical methods are typically based on limited datasets, reducing their applicability to specific soil types or regions (Noble, 1966; Zein 1987). Suction-based methods, while theoretically sound, require extensive parameter determination, including the Soil-Water Characteristic Curve (SWCC), which is difficult and labor-intensive to measure (Snethen, 1980; Fredlund, 1983). As a result, these approaches are often impractical for routine engineering applications and are insufficient as reliable tools for predicting the volumetric behavior of expansive soils (Adem, 2015).

1.2 Objectives, novelty and methodology

The primary objective of this thesis is to investigate and predict the swelling and compression behavior of expansive soils. To achieve this, a series of prediction methods and models are developed to estimate key geotechnical parameters that govern the behavior of expansive soils. The three main objectives and their associated novel contributions are summarized as follows:

1.2.1 To propose a method for predicting swelling index and swelling pressure

The swelling index (C_s) and swelling pressure (P_s) are two fundamental parameters for evaluating the expansive behavior of soils. However, obtaining these parameters through traditional laboratory tests, such as oedometer testing, is time-consuming and labor-intensive, often requiring several days or weeks to complete. Furthermore, existing empirical prediction methods are generally limited by regional datasets and soil-specific characteristics, restricting their broader applicability. To overcome these limitations, this study develops regression-based models for estimating the swelling index and swelling pressure using basic soil properties. A comprehensive database was established, incorporating expansive soil data from diverse geographical locations worldwide, thus enhancing the generalization capability of the models. Three machine learning (ML) algorithms—Multilayer Perceptron (MLP), Support Vector Machine (SVM), and Extreme Learning Machine (ELM)—were employed to capture the nonlinear relationships between soil properties and the target swelling parameters. Among these algorithms, MLP demonstrated the best prediction performance for swelling index. To improve its transparency and practical applicability, an explicit equation was derived from the optimized MLP model by extracting its architecture, weights, and biases. This formulation captures the model's internal structure and enables a direct mathematical expression of the input–output relationship, thereby enhancing its interpretability and facilitating its application in engineering practice. The prediction accuracy of the developed models was rigorously validated using statistical indicators and independent test datasets, confirming their robustness and reliability across a wide range of soil types.

The research was further extended to predict swelling pressure (P_s), which is a key parameter affecting the design and stability of structures founded on expansive soils. The same ML algorithms (MLP, SVM, and ELM) were applied to model the relationship between soil properties and swelling pressure, including both the constant volume swelling pressure and the consolidation-swell swelling pressure. Sensitivity analyses were conducted to identify the most influential variables, such as plasticity index, dry density, and initial water content, which were used to optimize the model inputs. Four explicit MLP-based prediction formulas were proposed—two for cases with complete soil property datasets and two simplified versions for situations with limited information. These explicit equations address the "black-box" nature typically associated with neural networks, thereby improving model interpretability and facilitating practical engineering use. Comprehensive validation against laboratory test results and multiple case studies confirmed that the proposed MLP-based formulas can reliably predict swelling pressure across a broad spectrum of expansive soils without the need for recalibration, offering a significant advantage over traditional empirical and regression-based approaches (Tu and Vanapalli, 2016).

1.2.2 To propose a method for predicting swelling potential

Swelling potential (ε%) is another critical parameter for evaluating the expansive behavior of soils, representing the maximum vertical heave that these soils can undergo. Conventional experimental and empirical methods are generally limited to saturated conditions, which do not adequately reflect the unsaturated environments expansive soils often experience in the field. Variations in moisture content caused by seasonal precipitation and evaporation cycles significantly affect the swelling behavior of these soils (Adem, 2015). To address these limitations, this study develops a machine learning (ML)-based method for predicting the one-dimensional vertical swelling potential of expansive soils under unsaturated conditions. Two advanced ML algorithms—Multivariate Adaptive Regression Splines (MARS) and Multilayer Perceptron (MLP)—were employed to capture the complex nonlinear relationships between swelling potential and key influencing factors. These factors include swelling index, swelling pressure, fundamental soil properties, and

parameters from the Soil-Water Characteristic Curve (SWCC). A comprehensive database of 173 expansive soil samples from different regions was compiled to ensure the generality and robustness of the developed models.

The prediction accuracy of the proposed models was rigorously validated through statistical analysis, confirming their reliability and applicability across diverse soil types. An explicit equation derived from the optimized MLP model was also proposed to enhance interpretability and facilitate practical use in engineering applications. Furthermore, a detailed sensitivity analysis was conducted using Garson's algorithm (Garson, 1991) to evaluate the relative importance of each input parameter on the predicted swelling potential. The results indicate that plasticity index, clay content, and dry density are the most influential factors. To demonstrate its application in geotechnical engineering practice, the proposed method, five case studies were analyzed, covering different field conditions such as natural ground heave due to rainfall infiltration, pipeline leakage-induced heave, and excavation-related ground movement. These case studies, conducted in regions such as Australia, Canada, China, Saudi Arabia, and the United States, confirmed that the proposed ML-based prediction models can reliably estimate swelling potential under varying environmental and geotechnical conditions. The findings highlight the superior adaptability and accuracy of the proposed models compared to traditional empirical equations.

1.2.3 To propose a method for predicting compression index

The compression index (C_s) is a fundamental parameter that governs the consolidation and settlement behavior of compressible soils, particularly expansive clays. Conventional laboratory methods for determining the compression index, such as consolidation tests, are time-consuming, labor-intensive, and often impractical for routine geotechnical investigations. Existing empirical correlations are typically developed from limited datasets and are constrained by soil-specific conditions, which restrict their general applicability. To address these limitations, this study proposes advanced machine learning approaches for predicting the compression index of expansive soils based on readily available soil properties. A comprehensive global database comprising 238 expansive soil

samples was established from nearly six decades of published literature, covering a wide range of soil types, geological conditions, and geotechnical properties. Two different prediction models were developed in this research: a hybrid NRBO-XGBoost model and an MLP-based model, both demonstrating superior accuracy and generalization capabilities. Additionally, a simplified explicit equation was derived from the optimized MLP model to facilitate practical engineering applications without requiring complex computational tools.

The proposed prediction models were rigorously validated using statistical metrics and a case study involving Black Cotton Soil (BCS), a highly compressible and expansive soil found in regions such as Australia, India, and Sudan. The explicit equation for compression index was incorporated into classical consolidation settlement equations, and the predicted settlements were compared with field-monitored data. The results demonstrated a close agreement, with a relative error of less than 7%, confirming the reliability and practical applicability of the proposed methods in engineering design. The findings indicate that the ML-based models developed in this study offer a reliable and efficient alternative to traditional methods for estimating the compression index of expansive soils, significantly improving the efficiency of settlement prediction and design processes in geotechnical engineering practice.

1.2.4 To validate the proposed models independently

To assess the prediction reliability and general applicability of the proposed models, each was evaluated individually using independent laboratory and field datasets. This validation covered four key parameters: swelling index, swelling pressure, swelling potential, and compression index.

The swelling index models were validated by comparing predicted values with measured results and by integrating them into a semi-empirical equation for estimating swelling potential. The predicted values produced results consistent with observed swelling behavior, with the MLP-based model offering stable performance across a range of soil conditions.

The swelling pressure equations, derived from the MLP model, were applied to eight different expansive soils. Predictions were compared with laboratory data under both constant-volume and consolidation-swell conditions. Results showed that the models captured the effect of suction on swelling pressure with good accuracy, particularly when more input variables were available. Simplified forms of the equations also yielded acceptable predictions, especially when data availability was limited.

For swelling potential ($\varepsilon\%$), the model was tested against five published field case studies from Australia, Canada, China, Saudi Arabia, and the United States. These cases involved various causes of ground heave, including rainfall infiltration and leakage beneath structures. The predicted swelling potentials generally agreed well with field observations, typically within one to two percentage points, confirming the model's usefulness under practical conditions.

The compression index (C_s) model was evaluated using three settlement case studies. Predicted compression index values were applied in classical consolidation equations, and the resulting settlements were compared with monitored values. The relative differences were within 5% to 14%, demonstrating the model's ability to support settlement estimation in expansive soils.

In summary, these results confirm that the proposed models can produce reliable predictions and are suitable for field-scale applications.

1.2.5 To validate the proposed models through integrated application

In addition to independent validation, the proposed models were jointly applied to predict the complete volume change behavior of expansive soils under constant-volume and consolidation-swell loading conditions. The predicted swelling index, swelling pressure, swelling potential, and compression index were used together to simulate how volumetric deformation evolves with changes in vertical stress and moisture content in oedometer tests.

Six representative expansive soils from Canada, the United States, Saudi Arabia, and India were used for validation. The predicted results showed good agreement with laboratory

measurements, with most values falling within typical engineering ranges. In one case involving a high-plasticity soil, the compression index was slightly underestimated due to limitations in the training data, but the result remained within a practical range.

These findings confirm that the models, though developed independently, can be reliably applied in combination to characterize the volume change behavior of expansive soils driven by both stress and moisture variation. This integrated framework provides a practical tool for assessing the swelling and compressibility of expansive soils using only basic soil properties.

1.3 Layout

This thesis is organized into seven chapters. Fig. 1.2 illustrates the structure of the thesis and highlights the key components addressed in each chapter.

Chapter 1 introduces the volume change behavior of expansive soils, outlines the objectives, novelty, and methodology of the research, and presents the overall structure of the thesis. This chapter establishes the significance of the study and serves as a guide for the subsequent chapters.

Chapter 2 presents a comprehensive review of the existing literature related to expansive soils, focusing on their swelling and compression behavior under unsaturated conditions. The chapter summarizes conventional experimental methods, empirical correlations, and suction-based approaches for predicting the deformation behavior of expansive soils, along with their associated limitations. This review forms the basis for the development of the prediction methods proposed in this thesis.

Chapter 3 introduces predictive models for estimating the swelling index and swelling pressure of expansive soils based on fundamental soil properties. Three machine learning algorithms—Multilayer Perceptron (MLP), Support Vector Machine (SVM), and Extreme Learning Machine (ELM)—are applied to establish reliable correlations. In addition, explicit equations based on the optimized MLP models are proposed to enhance model

transparency and practical application. The predictive performance of the developed models is validated through statistical analyses and case studies.

Chapter 4 focuses on predicting the swelling potential of expansive soils using data-driven modeling approaches. In this chapter, two machine learning techniques—Multivariate Adaptive Regression Splines (MARS) and Multilayer Perceptron (MLP)—are applied to develop predictive models based on a comprehensive dataset of expansive soils. An explicit equation is proposed based on the optimized MLP model to enhance the interpretability and practical application of the prediction method. The accuracy and generalization capability of the proposed equation are verified through five published case studies involving different soil types and environmental conditions. The results demonstrate that the equation provides reliable predictions of swelling potential and can be effectively applied in geotechnical engineering practice.

Chapter 5 presents predictive models for estimating the compression index of expansive soils. A hybrid Newton-Raphson-Based Optimizer Enhanced Extreme Gradient Boosting (NRBO-XGBoost) model and an optimized MLP model are developed to predict the compression index based on basic soil properties. An explicit equation derived from the MLP model is proposed for practical engineering use. The predictive performance of these models is validated through statistical analysis and a case study involving Black Cotton Soils (BCS), confirming their effectiveness in settlement prediction.

Chapter 6 provides a comprehensive validation of the proposed prediction models using multiple case studies. The chapter demonstrates the accuracy and practical applicability of the swelling index, swelling pressure, swelling potential, and compression index prediction models developed in Chapters 3 to 5. The case studies include different environmental and geotechnical conditions from various regions, highlighting the generalization capability of the proposed methods.

Chapter 7 demonstrates the joint use of all proposed models to interpret the overall deformation behavior of expansive soils. By linking the predicted parameters to constant-volume and consolidation-swell test results, this chapter assesses the consistency of the

models when applied together. The results highlight the practical value of the integrated approach for evaluating the combined effects of stress and moisture on soil volume change.

Chapter 8 summarizes the main findings and contributions of this thesis and provides recommendations for future work.

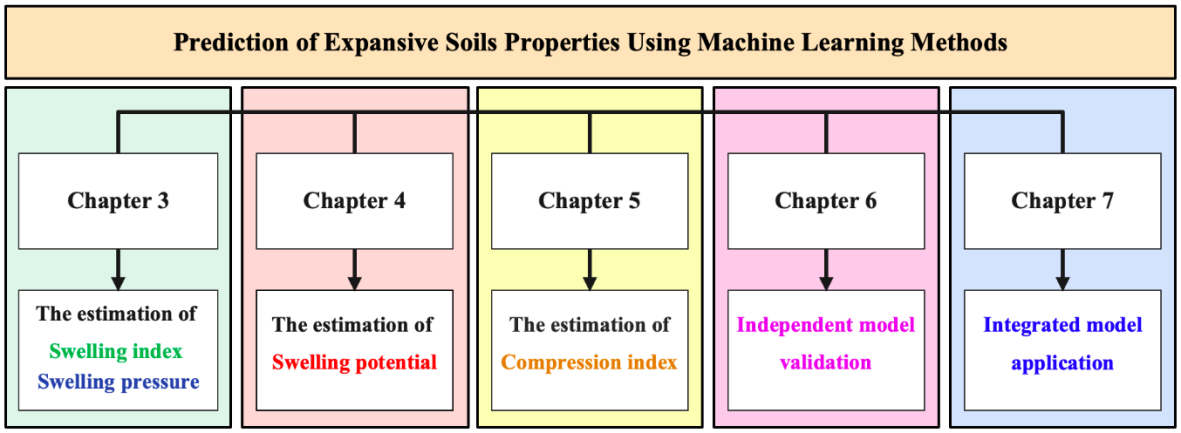


Fig. 1.2 Research framework and layout of the thesis

References

Adem, H.H., 2015. Modulus of elasticity based method for estimating the vertical movement of natural unsaturated expansive soils. Ph.D. thesis, Université d'Ottawa/University of Ottawa, Ottawa, ON.

Adem, H.H., and Vanapalli, S.K., 2013. Constitutive modeling approach for estimating 1-D heave with respect to time for expansive soils. International Journal of Geotechnical Engineering, 7(2): 199-204.

Adem, H.H., and Vanapalli, S.K., 2015. Review of methods for predicting in situ volume change movement of expansive soil over time. Journal of Rock Mechanics and Geotechnical Engineering, 7(1): 73-86.

Alonso, E.E., Vaunat, J., and Gens, A., 1999. Modelling the mechanical behaviour of expansive clays. Engineering Geology, 54(1-2): 173–183.

Bishop, A.W., 1959. The principle of effective stress. Teknisk Ukeblad, 39: 859–863.

Chen, F.H., 2012. Foundations on expansive soils. Vol. 12. Elsevier.

Djellali, A., Houam, A., and Saghafi, B., 2017. Indirect estimation of swelling pressure of clayey subgrade under pavement structures. Arabian Journal for Science and Engineering, 42: 3991–3999.

Driscoll, R., and Crilly, M. 2000. Subsidence damage to domestic buildings. Lessons learned and questions asked. Building Research Establishment, London.

Fredlund, D.G. 1983. Prediction of ground movements in swelling clays, paper presented to the Thirty-First Annual ASCE Soil Mechanics and Foundation Engineering Conference, Earle Brown Center, University of Minnesota, Minneapolis, MN.

Fredlund, D.G., and Morgenstern, N.R., 1977. Stress state variables for unsaturated soils. Journal of the Geotechnical Engineering Division, 103(5): 447–466.

Fredlund, D.G., and Rahardjo, H., 1993. Soil mechanics for unsaturated soils. John Wiley & Sons.

Gao, Y., Sun, D.A., Zhou, A., and Li, J., 2020. Predicting shear strength of unsaturated soils over wide suction range. International Journal of Geomechanics, 20(2): 04019175.

Garson, G.D. 1991. Interpreting neural-network connection weights. AI Expert, 6: 46–51.

Huang, J., Ji, M., Xie, Y., Wang, S., He, Y., and Ran, J., 2016. Global semi-arid climate change over last 60 years. Climate Dynamics, 46: 1131–1150.

Johnson, L. D., 1973. Influence of suction on heave of expansive soils.

Jones, L.D., and Jefferson, I., 2012. Expansive soils.

Leong, E.C., and Rahardjo, H., 1997. Review of soil-water characteristic curve equations. Journal of Geotechnical and Geoenvironmental Engineering, 123(12): 1106–1117.

Li, T., Kong, L., and Guo, A., 2021. The deformation and microstructure characteristics of expansive soil under freeze–thaw cycles with loads. Cold Regions Science and Technology, 192: 103393.

Liu, Y., and Vanapalli, S.K., 2017., Influence of lateral swelling pressure on the geotechnical infrastructure in expansive soils. Journal of Geotechnical and Geoenvironmental Engineering, 143(6): 04017006.

Lu, N., and Likos, W.J., 2006., Suction stress characteristic curve for unsaturated soil. Journal of Geotechnical and Geoenvironmental Engineering, 132(2): 131–142.

Mitchell, J.K., and Soga, K., 2005. Fundamentals of soil behavior. 3rd ed. John Wiley & Sons, New York.

Mohamed, O.Z., Taha, Y.K., and El-Aziz, E.-S.M.A., 2014. Field study of the distribution of lateral swelling pressure of expansive soil on retaining structure. JES. Journal of Engineering Sciences, 42(2): 289–302.

Mokhtari, M., and Dehghani, M., 2012. Swell-shrink behavior of expansive soils, damage and control. Electronic Journal of Geotechnical Engineering, 17: 2673–2682.

Nelson, J.D., Chao, K.C., Overton, D.D., and Nelson, E.J., 2015. Foundation engineering for expansive soils. John Wiley & Sons.

Ng, C.W.W., Zhan, L.T., Bao, C.G., Fredlund, D.G., and Gong, B.W., 2003. Performance of an unsaturated expansive soil slope subjected to artificial rainfall infiltration. Geotechnique, 53(2): 143–157.

Noble, C.A. 1966. Swelling measurements and prediction of heave for a lacustrine clay. Canadian Geotechnical Journal, 3(1): 32–41.

Osman, N., McManus, K., and Ng, A., 2005. Management and analysis of data for damage of light structures on expansive soils in Victoria, Australia.

Puppala, A.J., and Cerato, A., 2009. Heave distress problems in chemically-treated sulfate-laden materials. Geo-Strata—Geo Institute of ASCE, 10(2): 28.

Puppala, A.J., Punthutaecha, K., and Vanapalli, S.K., 2006. Soil-water characteristic curves of stabilized expansive soils. Journal of Geotechnical and Geoenvironmental Engineering, 132(6): 736–751.

Ruwaih, I.A., 1987. Experiences with expansive soils in Saudi Arabia. In Proceedings of

the 6th International Conference on Expansive Soils, New Delhi, India, pp. 317–322.

Sheng, D., Zhou, A., and Fredlund, D.G., 2011. Shear strength criteria for unsaturated soils. Geotechnical and Geological Engineering, 29: 145–159.

Snethen, D.R. 1980. Characterization of expansive soils using soil suction data. In Proceedings of the Fourth International Conference on Expansive Soils. Denver, Colorado, pp. 54–75.

Tang, C., and Shi, B., 2011. Swelling and shrinkage behaviour of expansive soil during wetting-drying cycles. Chinese Journal of Geotechnical Engineering, 33(9), 1376-1384.

Vanapalli, S., Fredlund, D., Pufahl, D., and Clifton, A., 1996. Model for the prediction of shear strength with respect to soil suction. Canadian Geotechnical Journal, 33(3): 379–392.

Vanapalli, S., and Lu, L., 2012. A state-of-the-art review of 1-D heave prediction methods for expansive soils. International Journal of Geotechnical Engineering, 6(1): 15–41.

Venkatesan, S., Droniou, J., Roy, I., Robert, D., and Zhou, A., 2021. Application of diffusion-advection equations to in-field monitoring of soil suction profiles. Computers and Geotechnics, 139, 104329.

Wray, W.K., and Meyer, K.T., 2004. Expansive clay soil... a widespread and costly geohazard. Geo-Strata—Geo Institute of ASCE, 5(4): 24.

Zein, A.K. 1987. Comparsion of measured and predicted swelling behaviour of a compacted Black Cotton Soil. In Proceedings of the Sixth International Conference on Expansive Soils. New Delhi, India, pp. 121–126.

Zumrawi, M.M., 2013. Pavement design for roads on expansive clay subgrades. University of Khartoum Engineering Journal, 3(1).

CHAPTER 2

LITERATURE REVIEW

2.1 Introduction

Expansive soils are widely found in arid and semi-arid regions of the world that exist in an unsaturated state and exhibit pronounced swell-shrink behaviors due to natural wetting and drying cycles. The volume of these soils increases as they imbibe moisture, leading to softening; conversely, they shrink and harden as they lose water, often resulting in desiccation cracks. This behavior is particularly evident in regions with distinct wet and dry seasons. During the rainy season, expansive soils near the surface transit from an unsaturated to a saturated state, with maximum ground heave occurring at fully saturated condition. In contrast, during the dry season, evaporation drives the saturated soil conditions back to an unsaturated or nearly dry state, leading to significant volume reduction and desiccation cracking. Volume changes in expansive soils pose considerable risks to geo-infrastructure, particularly lightly loaded structures such as the pavements and residential buildings with shallow foundations. This chapter focuses on elucidating the fundamental principles of unsaturated soil mechanics and the governing volume change behavior in expansive soils. Furthermore, it critically evaluates various methods available in the literature for predicting swelling properties such as the swelling index, swelling pressure, and swelling potential highlighting their respective advantages and limitations. Drawing on insights from the literature, the chapter concludes by emphasizing the need for a straightforward, reliable, and universally applicable approach to predict the swelling properties of expansive soils.

2.2 Expansive minerals

Expansive soils typically have large clay content, high plasticity, and an abundance of hydrophilic clay minerals that include montmorillonite and illite. The soils that are rich in

montmorillonite exhibit the greatest water absorption capacity, leading to significant expansion, while soils with illite typically exhibit lesser swelling. The swelling potential of clay minerals is closely linked to their microstructure, which is predominantly defined by a lattice structure featuring flat surfaces with a net positive charge. Within the lattice structure of clay minerals, two fundamental molecular units are present: the silica tetrahedron and the alumina octahedron. The silica tetrahedron, composed of a central silicon atom with a 4+ valence, is bonded to four surrounding negatively charged oxygen atoms. This tetrahedral structure forms a repeating pattern in the lattice, where six silica tetrahedra are arranged to share oxygen atoms at their lower surfaces, as depicted in Fig. 2.1. Similarly, the alumina octahedron consists of a central aluminum atom surrounded by six hydroxyl ions. In the lattice, these octahedra form sheet structures, with four such units making up each sheet, as illustrated in Fig. 2.2.

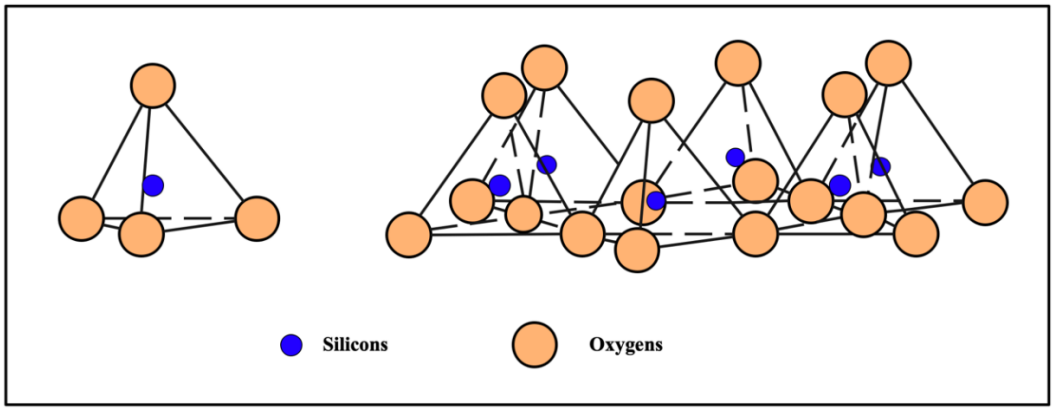


Fig. 2.1 A single silica tetrahedron and the sheet structure of silica tetrahedrons arranged in a hexagonal network (modified after Mitchell and Soga (2005))

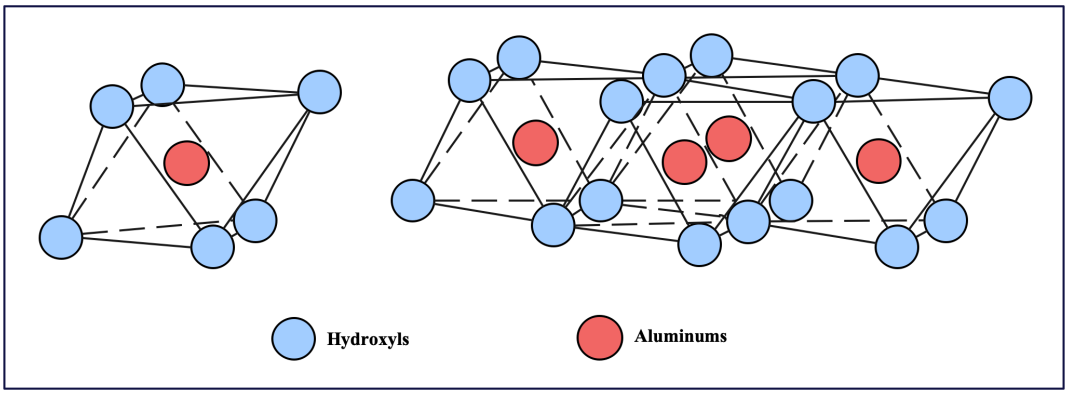


Fig. 2.2 A single octahedral unit and the sheet structure of the octahedral units (modified after Mitchell and Soga (2005))

The sheet structures of silica tetrahedra and aluminum octahedra can combine to form two distinct lattice structures, as illustrated in Fig. 2.3. The microstructures of montmorillonite and illite are closely associated with these two types of unit lattice structures. The first type is a 1:1 unit lattice structure, consisting of one silica tetrahedral layer and one aluminum octahedral layer, as shown in Fig. 2.3a. The second type is a 2:1 unit lattice structure, characterized by a sandwich-like arrangement with two silica tetrahedral layers flanking one aluminum octahedral layer, as shown in Fig. 2.3b. The unique microstructures of montmorillonite and illite arise from the stacking of multiple lattice structures, as illustrated in Fig. 2.4.

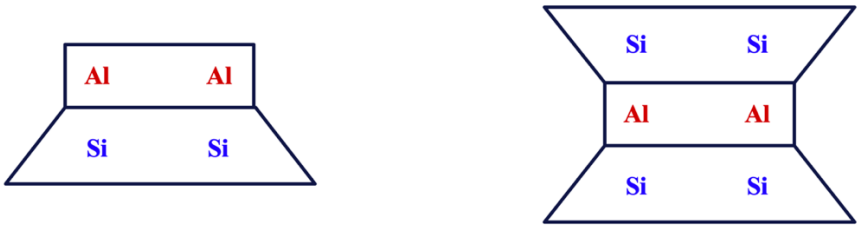


Fig. 2.3 Schematic diagrams of the structures of (a) 1:1 unit lattice, (b) 2:1 unit lattice (modified after Mitchell and Soga (2005))

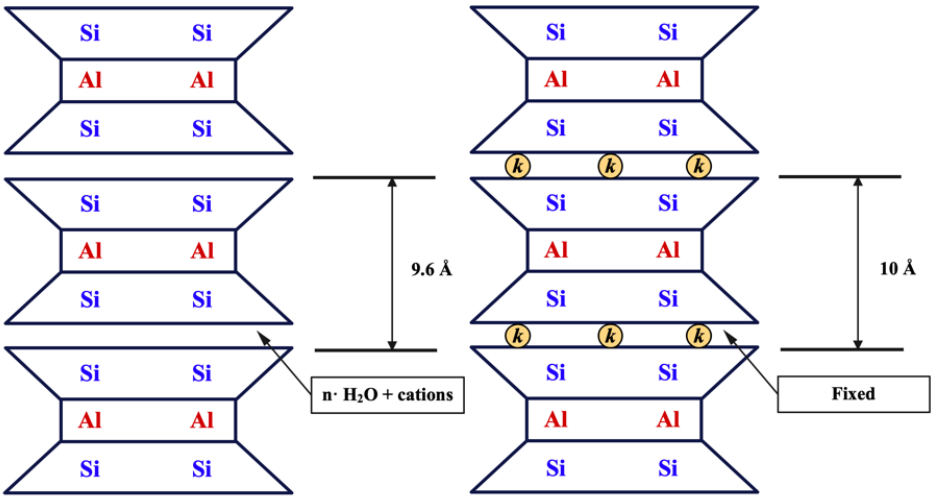


Fig. 2.4 Schematic diagrams of the structures of (a) montmorillonite, (b) illite (modified after Mitchell and Soga (2005))

Montmorillonite consists of multiple unit lattices with a 2:1 structure, as highlighted in Fig. 2.4a. The bonding between successive layers involves van der Waals forces and cations that balance charge deficiencies in the structure. These bonds, being weak, are easily disrupted by the adsorption of water (Mitchell and Soga, 2005). Consequently, the expansion of montmorillonite after absorbing water is highly pronounced. Depending on the type of exchangeable cations in the interlayer, montmorillonite can be classified mainly into sodium montmorillonite (Na-montmorillonite) or calcium montmorillonite (Ca-montmorillonite). The hydration capacity and swelling behavior of Na-montmorillonite are much greater than those of Ca-montmorillonite because Na^+ ions have higher hydration energy and weaker interlayer bonding, allowing more water molecules to enter between layers. In contrast, Ca-montmorillonite exhibits relatively restrained expansion due to stronger electrostatic attraction between divalent Ca^{2+} ions and the clay layers (Mitchell and Soga, 2005).

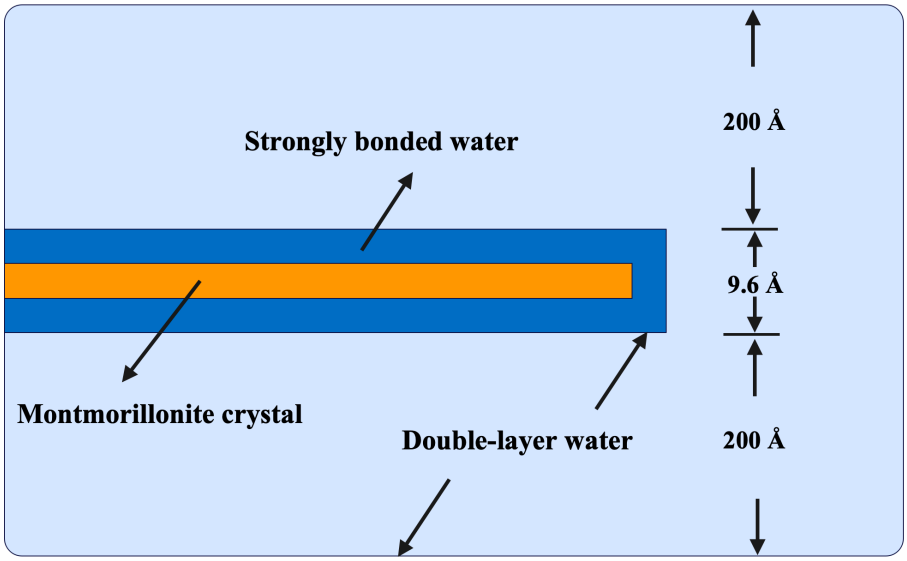
The clay mineral illite shares a structural similarity with montmorillonite, with aluminum atoms partially replacing silicon atoms within the lattice. A key distinction lies in the presence of potassium ions positioned between the silica sheets and adjacent crystal layers, as shown in Fig. 2.3b. The potassium ions contribute to the relatively fixed layers within

the illite structure, making it difficult for polar ions to infiltrate and thereby restricting expansion. Additionally, the potassium ions form strong bonds between layers, limiting their ability to undergo ion exchange. As a result, the interlayer potassium bonding in illite maintains stable basal spacing, even in the presence of water, which significantly reduces its swelling potential compared to montmorillonite (Mitchell and Soga, 2005). In comparison, the expansion characteristics exhibited by illite falls behind montmorillonite.

2.3 Swelling mechanism

The mechanism associated with soil swelling has been described by several researchers (e.g., Anderson et al., 1973; Schafer and Singer, 1976; Nelson and Miller, 1997; Mitchell and Soga, 2005; Chen, 2012). One proposed mechanism of soil swelling is linked to the interlayer expansion of the clay mineral montmorillonite, influenced by hydration energy, as shown in Fig. 2.5a. The molecular structure of montmorillonite exhibits a pronounced affinity for attracting and retaining water molecules between its clay lattice sheets. During the wetting process of unsaturated expansive soil, montmorillonite can absorb substantial quantities of water molecules into the gaps between the clay sheets. With increased water absorption, the bond layers are compelled to move apart, resulting in an elevation of swelling pressure and an expansion of the soil volume. Another suggested mechanism of soil swelling is associated with the diffused double layers of the clay mineral montmorillonite driven by electrical effects, as shown in Fig. 2.5b. As per the earlier summarized discussions, the clay mineral surface carries a negative charge, attracting dipolar water molecules in the surrounding water. The positively charged end of the water molecule moves closer to the clay layer and adheres to the surface, creating a water film, also known as strongly bound water. This assembly of a clay layer and a strongly bound water film constitutes a diffuse double layer structure. When two such structures approach and reach proximity, the negatively charged strongly bound water layers on both sides repel each other, resulting in the separation of the double-layer structures and causing swelling. Subsequently, as the strongly bound water surfaces of the two double-layer structures are both negatively charged, they attract additional dipolar water molecules or hydrated cations from the water or solution, entering the space between the clay sheets. To maintain charge

balance, more water is drawn between the clay sheets to neutralize these free charges, leading to further diffusion of the double-layer structure. Moreover, the chemical composition of the pore water also affects the swelling mechanism. Different types of exchangeable cations and their concentrations can change the diffuse double layer thickness and the interparticle repulsive forces. Soils dominated by monovalent cations such as Na^{+} exhibit higher swelling potential than those dominated by divalent cations such as Ca^{2+} or Mg^{2+} (Mitchell and Soga, 2005; Zou et al., 2018). Therefore, the swelling behavior of expansive soils is a coupled outcome of mineralogical structure, electrochemical interaction, and pore-water chemistry.



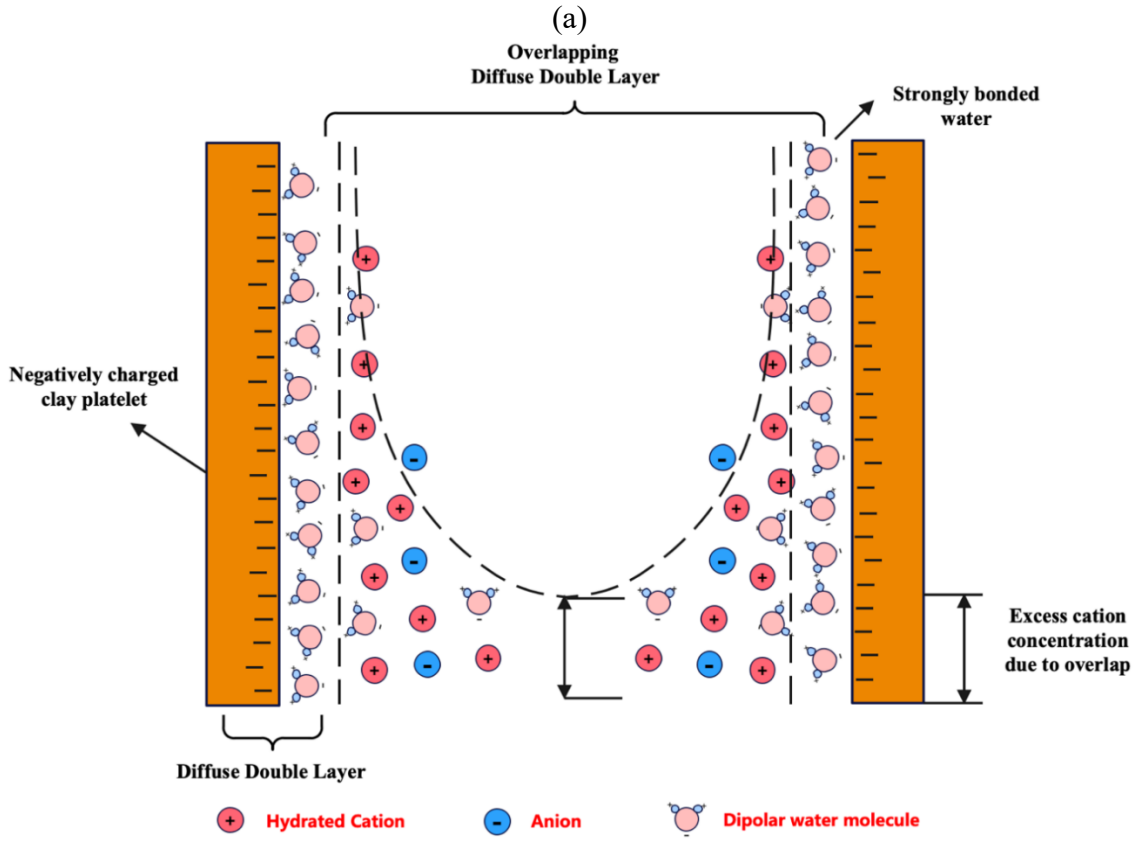


Fig. 2.5 (a) Schematic diagrams of the interlayer expansion of the clay mineral montmorillonite (b) Schematic diagrams of diffuse double layers

2.4 Factors affecting soil movement

Expansive soils are typically subjected to prolonged cycles of expansion and contraction due to periodic wet-dry cycles. In an unrestricted, free-swelling state, these volumetric changes occur uniformly in all three dimensions, leading to consistent swelling characteristics in every direction. However, scenarios that are encountered in engineering practice often have volume changes constrained in certain directions. Typically, soil swelling is classified into two types: vertical and lateral. In lightly loaded structures, such as residential buildings with shallow foundations and pavements, expansive soils primarily experience vertical deformation. This occurs because the self-weight of these structures is insufficient to counteract the vertical swelling pressure, potentially leading to structural

damage, including wall cracks, differential settlement of foundations, and pavement distress (Chen, 1975; Fredlund and Rahardjo, 1993). Lateral deformation, on the other hand, is more common in earth-retaining structures with expansive soil as backfill material. Inadequate drainage can lead to water accumulation in the active zone, causing significant lateral expansion and imposing substantial lateral swelling pressure against the retaining wall. The stiffness and stability of the retaining wall are critical in resisting these lateral swelling forces (Liu and Vanapalli, 2018). If the wall lacks sufficient stiffness, it may become susceptible to lateral deformation, and in severe cases, sliding failure can occur if the passive earth pressure is inadequate to counterbalance the active earth pressure. Several factors influence the deformation characteristics of expansive soils. The primary influencing factors can be succinctly summarized as follows:

2.4.1. Soil type

Fine-grained clay exhibits a significantly higher propensity for swelling compared to coarse-grained soils such as gravel and sand. This is primarily due to the presence of swelling minerals such as montmorillonite and illite within fine-grained soils such as clay that constitute of smaller particle sizes. Clay particles have a larger specific surface area, which is strongly correlated with the swelling index (Ross, 1978), and a relatively higher surface charge that attracts surrounding water molecules, causing them to adhere to the particle surfaces and induce expansion. In contrast, sand particles are larger with a smaller specific surface area, resulting in a comparatively lower surface charge. The larger gaps between sand particles also facilitate more unrestricted water movement, leading to weaker water absorption and retention capabilities. As a result, sandy soils exhibit a much lower swelling potential compared to fine-grained clays.

2.4.2. Soil structure

The structural organization of soil significantly affects its swelling characteristics, with flocculated and dispersed configurations yielding markedly different behaviors. In a flocculated structure, soil particles cluster into larger, more stable aggregates. This aggregate formation leads to the development of larger pore spaces and diminishes the

molecular forces between individual clay particles, resulting in reduced crystalline and osmotic swelling. Conversely, a dispersed soil structure features particles aligned in parallel, lacking significant aggregation. This alignment fosters smaller pores and stronger inter-particle interactions, making the soil more susceptible to both crystalline and osmotic swelling due to the enhanced proximity and orderly arrangement of particles. These structural variations fundamentally influence the capacity of soils to absorb and retain water, thus directly impacting its swelling potential (Gokhale and Jain, 1972; Elbrahmi and Zoukaghe, 2016).

2.4.3. Initial water content

The swelling behavior of expansive soil is significantly influenced by its initial water content. A lower initial water content in the soil indicates a higher potential for water absorption, which can lead to more substantial swelling (Tu and Vanapalli, 2016). On the other hand, a higher initial moisture content tends to result in smaller volumetric changes upon subsequent water absorption. This understanding is crucial for predicting the expansive behavior of soils under varying moisture conditions.

2.4.4. Plasticity index

The plasticity index is a key indicator for assessing the plastic characteristics of soil. It is calculated as the difference between the liquid limit and the plastic limit. This index primarily represents the soil water absorption potential and reflects the level of adsorption and cohesion among soil particles. Generally, a higher plasticity index is associated with greater soil swelling upon water absorption (Israr et al., 2014).

2.4.5. Dry density

A higher dry density is associated with a lower void ratio, which leads to closer particle contact and stronger interparticle forces upon wetting. The reduction in void ratio restricts the space available for water infiltration, resulting in a more significant buildup of swelling pressures as expansive minerals, such as montmorillonite, absorb water. Furthermore, a higher dry density implies a greater number of soil particles per unit volume, indicating a

higher concentration of swelling mineral components, thereby further enhancing the swelling potential.

The relationship between dry density and swelling pressure is well-established in the literature. Fredlund and Rahardjo (1993) demonstrated that an increase in dry density typically results in elevated swelling pressure in expansive soils due to the reduction in void ratio, which enhances particle contact and increases the stress transmitted within the soil matrix during wetting. Komine and Nobuhide (2003) investigated the effect of dry density on the swelling behavior of various bentonite mixtures and concluded that swelling pressure increases with higher initial dry density, particularly in soils with a greater proportion of bentonites. Chen (2012) similarly observed that soils with higher dry densities tend to exhibit increased swelling pressures and volume changes upon wetting. Tu and Vanapalli (2016) further emphasized that expansive soils with higher dry densities generally exhibit more substantial constant volume swelling pressures due to the denser packing of particles, which intensifies force interactions during the hydration process.

2.4.6. Soil salinity

The salt content in soil significantly influences its physical and chemical properties, thereby affecting the swelling behavior of expansive soils. Soil salts induce an osmotic effect, where higher salt concentrations increase the osmotic pressure of the soil water, effectively reducing the available water content. This reduction inhibits the soil's swelling ability, leading to limited expansion. Additionally, soil salts can alter the soil structure through ion exchange processes, impacting swelling properties. For instance, a high-concentration sodium chloride solution can transform a dispersed soil structure into a flocculated one, increasing surface roughness and reducing the swelling potential. Furthermore, a high concentration of sodium chloride solution reduces the thickness of the diffuse double layer, thereby curbing the swelling of expansive soils by minimizing the repulsive forces between clay particles (Zou et al., 2018).

2.4.7. Loading

The repulsive force between the soil particles is reduced due to the influence of application of vertical direction, for example as load from the building superstructure to the expansive soil foundation (Nelson and Miller, 1997). This principle aligns with the findings of Sridharan et al. (1986), who conducted a comprehensive study on the effects of loading conditions and loading rate on swelling pressure in clays. Their research indicates that different loading scenarios significantly impact the swelling behavior of soils. For instance, the free-swell test, which simulates conditions with minimal external loading, produces the highest swelling pressure, whereas the loaded-swell test, which applies a greater load, results in the lowest swelling pressure. The constant volume test yields an intermediate value, further demonstrating how applied load influences soil expansion. Additionally, Sridharan et al. (1986) observed that the rate at which the load is applied plays a crucial role: slower loading rates or smaller load increments result in higher swelling pressures, while faster rates lead to reduced pressures. This underscores the importance of allowing sufficient time for the soil to respond to the applied load to achieve accurate measurements. Moreover, the study highlights that the sequence of loading and unloading, or stress path, is critical in determining the final swelling pressure, with different stress paths yielding significantly varied results.

2.4.8. Permeability

Soil permeability refers to the ease of water to flow through soil pores. Expansive soils, characterized by their abundance of fine particles, have very small pore diameters, which restrict the rapid and unimpeded flow of water, unlike in sands, resulting in poor permeability. Bentonite, a type of clay with extremely low permeability, is widely used as a backfill material in basement waterproofing systems (Daniels et al., 2017). Shirazi et al. (2010) conducted an in-depth study on the permeability characteristics of bentonite and bentonite-sand mixtures, revealing that the coefficient of permeability varies significantly depending on the bentonite content and void ratio. Their results show that permeability decreases as the bentonite proportion increases, with values ranging from approximately 10^{-8} to 10^{-12} cm/s, depending on the specific mixture and conditions. Additionally, the study

highlighted that the permeability of these mixtures is strongly influenced by compaction energy and the method of specimen preparation, with higher compaction energies generally leading to lower permeability. However, expansive soils can develop fissures and cracks through multiple dry-wet cycles, which can accelerate water infiltration and lead to rapid soil expansion. It is important to note that the swelling potential of expansive soils may decrease after repeated drying-wetting cycles (Tang and Shi, 2011).

2.5 Unsaturated soils

In conventional geotechnical engineering practice, soils are typically assumed to be fully saturated (i.e., voids within the soil are entirely filled with water) and traditional soil mechanics principles are used for their interpretation. This assumption is valid for the soil beneath the groundwater table. Soil above the groundwater table is typically in an unsaturated state and the voids partially filled by both water and air. Due to this reason, pore-water pressures in the soil are positive below the groundwater table and negative above it. The degree of saturation of topsoil is susceptible to environmental factors that include evaporation, rainfall, vegetation, and the structures that are constructed, leading to fluctuations in pore water pressure. During the dry season, elevated temperatures intensify surface evaporation and plant transpiration, causing the near-surface soil layer to dry and crack due to excessive water loss. Conversely, during the rainy season, intense rainfall accumulates water in the topsoil, increasing its degree of saturation and reducing negative pore water pressure towards zero. Soil layers beneath geotechnical infrastructures, such as foundations and pavements, are less influenced by environmental factors. Their degree of saturation and pore-water pressure exhibit lower fluctuations and remain in a hydrostatic state. A typical suction profile along depth is illustrated in Fig. 2.6.

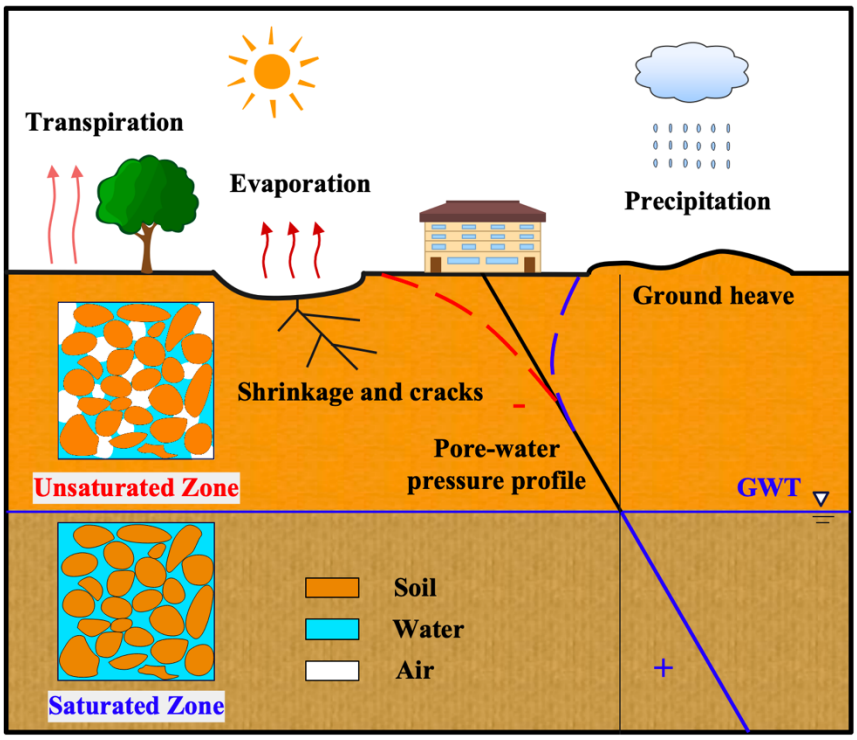


Fig. 2.6 Variation of suction with respect to depth

Total suction, defined as the overall free energy of soil water, is determined as the ratio of the partial pressure of water vapor in equilibrium with a solution mirroring the composition of the soil water to the partial pressure of water vapor in equilibrium with a reservoir of pure water (Aitchison, 1965). The calculation of total suction adheres to the principles of thermodynamics, employing the Kelvin equation (Richards, 1965), as shown in Eq. 2.1.

$$\psi = -\frac{RT}{V_{mol}} \ln(R_h) \tag{2.1}$$

where R_h is the relative humidity, which equals the ratio between the partial pressure of pore water vapor P and the saturation pressure of water vapor over a flat surface of pure water at the same temperature P_0, R is the universal gas constant (8.31432 J/(mol K)), V_{mol} is the molecular volume of water vapor (0.01802 m^3), and T the absolute temperature (°K).

The total suction can be decomposed into two components: matric suction and osmotic suction, expressed in the Eq. 2.2 :

$$\psi = (u_a - u_w) + \pi \qquad (2.2)$$

where, (u_a - u_w) is matric suction, u_a is pore-air pressure, u_w is pore-water pressure, π is the osmotic suction.

2.5.1 Matric suction

Matric suction is defined as the differential between the pore air and pore water pressure (Fredlund and Rahardjo, 1993). Matric suction, viewed through the lens of thermodynamics, is alternatively defined as the ratio of the partial pressure of water vapor in equilibrium with the soil water to the partial pressure of water vapor in equilibrium with a solution matching the composition of the soil water (Aitchison, 1965). Matric suction is frequently associated with capillarity induced by the surface tension of water. In the soil, small pores function as capillaries, elevating water in the soil above the water table and creating a water column with negative pressure, as illustrated in Fig. 2.7.

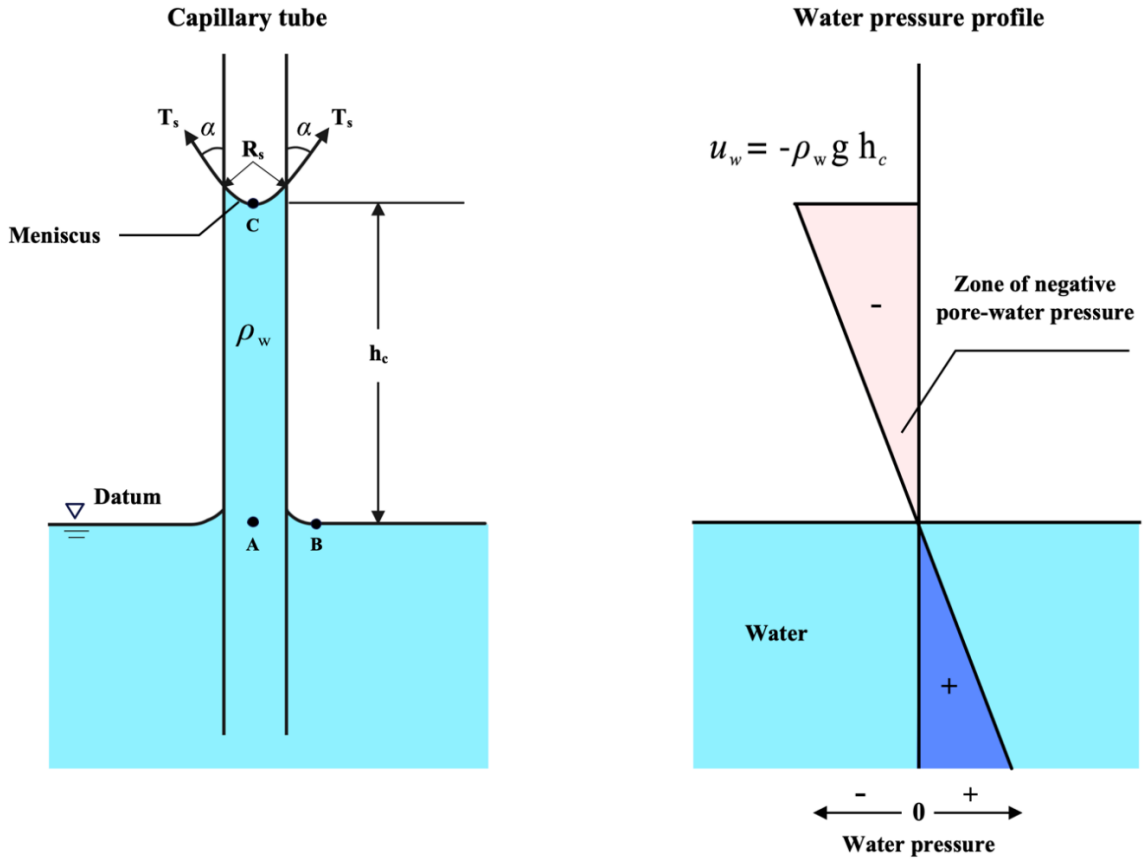


Fig. 2.7 Capillarity and negative water pressure (modified after Fredlund and Rahardjo (1993))

The meniscus forms on the water surface within the capillary pores. The upper part of the meniscus represents air pressure, while the lower part signifies water pressure. The disparity between the two is termed matric suction. The magnitude of matric suction correlates with surface tension and the radius of curvature of the meniscus, as depicted in Eq. 2.3 (Fredlund and Rahardjo, 1993).

$$(u_a - u_w) = \frac{2T_s}{R_s} \tag{2.3}$$

where T_s is the surface tension of water, and R_s is the radius of curvature.

Based on the correlation, it can be deduced that the magnitude of matric suction is directly proportional to the surface tension of water while inversely proportional to the radius of curvature of the meniscus. The radius of curvature of the meniscus is directly linked to the diameter of the capillary. A smaller capillary diameter results in a reduced radius of curvature and an amplified generation of matric suction (Janssen and Dempsey, 1980). In general, fine-grained soil exhibits smaller particle diameter and pore radius compared to coarse-grained soil, resulting in higher matric suction, as shown in Fig. 2.8.

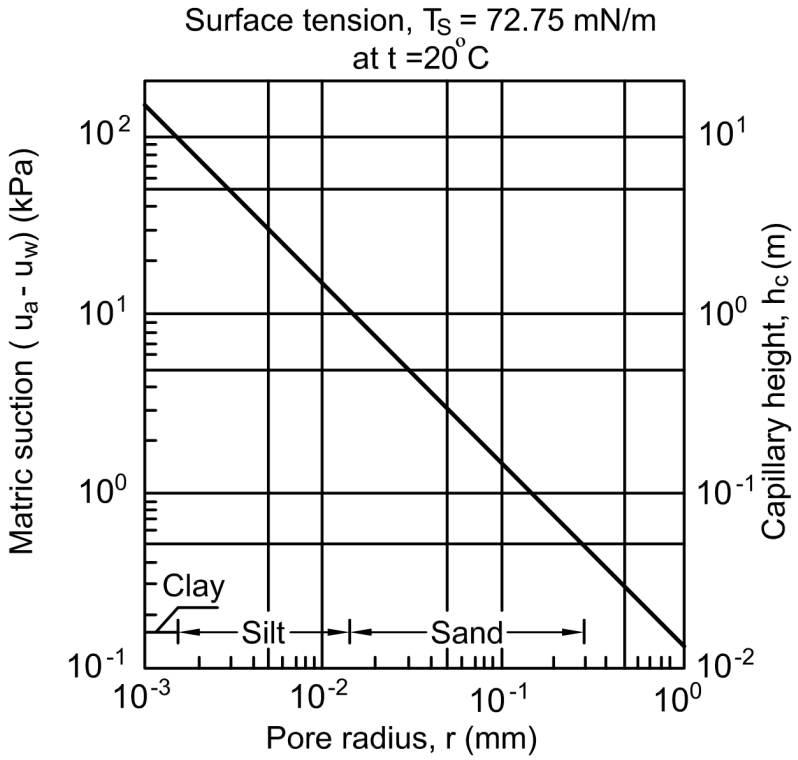


Fig. 2.8 The relationship among pore radius, matric suction, and capillary height (modified after Fredlund and Raharjio (1993))

As saturated soil undergoes dehumidification, its degree of saturation gradually decreases with the introduction of air, a solid-liquid-air interface emerges between the soil particles, illustrated in Fig. 2.9. The water phase becomes disconnected and remains in the form of menisci or liquid bridges at the interparticle contacts as the soil continues to dry. The curved air-water interface produces pore water tension, which, in turn, generates interparticle compressive forces (suction forces) that only act at particle contacts (Mitchell and Soga, 2005).

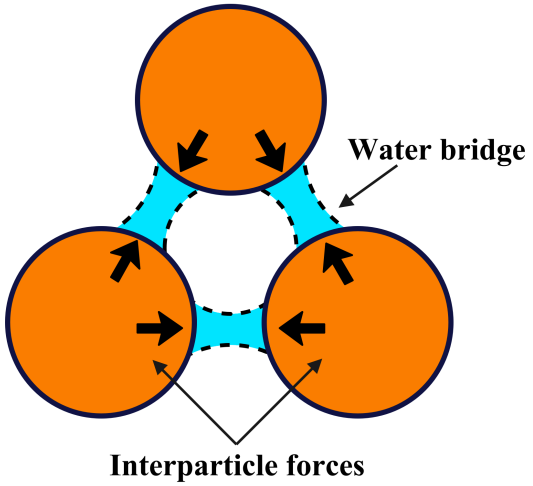


Fig. 2.9 Microscopic soil-water-air interaction in unsaturated soils (modified after Mitchell and Soga (2005))

2.5.2 Osmotic suction

Osmotic suction is the equivalent suction derived from the measurement of partial pressure of the water vapor in equilibrium with a solution identical in composition with the soil water, relative to the partial pressure of water vapor in equilibrium with free pure water (Aitchison, 1965). The osmotic suction can be calculated using van't Hoff equation (Eq. 2.4).

$$\pi = R_s T_s \Delta c \tag{2.4}$$

where Δc is the difference in the concentration between two solutions.

Osmotic suction, related to the salt content in the pore water of unsaturated soils, plays a significant role in influencing the mechanical behavior of soils. Thyagaraj and Salini (2015) and Rao et al. (2006) have investigated the impact of osmotic suction on the matric and total suctions of compacted expansive soils. Thyagaraj and Salini (2015) found that an increase in osmotic suction reduces the diffuse double layer thickness, leading to structural changes such as a decrease in micropore size and an increase in macropore size, which

subsequently elevates matric suction. Rao et al. (2006) further suggested that osmotic suction differences, driven by salt diffusion, can significantly alter the volume change behavior of expansive soils. However, both studies indicate that while osmotic suction affects the swelling response, its influence is secondary to that of matric suction, which primarily governs the mechanical behavior of soils during wetting. This interplay between osmotic and matric suctions is crucial in determining the overall behavior of expansive soils. Although osmotic suction dominates total suction measurements, as noted by Miller and Nelson (2006), its impact on soil behavior is relatively minor compared to changes in matric suction, with salt addition having little effect on the volumetric response to matric suction variations. Therefore, when interpreting the behavior of unsaturated soils, it is recommended to focus primarily on matric suction, assuming a constant ionic concentration influencing osmotic suction (Alonso et al., 1987). Thus, matric suction alone has been closely linked to the engineering properties of soils, serving as a valuable tool for numerous researchers to estimate soil characteristics such as hydraulic conductivity, swelling behavior, shear strength, thermal conductivity, and compressibility e.g., (van Genuchten, 1980; Alonso et al., 1990; Vanapalli et al., 1996; Rassam and Williams, 1999; Vanapalli and Oh, 2010; Adem and Vanapalli, 2016; Tu and Vanapalli, 2016; Lu et al., 2019; Chen et al., 2020; Ying et al., 2021).

2.6 Volumetric behavior in unsaturated soils

This section provides a succinct literature review on stress state variables and theoretical framework for interpreting volume change behavior of unsaturated soils. The volume change behavior of expansive soils can be elucidated by employing the mechanics of unsaturated soils, utilizing constitutive relationships that connect deformation state variables to stress state variables. These deformation state variables encompass alterations in both soil structure and water volume within an unsaturated soil element.

2.6.1 Stress state variables

As a pioneer in the field of conventional soil mechanics, Terzaghi (1936) introduced the concept of effective stress for saturated soils, a concept further advanced by several

researchers (e.g., Rendulic, 1936; Bishop and Eldin, 1950; Nur and Byerlee (1971); Skempton, 1984; Helm, 1987; De Boer and Ehlers, 1990). Following these foundational works, the effective stress principle has found extensive application in modeling various geotechnical engineering scenarios, establishing a straightforward connection between elastic deformation and stress within the soil. The equilibrium state of saturated soil is intricately linked to effective stress, with changes in effective stress capable of disturbing this equilibrium and inducing alterations in both the shear strength and volume of the soil.

The effective stress σ' is a combination of both the externally applied stress σ and the internal pressure of pore water u_w, and it is expressed in Eq. 2.5

$$\sigma' = \sigma - u_w \tag{2.5}$$

Terzaghi's effective stress has gained widespread acceptance for saturated soils. The success of applying Terzaghi's effective stress principle to saturated soils has motivated early researchers to extend this principle to unsaturated soils, offering unified formulations of effective stress as shown in Table 2.1 (Hilf, 1956; Croney et al., 1958; Bishop, 1959; Donald, 1961; Jennings, 1961; Newland, 1965; Richards, 1965; Aitchison and Peter, 1973; Lambe and Whitman, 1979; Allam and Sridharan, 1981; Aitchison, 1985; Khalili and Khabbaz, 1998; Jommi, 2000).

Table 2.1 Effective stress equations for unsaturated soils modified after (Vanapalli, 1994; Lu, 2010)

Author(s)	Equation	Notations	
Hilf (1956)	$\sigma' = \sigma - (u_a + u_c)$	u_c : capillary pressure	(2.6)

Croney et al. (1958)	$\sigma' = \sigma - \beta' u_w$	β' : holding or bonding factor which is a measure of the number of bonds under tension effective in contributing to shear strength of the soil	(2.7)
Bishop (1959)	$\sigma' = (\sigma - u_a) + \chi (u_a - u_w)$	χ : effective stress parameter related to the soil degree of saturation	(2.8)
Aitchison (1960)	$\sigma' = \sigma + \psi p''$	ψ=parameter varying between zero to one depending on degree of saturation p'': pore-water pressure deficiency	(2.9)
Lambe (1960)	$\sigma' = \sigma a_m + u_a a_a + u_w a_w + R\text{-}A$	σ'= constant stress where the particles are in mineal-mineal contact a_m= ratio of mineal-mineal contact to total area a_a= friction of total area that is air-mineral contact a_w= friction of total area that is water-mineral contact R-A= repulsive minus attractive pressure between particles	(2.10)
Donald (1961)	$\sigma' = \sigma + p''$	p'': pore-water pressure deficiency	(2.11)
Jennings (1961)	$\sigma' = \sigma - \beta p''$	β : statistical factor of the same type as the contact area	(2.12)
Skempton (1961)	$\sigma' = \sigma\text{-}(1\text{-}C_s/C) S_x u_w$	C_s = compressibility of solids C = volume compressibility $S_x = 1+(1-\chi)\ (u_a - u_w)/\ u_w$	(2.13)
Newland (1965)	$\sigma' = \sigma_i - (u_a - u_w) + \chi (\sigma - u_a)$	σ_i : intrinsic stress arising from inter- particle forces	(2.14)
Richards (1965)	$\sigma' = \sigma - u_a + \chi_m (h_m + u_a) + \chi_s (h_s + u_a)$	h_m : matric suction h_s : solute suction	(2.15)

		χ_m : effective stress parameter for matric suction χ_s : effective stress parameter for solute suction	
Sridharan (1968)	$\sigma'=(\sigma - u_a)+ a_w(u_a u_w) +$ $(A\text{-}R)$	a_w= ratio of area of water-mineral and water-water contact to total area of "wavy plane" A= stress due to inter-particle attractive forces R= stress due to inter-particle repulsive forces	(2.16)
Aitchison and Peter (1973)	$\sigma' = \sigma + \chi_m p_m'' + \chi_s p_s''$	p_m'': matric suction p_s'': solute suction χ_m, χ_s : soil parameters which are dependent upon the stress path	(2.17)
Lambe and Whitman (1979)	$\sigma' = (\sigma - u_a) + a_w (u_a - u_w)$	a_w : ratio of area of water-mineral and water-water contact of total area of "wavy" plane	(2.18)
Allam and Sridharan (1981)	$\sigma' = (\sigma - u_a) + \chi (u_a - u_w)$ $- R - \varsigma T_s$	χ : the parameter representing the proportion of the total void area occupied the water on a reference plane R : osmotic suction ς : interface parameter on the reference plane	(2.19)
Khalili and Khabbaz (1998)	$\sigma' = (\sigma - u_a)+ \chi (u_a - u_w)$	χ : effective stress parameter	(2.20)
Jommi (2000)	$\sigma_{ij}^* = \sigma_{ij} - (S u_w +(1 - S) u_a) \delta_{ij}$	σ_{ij}^* : Bishop's average soil skeleton stress σ_{ij} : total stress tensor S : degree of saturation δ_{ij} : Kroneker delta	(2.21)

In the early explorations related to effective stress in unsaturated soils, numerous scholars endeavored to utilize a single stress state variable to characterize the mechanical behavior of unsaturated soils. The application of the single-valued effective stress principle transforms the analysis of a multiphase porous media into a mechanically equivalent, single-phase, single-stress state continuum comprehension (Nuth and Laloui, 2008). The correlation between effective stress in unsaturated soil was established by several researchers that include Bishop (1959); Allam and Sridharan (1981); Aitchison (1985); Khalili and Khabbaz (1998) who incorporated the contribution of matric suction to soil stress. These researchers linked soil parameters χ and φ, linked to the degree of saturation, and were introduced to characterize the magnitude of matric suction in the soil. Bishop and Henkel (1962) emphasized that while χ exhibits a clear direct proportional relationship with soil saturation—attaining a value of 1 when the soil is fully saturated and 0 when it is dry—the association between χ and degree of saturation is not universally consistent and is influenced by the soil type and its properties. The integration of soil properties into the description of stress state variables poses challenges and complexities in interpretation. Therefore, variables characterizing the stress state should ideally be independent of soil properties (Fredlund and Morgenstern, 1977; Fung, 1977). Furthermore, Jennings and Burland (1962) have shown that there is no unique relationship between volumetric deformation and effective stress, and that single-valued effective stress principle is not valid. Therefore, the volume change and shear strength of unsaturated soils cannot be related to a single effective stress so that more than one stress state variable should be used to describe the behavior of unsaturated soils.

Fredlund and Morgenstern (1977) put forth a framework in terms of two independent stress variables to elucidate the constitutive behavior of unsaturated soils. The identification of state variables draws from multiple continuum mechanics perspectives, establishing that any two out of the three potential state variables (σ, u_w, u_a) can be utilized to articulate the stress state (Fredlund and Morgenstern, 1977). The subsequent combinations are detailed below:

$$(\sigma - u_a) \text{ and } (u_a - u_w) \tag{2.22a}$$

$$(\sigma - u_w) \text{ and } (u_a - u_w) \tag{2.22b}$$

$$(\sigma - u_a) \text{ and } (u_a - u_w) \tag{2.22c}$$

Due to physical and practical considerations, the prevailing stress variables in the two independent stress state variables approach are commonly identified as the net normal stress $(\sigma - u_a)$ and the matric suction $(u_a - u_w)$ (Fredlund and Rahardjo, 1993). This combination facilitates the distinction between the impacts arising from changes in normal stress and those arising from changes in pore-water pressure. In practice, the assumption that pore-air pressure equals atmospheric pressure is made. Consequently, the net normal stress typically aligns with the total normal stress, and matric suction corresponds to the absolute value of the negative pore-water pressure. To validate the efficacy of this pair of stress state variables, Fredlund and Morgenstern (1977) have investigated performing null tests and confirmed the principle of independent stress state variables for unsaturated soils. In these tests, they systematically varied the components of the proposed stress state variables while maintaining constant values for the composite stress state variables $(\sigma - u_a)$ and $(u_a - u_w)$. The absence of significant alterations in the overall state of the soil, despite changes in the components of the stress state variables, affirms the validity of these stress state variables for unsaturated soils. Building on the foundation of earlier researchers, in recent years, several others have also contributed to deepening the understanding of stress state variables in unsaturated soils (Alonso at al., 1990; Kato et al. 1995; Gens, 1996; Houlsby, 1997; Wheeler and Karube, 1996; Gallipoli et al., 2003; Kohgo, 2003; Wheeler et al., 2003; Gens et al., 2006; Russell and Khalili, 2006; Sheng and Fredlund, 2008; Cui and Sun, 2009; Gens Solé, 2009; Sheng, 2011; Duan et al., 2019; Ng et al., 2020). Some of these efforts encompass refining constitutive relations to ensure work conjugacy between stress and strain variables (Houlsby, 1997), developing more comprehensive combinations of stress state variables (Wheeler and Karube, 1996), investigating the state

dependence of unsaturated soils (Ng et al., 2020), and exploring models that consider unsaturated soils as a six-phase medium (Duan et al., 2019). These studies hold significant value in examining the stress state variables and constitutive relationships of unsaturated soils from diverse perspectives offering a more comprehensive and rational analysis.

2.7 Volume change constitutive relationship

The soil volume variations can be rationally interpreted using stress state variables and corresponding strain variables within specified constitutive relations. For a precise depiction of volume change in an unsaturated soil, it is crucial to account for two distinct sets of deformation state variables. One set pertains to soil structure, measured through void ratio or volumetric strain, while the other addresses the water phase, expressed by the degree of saturation or water content. These formulations employ two independent stress variables: namely, net normal stress and matric suction. In total, four volumetric deformation coefficients are essential to establish the connection between stress and deformation states.

Unsaturated soil, conceptualized as a four-phase porous medium comprising solid, liquid, air, and contractile skin, undergoes deformation under stress gradient influence. The total volume change during deformation is considered as the sum of individual phase volume changes. The solid phase, represented by soil particles, is treated as incompressible entities. Additionally, the volume change of the contractile skin is assumed to be internal to the element. Consequently, the continuity requirement for the volume change in unsaturated soil is simplified as follows:

$$\frac{\Delta V_v}{V_0} = \frac{\Delta V_w}{V_0} + \frac{\Delta V_a}{V_0} \tag{2.23}$$

where V_0 is initial overall volume of an unsaturated soil element, V_v is volume of soil voids, V_w is volume of water in the soil element, and V_a is volume of air in the soil element.

The above continuity condition states that the volume change associated with two of the three variables must be measured, allowing the volume change caused by the third variable to be calculated. The total volume change and water volume change are usually measured, while the air volume change is calculated (Fredlund and Rahardjo, 1993). The constitutive relations can be presented in different forms; namely soil mechanics formulation, compressibility formulation, and elasticity formulation (Fredlund, 2006).

In the elastic form of constitutive relations, unsaturated soil is assumed to be an isotropic and linear elastic medium. Therefore, the following strain relationships (Eq. 2.24 and Eq. 2.25) for soil structures in the three principal stress directions can be obtained.

$$d\varepsilon_x = \frac{d(\sigma_x - u_a)}{E} - \frac{\mu}{E}\left[d(\sigma_y - u_a) + d(\sigma_z - u_a)\right] + \frac{d(u_a - u_w)}{H} \tag{2.24a}$$

$$d\varepsilon_y = \frac{d(\sigma_y - u_a)}{E} - \frac{\mu}{E}\left[d(\sigma_x - u_a) + d(\sigma_z - u_a)\right] + \frac{d(u_a - u_w)}{H} \tag{2.24b}$$

$$d\varepsilon_z = \frac{d(\sigma_z - u_a)}{E} - \frac{\mu}{E}\left[d(\sigma_x - u_a) + d(\sigma_y - u_a)\right] + \frac{d(u_a - u_w)}{H} \tag{2.24c}$$

$$d\gamma_{yz} = \frac{d\tau_{yz}}{G}, \quad d\gamma_{zx} = \frac{d\tau_{zx}}{G}, \quad d\gamma_{xy} = \frac{d\tau_{xy}}{G} \tag{2.25}$$

where σ_x, σ_y , and σ_z are normal stresses in the x-, y-, and z-directions, respectively, ε_x , ε_y, and ε_z are normal strains in the x-, y-, and z-directions, respectively, (σ_x - u_a), (σ_y - u_a), and (σ_z - u_a) are net normal stresses in the x-, y-, and z-directions, respectively, μ is Poisson's ratio, E is modulus of elasticity for the soil structure with respect to a change in net normal stress, H is modulus of elasticity for the soil structure with respect to a change in matric suction, γ_{yz} , γ_{zx} , and γ_{xy} are shear strains on the x-, y-, and z-planes, respectively, and G is shear modulus.

The equations indicate the connection between the deformation state variables and stress state variables in unsaturated soil. The total volume change of the solid phase within each incremental section equals the combined volume change components across the three principal stress directions, as illustrated in the Eq. 2.26 and Eq. 2.27 below.

$$d\varepsilon_v = d\varepsilon_x + d\varepsilon_y + d\varepsilon_z \tag{2.26}$$

$$\frac{dV_v}{V_0} = 3\left(\frac{1-2\mu}{E}\right)d(\sigma_{mean} - u_a) + \frac{3}{H}d(u_a - u_w) \tag{2.27}$$

where ε_v is volumetric strain, σ_{mean} is mean total normal stress ($\sigma_{mean} = (\sigma_x + \sigma_y + \sigma_z) / 3$), in which σ_x, σ_y, and σ_z are normal stresses in the x-, y-, and z- directions, respectively.

The constitutive formulation for the water phase delineates the variation in water volume within the soil element in response to alterations in total stress and matric suction. The constitutive equation for the water phase can be expressed as a linear combination of changes in the stress state variables extending the assumption that water is incompressible, as illustrated below (Fredlund and Rahardjo, 1993).

$$\begin{aligned}\frac{dV_w}{V_0} &= \frac{d(\sigma_x - u_a)}{E_w} + \frac{d(\sigma_y - u_a)}{E_w} + \frac{d(\sigma_z - u_a)}{E_w} + \frac{d(u_a - u_w)}{H_w} \\ &= \frac{3}{E_w}d(\sigma_{mean} - u_a) + \frac{1}{H_w}d(u_a - u_w)\end{aligned} \tag{2.28}$$

where E_w is water volumetric modulus associated with a change in net normal stress, and H_w is water volumetric modulus associated with a change in matric suction.

Fredlund and Morgenstern (1976) introduced constitutive relationships, presented in a compressibility form, to encapsulate the volume change behaviors of both the soil structure and the water phase:

$$d\varepsilon_v = \frac{dV_v}{V_0} = m_1^s d(\sigma_{mean} - u_a) + m_2^s d(u_a - u_w) \tag{2.29}$$

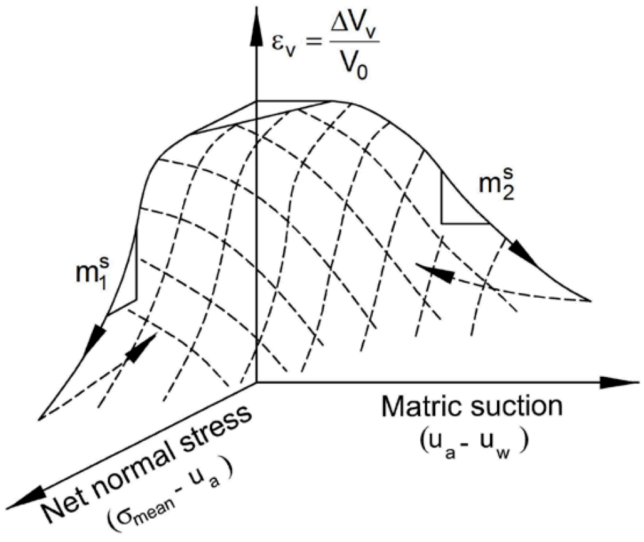
$$d\theta = \frac{dV_w}{V_0} = m_1^w d(\sigma_{mean} - u_a) + m_2^w d(u_a - u_w) \tag{2.230}$$

where m_1^s is coefficient of total volume change with respect to change in net normal stress, m_2^s is coefficient of total volume change with respect to change in matric suction, m_1^w is coefficient of water volume change with respect to change in net normal stress, m_2^w is coefficient of water volume change with respect to change in matric suction.

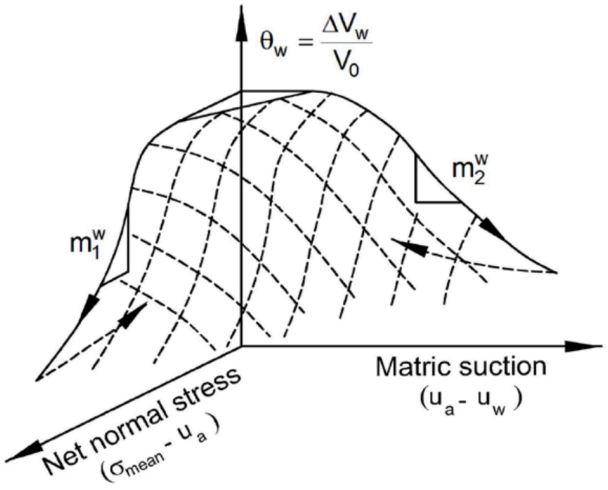
The volume change coefficients can be related to the elastic moduli E and H, volumetric modulus E_w and H_w, and Poisson's ratio μ as follows:

$$m_1^s = 3\left(\frac{1-2\mu}{E}\right),\ m_2^s = \frac{3}{H},\ m_1^w = \frac{3}{E_w},\ \text{and}\ m_2^w = \frac{1}{H_w} \tag{2.31}$$

Graphical representation of constitutive relationships for the soil structure and water phase in unsaturated soil can be achieved through the depiction of constitutive surfaces. The deformation state is graphically correlated with stress state variables, specifically (σ_{mean} - u_a) and ($u_a - u_w$). The determination of all volume change coefficients in the equations is facilitated by the examination of the constitutive surfaces, illustrated in Fig. 2.10, where these coefficients correspond to the slopes of the constitutive surface at a given point.



(a)



(b)

Fig. 2.10 Three-dimensional constitutive surfaces for unsaturated soil: (a) soil structure constitutive surface, (b) water phase constitutive surface (modified after Fredlund and Rahardjo (1993))

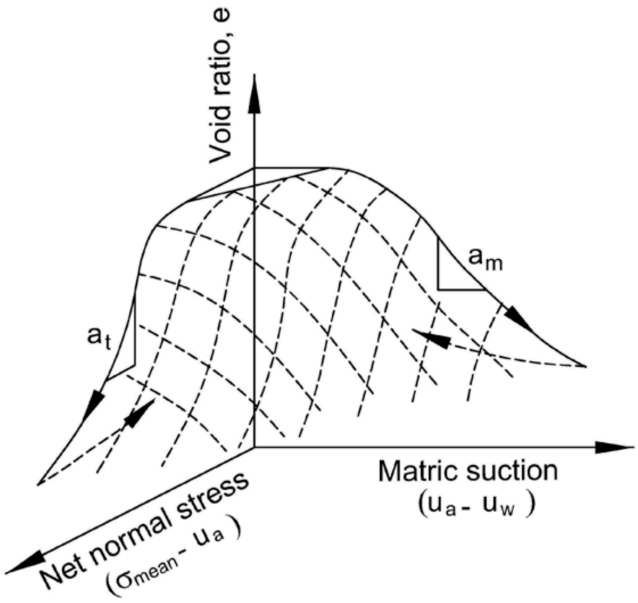
Traditional soil mechanics terminology employs void ratio (*e*), gravimetric water content (*w*), and degree of saturation (*S*) to characterize the volume-mass properties of unsaturated soils. However, constitutive equations for unsaturated soils can be expressed using void ratio and gravimetric water content as the deformation state variables for soil structure and the water phase, respectively.

$$de = a_t\, d(\sigma_{mean} - u_a) + a_m\, d(u_a - u_w) \tag{2.32}$$

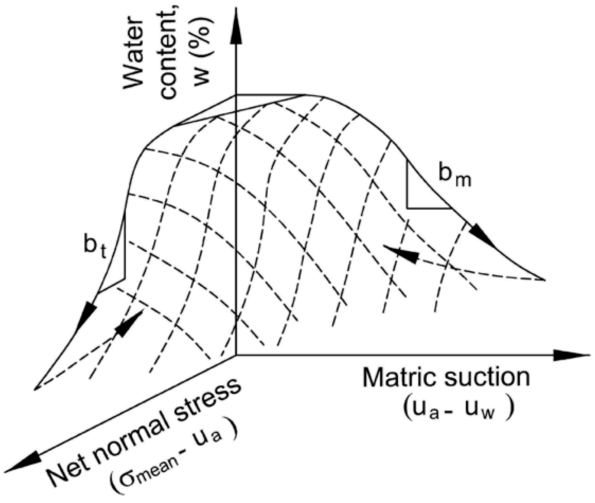
$$dw = b_t\, d(\sigma_{mean} - u_a) + b_m\, d(u_a - u_w) \tag{2.33}$$

where a_t is coefficient of compressibility with respect to change in net normal stress, a_m is coefficient of compressibility with respect to change in matric suction, b_t is coefficient of water content change with respect to a change in net normal stress, and b_m is coefficient of water content change with respect to a change in matric suction.

The above relationships can be further elucidated by visualizing them as constitutive surfaces on a three-dimensional plot. In this representation, each abscissa corresponds to one of the stress state variables, the ordinate delineates the soil volume-change properties, and the compressibility coefficients (a_t, a_m, b_t, and b_m) can be determined as the slopes of the void ratio and water content constitutive surfaces at a specific point, as depicted in Fig. 2.11.



(a)



(b)

Fig. 2.11 Three-dimensional constitutive surfaces for unsaturated soil expressed using soil mechanics terminology: (a) void ratio constitutive surface, (b) water content constitutive surface (modified after Fredlund and Rahardjo (1993))

2.8 Prediction methods for swelling properties

Most prediction methods available in the literature primarily concentrate on estimating swelling characteristics, specifically the swell potential, swelling pressure, and swelling index of expansive soils. Swell potential is quantified as the ratio of the increase in thickness (ΔH) to the original thickness (H) of a laterally confined sample under a specified load, subsequent to compaction to maximum density at the optimum water content in the standard AASHTO compaction test (Seed et al., 1962). Swelling pressure is defined as the pressure necessary to either retain the soil at its original void ratio or return it to this state when exposed to water (Shuai, 1998). The swelling index is conventionally determined by the slope of the rebound curve of void ratio and the logarithmic effective stress from the oedometer envelope. In this section, a concise overview is provided for estimating swelling properties. The available methods can be categorized into: (i) oedometer test methods, (ii) empirical methods, (iii) suction-based methods, (iv) and more recently artificial intelligence methods.

2.8.1 Oedometer test methods

Oedometer tests can be used to determine the volume change indices as well as initial and final void ratio. On one hand, the obtained data of swell strain, S % or void ratio, e (initial and final) can be directly used for ground heave estimation, on the other hand, the information of swelling pressure, P_s and swelling index, C_s facilitate the ground heave estimation based on certain assumptions on the stress path. Extensive research has been undertaken to estimate the ground heave based on the results of different types of oedometer tests. The oedometer test-based heave prediction methods are summarized in Table 2.2.

Table 2.2 The oedometer test-based heave prediction methods modified after (Singhal, 2010; Vanapalli and Lu, 2012)

Author (s)	Methods	Location
Jennings & Knight (1957)	Double Oedometer method	South Africa
De Bruijn (1961)	Volumemeter method	South Africa
Burland (1962)	Salas & Serratosa method	Spain
Sampson et al. (1965)	Sampson, Shuster & Budge method	U.S.
Noble (1966)	Noble method	Canada
Sullivan & McClelland (1969)	Sullivan & McClelland method	U.S.
Komornik et al. (1969)	Komornik, Wiseman & Ben-Yacob method	Israel
Holtz (1970)	Holtz method	U.S.
NAVFAC (1971)	Navy method (Direct method)	U.S.
Wong & Yong (1973)	Wong & Yong method	U.K.
Gibbs (1973)	U.S.B.R. method	U.S.
Jennings et al. (1973)	Simple Oedometer method	South Africa
Smith (1973)	PVR Method (Texas Highway Department)	U.S.
Teng et al. 1972	Mississippi method	U.S.
Porter & Nelson (1980)	Controlled strain test	U.S.
Fredlund et al. (1980)	Fredlund, Hasan & Filson method	Canada

Sridharan et al. (1986)	Sridharan, Rao & Sivapullaiah method	India
Erol et al. (1987)	Erol, Dhowian & Youssef methof	Saudi Arabia
Shanker et al. (1987)	Shankar, Ratnam & Rao method	India
Nelson et al. (1998)	Heave index method	U.S.
Al-Shamrani & Al-Mhaidib	Al-Shamrani & Al-Mhaidib method	Saudi Arabia
Basma et al. (2000)	Basma, Al-Homoud & Malkawi method	Jordan
Subba Rao & Tripathy (2003)	Subba Rao & Tripathy method	India

Sullivan and McClelland (1969) method

Sullivan and McClelland (1969) introduced a heave prediction method based on constant volume (CV) oedometer tests conducted on undisturbed specimens. In this approach, an undisturbed specimen undergoes in situ overburden pressure initially and is allowed to reach equilibrium (refer to Fig. 2.13). Subsequently, the specimen is given unrestricted access to water and maintained at a constant volume by adding loads until no further swelling tendency is observed, indicating the attainment of swelling pressure. Following this, the specimen is unloaded, and swelling is allowed by gradually decreasing the applied loads. This method proves to be useful in estimating soil heave resulting from a reduction in overburden pressure (Fredlund and Rahardjo, 1993). While the CV oedometer test is widely employed and regarded as one of the most dependable techniques for determining swell characteristics, such as heave potential and swell pressure, it is acknowledged as one of the more challenging and cumbersome methods for measuring these characteristics. This method is expected to underestimate the actual heave if the sampling disturbance is not taken into consideration. It was suggested that the results of CV tests should be adjusted for the effects of compressibility of the apparatus prior to their interpretation (Fredlund, 1983; Fredlund and Rahardjo, 1993).

Fredlund (1983) method

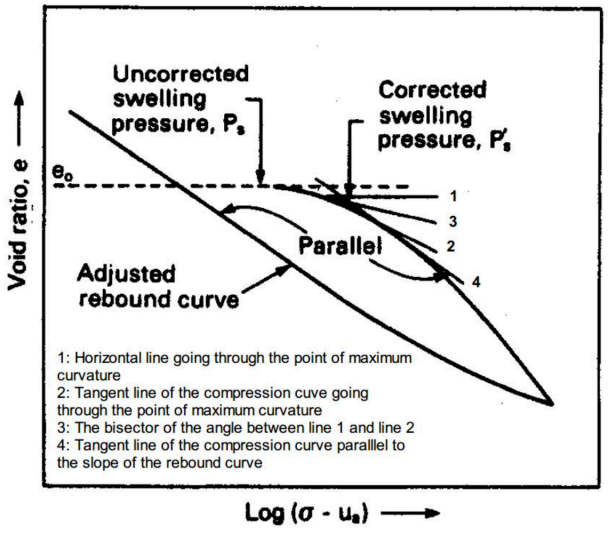
Given the limitations of the Sullivan and McClelland (1969) method, Fredlund (1983) proposed a procedure to correct the swelling pressure P_s' by accounting for the influence of sampling disturbance, as illustrated in Fig. 2.12a. To determine P_s', first locate the point

of maximum curvature where the void ratio versus pressure curve transitions onto the recompression branch. At this point, draw both a horizontal line and a tangent to the curve. The corrected swelling pressure P_s' is defined as the intersection of the bisector of the angle formed by these lines with a line that is tangent to the curve and parallel to the slope of the rebound curve.

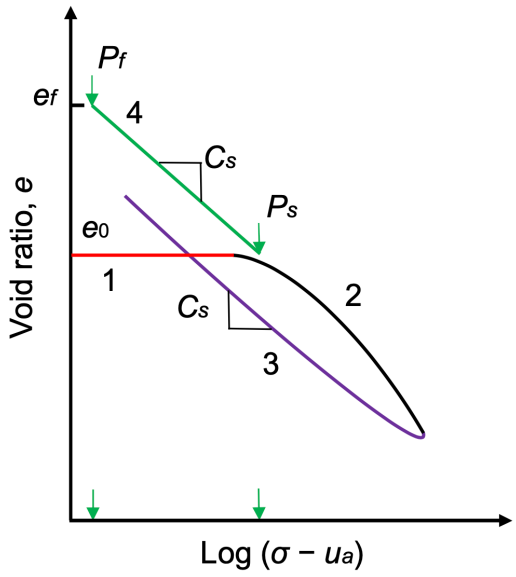
Additionally, Fredlund (1983) assumed that the stress path (green line in Fig. 2.12b) from the initial stress state to the final stress state is parallel to the rebound curve of the consolidation test, where the slope is known as the swelling index C_s. Based on this assumption, Fredlund proposed an equation to estimate the ground heave of expansive soils using the corrected swelling pressure obtained from a CV test, as shown in Eq. 2.34.

$$\Delta H = C_s \frac{H}{1+e_0} \log\left(\frac{P_f}{P_s'}\right) \tag{2.34}$$

where, H = the thickness of soil layer, C_s = swelling index, e_0 = initial void ratio, P_s' = corrected swelling pressure, P_f (= $\sigma_y + \Delta\sigma_y - u_{wf}$) = final stress state, (σ_y is total overburden pressure, $\Delta\sigma_y$ is the change in total stress, u_{wf} is pore-water pressure), and ΔH = the heave of the soil layer.



(a)



(b)

Fig. 2.12 (a) procedure for correcting swelling pressure (from Fredlund and Rahardjo, 1993) (b) Schematic of heave estimation using Fredlund (1983) method (from Tu and Vanapalli, 2016)

Nelson et al. (2006) method

Nelson et al. (2006) method is based on data obtained from the overburden swell test and the CV oedometer test. These two tests were conducted on identical specimens obtained from the same depth. Typical test results for both types of oedometer tests are shown in Fig. 2.13. In the overburden swell test, the percent swell S (%) corresponds to the value of the vertical stress applied at the time of inundation σ_i' for the conditions under which heave is being computed. In the CV test, the percent swell is zero at an inundation pressure of σ_{cv}'. Thus, points A and C, as shown in Fig. 2.13, fall on the line representing the desired relationship between σ_i' and S (%). This relationship is a straight line (i.e., heave line BD) on a semi-logarithmic plot. At any depth in the soil, the percent swell S (%) will fall along the straight-line CB. The slope of that line is defined as the heave index C_H and is given by:

$$C_H = \frac{S(\%)}{\log\left(\frac{\sigma'_{cv}}{\sigma'_i}\right)} \tag{2.35}$$

$$\Delta H = \sum h_i \, C_H \log\left(\frac{\sigma'_{cv}}{\sigma'_{v0}}\right) \tag{2.36}$$

where, C_H = heave index, S % = vertical swell strain, σ_{cv}' = constant volume swelling pressure, σ_i' = inundation pressure during the CVS test, σ_{v0}' = overburden pressure, ΔH = the heave of the soil layer, h_i = the thickness of i^{th} layer, i = the number of the soil layers.

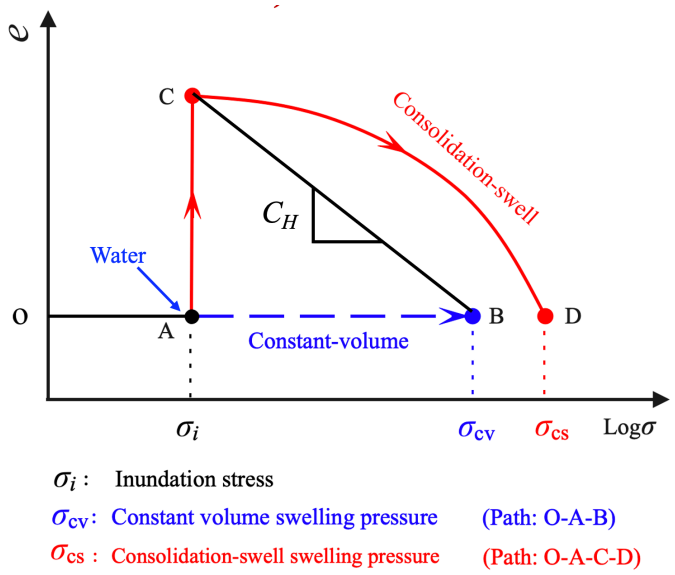


Fig. 2.13 Hypothetical oedometer test results (modified after Nelson et al. (2006))

Singhal et al. (2011) method

Singhal et al. (2011) developed a method for predicting heave using a combination of a loaded swell (LS) test and a constant volume swell (CV) test. In this method, both test specimens are confined under an overburden stress σ_{ob} corresponding to the sample's depth from the field. When the maximum swell occurs, it is assumed that the matric suction approaches zero, indicating a fully saturated condition. Instead of using a three-dimensional stress path, a surrogate path (*SP*) on the *ε-log p* plot can be utilized to

determine the maximum potential heave, provided that the initial and final stress states are known (Fig. 2.14). According to Singhal et al. (2011), the initial stress state can be considered equivalent to the constant volume swelling pressure as measured, while the final stress state must be estimated based on matric suction data.

$$C_{SP} = \frac{\varepsilon_{ob} - 0}{\log\left[\frac{\sigma_{ocv}}{\sigma_{ob}}\right]} \tag{2.37}$$

where, C_{SP} = slope of the surrogate path (SP), ε_{cv} = swell strain determined from the LS test applying a load equal to σ_{ob}, σ_{ob} = confining pressure for the swell test, which is the overburden stress for the sample, σ_{ocv} = swelling pressure determined form the CV pressure for a test specimen initially subjected to σ_{ob}.

$$\varepsilon_Q = C_{SP} \log\left[\frac{\sigma_{ocv}}{\sigma_f}\right] \tag{2.38}$$

where, ε_Q = swell strain, σ_f = final stress state.

$$\sigma_f = \sigma_{ob} + R_w(\sigma_{ocv} - \sigma_{ob}) \tag{2.39}$$

where,

$$R_w = \frac{(u_a - u_w)_f}{(u_a - u_w)_i} \tag{2.40}$$

where, $(u_a - u_w)_i$, $(u_a - u_w)_f$ = initial and final matric suction

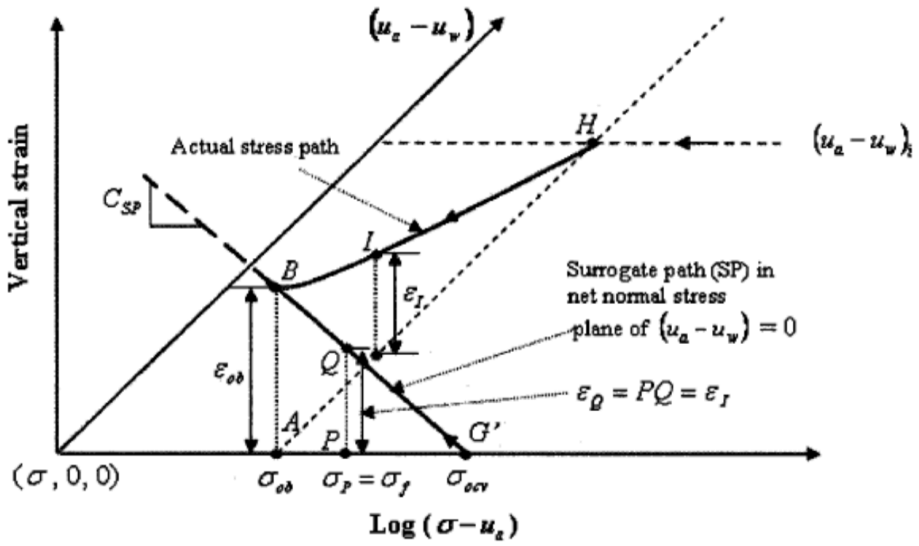


Fig. 2.14 Strain-based "equivalence" of reduction of suction from $(u_a - u_w)_i$ to zero (path HB) to reduction in net normal stress from σ_{ocv} to σ_{ob} (along path G'B, the SP) (from Singhal et al. (2011))

2.8.2 Empirical methods

Several researchers proposed empirical relationships using published oedometer test data with other soil properties to reduce the amount of time required for measuring the swelling properties. The Atterberg limits, plasticity index, clay fraction, activity, dry density, and initial water content are typically used in the empirical methods to estimate the swelling behavior of expansive soils. Empirical relations between percent swell, S %, swelling pressure, P_s , swelling index C_s and the soil parameters are summarized in Table 2.3. Such empirical equations are extensively embraced in engineering practice due to their convenience, requiring only basic soil properties for estimation of the swelling properties. However, their applicability is confined to specific soil types for which they have been developed.

Table 2.3 Summary of the empirical methods modified after (Nelson and Miller, 1997; Rao et al., 2004; Çimen et al., 2012; Vanapalli et al., 2012; Adem, 2015)

Author (s)	Methods	
Seed et al. (1962)	$S\,\% = 0.00216\ I_p^{2.44}$ for undisturbed	(2.41a)
	$S\,\% = 0.0036\ I_p^{2.44}$ for disturbed soils	(2.41b)
	$S\,\% = 3.6\times10^{-5}\ A^{2.44}\ c^{3.44}$	(2.41c)
	I_p = plasticity index	
	c = clay content	
	A = activity = (I_p / c)	
van der Merve (1964)	$\Delta H = Fe^{-0.377D}(e^{-0.377H} - 1)$	(2.42)
	H = volume change	
	ΔH = total heave	
	F = correction factor for degree of expansiveness	
	D = the thickness of non-expansive layer	
Ranganatham & Satyanarayana (1965)	$S\,\% = 0.000413\ I_s^{2.67}$ I_s = shrinkage index, $(w_l - w_s)$ w_l = liquid limit w_s = shrinkage limit	(2.43)
Komornik and David (1969)	$\text{Log}\ p_s = -2.132 + 0.0208 w_l + 0.000665 \gamma_d - 0.0269 w_i$	(2.44)
Nayak & Christensen (1971)	$S\,\% = 0.00229\ I_p^{2.67}\ (1.45\ c) / w_i + 6.38$	(2.45a)
	$p_s\,(\text{psi}) = [(3.58 \cdot 10^{-2})\ I_p^{1.12}\ c^2 / w_i^2] + 3.79$	(2.45b)
	w_i = initial water content	
	p_s = the swelling pressure	
Vijayvergiya & Ghazzaly (1973)	$S\,\% = (0.44 w_l - w_i + 5.5)/12$	(2.46a)
	$\text{Log}\ (S\,\%) = 0.0526 \gamma_d + 0.033 w_l - 6.8$	(2.46b)
	γ_d = dry unit weight	

Schneider & Poor (1974)	$\text{Log}\,(S\,\%) = 0.9\,(I_p / w_i) - 1.19$	(2.47)
McCormack & Wilding (1975)	$S\,\% = 7.5 - 0.8w_i + 0.203c$	(2.48)
Brackley (1975b)	$S\,\% = (5.3 - (147e / I_p) - \text{Log}\,P)\times(0.525I_p + 4.1 - 0.85w_i)$ P = surcharge	(2.49)
O'Neil & Ghazzally (1977)	$S\,\% = 2.77 + 0.131w_l - 0.27w_n$ w_n = natural water content	(2.50)
Chen (1975)	$S\,\% = 0.2558\ e^{0.00838\ Ip}$	(2.51)
Johnson (1978)	$S\,\% = 23.82 + 0.7346I_p - 0.1458H - 1.7w_0 + (0.0025I_p)w_0 - (0.00884I_p)H$ $S\,\% = -9.18 + 1.5546I_p + 0.08424H + 0.1w_0 - (0.0432I_p)w_0 - (0.01215I_p)H$	(2.52a) (2.52b)
Weston (1980)	$S\,\% = 0.00411\ w_{lw}^{4.17}\,\sigma_v^{-3.86}\,w_i^{-2.33}$ w_{lw} = weighted liquid limit	(2.53)
Bandyopadhyay (1981)	$S\,\% = 0.00114\ A^{2.559}c^{3.44}$	(2.54)
Picornell & Lytton (1984)	$\Delta H = \sum[f_i\,(\Delta v/v)_i]H$ H = the stratum thickness $(\Delta v/v)_i$ = volumetric strain f_i = factor to include the effects of the lateral confinements	(2.55)
Nagaraj and Murty (1985)	$C_s = 0.0463[LL(\%)/100]G_s$	(2.56)
Mowafy and Bauer (1985)	$Log\ p_s = 0.008951c + 1.366\gamma_d - 0.02179w_n - 2.84$	(2.57)
Nakase et al. (1988)	$C_s = 0.00194\ (I_P - 4.6)$	(2.58)
Dhowian (1990a)	$\Delta H = (S\,\%)\ H$	(2.59)

Basma (1993)	$S\,\% = 0.00064 I_p^{1.37} c^{1.37}$	(2.60)
Çokça (2002)	$S\,\% = -121.807 + 12.1696\ \text{MBV} + 27.6579\ \text{Log}\ \psi_i$ MBV = methylene blue value	(2.61)
Erguler & Ulusay (2003)	$p_s = -227.27 + 2.14 w_i + 1.54 w_l + 72.49 \gamma_d$	(2.62)
Rao et al. (2004)	$S\,\% = 4.24 \gamma d_i - 0.47 w_i - 0.14 q_i - 0.06\text{FSI} - 55$ γd_i = dry unit weight q_i = initial surcharge FSI = free swell index	(2.63)
Erzin & Erol (2004)	$\text{Log}\ p_s = -4.812 + 0.01405 I_p + 2.394 \gamma_d - 0.0163 w_i$	(2.64a)
	$\text{Log}\ p_s = -5.020 + 0.01383 I_p + 2.356 \gamma_d$	(2.64b)
Sabtan (2005)	$S\,\% = 1.0 + 0.06\ (c + I_p - w_i)$ $p_s = 135.0 + 2.0\ (c + I_p - w_i)$	(2.65a) (2.65b)
Azam (2007)	$S\,\% = 0.6\ I_p^{1.188}$	(2.66)
Yilmaz (2009)	$S\,\% = 2.0981 e^{-1.7169\ IL}$ IL = liquidity index = $[(w_l - w) / I_p]$	(2.67)
(Işık, 2009)	$C_s = 0.0133 e^{0.036 w_n}$	(2.68a)
	$C_s = 0.0121 e^{1.3131 e_0}$	(2.68b)
	$C_s = 0.1257 \gamma_d^{-2.8826}$	(2.68c)
	$C_s = (-0.000319 w_n) - (0.027277 \gamma_d) + 0.0131\ (0.064019 e_0) + 0.037$	(2.68d)
Türköz and Tosun (2011)	$S\,\% = -57.865 + 37.076\ \rho_d + 0.524\text{MBV} + \varepsilon$ ε = mean-zero Gaussian random error term	(2.69)
Tiwari and Ajmera (2011)	$C_s = 0.0000006\ (I_p)^2 + 0.0026\ (I_p)$	(2.70)

Vanapalli and Lu (2012)	$C_s = 0.019\ e^{0.0343 I_p}$	(2.71)
Çimen et al. (2012)		(2.72a)
	$(S\,\%)_1 = (0.3139\gamma_d^{0.3552} - 0.1177\ w_i^{0.4470}) I_p^{0.9626}$	(2.72b)
	$(Log\ p_s)_1 = 0.0276 I_p - 365.2118\gamma_d^{-2.4616} - 0.0320 w_i + 2.2292$	
	$(S\,\%)_2 = (0.4768\gamma_d^{0.3888} - 0.0033\ w_i^{1.6045}) I_p^{0.7224}$	(2.72c)
	$(Log\ p_s)_2 = 0.0239 I_p - 1285.3723\gamma_d^{-3.2768} - 0.0396 w_i + 2.3238$	(2.72d)
	$(S\,\%) = \text{mean}\ (SP_1, SP_2)$	
	$Log\ p_s = \text{mean}\ [(\text{Log}\ p_s)_1, (\text{Log}\ p_s)_2]$	
Elisha (2012)	$Log\ p_s = 0.0139 I_p + 2.461\gamma_d - 5.402$	(2.73)
Zumrawi (2013)	$S\,\% = 24.5\ (q^{-0.26})\ (I_p c)^{1.26}\ [F_i - 7.1\ (q^{0.22})\ (I_p c)^{1.26}]$ q = surcharge F_i = initial state factor	(2.74)
Israr et al. (2014)	$p_s = 43.6A + 68 w_n - 915$	(2.75)
Tu and Vanapalli (2016)	$C_s = 0.188/[1 + e^{(44.526 - I_p)/15.636}]$	(2.76a)
	$P_{sn} = (\sigma_y - u_a)_{field} + \beta_n \cdot \psi_{field} \cdot \left(\frac{S}{100}\right)^2$	(2.76b)

$$P_{sc} = P_{s0} + \beta_c \cdot \psi_i \cdot \left(\frac{S}{100}\right)^2$$

P_{sn} = swelling pressure of natural expansive soil

β_n = model parameter for natural expansive soil

$(\sigma_y - u_a)_{field}$ = *in-situ* overburden pressure

ψ_{field} = *in-situ* soil suction

Cantillo et al. (2017)	$\ln p_s = 7.77 - 0.12w + 0.0054I_p$	(2.77)
Gawriuczenkow and Wójcik (2018)	$p_s = 25.202 + 0.643LL - 2.089w_n$	(2.78)

2.8.3 Suction-based methods

In suction-based methods, the displacement linked to the volume change of expansive soils can be assessed by measuring the current in situ suction for predicting the potential future suction condition in a specific environment. The fundamental premise of these methods lies in the concept that the volume change of unsaturated soils exhibits a linear proportionality to soil suction when plotted on a logarithmic scale across the moisture content range spanning from shrinkage limit to plastic limit (Johnson and Snethen 1978, Mitchell and Avalle 1984, Hamberg 1985). Table 2.4 provides a summary of widely used suction-based methods for predicting swelling potential of various expansive soils.

Table 2.4 Suction-based methods for predicting ground heave (modified after Adem (2015))

Author (s)	Equation

$$\Delta H = \sum_{\text{layers}} \frac{H}{3} \frac{(w_f - w_i)G_s}{(100 + w_i G_s)}$$

Richards (1967)

ΔH = soil heave

H = soil layer thickness

w_i = initial water content (measured)
w_f = final water content (estimated in terms of the equilibrium matric suction)
G_s = specific gravity

(2.79)

$$\delta = \sum_{i=1}^{n} I_{pt}(\Delta u)(\Delta z_n)$$

Aitchison (1973)

δ = vertical shrinkage or heave

I_{pt} = instability index
Δu = soil suction change

Δz_i = thickness of i^{th} soil layer
n = total number of soil layers considered

(2.80)

$$S_f = \sum_{i=1}^{n} f_i \left(\frac{\Delta V}{V}\right)_i \Delta z_i$$

$$\left(\frac{\Delta V}{V}\right)_i = -\gamma_h \log\left(\frac{h_f}{h_i}\right) - \gamma_\sigma \log\left(\frac{\sigma_f}{\sigma_i}\right)$$

Lytton (1977b)

S_f = surface displacement

f_i = lateral confine factor

$(\Delta V/V)_i$ = average volume strain
Δz_i = thickness of i^{th} soil layer
n = total number of soil layers considered
h_i, h_f = initial and final water potentials
σ_f = applied octahedral normal stress
σ_i = octahedral normal stress above which overburden pressure restricts volumetric expansion

(2.81)

	γ_h = matric suction compression index γ_σ = mean principal stress compression index	
Johnson & Snethen (1978)	$$\Delta H = H \frac{C_\tau}{1+e_0} \log \frac{h_0}{h_f + \alpha\sigma_f}$$ ΔH = soil heave H = soil layer thickness C_τ = suction index e_0 = initial void ratio h_0 = matric suction without surcharge pressure log $h_0 = A - (Bw_0)$ h_f = final matric suction σ_f = final applied pressure (overburden plus external load) α = compressibility index	(2.82)
Fredlund (1979)	$$\Delta H = \sum_{i=1}^{n} \frac{H_i}{1+e_0} \left[C_t \Delta \log(\sigma - u_a) + C_m \Delta \log(u_a - u_w) \right]$$ ΔH = soil heave H_i = thickness of the i^{th} soil layer n = total number of soil layers considered e_i = void ratio of the i^{th} soil layer C_t = compressive index with respect to total stress C_m = compressive index with respect to matric suction $(\sigma - u_a)$ = total stress $(u_a - u_w)$ = matric suction	(2.83)
Mitchell & Avalle (1984)	$$\Delta H = \sum_{i=1}^{n} \left(I_{pt} \, \Delta u \, H_i \right)$$ ΔH = vertical surface movement I_{pt} = instability index Δu = soil suction change H_i = soil layer thickness over which I_{pt} can be taken as constant n = number of layers to depth of the active zone Δw = moisture content change	(2.84)

$\Delta\varepsilon_v$ = change in vertical strain

$$\Delta H = \sum_{i=1}^{n} \frac{H_i}{1+e_0} \left(C_h \Delta \log h\right)_i$$

Wray (1984)

ΔH = shrinkage or swell over vertical increment

(2.85)

H = vertical increment over which shrink or swell is occurring
γ_h = suction compression index
ΔpF = change in soil suction over vertical increment
ΔpP = change in soil overburden over vertical increment

$$\Delta H = H \frac{C_\psi}{1+e_0} \log \frac{\psi_i}{\psi_f}$$

ΔH = soil heave

Dhowian (1990a)

H = soil layer thickness

(2.86)

C_ψ = suction index = (α G_s) / (100 B)
e_0 = initial void ratio
ψ_i, ψ_f = initial and final suction
α = volume compressibility factor
G_s = specific gravity of solid particles
B = slope of suction versus water content relationship

$$\Delta H = C_h \, \Delta u \, \Delta t \, f \, s$$

ΔH = surface heave

C_h = suction compression index

$=(-0.02673)\,(\Delta u / \Delta w) - 0.38704$

Δu = suction change
Δt = soil layer thickness

McKeen (1992) (2.87)

f = lateral restraint factor

$= (1 + 2K_0) / 3$

s = reduction factor to account for overburden

$= 1 - 0.01(\%SP)$

Δw = moisture content change
K_0 = coefficient of lateral earth pressure at rest

SP = swell pressure applied to the soil due to overburden pressure

$$S_f = \sum_{i=1}^{n} f_i \left(\frac{\Delta V}{V}\right)_i \Delta z_i$$

$$\left(\frac{\Delta V}{V}\right)_i = -\gamma_h \log\left(\frac{h_f}{h_i}\right) - \gamma_\sigma \log\left(\frac{\sigma_f}{\sigma_i}\right)$$

$$\gamma_h = \frac{\gamma(\text{swellingcase}) + \gamma(\text{shrinkagecase})}{2}$$

$$\gamma(\text{swelling case}) = \left(\frac{\text{COLE}}{100} + 1\right)^3 - 1$$

$$\gamma(\text{shrinkage case}) = 1 - \frac{1}{\left(\frac{\text{COLE}}{100} + 1\right)^3}$$

Cover & Lytton (2001) (2.88)

S_f = surface displacement

f_i = lateral confine factor

$(\Delta V/V)_i$ = average volume strain
Δz_i = thickness of i^{th} soil layer
n = total number of soil layers considered
h_i, h_f = initial and final water potentials
σ_f = applied octahedral normal stress
σ_i = octahedral normal stress above which overburden pressure restricts volumetric expansion
γ_h = matric suction compression index
γ_σ = mean principal stress compression index

COLE = coefficient of linear extensibility

$$\Delta H = \sum_{i=1}^{n} f \left(\frac{\Delta V}{V} \right)_i \Delta z_i$$

$$\left(\frac{\Delta V}{V} \right)_{i,\ swelling} = -\gamma_h \log \left(\frac{h_f}{h_i} \right) - \gamma_\sigma \log \left(\frac{\sigma_f}{\sigma_i} \right)$$

$$\left(\frac{\Delta V}{V} \right)_{i,\ shrinkage} = -\gamma_h \log \left(\frac{h_f}{h_i} \right) + \gamma_\sigma \log \left(\frac{\sigma_f}{\sigma_i} \right)$$

ΔH = surface displacement
f = crack fabric factor = 0.67 – 0.44 ΔpF, $1/3 \leq f \leq 1.0$
$(\Delta V/V)_i$ = volume strain
Lytton et al. (2004) — Δz_i = the i^{th} depth increment — (2.89)
n = number of depth increment
h_i, h_f = initial and final values of matric suction

σ_i, σ_f = initial and final values of mean principal stress
γ_h = matric suction compression index
γ_σ = mean principal stress compression index

$= C_c / (1 + e_0)$
ΔpF = change of suction

C_c = compression index

e_0 = void ratio

2.8.4 Artificial intelligence-based methods

Several research contributed in recent years focusing on using artificial intelligence methods as a tool for the prediction of swelling index of expansive soils to simplify prediction methods, enhance prediction efficiency, and mitigate overreliance on time consuming and laborious experiments (Işık, 2009; Abdulkareem and Aziz, 2020; Amin Benbouras and Petrisor, 2021); swelling pressure (Erzin, 2007; Das et al., 2010; Ikizler et al., 2010; Erzin and Güneş, 2011; Ikizler et al., 2014; Merouane and Mamoune, 2018; Jalal et al., 2021; Aneke et al., 2022; Taherdangkoo et al., 2023); swelling potential (Najjar et al., 2000; Kayadelen et al., 2009; Erzin and Güneş, 2011; Yilmaz and Kaynar, 2011; Çimen et al., 2012; Onyelowe et al., 2021; Eyo et al., 2022; Nguyen et al., 2022).

Employing the artificial neural network algorithm, Işık (2009) made predictions for the swelling index by incorporating water content and initial void ratio. However, the accuracy and effectiveness of this model warrant additional analysis and verification. Abdulkareem and Aziz (2020) employed the multi-layer perceptron (MLP) algorithm to predict the swelling index of Ramadi cohesive soil. In their study, a broader array of soil properties served as input parameters for reliable estimate of the swelling index. Amin Benbouras and Petrisor (2021) also employed various artificial intelligence algorithms and incorporated a broader set of soil properties to estimate the swelling index of expansive soils. The findings from this study suggest a substantial influence of liquid limit and plasticity index on the swelling index, whereas the relationship between water content, dry density, and the swelling index is comparatively weaker. Erzin (2007) applied the ANN algorithm to predict the swelling pressure of a bentonite-kaolin mixture, utilizing the initial matric suction as an input parameter. This research indicated the impact of initial matric suction on swelling pressure and substantiated a robust correlation between them. Two approaches of artificial neural network (ANN) and adaptive neuro-fuzzy inference systems (ANFIS) are employed by Ikizler et al. (2014) to predict both vertical and lateral swelling pressure of expansive soils. Jalal et al. (2021) adopted three machine learning algorithms; namely, artificial neural networks (ANNs), adaptive neuro fuzzy inference system (ANFIS), and gene expression programming (GEP) to predict swelling pressure. The study reveals that maximum dry density significantly influences swelling pressure, whereas specific gravity exerts minimal impact on the swelling pressure. Taherdangkoo et al. (2023) employed a feed-forward neural network algorithm trained with multiple training functions to predict swelling pressure. The study shows feed-forward neural network with Bayesian regularization (FFNN-BR) providing an accurate alternative to traditional soil mechanics approaches. In the nascent phase of artificial intelligence development, Najjar et al. (2000) developed two neural network-based models to predict swelling potential, taking into account the influence of various combinations of soil parameters as input parameters. Erzin and Güneş (2011) employed a variety of soil properties, including clay fraction, cation exchange capacity, plasticity index, dry unit weight, water content, and utilized both the ANN algorithm and multiple regression method to estimate the swelling potential of a kaolin-

bentonite mixture. The findings of this study highlight that the prediction efficacy of the ANN algorithm markedly surpasses that of the regression fitting method. Onyelowe et al. (2021) employed ANFIS to predict the swelling potential of expansive soils, demonstrating that ANFIS offers strong predictive performance with high correlation coefficients, making it an effective tool for modeling complex relationships associated with expansive soils. Nguyen et al. (2022) present a series of machine learning models; namely, Gaussian Process (GP), Multilayer Perceptron (MLP), and Bagging-MLP neural network models for the prediction of the swelling potential of expansive soils; based on these studies, it was shown that Bagging-MLP has the highest prediction accuracy.

2.9 Compression behavior and compression index of expansive soils

In addition to the prominent swelling behavior of expansive soils, their compressibility characteristics are equally critical in determining the performance and stability of geo-infrastructures. The compression index is a fundamental parameter used to evaluate the compressibility of fine-grained expansive soils. It plays a key role in estimating settlement in foundation design, embankment construction, and other geotechnical applications. Although the swelling behavior of expansive soils has been widely studied, comparatively less attention has been given to their compression behavior, despite its significance in predicting long-term deformation under sustained loads.

Conventionally, the compression index is determined through oedometer consolidation tests, which are both time-consuming and labor-intensive. These procedures typically require several days or even weeks to complete, making them impractical for large-scale investigations or projects with tight schedules. To address these challenges, various empirical correlations have been proposed to estimate the compression index based on easily measurable soil properties, such as liquid limit, plasticity index, initial void ratio, and dry density (Terzaghi and Peck, 1967; Sridharan and Nagaraj, 2000; Tiwari and Ajmera, 2011). However, these empirical equations are often developed from datasets of general fine-grained soils and may not adequately capture the distinctive characteristics of expansive soils, particularly those related to mineralogical composition.

Recent advancements in machine learning have introduced new possibilities for developing more accurate and generalized models to predict the compression index of expansive soils. Machine learning algorithms are capable of processing large and complex datasets, identifying nonlinear relationships between basic soil properties and compressibility parameters. Nonetheless, studies focusing specifically on expansive soils remain limited. Incorporating machine learning-based predictions of the compression index into the evaluation of expansive soils can provide a more comprehensive understanding of their compressibility behavior, supporting more reliable settlement analyses and foundation designs.

The inclusion of compression index prediction in this study complements the analysis of swelling properties, contributing to a more comprehensive framework for assessing the volume change behavior of expansive soils. A detailed discussion on recent developments in compression index prediction, including the application of machine learning techniques, is presented in Section 5.1.

2.10 Summary

In recent decades, research on expansive soils has experienced rapid development. These studies predominantly concentrate on predicting swelling characteristics, including the swelling index, swelling pressure, and swelling potential, primarily for saturated soils; however, some studies also focused on unsaturated expansive soils. These methods can be primarily categorized into four groups: empirical methods, oedometer methods, suction-based methods, and artificial intelligence-based methods. While these methods are found to be valuable and have unique advantages, it is essential to also acknowledge some of their limitations. For example, oedometer methods are time consuming, need trained personnel and expensive equipment. Suction-based methods, characterized by their complexity, pose challenges in interpreting the intricate relationship between suction and swelling properties. Moreover, the measurement of suction itself is a time-consuming and challenging task. Empirical methods, while simple to use, are significantly influenced by soil types and have limitations for universal application. Consequently, their predictive effectiveness may be optimal for specific soils, limiting their applicability across diverse soil types. Artificial

intelligence-based methods leverage robust predictive and big data analysis capabilities, offering a simpler and more reliable prediction of soil properties compared to the other three methods. More detailed information on these methods is summarized in Table 2.5 focusing the six different aspects: accuracy, scope of application, simplicity, cost, efficiency, and interpretation. However, it is also important to note that artificial intelligence has common limitations in predicting swelling properties. Firstly, certain algorithms rely on probability and statistical methods or approaches, and each iteration can yield different results, substantially diminishing the reusability of models. Furthermore, currently, the primary focus of research is utilizing machine learning algorithms to build models for predicting swelling properties. However, the black box nature of some algorithms hinders the provision of explicit relationships, leading to reduced interpretability of the predicted results. Additionally, the AI prediction outcomes are heavily reliant on the reliability of the training set data, making it challenging to predict entirely unknown factors. Simply put, inaccurate measurement of input parameters, specifically soil properties, leads to inaccurate prediction results. Hence, the objective of this study is to craft artificial intelligence algorithms that yield consistent prediction outcomes, possess high interpretability, and have the capability to generate straightforward and explicit equations, thereby enhancing their applicability in geotechnical engineering practice.

Table 2.5 Summary of the comparison among methods

Methods	Accuracy	Scope	Simplicity	Cost	Efficiency	Interpretation
Oedometer	☆ ☆ ☆	☆ ☆ ☆	☆	☆	☆	☆ ☆ ☆
Empirical	☆ ☆	☆	☆ ☆ ☆	☆ ☆ ☆	☆ ☆ ☆	☆ ☆
Suction-based	☆ ☆	☆	☆ ☆	☆ ☆ ☆	☆ ☆	☆ ☆
AI	☆ ☆	☆ ☆ ☆	☆ ☆ ☆	☆ ☆ ☆	☆ ☆ ☆	☆ ☆

Note: ☆ ☆ ☆ means good, ☆ ☆ means moderate, and ☆ means limited.

References

Abdulkareem, A. H., and Aziz, D. O., 2020. Multiple regression and ANN (MLP) model for predicting swelling index of Ramadi cohesive soil. IOP Conference Series: Materials Science and Engineering, 737(1), 012116.

Adem, H. H., 2015. Modulus of elasticity based method for estimating the vertical movement of natural unsaturated expansive soils. Ph.D. thesis, Université d'Ottawa/University of Ottawa.

Adem, H. H., and Vanapalli, S. K., 2016. Heave prediction in a natural unsaturated expansive soil deposit under a lightly loaded structure. Geotechnical and Geological Engineering, 34, 1181-1192.

Aitchison, G.D., 1960. Effective stresses in multiphase systems. Proceedings of the Third Australia-New Zealand Conference on Soil Mechanics and Foundation Engineering, pp. 209-212.

Aitchison, G. D., 1965. Soil properties, shear strength, and consolidation. Proceedings of the 6th International Conference on Soil Mechanics and Foundation Engineering, Vol. 3, pp. 318-321.

Aitchison, G., 1985. Relationships of moisture stress and effective stress functions in unsaturated soils. Golden Jubilee of the International Society for Soil Mechanics and Foundation Engineering: Commemorative Volume, Institution of Engineers, Australia, Barton, ACT, pp. 20-25.

Aitchison, G. D., 1973. The quantitative description of the stress deformation behaviour of expansive soils. CSIRO, Division of Applied Geomechanics.

Allam, M. M., and Sridharan, A., 1981. Effect of wetting and drying on shear strength. Journal of the Geotechnical Engineering Division, 107(4), 421-438.

Alonso, E. E., Gens, A., and Hight, D. W., 1987. General report. Special problem soils. Proceedings of the 9th European Conference on Soil Mechanics and Foundation Engineering, Dublin, Vol. 3, pp. 1087-1146.

Alonso, E. E., Gens, and A., Josa, A., 1990. A constitutive model for partially saturated soils. Géotechnique, 40(3), 405-430.

Amin Benbouras, M., Petrisor, and A.-I., 2021. Prediction of swelling index using advanced machine learning techniques for cohesive soils. Applied Sciences, 11(2), 536.

Anderson, J., Fadul, K. E., and O'Connor, G., 1973. Factors affecting the coefficient of

linear extensibility in Vertisols. Soil Science Society of America Journal, 37(2), 296-299.

Aneke, F. I., Onyelowe, K. C., Ebid, A. M., Nwobia, L. I., and Adu, J. T., 2022. Predictive models of swelling stress—a comparative study between BP-and GRG-ANN. Arabian Journal of Geosciences, 15(17), 1438.

Bishop, A. W., 1959. The principal of effective stress. Teknisk ukeblad, 39, 859-863.

Bishop, A. W., and Eldin, G., 1950. Undrained triaxial tests on saturated sands and their significance in the general theory of shear strength. Géotechnique, 2(1), 13-32.

Bishop, A. W., and Henkel, D. J., 1962. The measurement of soil properties in the triaxial test.

Burland, J. B., 1962. The estimation of field effective stresses and the prediction of total heave using a revised method of analyzing the double oedometer test. The Civil Engineer in South Africa, Transactions of South African Institute of Civil Engineering.

Cantillo, V., Mercado, V., and Pájaro, C., 2017. Empirical correlations for the swelling pressure of expansive clays in the city of Barranquilla, Colombia. Earth Sciences Research Journal, 21(1), 45-49.

Chen, F. H., 1975. Foundations on expansive soils. Elsevier Scientific Publishing Co., Amsterdam, Netherlands.

Chen, F. H., 2012. Foundations on Expansive Soils, Vol. 12. Elsevier.

Chen, W. B., Liu, K., Feng, W. Q., Borana, L., and Yin, J. H., 2020. Influence of matric suction on nonlinear time-dependent compression behavior of a granular fill material. Acta Geotechnica, 15, 615-633.

Çimen, Ö., Keskin, S. N., and Yıldırım, H., 2012. Prediction of swelling potential and pressure in compacted clay. Arabian Journal for Science and Engineering, 37, 1535-1546. c

Croney, D., Coleman, J., and Black, W., 1958. Movement and distribution of water in soil in relation to highway design and performance. Highway Research Board Special Report, 40.

Cui, Y., Sun, D., 2009. Constitutive modelling: From isothermal to non-isothermal behaviour of unsaturated soils. In Unsaturated Soils, CRC Press, pp. 493-506.

Daniels, K. A., Harrington, J. F., Zihms, S. G., and Wiseall, A. C., 2017. Bentonite permeability at elevated temperature. Geosciences, 7(1), 3.

Das, S. K., Samui, P., Sabat, A. K., and Sitharam, T., 2010. Prediction of swelling pressure

of soil using artificial intelligence techniques. Environmental Earth Sciences, 61, 393-403.

De Boer, R., and Ehlers, W., 1990. The development of the concept of effective stresses. Acta Mechanica, 83(1-2), 77-92.

De Bruijn, C. M. A., 1961. Swelling characteristics of a transported soil profile at Leeuhof Vereeniging (Transvaal). Proceedings of the 5th International Conference on Soil Mechanics and Foundation Engineering, Paris, Vol. 1, pp. 43–49.

Donald, I., 1961. The mechanical properties of saturated and partly saturated soils with special reference to negative pore water pressure. Ph.D. thesis, University of London.

Duan, X., Zeng, L., and Sun, X., 2019. Generalized stress framework for unsaturated soil: demonstration and discussion. Acta Geotechnica, 14, 1459-1481.

Elbrahmi, J., and Zoukaghe, M., 2016. Evolution of expansive soils structure with different solicitations and effect of some parameters on swelling properties – review article. Theoretical & Applied Science, 5, 68-77.

Erol, A. O., Dhowian, A., and Youssef, A., 1987. Assessment of oedometer methods for heave prediction. Proceedings of the 6th International Conference on Expansive Soils, New Delhi, India, pp. 99-103.

Erzin, Y., 2007. Artificial neural networks approach for swell pressure versus soil suction behaviour. Canadian Geotechnical Journal, 44(10), 1215-1223.

Erzin, Y., and. Güneş, N., 2011. The prediction of swell percent and swell pressure by using neural networks. Mathematical and Computational Applications, 16(2), 425-436.

Eyo, E., Abbey, S., Lawrence, T., and Tetteh, F., 2022. Improved prediction of clay soil expansion using machine learning algorithms and meta-heuristic dichotomous ensemble classifiers. Geoscience Frontiers, 13(1), 101296.

Fredlund, D. G., 1983. Prediction of ground movements in swelling clays. 31st Annual Soil Mechanics and Foundation Engineering Conference.

Fredlund, D. G., 2006. Unsaturated soil mechanics in engineering practice. Journal of geotechnical and geoenvironmental engineering, 132(3), 286-321.

Fredlund, D. G., Hasan, J. U., and Filson, H., 1980. The prediction of total heave. Proceedings of the 4th International Conference on Expansive Soils, Denver, Colorado, pp. 1-17.

Fredlund, D. G., and Morgenstern, N., 1976. Constitutive relations for volume change in unsaturated soils. Canadian Geotechnical Journal, 13(3), 261-276.

Fredlund, D. G., and Morgenstern, N. R., 1977. Stress state variables for unsaturated soils. Journal of the geotechnical engineering division, 103(5), 447-466.

Fredlund, D. G., and Rahardjo, H., 1993. Soil mechanics for unsaturated soils. John Wiley & Sons.

Fung, Y. C., 1977. A First Course in Continuum Mechanics. Englewood Cliffs, NJ: Prentice-Hall.

Gallipoli, D., Gens, A., Sharma, R., and Vaunat, J., 2003. An elasto-plastic model for unsaturated soil incorporating the effects of suction and degree of saturation on mechanical behaviour. Géotechnique, 53(1), 123-135.

Gawriuczenkow, I., and Wójcik, E., 2018. Prediction of swell pressure in Neogene clays from Warsaw, based on the swell index. Geology, Geophysics and Environment, 44(2), 219-229.

Gens, A., 1996. Constitutive modelling: application to compacted soils. Proceedings of the First International Conference on Unsaturated Soils (UNSAT'95), Vol. 3, pp. 6-8.

Gens, A., Sánchez, M., Sheng, D., 2006. On constitutive modelling of unsaturated soils. Acta Geotechnica, 1, 137-147.

Gens Solé, A., 2009. Some issues in constitutive modelling of unsaturated soils. Proceedings of the 4th Asia-Pacific Conference on Unsaturated Soils, Taylor & Francis, pp. 613-626.

Gokhale, K., and Jain, K., 1972. Anisotropic swelling in black cotton soil. Bulletin of the International Association of Engineering Geology - Bulletin de l'Association Internationale de Géologie de l'Ingénieur, 5, 63-71.

Hamberg, D. J., 1985. A simplified method for predicting heave in expansive soils. Ph.D. thesis, Colorado State University.

Hasan, F. D., and Filson, H., 1980. The prediction of total heave. Proceedings of the 4th International Conference on Expansive Soils, Denver, CO, USA, Vol. 1, pp. 1-17.

Helm, D., 1987. Three-dimensional consolidation theory in terms of the velocity of solids. Géotechnique, 37(3), 369-392.

Hilf, J. W., 1956. An Investigation of Pore-Water Pressure in Compacted Cohesive Soils. Ph.D. thesis, University of Colorado at Boulder.

Ikizler, S. B., Aytekin, M., Vekli, M., and Kocabaş, F., 2010. Prediction of swelling pressures of expansive soils using artificial neural networks. Advances in Engineering Software, 41(4), 647-655.

Ikizler, S. B., Vekli, M., Dogan, E., Aytekin, M., and Kocabas, F., 2014. Prediction of swelling pressures of expansive soils using soft computing methods. Neural Computing and Applications, 24, 473-485.

Işık, N. S., 2009. Estimation of swell index of fine grained soils using regression equations and artificial neural networks. Scientific Research and Essays, 4(10), 1047-1056.

Israr, J., Farooq, K., and Mujtaba, H. H., 2014. Modelling of swelling parameters and associated characteristics based on index properties of expansive soils. Pakistan Journal of Engineering and Applied Sciences.

Jalal, F. E., Xu, Y., Iqbal, M., Javed, M. F., and Jamhiri, B., 2021. Predictive modeling of swell-strength of expansive soils using artificial intelligence approaches: ANN, ANFIS and GEP. Journal of Environmental Management, 289, 112420.

Janssen, D. J., and Dempsey, B. J., 1980. Soil water properties of subgrade soils. Final Report.

Jennings, J., 1961. A revised effective stress law for use in the prediction of the behaviour of unsaturated soils. Pore pressure and suction in soils, 26-30.

Jennings, J., Burland, J., 1962. Limitations to the use of effective stresses in partly saturated soils. Géotechnique, 12(2), 125-144.

Jennings, J. E., Firth, R. A., Ralph, T. K., and Nagar, N., 1973. An improved method for predicting heave using the oedometer test. Proceedings of the International Conference on Expansive Soils, Haifa, Israel, pp. 149-154.

Jennings, J.E.B., and Knight, K., 1957. The prediction of total heave from double oedometer test. Proceedings of the Symposium on Expansive Clays, South African Institution of Civil Engineers, Johannesburg, pp. 13–19.

Jommi, C., 2000. Remarks on the constitutive modelling of unsaturated soils. Experimental evidence and theoretical approaches in unsaturated soils, 153, 139-153.

Kato, S., Matsuoka, H., and Sun, D.A., 1995. A constitutive model for unsaturated soil based on extended SMP. Proceedings of the First International Conference on Unsaturated Soils, UNSAT-95, Paris, pp. 739–744.

Kayadelen, C., Taşkıran, T., Günaydın, O., Fener, and M., 2009. Adaptive neuro-fuzzy modeling for the swelling potential of compacted soils. Environmental Earth Sciences, 59, 109-115.

Khalili, N., Khabbaz, and M., 1998. A unique relationship for χ for the determination of the shear strength of unsaturated soils. Géotechnique, 48(5), 681-687.

Kohgo, Y., 2003. Review of constitutive models for unsaturated soils and initial-boundary value analyses. Unsaturated Soils – Geotechnical and Geoenvironmental Issues, 2, 21-40.

Komine, H., and Ogata, N., 2003. New equations for swelling characteristics of bentonite-based buffer materials. Canadian Geotechnical Journal, 40(2): 460-475.

Komornik, A., Wiseman, G., and Ben-Yaacob, Y., 1969. Studies of in-situ moisture and swelling potential profiles. Proceedings of the 2nd International Conference on Expansive Soils, Texas, pp. 348-361.

Lambe, T.W., 1960. A mechanistic picture of shear strength in clay. Research Conference on Shear Strength of Cohesive Soils, ASCE, Boulder, Colorado, pp. 555-580.

Lambe, T., and Whitman, R., 1979. Soil Mechanics. Wiley, New York.

Liu, Y., Vanapalli, and S. K., 2017. Influence of lateral swelling pressure on the geotechnical infrastructure in expansive soils. Journal of Geotechnical and Geoenvironmental Engineering, 143(6), 04017006.

Lu, L., 2011. A Simple Technique for Estimating the One-Dimensional Heave of Natural Expansive Soils. Library and Archives Canada/Bibliothèque et Archives Canada, Ottawa.

Lu, S., Lu, Y., Peng, W., Ju, Z., and Ren, T., 2019. A generalized relationship between thermal conductivity and matric suction of soils. Geoderma, 337, 491-497.

Lytton, R. L., 1977. The characterization of expansive soils in engineering. Presentation at the Symposium on Water Movement and Equilibria in Swelling Soils, American Geophysical Union, San Francisco, California.

McKeen, R. G., 1992. A model for predicting expansive soil behavior. International Conference on Expansive Soils, pp. 1-6.

Merouane, F. Z., and Mamoune, S. M. A., 2018. Prediction of swelling parameters of two clayey soils from Algeria using artificial neural networks. Modelling in Civil Environmental Engineering, 14(3), 11-26.

Miller, D. J., and Nelson, J. D., 2006. Osmotic suction in unsaturated soil mechanics. Unsaturated Soils 2006, pp. 1382-1393.

Mitchell, J. K., and Soga, K., 2005. Fundamentals of Soil Behavior, 3rd ed. John Wiley & Sons, New York.

Mitchell, P. W., and Avalle, D. L., 1984. A technique to predict expansive soils movement. Proceedings of the 5th International Conference on Expansive Soils, Adelaide,

Australia, pp. 124–130.

Najjar, Y. M., Basheer, I. A., Ali, H. E., and McReynolds, R. L., 2000. Swelling potential of Kansas soils: Modeling and validation using artificial neural network reliability approach. Transportation research record, 1736(1), 141-147.

Nelson, J., and Miller, D. J., 1997. Expansive Soils: Problems and Practice in Foundation and Pavement Engineering. John Wiley & Sons.

Nelson, J.D., Durkee, D.B., and Bonner, J.P., 1998. Prediction of free field heave using oedometer test data. Proceedings of the 46th Annual Geotechnical Engineering Conference, University of Minnesota, St. Paul, MN.

Nelson, J. D., Reichler, D. K., and Cumbers, J. M., 2006. Parameters for heave prediction by oedometer tests. Unsaturated Soils 2006, pp. 951-961.

Newland, P., 1965. The behavior of soils in terms of two kinds of effective stress.

Ng, C. W. W., Zhou, C., and Chiu, C. F., 2020. Constitutive modelling of state-dependent behaviour of unsaturated soils: an overview. Acta Geotechnica, 15, 2705-2725.

Nguyen, D. D., Roussis, P. C., Pham, B. T., Ferentinou, M., Mamou, A., Vu, D. Q., Bui, Q.-A. T., Trong, D. K., and Asteris, P. G., 2022. Bagging and multilayer perceptron hybrid intelligence models predicting the swelling potential of soil. Transportation Geotechnics, 36, 100797.

Nur, A., and Byerlee, J. D., 1971. An exact effective stress law for elastic deformation of rock with fluids. Journal of geophysical research, 76(26), 6414-6419.

Nuth, M., and Laloui, L., 2008. Effective stress concept in unsaturated soils: Clarification and validation of a unified framework. International journal for numerical and analytical methods in Geomechanics, 32(7), 771-801.

Onyelowe, K. C., Fazal, E., Michael, E., Ifeanyichukwu, C., Alaneme, G. U., and Chidozie, I., 2021. Artificial intelligence prediction model for swelling potential of soil and quicklime activated rice husk ash blend for sustainable construction. Jurnal Kejuruteraan, 33(4), 845-852.

Porter, A. A., and Nelson, J. D., 1980. Strain controlled testing of expansive soils. Proceedings of the 4th International Conference on Expansive Soils, Denver, Colorado, pp. 34-44.

Ranganatham, B. V., and Satyanarayana, B., 1965. A rational method of predicting swelling potential for compacted expansive clays. Proceedings of the 6th International Conference on Soil Mechanics and Foundation Engineering, Montreal, pp. 92-96.

Rao, A., Phanikumar, B., and Sharma, R. S., 2004. Prediction of swelling characteristics of remoulded and compacted expansive soils using free swell index. Quarterly Journal of Engineering Geology and Hydrogeology, 37(3), 217-226.

Rao, S. M., Thyagaraj, T., and Thomas, H. R., 2006. Swelling of compacted clay under osmotic gradients. Géotechnique, 56(10), 707-713.

Rassam, D. W., and Williams, D. J., 1999. A relationship describing the shear strength of unsaturated soils. Canadian Geotechnical Journal, 36(2), 363-368.

Rendulic, L., 1936. Relation between void ratio and effective principal stresses for a remolded silty clay. Proceedings of the 1st International Conference on Soil Mechanics and Foundation Engineering, Vol. 3, pp. 48-51.

Richards, B. G., 1965. Measurement of free energy of soil moisture by the psychrometric technique, using thermistors. Proceedings of the Symposium on Moisture Equilibria and Moisture Changes in Soils Beneath Covered Areas, pp. 39-46.

Ross, G. J., 1978. Relationships of specific surface area and clay content to shrink-swell potential of soils having different clay mineralogical compositions. Canadian Journal of Soil Science, 58(2), 159-166.

Russell, A., and Khalili, N., 2006. A unified bounding surface plasticity model for unsaturated soils. International Journal for Numerical and Analytical Methods in Geomechanics, 30(3), 181-212.

Seed, H. B., Woodward Jr, R. J., and Lundgren, R., 1962. Prediction of swelling potential for compacted clays. Journal of the soil mechanics and foundations division, 88(3), 53-87.

Schafer, W. M., and Singer, M. J., 1976. A new method of measuring shrink-swell potential using soil pastes. Soil Science Society of America Journal, 40(5), 805-806.

Schneider, G. L., and Poor, A. R., 1974. The prediction of soil heaves and swell pressures developed by expansive clay. Construction Research Centre, CRC Publications, Tex. Research Report TR-9-74.

Sheng, D., 2011. Constitutive modelling of unsaturated soils: Discussion of fundamental principles. Unsaturated soils, 1, 91-112.

Sheng, D., and Fredlund, D. G., 2008. Elastoplastic modelling of unsaturated soils: an overview. Keynote lecture, 12th International Conference of the International Association for Computer Methods and Advances in Geomechanics (IACMAG).

Shirazi, S.M., Kazama, H., Salman, F.A., Othman, F., and Akib, S., 2010. Permeability and

swelling characteristics of bentonite. International Journal of the Physical Sciences, 5(11), 1647–1659.

Shuai, F., 1998. Simulation of Swelling Pressure Measurements on Expansive Soils. Ph.D. thesis, University of Saskatchewan.

Singhal, S., 2010. Expansive Soil Behavior: Property Measurement Techniques and Heave Prediction Methods. Ph.D. thesis, Arizona State University.

Singhal, S., Houston, S., and Houston, W., 2011. Effects of testing procedures on the laboratory determination of swell pressure of expansive soils. Geotechnical Testing Journal, 34(5), 476-488.

Skempton, A.W., 1961. Effective stress in soils, concrete, and rocks. Conference on Pore Pressure and Suction in Soils, London, Butterworths, pp. 4-16.

Skempton, A., 1984. Effective stress in soils, concrete and rocks. Selected papers on soil mechanics, 1032, 4-16.

Sridharan, A., 1968. Some studies on the strength of partly saturated clays. Ph.D. Thesis, Purdue University, U.S.A.

Sridharan, A., Rao, A. S., and Sivapullaiah, P. V., 1986. Swelling pressure of clays. Geotechnical Testing Journal, 9(1): 24-33.

Sullivan, R. A., and McClelland, B., 1969. Predicting heave of buildings on unsaturated clay. Proceedings of the Second International Research and Engineering Conference on Expansive Clay Soils, Texas A&M University Press, College Station, TX, pp. 404–420.

Taherdangkoo, R., Tyurin, V., Shehab, M., Ardejani, F. D., Tang, A. M., Narmandakh, D., and Butscher, C., 2023. An efficient neural network model to determine maximum swelling pressure of clayey soils. Computers and Geotechnics, 162, 105693.

Tang, C., and Shi, B., 2011. Swelling and shrinkage behaviour of expansive soil during wetting-drying cycles. Chinese Journal of Geotechnical Engineering, 33(9), 1376-1384.

Terzaghi, K. V., 1936. The shearing resistance of saturated soils and the angle between the planes of shear. First International Conference on Soil Mechanics and Foundation Engineering, Vol. 1, pp. 54-59.

Thyagaraj, T., and Salini, U. (2015). Effect of pore fluid osmotic suction on matric and total suctions of compacted clay. Géotechnique, 65(11), 952-960.

Tu, H., Vanapalli, and S. K., 2016. Prediction of the variation of swelling pressure and one-

dimensional heave of expansive soils with respect to suction using the soil-water retention curve as a tool. Canadian Geotechnical Journal, 53(8), 1213-1234.

Van Genuchten, and M. T., 1980. A closed-form equation for predicting the hydraulic conductivity of unsaturated soils. Soil science society of America journal, 44(5), 892-898.

Vanapalli, S.K., 1994. Simple test procedures and their interpretation in evaluating the shear strength of an unsaturated soil. Ph.D. Thesis, University of Saskatchewan, Saskatoon, Canada.

Vanapalli, S., Fredlund, D., Pufahl, D., and Clifton, A., 1996. Model for the prediction of shear strength with respect to soil suction. Canadian Geotechnical Journal, 33(3), 379-392.

Vanapalli, S., and Lu, L., 2012. A state-of-the art review of 1-D heave prediction methods for expansive soils. International Journal of Geotechnical Engineering, 6(1), 15-41.

Vanapalli, S., and Oh, W., 2010. A model for predicting the modulus of elasticity of unsaturated soils using the soil-water characteristic curve. International Journal of Geotechnical Engineering, 4(4), 425-433.

Vanapalli, S. K., Lu, L., Sedano, J. I., and Oh, W. T., 2012. Swelling characteristics of sand-bentonite mixtures. In Unsaturated Soils: Research and Applications, Vol. 2, pp. 77-84.

Vijayvergiya, V. N., and Ghazzaly, O. I., 1973. Prediction of swelling potential for natural clays. Proceedings of the 3rd International Conference on Expansive Clay Soils, Haifa, Israel, Vol. 1, pp. 227–234.

Wheeler, S., and Karube, D., 1995. State of the art report—constitutive modelling. Proceedings of the 1st International Conference on Unsaturated Soils, Paris, Vol. 3.

Wheeler, S., Sharma, R., and Buisson, M., 2003. Coupling of hydraulic hysteresis and stress–strain behaviour in unsaturated soils. Géotechnique, 53(1), 41-54.

Wong, H. Y., and Yong, R. M., 1973. A study of swelling and swelling force during unsaturated flow in expansive soils. Proceedings of the 3rd International Conference on Expansive Soils, Haifa, Israel, pp. 143-151.

Yilmaz, I., and Kaynar, O., 2011. Multiple regression, ANN (RBF, MLP) and ANFIS models for prediction of swell potential of clayey soils. Expert systems with applications, 38(5), 5958-5966.

Ying, Z., Cui, Y. J., Benahmed, N., and Duc, M., 2021. Salinity effect on the compaction

behaviour, matric suction, stiffness and microstructure of a silty soil. Journal of Rock Mechanics and Geotechnical Engineering, 13(4), 855-863.

Zou, W. L., Ye, J. B., Han, Z., Vanapalli, S. K., and Tu, H. Y., 2018. Effect of montmorillonite content and sodium chloride solution on the residual swelling pressure of an expansive clay. Environmental Earth Sciences, 77, 1-12.

Zumrawi, M., 2013. Swelling potential of compacted expansive soils. International Journal of Engineering Research and Technology, 2(3), 1-6.

CHAPTER 3

PREDICTING SWELLING INDEX AND SWELLING PRESSURE OF EXPANSIVE SOILS USING MULTIPLE ARTIFICIAL INTELLIGENCE TECHNIQUES

3.1 Introduction[1]

Expansive soils typically contain a high proportion of fine particles that include hydrophilic clay minerals like montmorillonite, which have significantly higher values of the plasticity index (Lin et al., 2022). These soils swell when they imbibe moisture and exhibit high swelling pressures when their volume changes are restricted (Han et al., 2024). Consequently, geotechnical engineers face numerous challenges when designing and evaluating geo-infrastructures on expansive soils. Conventional soil mechanics, typically employed for assuming saturated conditions for the design of geo-infrastructure may not be suitable for expansive soils that are typically in an unsaturated state. In a saturated state, all the pores within the soil are filled with water. During consolidation of a saturated soil, its volume change arises from the movement of pore water, as the soil particles themselves are incompressible. Thus, the total volume change in a saturated soil corresponds to changes in the soil structure. Void ratio is used as an indicator to determine the volume change behavior of a saturated soil associated with soil structure alterations. However, the hydro-mechanical constitutive relationship between soil structure and the water phase should be used for rational analysis of the volume change behavior of unsaturated soils. The void ratio change can be used as the deformation state variable of the soil structure, and the variation in water content represents the deformation state variable of the water phase (Fredlund and Rahardjo, 1993). The reduction of void ratio and water content can be

[1] The contents presented in this chapter are published as a journal article: **Zhang, A.**, & Vanapalli, S. K. (2025). Estimation of the swelling index and swelling pressure of expansive soils using multiple artificial intelligence techniques. *International Journal of Geomechanics*, 25 (11), 04025244.

attributed to an increase in net normal stress and matric suction. The change in void ratio exhibits greater sensitivity to variations in net normal stress, whereas the water content is more sensitive to changes in matric suction. As water infiltrates the soil, the suction gradually diminishes, leading to volumetric expansion in expansive soils. When loads associated with the structure constrain soil volume expansion, significant swelling pressure is generated, contributing to geo-structural damages such as pavement cracking, slope instability, and foundation damages (Mokhtari and Dehghani, 2012; Zumrawi, 2013; Mohamed et al., 2014; Djellali et al., 2017; Liu and Vanapalli, 2017; Li et al., 2021; Venkatesan et al., 2021; Abbas et al., 2023).

In recent decades, behavior of expansive soils have been attributed for numerous structural damages and significant economic losses worldwide (Adem and Vanapalli, 2016). For example, the annual cost of dealing with damages due to expansive soils in the USA has increased from $2.3 billion in 1973 (Jones Jr and Holtz, 1973) to $13 billion in 2009 (Puppala and Cerato, 2009). Extensive efforts by many researchers over the last four decades have led to the development of methods for determining and estimating the swelling index and swelling pressure, contributing to enhanced safety and reducing economic losses to a certain extent. These methods encompass the oedometer test methods (Fredlund, 1983; Nelson and Miller, 1997), empirical approaches (Elisha, 2012; Vanapalli and Lu, 2012; Israr et al., 2014; Tu and Vanapalli, 2016), and artificial intelligence techniques (Das et al., 2010; Abdulkareem and Aziz, 2020; Amin Benbouras and Petrisor, 2021; Li et al., 2024). A detailed discussion of recent advancements, including experimental methods, empirical equations, and AI applications in predicting swelling characteristics is included in the Section 3.2 for providing a comprehensive background related to these studies.

In this study, three AI methods, namely multilayer perceptron (MLP), support vector machine (SVM), and extreme learning machine (ELM), are employed to predict the swelling index and swelling pressure. The performance of each model is evaluated using statistical indices to determine the most reliable prediction models for use in practice. Additionally, sensitivity analyses are conducted to examine the impact of soil properties

on swelling pressure prediction. Furthermore, by utilizing the MLP algorithm and regression analysis tool, two simple equations are proposed: an MLP-based equation and an empirical equation for predicting swelling index based on the plasticity index. These equations demonstrate reliable prediction capabilities within a plasticity index range of 25% to 100%, catering to the needs for swelling index information required in most geotechnical engineering applications. Moreover, the study also predicts the swelling pressure for different experimental methods, including the constant volume (CV) oedometer test and consolidation-swell (CS) tests, based on four prediction equations employing the MLP algorithm. The AI models and proposed equations presented in this study offer practical and user-friendly tools for implementation in conventional geotechnical engineering applications.

3.2 Background

3.2.1. Swelling index

The swelling index, C_s, is a key parameter for characterizing the deformation behavior of expansive soils. This parameter is conventionally determined from the slope of the rebound curve of void ratio and the logarithmic effective stress from oedometer tests to estimate the heave of fine-grained soils (e.g., (Fredlund, 1983; Tu and Vanapalli, 2016)). The swelling index can be measured from different tests, such as the free swell (FS) test (Indiramma et al., 2020), consolidation-swell (CS) test (Soltani et al., 2019), and constant volume (CV) test (Ma et al., 2021). The oedometer test despite being a rigorous method has certain limitations for measuring the swelling index. Firstly, expensive equipment and trained personnel are required for conducting oedometer tests making it less suitable for conventional geotechnical engineering projects with limited budgets (Alptekin and Taga, 2019; Fondjo et al., 2021). Furthermore, oedometer test results can be operator-dependent and are highly sensitive to soil sample disturbance, leading to inaccurate data. Maintaining the integrity of the soil sample collected from the field to the laboratory can be a cumbersome task. Additionally, the time required to perform an oedometer test typically ranges from a week to two, making it a time-consuming process that is impractical for many engineering applications (Tu and Vanapalli, 2016; Gratchev and Saeidi, 2020).

During the last two decades, recognizing the limitations of oedometer tests, several empirical equations have been developed based on conventional soil properties to predict the swelling index. These equations are summarized in Table 3.1.

Table 3.1 Empirical equations for predicting swelling index

Author	Equations	Soil type	Range of I_p	R^2
Tiwari and Ajmera (2011)	$C_s = 6*10^{-6}(I_p)^2 + 0.0026(I_p)$	Montmorillonite-dominated soils	$5 \le I_P \le 430$	0.93
Vanapalli and Lu (2012)	$C_s = 0.019e^{0.0343I_p}$	Diverse clays	$28 \le I_P \le 65$	0.97
Tu and Vanapalli (2016)	$C_s = 0.188/\left[1+e^{(44.526-I_p)/15.636}\right]$	Diverse clays	$28 \le I_P \le 100$	0.92

Note: C_s is swelling index; I_p is plasticity index; e is natural number, "Diverse clays" refers to different types of clay, that include minerals such as montmorillonite, kaolinite, and illite. R^2 indicates the coefficient of determination for each correlation.

Based on extensive research studies, it has been established that the plasticity index exhibits a strong correlation with the swelling characteristics of most clays, making it a viable standalone parameter for predicting the swelling index (Chen, 2012; Mir, 2015). Tiwari and Ajmera (2011) proposed an equation (Eq. 3.1) to predict the swelling index of expansive based on the plasticity index information. This equation was proposed based on using only montmorillonite-dominated expansive soil samples. For this reason, it may have limited applicability to illite-dominated expansive soils which are less sensitive in comparison to montmorillonite mineral, and hence tends to overestimate the swelling index. Vanapalli and Lu (2012) research studies suggest that the swelling index is positively correlated with the plasticity index, which can be described by Eq. 3.2. This equation provides a reasonably accurate prediction of the swelling index, particularly when the plasticity index of expansive soil is below 65%. However, it tends to overestimate the swelling index when the plasticity index value is higher than the range for which it is proposed (Tu and Vanapalli, 2016). To comprehensively investigate the influence of the

plasticity index on the swelling index across a wider range, Tu and Vanapalli (2016) extended the estimation method, incorporating data from additional expansive soils. Drawing upon data from nine expansive soils, Tu and Vanapalli (2016) formulated Eq. 3.3 as an extension of Eq. 3.2, enabling more reliable predictions of the swelling index within the plasticity index range of 0-100%. In the present study, an expanded dataset of experimental data is collected to validate the Eq. 3.3 within its proposed range. Building upon this, regression analysis was employed to refine the coefficients of Eq. (3), resulting in a modified relationship (Eq. (3.4)). This improved equation can be used for estimating the swelling index of different types of expansive soils with various clay minerals.

$$C_s = 0.18 - 0.13 / \left[1 + e^{0.12\left(I_p - 52.03\right)}\right] \tag{3.4}$$

Fig. 3.1 illustrates the curves generated using relationships Eq. (3.3) and Eq. (3.4). Comparative analysis suggests that the two correlation curves exhibit similar shapes and capture the strong correlation between the plasticity index and the swelling index. Notably, the proposed estimation curve (Eq. 3.4) demonstrates sharper trends within the plasticity index range of 35% to 75%, while trends are gradual in the lower and higher plasticity zones. This sharper trend within the 35% to 75% range highlights the improved sensitivity of the proposed Eq. (3.4) in capturing the variation of the swelling index in this critical zone. For plasticity index values below 35% and above 75%, the proposed Eq. (3.4) provides close comparisons with the measured data, particularly in the lower plasticity index range, which is supported by a slightly higher coefficient of determination (R^2) and a lower root mean square error (RMSE).

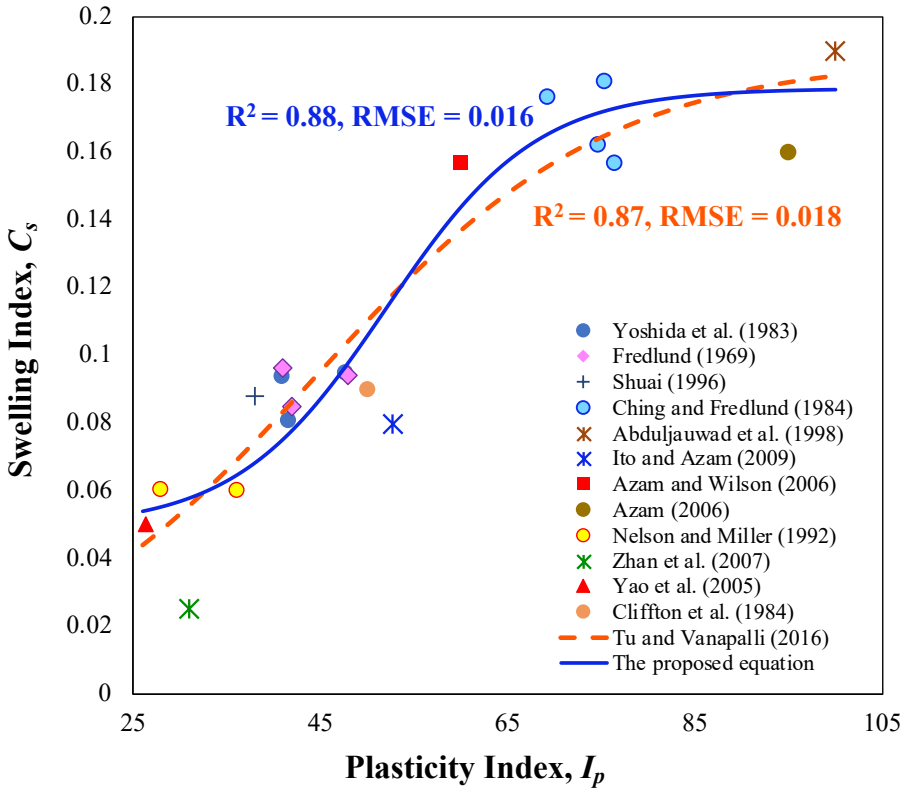


Fig. 3.1. Prediction performance of the proposed equation for predicting swelling index.

3.2.2. Swelling pressure

Expansive soils exhibit significant swelling pressure when their volume expansion is restricted during water infiltration. Swelling pressure is a key parameter that significantly impacts and contributes towards damages to several geotechnical structures. Therefore, reliable determination or estimation of the swelling pressure is required for the design of geotechnical structures situated on expansive soil sites (Jones and Jefferson, 2012; Du et al., 2021). Two different oedometer tests; namely the CS and CV tests are widely used for determining the swelling pressure. In the CS test, the soil sample undergoes swelling during the wetting process. Once the volume expansion under a certain load reaches equilibrium condition, an additional load is applied to the soil sample. The pressure required to return the sample to its original volume is defined as the consolidation-swell swelling pressure (P_{scs}). In the CV test, the soil volume remains constrained as pressure is progressively

applied. Once the soil sample swelling reaches a state of equilibrium under the applied pressure, it signifies the CV swelling pressure (P_{scv}) of the soil. In both tests, the soil samples are initially in an unsaturated state and gradually reach a fully saturated condition. The oedometer test is considered a relatively precise method for measuring swelling pressure under saturated conditions. However, the measured swelling pressure can be susceptible to soil disturbance and the compressibility of the testing equipment, potentially impacting the accuracy of the results (Fredlund, 1983). Soil sample disturbance alters the soil microstructure, affecting factors such as particle orientation and reducing inter-particle interactions, which can lead to an underestimation of the actual swelling pressure. Expansive soils may have experienced significant pre-consolidation pressure, resulting in substantial swelling pressure during testing and causing compression of the oedometer equipment (Nelson et al., 2015). Therefore, it is essential to consider the compressibility of the equipment to avoid underestimating the swelling pressure leading to unexpected damages of geo-infrastructures. Research indicates that under the same vertical strain, the corrected swelling pressure value is typically 1.2-3 times higher than the uncorrected value, emphasizing the importance of accounting for equipment compressibility (Fredlund and Rahardjo, 1993; Shuai, 1998; Nelson et al., 2015). Due to these reasons, it is essential to calibrate the test data accordingly considering these influencing factors. Fredlund (1983) proposed a calibration approach that involves first correcting for the compressibility of the testing equipment, followed by addressing the impact of soil sample disturbance on the test results. While the oedometer test method is considered rigorous, it is both time-consuming and cumbersome and hence has motivated numerous efforts to develop prediction equations for swelling pressure. These equations are summarized in Table 3.2 that provide practical alternatives to the labor-intensive oedometer test method.

Table 3.2 Empirical equations for predicting swelling pressure

Author	Equations	Soil type	R^2
Elisha (2012)	$Log(P_s) = -5.402 + 0.0139I_p + 2.461\gamma_d$	Black cotton soil	0.88
Israr et al. (2014)	$P_s = 43.6A + 68W_n - 915$	DGK-bentonite mixture	0.99
Tu and Vanapalli (2016)	$P_{sn} = (\sigma_y - u_a) + \beta_n \Psi_{field}[S/100]^2$ $\beta_n = 0.096A^{4.467}(2.375\gamma_d - 0.017I_p) + 0.178$ (for natural expansive soils)	Diverse clays	-
Tu and Vanapalli (2016)	$P_{sc} = P_{s0} + \beta_c \Psi_i[S/100]^2$ $\beta_c = 0.25e^{5.306\gamma_{d,max}}/10000$ (for compacted expansive soils)	Diverse clays	-

Note: P_s is swelling pressure, P_{sn} is swelling pressure for natural expansive soils, P_{sc} is swelling pressure for compacted soils, P_{s0} is swelling pressure at saturated state, I_p is plasticity index, γ_d is dry density, $\gamma_{d,max}$ is maximum dry density, A is activity, W_n is natural water content, β_n and β_c are the model parameters, $(\sigma_y - u_a)$ is net normal stress, S is degree of saturation, ψ_i is the initial suction, e is natural number, "DGK-bentonite mixture" represents a mixture of soil in Dera Ghazi Khan (Pakistan) and bentonite.

Elisha (2012) introduced Eq. 3.5, which incorporates plasticity index and dry density to predict swelling pressure, specifically for soil mixtures comprising varying proportions of bentonite and kaolinite. This correlation exhibits favorable performance in estimating the swelling pressure of soils within a plasticity index range of 6 to 32. However, its applicability for predicting swelling pressure in highly plastic expansive soils lacks sufficient validation. Israr et al. (2014) introduced Eq. 3.6 using information of activity and natural water content for estimating swelling pressure. This equation was derived using the multiple linear regression method that suggests a positive correlation between swelling

pressure and activity. However, it should be noted that the experimental data presented in the study suggests that the relationship between activity and swelling pressure is not consistently linear and proportional. The swelling pressure exhibits a sharp increase when the activity is around 1.5, and a single activity value can correspond to multiple significantly different swelling pressures. Hence, the applicability of the equation in describing the relationship between activity and swelling pressure may be constrained to a specific range of activity values. Tu and Vanapalli (2016) introduced Eqs. 3.7 and 3.8 to predict the swelling pressure of natural and compacted expansive soils, considering the effects of in situ overburden pressure, swelling pressure under saturated condition, plasticity index, and maximum dry density. Besides, both equations employ the soil-water characteristic curve (SWCC) to investigate the relationship between initial soil suction and swelling pressure, revealing that the swelling pressure of expansive soils is strongly related to initial soil suction. The proposed equations were validated using a comprehensive database of compacted and natural expansive soils from various regions, demonstrating their good performance in predicting swelling pressure. However, despite their commendable prediction ability, it is important to acknowledge that Eqs. 3.7 and 3.8 still possess certain limitations. Firstly, calculation of swelling pressure using the proposed semi-empirical equations requires multiple soil properties, which may not always be readily available. Measuring all the necessary properties can be challenging, countering the purpose of developing semi-empirical equations. Moreover, the model parameter β_n is not measured directly but is obtained through regression analysis or back-calculation based on soil properties. The model parameter β_c is empirically derived and can vary depending on compaction methods and soil conditions. Additionally, measurement of the SWCC for the studied soils is a prerequisite for using the prediction equations, can be challenging, difficult and time-consuming (Azmi et al., 2019). Furthermore, Eq. 3.8 relies on the measurement of the saturated swelling pressure (P_{S0}) from oedometer tests. While an average value for P_{S0} in different soil types is suggested, using an average P_{S0} might oversimplify the model and potentially affect the accuracy of swelling pressure predictions.

3.2.3. AI technology in the study of expansive soils

Artificial intelligence (AI) technology has made significant advancements in geotechnical engineering applications in recent years with the rapid advancement of computational methods. Its application, particularly in the investigations of expansive soils has also provided an opportunity to decrease reliance on laborious experiments and enhance the efficiency of predicting swelling characteristics such as swelling pressure and swelling index. By harnessing the potential of AI, researchers have made notable progress in understanding and analyzing the behavior of expansive soils (Erzin and Güneş, 2011; Sabat, 2015; Ermias and Vishal, 2020; Amin Benbouras and Petrisor, 2021; Jalal et al., 2021; Tiwari and Satyam, 2021; Chen et al., 2022; Taherdangkoo et al., 2023). Erzin and Güneş (2011) successfully developed artificial neural network (ANN) and multiple regression analysis (MRA) models to estimate the swelling percent and swelling pressure. Ermias and Vishal (2020) employed two artificial models, namely the three-layer feedforward neural network and multiple regression (MR), to effectively predict the swelling potential of clay-rich soils. Jalal et al. (2021) established prediction models to evaluate swell-strength of expansive soils using ANN, adaptive neuro-fuzzy inference system (ANFIS), and gene expression programming (GEP). Chen et al. (2022) predicted uniaxial tensile strength of expansive soils using ensemble machine learning methods. Sabat (2015) predicted the California Bearing Ratio of expansive soil by incorporating both SVM and ANN algorithms. Tiwari and Satyam (2021) used the ANN algorithm to establish the prediction model of mechanical and durability parameters for expansive soils. For example, Taherdangkoo et al. (2023) employed a feedforward neural network to estimate the maximum swelling pressure of expansive clays. Amin Benbouras and Petrisor (2021) introduced a model for estimating the vital swelling index parameter employing advanced machine learning techniques, including the extreme learning machine (ELM).

3.3 Methodology

3.3.1 Multilayer perceptron (MLP)

The MLP is a feedforward artificial neural network that is an advanced AI model inspired by the biological functioning of the human brain (Cho, 2009). It offers a powerful computational network that mimics information processing and decision-making. Compared to traditional regression and statistical analysis models, ANN has a distinct advantage in handling non-linear relationships among input parameters and modeling accurately (Bandara et al., 2011; Dave and Dutta, 2014; Abiodun et al., 2019; Hossain et al., 2020; Zareef et al., 2020). Therefore, MLP is suitable for analyzing the non-linear variation of swelling pressure of expansive soils.

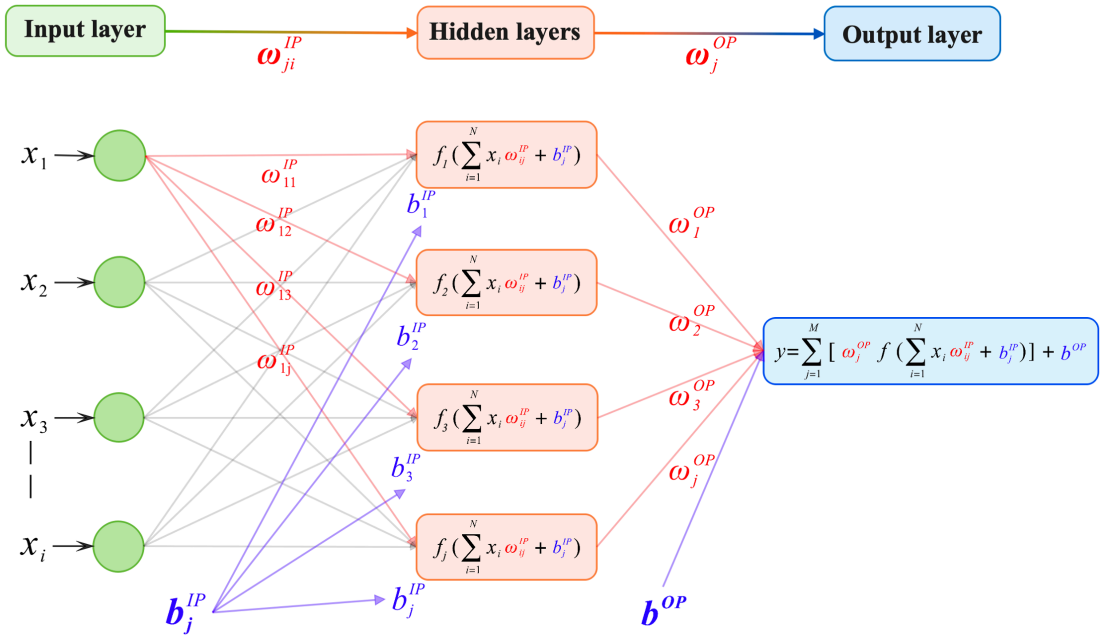


Fig. 3.2 The principle of the MLP algorithm.

Fig. 3.2 illustrates the structure and operation of the MLP algorithm, which consists of three layers: the input layer, hidden layer, and output layer. The input layer comprises nodes representing the independent elements of each sample in the dataset. The hidden layer consists of multiple neurons that simulate biological neurons in the human brain. Connections between the input layer and hidden layer have weights assigned to the

transmitted signals, which are then summed in the hidden neurons. Prior to leaving the neuron, the weighted signal passes through an activation function. If the sum value surpasses the activation function's threshold, the output value is converted to a numerical value between 0 and 1. This value is then passed to the next neuron for further weight learning and updating. This iterative process continues until the signal reaches the final output layer. In this study, the input layer is composed of basic soil properties used to predict the swelling index and swelling pressure in the output layer. Fig. 3.3 presents the flowchart outlining the process of MLP modeling in this study.

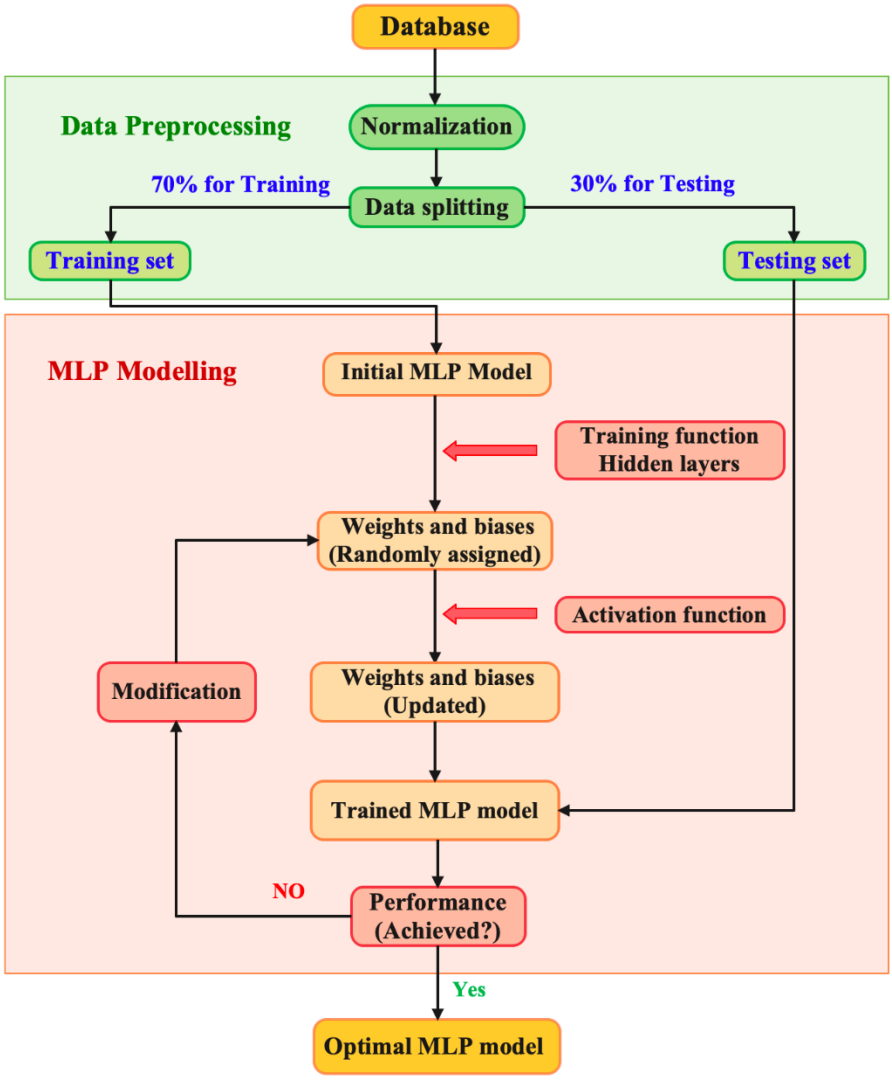


Fig. 3.3 Flow chart for MLP modelling.

Eq. 3.9 shows the general equation of MLP algorithm:

$$y = \sum_{j=1}^{M}\left[\omega_j^{OP} f\left(\sum_{i=1}^{N} x_i \omega_{ij}^{IP} + b_j^{IP}\right)\right] + b^{OP} \tag{3.9}$$

where, x_i is the i^{th} input parameter, y is the target parameter,ω_{ij}^{IP} are the weights assigned to input parameters, ω_j^{OP} are the weights assigned for the output layer, b_j^{IP} is the bias for the j^{th} hidden layer, b^{OP} is the bias for the output layer, f is the activation functions, N is the number of input parameters, M is the number of hidden layers.

3.3.2 Support Vector Machine (SVM)

The SVM is an advanced statistics-based algorithm for solving non-linear classification and regression problems (Wen et al., 2023). Compared with conventional AI algorithms, the SVM is more effective and reliable (Wang and Qu, 2017) and can better solve nonlinear and high-dimensional problems (Tao et al., 2018). Besides, SVM has proven to valuable when the available data sets are relatively small (Liang et al., 2020). Obtaining the swelling index and swelling pressure from experimental investigations is a time-consuming process, resulting in limited available data in the literature. Hence, utilizing SVM is highly suitable for predicting these two key swelling properties. While SVM is known for its problem-solving capabilities, a significant amount of time is often required to determine the most suitable kernel function and optimal parameters for constructing a well-trained SVM model (Sun et al., 2020). In SVM, the classification problem-solving involves determining a decision plane to separate linearly irrelevant data. When data points cannot be linearly separated, a kernel function is employed to achieve high-dimensional mapping and separate the data points. The classification principle of the SVM is to select a hyperplane from randomly distributed data, minimize its error, and translate it until reaching the closest data points on both sides, forming two new hyperplanes (dash lines in Fig. 3.4). The distance between these hyperplanes represents the margin, while the data points falling on them are known as support vectors. By adjusting the position of the decision boundary through the selection of support vectors, SVM maximizes the margin. A decision plane with a wider margin exhibits reduced generalization error. Thus, the primary objective of SVM is to

locate an optimal decision hyperplane with the maximum margin for effective data point classification.

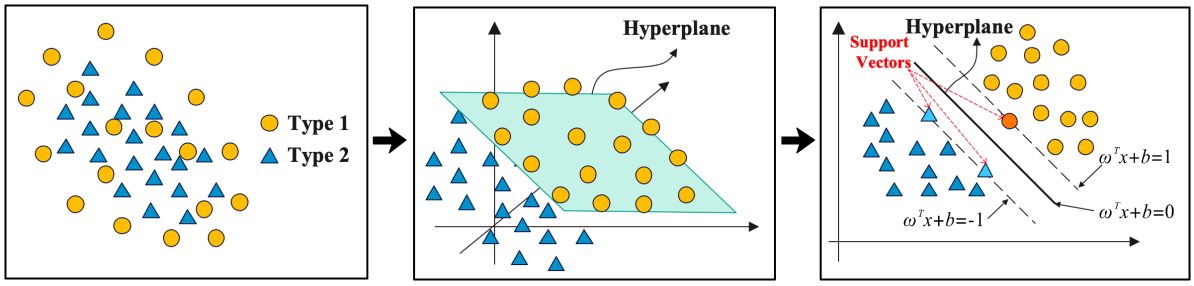


Fig. 3.4 The principle of the SVM algorithm

Fig. 3.5 illustrates the computational principle of the SVM algorithm. The input data must be projected from the original space to a higher-dimensional space to discover the linear decision boundary for nonlinear input data. While this nonlinear transformation is effective, uncertainty regarding the mapping function can result in data being projected into infinite dimensions. The calculation becomes more challenging, time-consuming, and expensive as the data dimension increases because finding the hyperplane is more difficult. However, the use of a nonlinear kernel function allows for the calculation of dot products in the high-dimensional space using the low-dimensional original space, greatly enhancing computational efficiency. Hence, the selection of the kernel function is a crucial aspect of the SVM computation process. Additionally, the bias, which signifies the distance between the decision plane and a hyperplane, is another critical parameter. By appropriately selecting the kernel function and optimizing the bias, precise prediction outcomes can be achieved.

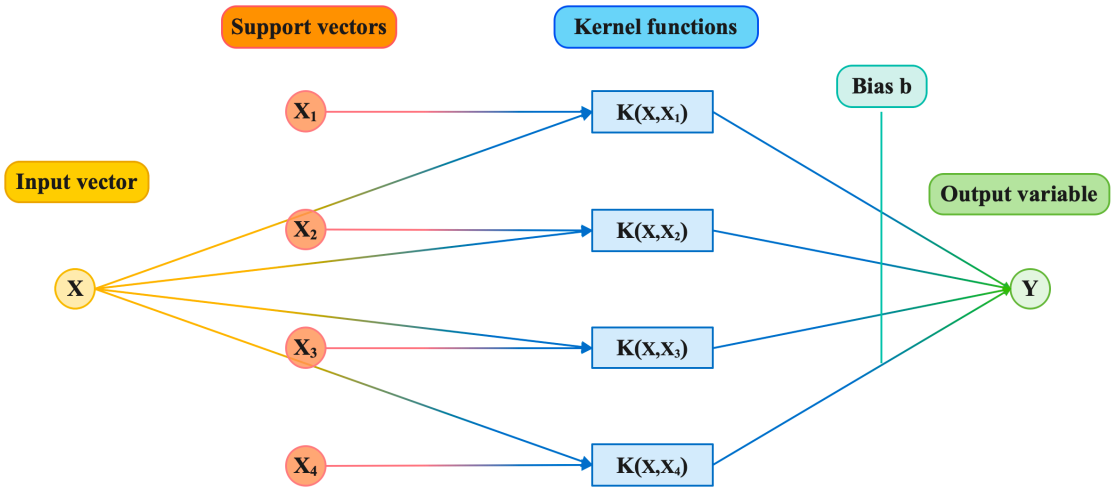


Fig. 3.5 The principle of the SVM algorithm.

3.3.3 Extreme Learning Machine (ELM)

There is a strong relationship between swelling pressure and various soil properties. However, constructing prediction models with multiple soil properties as input variables can be intricate and time-consuming. To enhance operational speed and streamline the algorithm structure, Huang et al. (2006) proposed the ELM which is a novel algorithm that builds upon the structure of a single hidden layer feedforward neural network. In contrast to traditional feedforward neural networks, ELM exhibits notable advantages in terms of processing speed and exceptional generalization performance (Ma et al., 2020). Therefore, ELM is beneficial for addressing prediction challenges associated with swelling pressure. The ELM consists of input, hidden, and output layers like conventional neural networks. However, ELM uniquely possesses a single hidden layer, significantly reducing the prediction time. Notably, ELM randomly assigns weights and biases to the hidden layer, without updating them during the training process. The weight of the output layer can be determined using the least mean square error method and generalized inverse matrix theory. The training process of ELM concludes upon obtaining the weights and biases for all network nodes. Fig. 3.6 visually represents the computational architecture of the ELM algorithm.

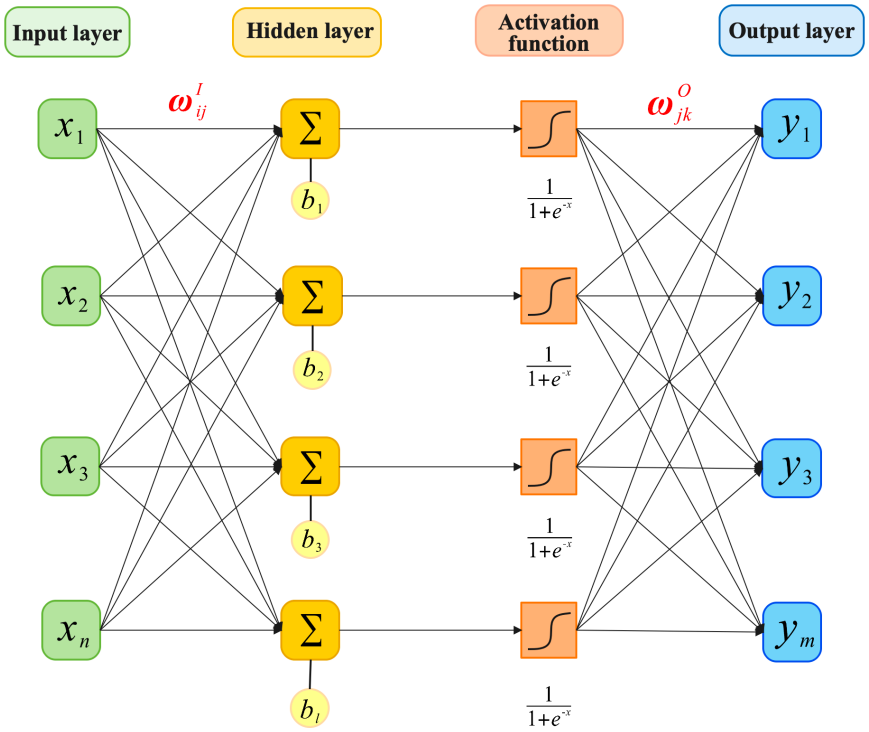


Fig. 3.6 The computation architecture of the ELM algorithm.

$$y_k = \sum_{j=1}^{l} \omega_{jk}^{o} G\left(\omega_{ij}^{l} \cdot x_i + b_j\right) \quad (i = 1,2...,n; j = 1,2,...,l; k = 1,2,...,m) \tag{3.10}$$

Eq. (10) shows the general form of the ELM prediction equation, where x_i is the i^{th} input parameter, y_k is the k^{th} output parameter, ω^{I}_{ij} are the weights of hidden neurons, ω^{O}_{jk} are the weights of output targets, b_j is the j^{th} bias of hidden neurons, G is the activation function, l is the number of hidden neurons.

3.3.4 Evaluation indexes

Eqs. 3.11-3.13 are evaluation index relationships. The Pearson correlation coefficient (R) is used to describe the strength of a linear relationship between measured and prediected variables, where the value R=1 means a perfect correlation. When R value is greater than 0.8, O_i and P_i have fairly strong correlation (Liu et al., 2020).

$$R = \frac{\sum_{i=1}^{N}\left(O_i - \bar{O}_i\right)\cdot\left(P_i - \bar{P}_i\right)}{\sqrt{\sum_{i=1}^{N}\left(O_i - O_i\right)^2 \cdot \sum_{i=1}^{N}\left(P_i - P_i\right)^2}} \tag{3.11}$$

$$\mathrm{VAF} = \left(1 - \mathrm{var}\left(O_i - P_i\right)/\mathrm{var}\left(O_i\right)\right)\times 100 \tag{3.12}$$

$$\mathrm{RMSE} = \sqrt{\frac{1}{N}\sum_{i=1}^{N}\left(O_i - P_i\right)^2} \tag{3.13}$$

where O_i is the i^{th} measured value and P_i is the i^{th} predicted value; $\overline{O}_i$ and $\overline{P}_i$ are the average values of the measured and predicted values, respectively, and N is the number of parameters.

To provide the proportion of variance of one variable that is predictable from another variable, the coefficient of determination (R^2) is introduced. If R^2 is 0.8, it means 80% of the total variation in predicted values P_i can be explained by measured values O_i (Piepho, 2019). Besides, variance accounted for (VAF) is another popular statistical index to verify the correctness of models. The closer the VAF value is to 100%, the higher the accuracy of the model. (Adoko and Yagiz, 2019). Root mean square error (RMSE) is the standard deviation of prediciton errors and it gives the information that how concentrated the data is around the best fit line. A lower value (closer to 0) indicates more accurate prediction results (Yang et al., 2019). In summary, a larger value for R, R^2, and VAF, along with smaller values of RMSE, indicate better prediction accuracy.

3.3.5 Database establishment and preprocessing

To ensure reliability of the data sources, only experimental results from peer-reviewed publications were selected. These studies provided detailed records of soil properties and testing methodologies, adhering to widely accepted ASTM standards. Data were screened for consistency, and only those with reproducible results and minimal experimental errors were included. This rigorous selection process ensures that the dataset used for model development is both accurate and representative of expansive soils from diverse regions.

Expansive soils information from various countries has been gathered to create a comprehensive database to enhance the reliability and generalization of the study. The plasticity index, an essential soil property, has been employed to predict the swelling index for 12 expansive soils, and the relevant details are provided in Table 3.3. The soils in Table 3.3 are sourced from regions with diverse geological and climatic conditions, including Canada, South Africa, Australia, Saudi Arabia, the United States, and China, ensuring the dataset captures variability in swelling index across different soil types. The selection of these input parameters was guided by their demonstrated physical relevance to expansive soil behavior and strong correlations with swelling characteristics. Parameters such as plasticity index, dry unit weight, clay fraction, and initial suction were identified as critical factors influencing swelling pressure and volumetric changes, based on extensive studies in the literature.

Table 3.3 Information of soils used to predict swelling index

ID	Soil	I_p	C_S	Location	Reference
1	Regina clay 1	40.9~47.6	0.081~0.095	Canada	Yoshida et al., 1983
2	Regina clay 2	41~48	0.085~0.096	Canada	Fredlund (1969)
3	Regina clay 3	38	0.088	Canada	Shuai (1998)
4	Eston clay	63-76.4	0.157~0.190	Canada	Ching and Fredlund (1984)
5	Cape Town clay	100	0.19	South Africa	Abduljauwad et al., 1998
6	Regina clay 4	52.7	0.08	Canada	Ito and Azam (2009)
7	Persian Gulf clay	60	0.057	Saudi Arabia	Azam and Wilson (2006)
8	Al-Qatif clay	95	0.16	Saudi Arabia	Azam (2006)

9	Colorado clay	28-36	0.06	US	Nelson and Miller (1997)
10	Guangxi expansive clay	26.4	0.05	China	Yao et al., 2005
11	Regina clay 5	50	0.09	Canada	Clifton et al., 1984
12	Zaoyang expansive clay	31	0.025	China	Zhan et al., 2007

According to a large number of studies, the soil properties that include dry unit weight (γ_d), plasticity index (I_p), initial gravimetric water content (w), clay fraction (C), initial void ratio (e_0), swelling index (C_s), and initial suction (Ψ) are typically used to develop empirical relationships for estimating the expansive soils swelling pressure (Fredlund and Rahardjo, 1993; Zhang et al., 2015; Tu and Vanapalli, 2016; Du et al., 2021; Fondjo et al., 2021; Jalal et al., 2021; Phanikumar et al., 2021; Watanabe and Tanaka, 2021; Ikechukwu and Mostafa, 2022). The swelling pressure is directly proportional to the dry unit weight of soils according to several studies (e.g., Elisha, 2012; Mawlood and Hummadi, 2020). The clay fraction and plasticity index together reflect the content of fine-grained particles and expansive hydrophilic minerals in the soil. Typically, soil is highly expansive when it has a larger clay fraction and a higher plasticity index. The variation of void ratio and water content signifies the alteration of solid and liquid phases within the volume change constitutive relationship of unsaturated soils. The change in suction value partially governs the fluctuation of void ratio and water content in unsaturated soil (Fredlund and Rahardjo, 1993). Moreover, the swelling index provides a direct relationship between the void ratio and effective stress, establishing a significant association with the volumetric behavior of expansive soils. Therefore, these soil properties become essential in selecting input parameters. As a result, the fundamental soil properties of 26 expansive soils have been gathered and summarized in Table 3.4 to develop AI models for predicting swelling pressure. These samples represent a wide range of environments, such as arid (e.g., Saudi Arabia), cold (e.g., Canada), and tropical regions (e.g., Brazil). The diversity in soil

classifications and testing methods ensures the dataset's suitability for use in geotechnical engineering practice applications.

Table 3.4 Information of soils used to predict swelling pressure

ID	Soil	Classification	Tests	Location	Reference
1	Regina clay 1	CH	CV	Canada	Yoshida et al., 1983; Vu and Fredlund (2004)
2	Texas clay 1	CH	CV	US	Pedarla et al., 2012
3	Oklahoma clay 1	CL	CV	US	Pedarla et al., 2012
4-5	Maryland clay 1-2	CH	CV	Australia	Fityus et al., 2004
6	Zaoyang expansive clay	CH	CS	China	Ng et al., 2003
7	Regina clay 6	CH	CV	Canada	Azam et al., 2013
8	Al-Ghat shale	CH	CV	Saudi Arabia	Al-Shamrani and Dhowian (2003)
9	French clay	CH	CV	France	ISRM (1989)
10	Burleson	CH	CS	US	Khattab et al., 2002
11	Colorado	CH	CS	US	Zhan et al., 2007
12	Grayson	CH	CS	US	Pedarla et al., 2012
13	San Diego	CH	CS	US	Pedarla et al., 2012
14-18	Guabirotuba soil 1-5	CH	CV	Brazil	Pedarla et al., 2012
19	Prescott clay	CH	CV	US	Singhal (2010)
20-26	San Antonio clay 1-7	CH	CS	US	Singhal (2010)

Several approaches have been employed to enhance the reliability of the prediction models, which are summarized as follows:

(i) The swelling pressure values determined from different types of experiments can be different even for identical soil samples (Zhang et al., 2020). To ensure accuracy and mitigate errors associated with experiment types, it is both logical and imperative to classify the collected data into two distinct groups based on the testing technique: the CV test group and the CS test group. This classification allows for separate predictions to be made, enhancing the reliability of the results.

(ii) In order to enhance the rate of convergence and improve the accuracy of the models, it is necessary to normalize the data, ensuring that all features are within the same range (Folorunso et al., 2018; Moreira et al., 2021). Hence, the min-max normalization method (Eq. 3.14) is selected, ensuring that the values of the collected data are normalized within the range of [-1, 1].

(iii) To develop a dependable prediction model, it is essential to split the data into training and testing datasets (Xu and Goodacre, 2018). Most of the data should be allocated to the training set for model training and optimization, while a smaller set of the data should be reserved to assess the performance of the trained model. As suggested by studies (Lyu et al., 2021; Vrigazova, 2021; Roshan Joseph, 2022), 70% of the data is used for training the AI models, and 30% of the data is for testing.

(iv) To improve the reliability of the prediction model, all measured data from experiments is included in the testing set to validate the accuracy of the models.

$$X_n = \frac{X - Min}{Max - Min}(D - B) + B \tag{3.14}$$

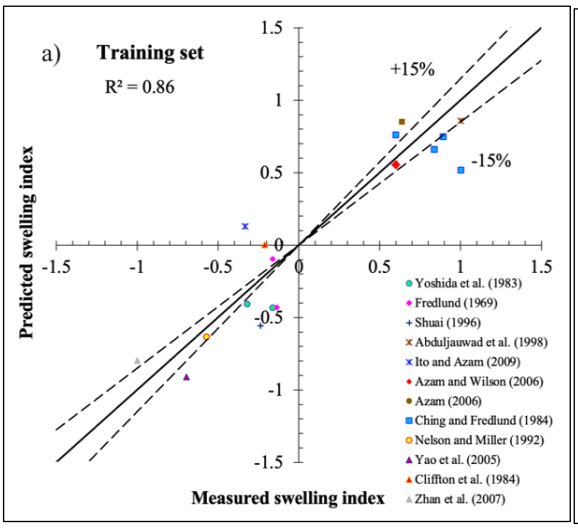
where, X is the data before normalization, X_n is the normalized data, [B, D] is the normalization range.

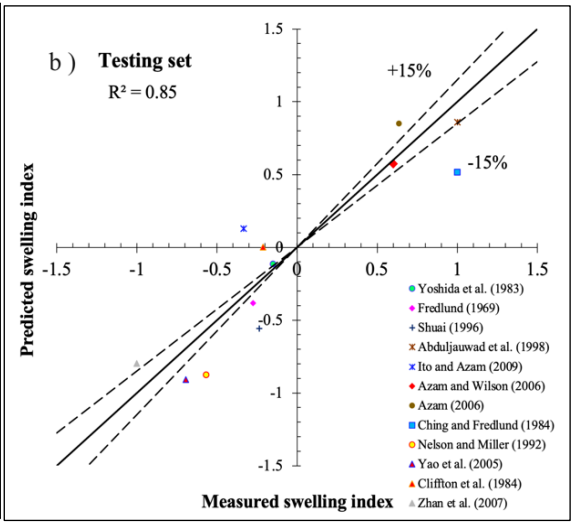
3.4 AI modeling and results

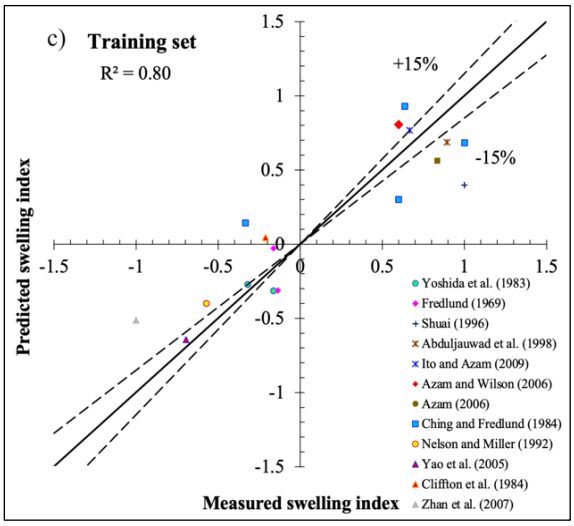
3.4.1 Prediction of swelling index

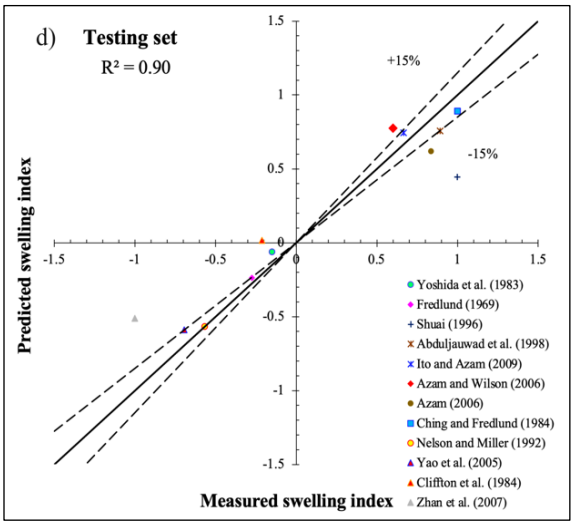
In this study, three AI techniques, MLP, SVM, and ELM, were employed to develop models for predicting the swelling index and swelling pressure. The prediction results for the swelling index generated by these models are summarized in Fig. 3.7. To ensure compatibility with the algorithms and enhance computational efficiency, the data underwent a normalization process during preprocessing, resulting in prediction values ranging from -1 to 1. The analysis of Fig. 3.7 reveals that all three algorithms reliably predict the swelling index, as evidenced by their R^2 values consistently exceeding 0.8. Notably, the ELM algorithm demonstrates outstanding prediction performance, exhibiting the highest R^2 value of 0.97 for the training dataset and 0.95 for the testing dataset. The R^2 values indicate that 97% and 95% of the predicted values can be linearly explained by the measured values, respectively. In addition to R^2 values, other performance indicators are incorporated and presented in Table 3.5 for a comprehensive assessment of each model. Based on this evaluation, ELM emerges as the most suitable algorithm for predicting the swelling index due to its highest R^2 value, VAF value, and lowest RMSE value among the three algorithms considered. To facilitate the practical application of the models, Table 3.6 provides the selection of relevant parameters for each model.

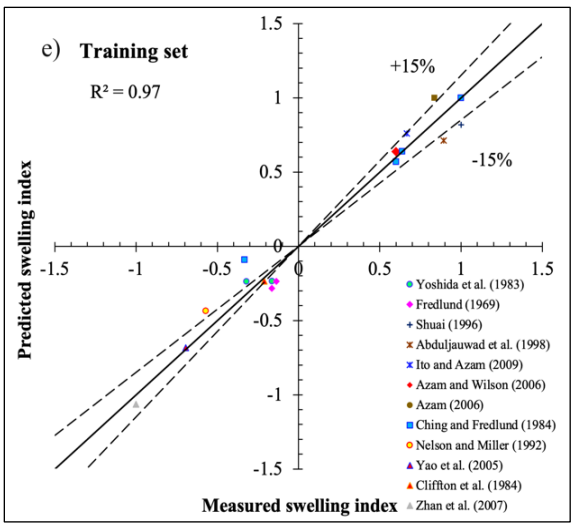
Moreover, an equation incorporating MLP algorithm and normalization method is proposed in Eq. 3.15 as a simple and rational approach for predicting the swelling index using the plasticity index, aiming to further facilitate the implementation of research findings in engineering practice applications.


a) Training set
R² = 0.86
+15%
-15%
Predicted swelling index
Measured swelling index
Yoshida et al. (1983)
Fredlund (1969)
Shuai (1996)
Abduljauwad et al. (1998)
Ito and Azam (2009)
Azam and Wilson (2006)
Azam (2006)
Ching and Fredlund (1984)
Nelson and Miller (1992)
Yao et al. (2005)
Cliffton et al. (1984)
Zhan et al. (2007)


b) Testing set
R² = 0.85
+15%
-15%
Predicted swelling index
Measured swelling index
Yoshida et al. (1983)
Fredlund (1969)
Shuai (1996)
Abduljauwad et al. (1998)
Ito and Azam (2009)
Azam and Wilson (2006)
Azam (2006)
Ching and Fredlund (1984)
Nelson and Miller (1992)
Yao et al. (2005)
Cliffton et al. (1984)
Zhan et al. (2007)


c) Training set
R² = 0.80
+15%
-15%
Predicted swelling index
Measured swelling index
Yoshida et al. (1983)
Fredlund (1969)
Shuai (1996)
Abduljauwad et al. (1998)
Ito and Azam (2009)
Azam and Wilson (2006)
Azam (2006)
Ching and Fredlund (1984)
Nelson and Miller (1992)
Yao et al. (2005)
Cliffton et al. (1984)
Zhan et al. (2007)


d) Testing set
R² = 0.90
+15%
-15%
Predicted swelling index
Measured swelling index
Yoshida et al. (1983)
Fredlund (1969)
Shuai (1996)
Abduljauwad et al. (1998)
Ito and Azam (2009)
Azam and Wilson (2006)
Azam (2006)
Ching and Fredlund (1984)
Nelson and Miller (1992)
Yao et al. (2005)
Cliffton et al. (1984)
Zhan et al. (2007)


e) Training set
R² = 0.97
+15%
-15%
Predicted swelling index
Measured swelling index
Yoshida et al. (1983)
Fredlund (1969)
Shuai (1996)
Abduljauwad et al. (1998)
Ito and Azam (2009)
Azam and Wilson (2006)
Azam (2006)
Ching and Fredlund (1984)
Nelson and Miller (1992)
Yao et al. (2005)
Cliffton et al. (1984)
Zhan et al. (2007)

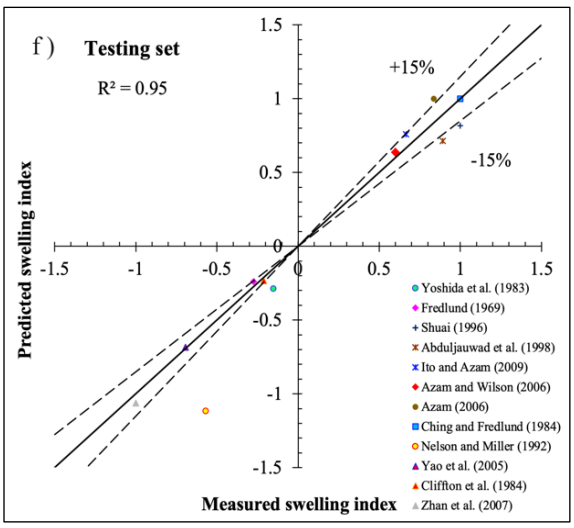

f) Testing set
R² = 0.95
+15%
-15%
Predicted swelling index
Measured swelling index
Yoshida et al. (1983)
Fredlund (1969)
Shuai (1996)
Abduljauwad et al. (1998)
Ito and Azam (2009)
Azam and Wilson (2006)
Azam (2006)
Ching and Fredlund (1984)
Nelson and Miller (1992)
Yao et al. (2005)
Cliffton et al. (1984)
Zhan et al. (2007)

Fig. 3.7 Swelling index prediction results of MLP (a) training and (b) testing sets; SVM (c) training and (d) testing sets; ELM (e) training and (f) testing sets.

Table 3.5 Statistical analysis for the established swelling index prediction models

Model	Soil type	Dataset Size	Set	R	R^2	VAF	RMSE
ELM	Diverse clays	29	Train	0.988	0.976	97.57	0.098
			Test	0.985	0.970	96.76	0.120
MLP			Train	0.927	0.858	85.61	0.243
			Test	0.920	0.846	83.97	0.258
SVM			Train	0.893	0.798	78.79	0.291
			Test	0.949	0.902	87.55	0.248

Table 3.6 Parameters of MLP, SVM and ELM swelling index prediction models.

	C	ε	Kernel function	Kernel option	Λ
SVM	1.05	0.1	Gaussian	3	0.01

	Hidden neurons	Activation function
ELM	9	Sigmoid

	Training function	Activation function	Iterations	Hidden layers
MLP	Trainlm	Tansigmoid	5000	1

ω_{ij}^{IP}	ω_{j}^{OP}	b_{j}^{IP}	b^{OP}
-1.35	-1	-0.78	-0.14

Note: C is the coefficient of penalty, ε is the maximum tolerable deviation, λ is the regularization parameter.

$$C_s = 0.195 - \frac{0.21}{e^{0.097 * I_p - 4.575} + 1} \tag{3.15}$$

$$C_s = 26658.252 \frac{1}{1 + e^{-(0.594 I_P + 0.162)}} + 10376.544 \frac{1}{1 + e^{-(-0.722 I_p + 0.892)}} - 12145.607 \frac{1}{1 + e^{-(-0.417 I_p + 0.006)}} - 24548.611 \frac{1}{1 + e^{-(0.644 I_p + 0.569)}} \tag{3.16}$$

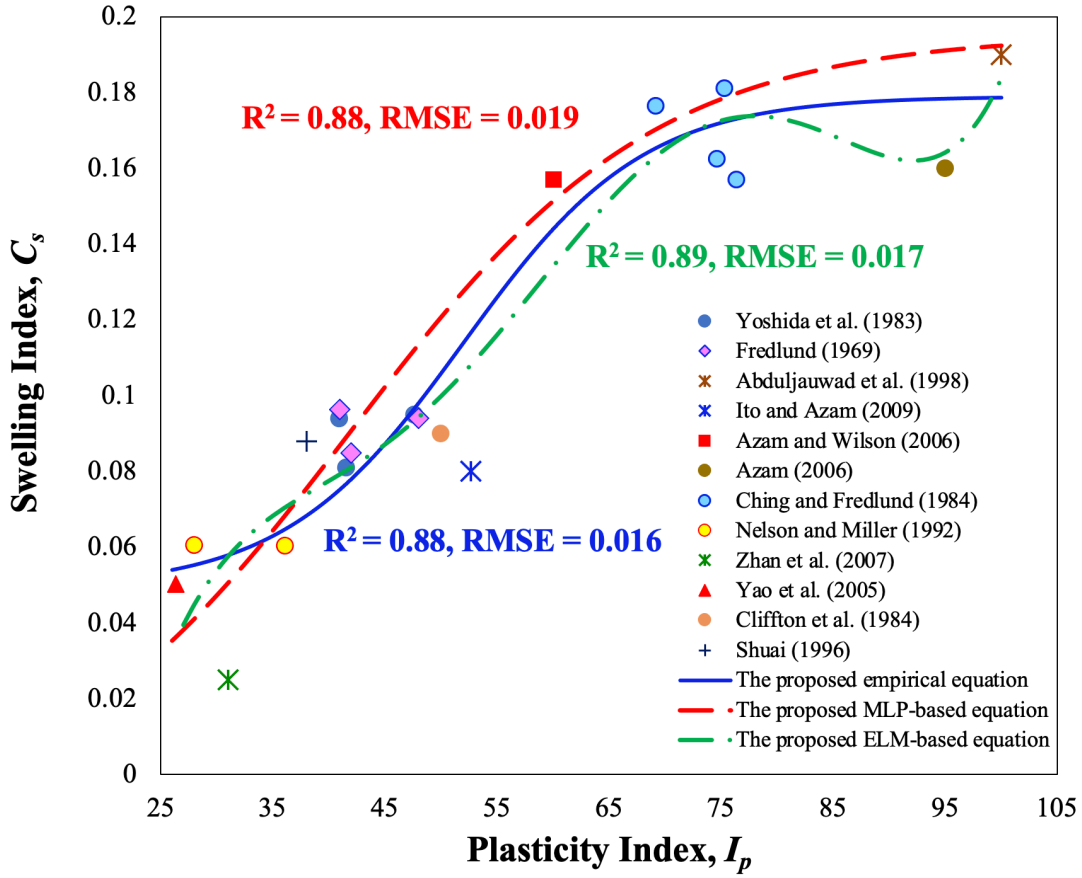


Fig. 3.8 Comparison of the two proposed equations for predicting swelling index.

Fig. 3.8 presents a comparison of three equations proposed in this study for predicting the swelling index: Eq. (3.4), derived from empirical regression analysis; Eq. (3.15), developed using the MLP model; and Eq. (3.16), obtained from the ELM model. The distribution of the measured data points illustrates a clear trend: the swelling index exhibits a significant nonlinear increase as the plasticity index (I_p) rises, indicating a strong positive correlation between them. Despite this general relationship, the data points display noticeable scatter, particularly in the low plasticity range, which may be attributed to variations in experimental methods, equipment, soil mineralogy, and human operation.

The three fitted curves effectively capture the nonlinear behavior of the data across a wide range of plasticity index values. Their predictive accuracy was validated through statistical analysis, with all models achieving a high coefficient of determination (R^2) of 0.88. The regression-based equation (Eq. 3.4) yields a root mean square error (RMSE) of 0.019, while the MLP-based equation (Eq. 3.15) further improves the prediction accuracy with an RMSE of 0.016. The ELM-based equation (Eq. 3.16), represented by the green dotted curve in Fig. 3.8, provides an RMSE of 0.017.

Notably, the MLP-based equation demonstrates superior generalization capabilities across the entire range of plasticity index values. It maintains a balance between accurately predicting the overall trend and minimizing local fluctuations, particularly within both the low ($I_p < 35$) and high ($I_p > 75$) plasticity zones. In contrast, although the ELM-based equation delivers competitive accuracy, it exhibits a tendency to closely fit individual data points. This characteristic, while improving localized precision, may reduce its ability to represent the broader trend consistently, suggesting a potential for slight overfitting.

Overall, the results indicate that the MLP-based model offers the most reliable and balanced predictive performance among the three approaches, combining high accuracy with strong generalization. This makes it a particularly effective tool for practical engineering applications where robust and consistent predictions are essential.

3.4.2 Prediction of swelling pressure

The hidden layer plays a critical role in the MLP algorithm, directly influencing both the prediction accuracy and convergence rate of the model. Theoretically, increasing the number of hidden layers can lead to improved prediction results, as more hidden layers allow for better updating and optimization of the weights and biases from the input layer. Accurate weights and biases are key to computationally interpreting the complex relationship between basic soil properties and swelling pressure. However, blindly increasing the number of hidden layers may lead to time-consuming computations and overfitting problems (Uzair and Jamil, 2020). Overfitting happens when a model struggles to generalize from measured data to unseen data, resulting in good performance on the training set but poor performance on the testing set. Overfitted models tend to memorize all data, including noise and irrelevant patterns, rather than truly grasping the underlying data patterns (Ying, 2019). From a structural perspective, the number of hidden layers and neurons determines the model's degrees of freedom, which represent the total number of trainable parameters (weights and biases). A higher degree of freedom allows the network to capture complex nonlinear relationships among input variables, but it also increases the risk of fitting noise, especially when the number of input parameters is large or the available dataset is limited. In other words, when the model's degrees of freedom exceed the amount of independent information contained in the data, the network is more likely to overfit. Therefore, it is necessary to determine the optimal number of hidden layers for MLP modeling. To alleviate these limitations, the collected data on swelling pressure in the current study are divided into two groups by test types, namely, the CS and CV test groups. Based on the previously summarized soil properties in Section 3.5 (i.e., γ_d, I_p, w, c, e_0, C_s, Ψ), multiple MLP models are established to determine the optimal hidden layer numbers. The influence of hidden layer numbers was graphically depicted in Fig. 3.9. Initially, the R^2-value of the prediction results is positively correlated with the number of hidden layers. In both the CV and CS test groups, it can be initially observed that as hidden layer increases, the R^2-value experiences a rapid growth, indicating the prediction accuracy of both models is highly contingent on the quantity of hidden layers in the early stage. Nevertheless, once the number of hidden layers exceeds three, the prediction accuracy of models does not

show substantial improvement; instead, it fluctuates within a narrow range. Additionally, the time taken for the model to run significantly increases at this stage, disproportionate to the marginal improvement in accuracy. Such trends indicate that the models may have reached the limit of their prediction accuracy. Accordingly, the optimal number of hidden layers for the CS test group and CV test group is determined to be 3, and their corresponding R^2 values are 0.986 and 0.976, respectively.

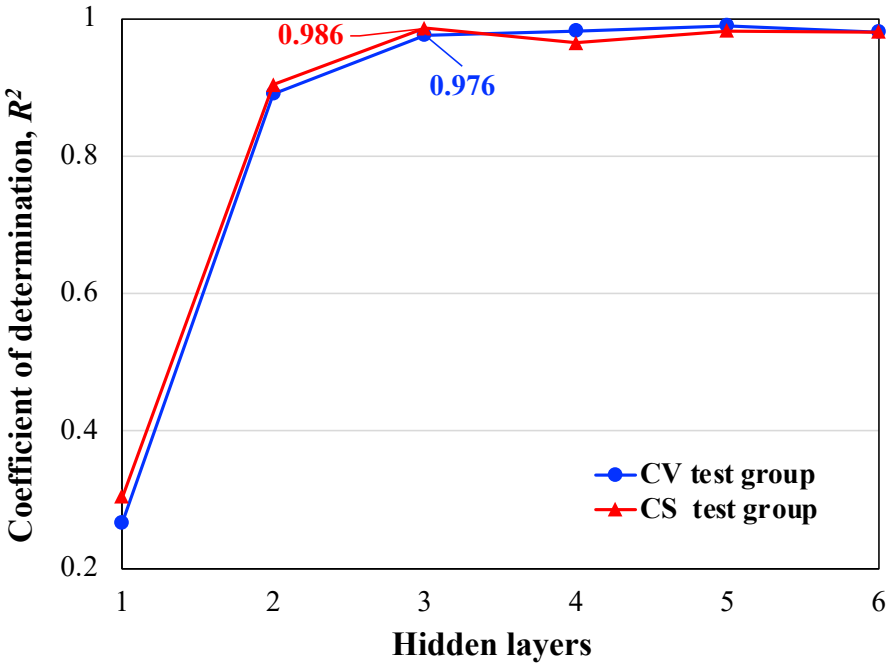


Fig. 3.9 Influence of hidden layer numbers on the prediction accuracy.

In addition to hidden layers, selecting the optimal input parameters is another indispensable part of achieving good prediction results. To further optimize and simplify the model, the single variable method is conducted to remove the less influential input parameters from the models. While performing sensitivity analysis, among seven input parameters, one input variable is removed from the data set at a time to assess its impact on the prediction results. Each newly built model for sensitivity analysis is comprehensively evaluated, and the corresponding results are summarized in Table 3.7. The optimal MLP-based prediction models can be determined through comparative analysis by incorporating the sensitivity analysis results. Compared with the original model with seven input parameters, the

prediction accuracy drops considerably when these parameters are removed, which means water content, clay content, dry unit weight, and initial suction significantly impact P_{scv}. Similarly, plasticity index, water content, dry unit weight, and initial suction are the properties with a notable influence on P_{scs}. Thus, 11 models with different combinations of these most influential input parameters (as shown in Table 3.8) are established to identify the best combination of input parameters for each group. The results clearly demonstrate that Model 1 and Model 5 emerge as the top-performing MLP models for the CV and CS test groups, respectively, boasting the highest level of prediction accuracy. Furthermore, Model 3 and Model 9 serve as alternative MLP models for the CV and CS test groups, respectively. These models have limited input parameters and perform with relatively high prediction accuracy, making them particularly valuable in scenarios with limited known soil properties. The scatter plots of the four models predicting swelling pressure at fully saturated condition are shown in Figs. 3.10 and 3.11.

Table 3.7 Sensitivity analysis of the MLP models

Models	CV test group				CS test group			
	R	**R^2**	**VAF**	**RMSE**	**R**	**R^2**	**VAF**	**RMSE**
Original model	0.99	0.98	97.52	0.042	0.99	0.99	98.59	0.059
	0.97	0.95	94.18	0.080	0.94	0.88	80.79	0.210
Remove γ_d	0.97	0.95	94.80	0.061	0.96	0.93	92.60	0.135
	0.96	0.92	91.72	0.098	0.95	0.91	82.93	0.199
Remove I_p	0.96	0.91	90.98	0.080	0.98	0.95	95.26	0.108
	0.96	0.92	90.66	0.102	0.92	0.85	81.01	0.209
Remove $w\%$	0.97	0.95	94.97	0.060	0.99	0.98	98.02	0.070

	0.98	0.95	95.08	0.075	0.91	0.82	27.94	0.424
Remove *C%*	0.97	0.94	93.74	0.067	0.98	0.95	95.18	0.109
	0.96	0.92	91.28	0.099	0.94	0.89	79.40	0.220
	0.98	0.97	96.77	0.048	0.99	0.98	98.34	0.064
Remove e_0	0.95	0.90	88.96	0.111	0.95	0.90	84.83	0.187
	0.99	0.99	98.56	0.032	0.98	0.95	95.43	0.106
Remove C_s	0.98	0.96	95.72	0.069	0.94	0.89	79.38	0.219
	0.50	0.25	25.29	0.231	0.34	0.12	10.56	0.468
Remove ψ	0.54	0.29	27.76	0.284	0.46	0.21	20.95	0.439

Note: γ_d is dry unit weight, I_p is plasticity index, *w%* is water content, *C %* is clay fraction, e_0 is initial void ratio, C_s is swelling index, ψ is initial suction

Table 3.8 Inputs combinations of the MLP models

Model groups	Models	Input combinations	Set	R	R^2	VAF	RMSE
CV test group	1	$\gamma_d, I_p, w\%, C\%, e_0, C_s, \psi$	Train	0.99	0.98	97.52	0.042
			Test	0.97	0.95	94.18	0.080
	2	$I_p, w\%, C\%, \psi$	Train	0.98	0.96	96.26	0.052
			Test	0.97	0.94	94.32	0.079
	3	$I_p, w\%, \psi$	Train	0.98	0.95	95.20	0.059
			Test	0.97	0.93	93.38	0.088

	4	I_p, ψ	Train	0.79	0.63	62.63	0.164
			Test	0.76	0.58	58.49	0.214
CS test group	5	γ_d, I_p, $w\%$, $C\%$, e_0, C_s, ψ	Train	0.99	0.99	98.59	0.059
			Test	0.94	0.88	80.79	0.210
	6	γ_d, I_p, $w\%$, ψ	Train	0.97	0.94	93.92	0.123
			Test	0.95	0.90	78.09	0.229
	7	γ_d, I_p, ψ	Train	0.96	0.92	92.12	0.139
			Test	0.90	0.80	74.70	0.241
	8	I_p, $w\%$, ψ	Train	0.95	0.91	90.47	0.153
			Test	0.90	0.81	80.86	0.219
	9	I_p, $C\%$, ψ	Train	0.98	0.96	96.41	0.094
			Test	0.93	0.86	79.07	0.220
	10	I_p, ψ	Train	0.94	0.89	89.17	0.163
			Test	0.92	0.84	80.51	0.212
	11	$C\%$, ψ	Train	0.92	0.85	84.78	0.193
			Test	0.88	0.77	73.03	0.249

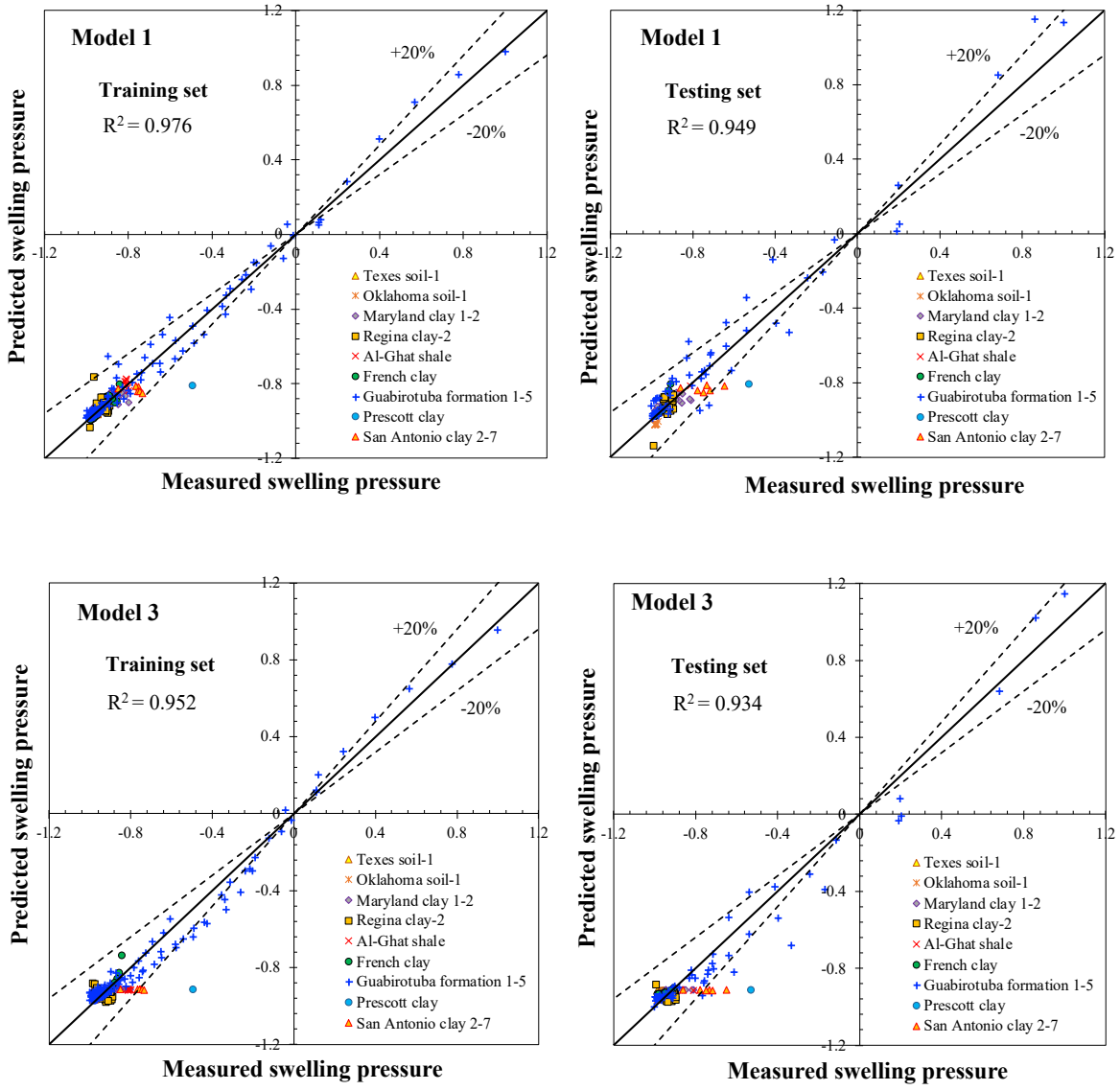


Fig. 3.10 Maximum constant volume swelling pressure (P_{scv}) predicted by Model 1 and Model 3 using MLP algorithm.

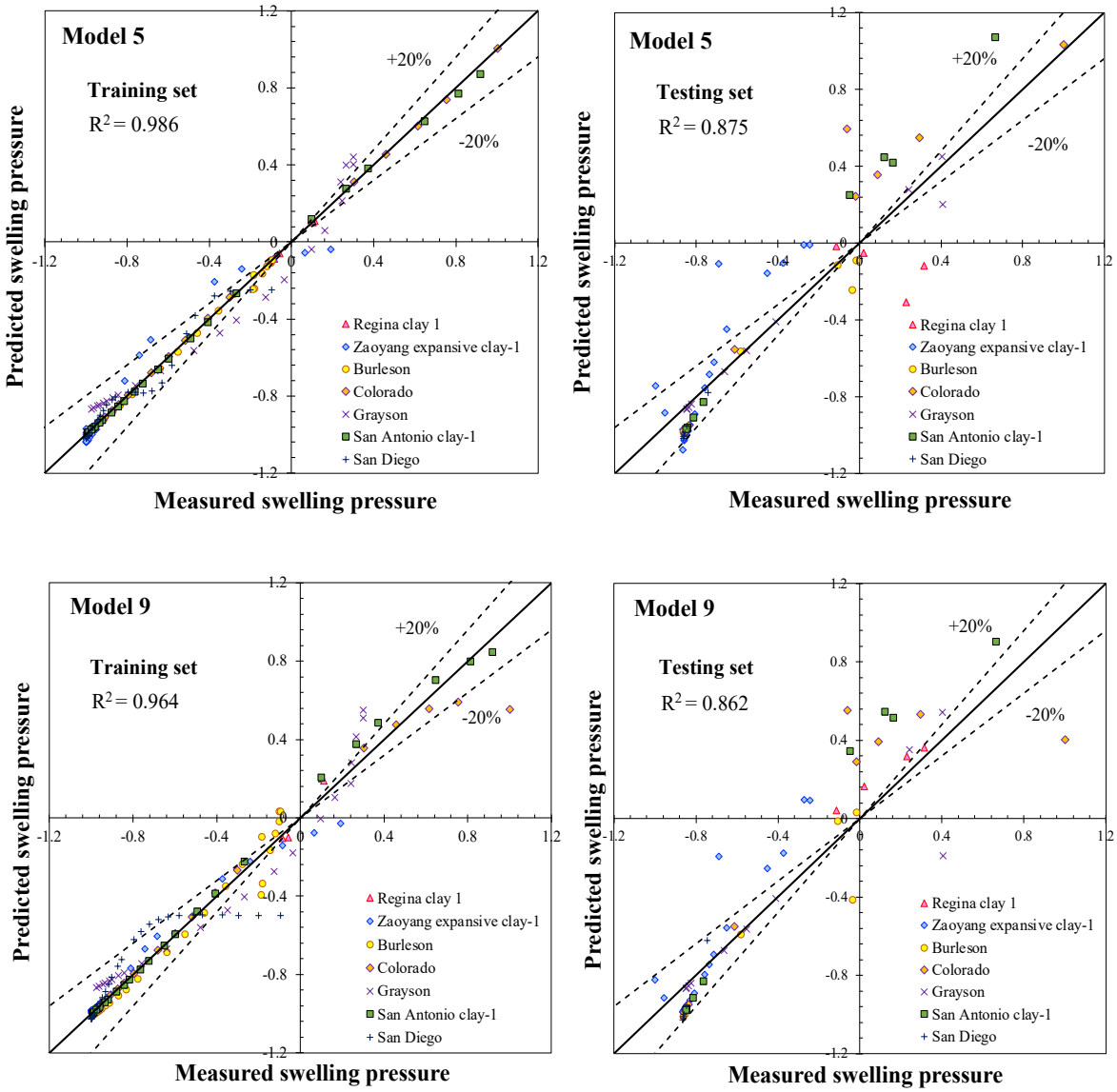


Fig. 3.11 Maximum consolidation-swell swelling pressure (P_{scs}) predicted by Model 5 and Model 9 using MLP algorithm.

In addition to the MLP algorithm, SVM and ELM, as comparative algorithms, are also used to predict swelling pressure. The input of the SVM and ELM models are consistent with the two essential MLP models (Model 3 and Model 9). The prediction results of the models based on the three algorithms are summarized in Table 3.9, and the model parameters are summarized in Table 3.10.

Table 3.9 Statistical analysis for the established swelling pressure prediction models

Model groups	Algorithms	Soil type	Inputs	Dataset Size	Set	R	R^2	VAF	RMSE
CV test group	MLP	Diverse clays	I_p, w%, ψ	471	Train	0.98	0.95	95.20	0.059
					Test	0.97	0.93	93.38	0.088
	SVM				Train	0.97	0.95	94.80	0.061
					Test	0.94	0.88	87.18	0.119
	ELM				Train	0.99	0.99	98.60	0.032
					Test	0.98	0.95	95.36	0.072
CS test group	MLP	Diverse clays	I_p, c%, ψ	245	Train	0.98	0.96	98.37	0.063
					Test	0.93	0.86	90.61	0.148
	SVM				Train	0.92	0.84	83.83	0.199
					Test	0.80	0.64	44.59	0.357
	ELM				Train	0.91	0.83	82.48	0.207
					Test	0.90	0.80	35.18	0.400

From the indicator analysis in Table 3.9, for CV test group, all the selected algorithms have high R^2 and low RMSE values. The results suggest that predicted values by the algorithms are close to the measured values. Therefore, all three algorithms can reasonably predict P_{scv}. Amongst them, the ELM model has the highest prediction accuracy, followed by the MLP and SVM models. For predicting P_{scs}, each evaluation index of the MLP model shows that it has apparent advantages over the other two algorithm models, with the highest prediction accuracy. The training set result of the SVM model is good, but the accuracy of

the test set is greatly reduced. It means that the model may have limited generalization capacity or overfitting problems, and there is room for further optimization and improvement of this model with future studies. This overfitting tendency may be related to the relatively high model flexibility and sensitivity of SVM to kernel parameters, which effectively increase its degrees of freedom and reduce generalization when the input dimensionality is high. Meanwhile, the similar performance between the ELM and MLP models can be attributed to their comparable neural network structures, which enable both to capture complex nonlinear relationships between soil properties and swelling pressure.

The observed prediction errors for certain soil samples can be attributed to two primary factors. First, some soil types are represented by only a limited number of samples, which restricts the model's ability to generalize and accurately capture their unique characteristics. Increasing the dataset size for these specific soils in future studies could enhance predictive accuracy. Second, while input parameters such as clay fraction may appear similar for certain soils, they may contain significant differences in montmorillonite content. This suggests the potential value of incorporating montmorillonite content as an additional input parameter in future research.

Table 3.10 Parameters of MLP, SVM and ELM swelling pressure prediction models

		C	***E***	**Kernel function**	**Kernel option**	***λ***
SVM	CV group	50	0.01	Polynomial	3	0.001
	CS group	500	0.01	Gaussian	1	0.001
		Hidden neurons			**Activation function**	
ELM	CV group	25			Sigmoid	
	CS group	18			Sigmoid	

		Training function	Activation function	Iterations	Hidden layers
MLP	CV group	Trainlm	Tansig	5000	3
	CS group	Trainlm	Tansig	5000	3

Table 3.11 shows the weights and biases of the model 1, 3, 5 and 9 based on the MLP algorithm. According to these weights and biases, four equations for predicting P_{scv} and P_{scs} are proposed, as shown in Eqs. 3.16 and 3.17 (P_{scv}) and Eqs. 3.18 and 3.19 (P_{scs}).

$$P_s = \frac{1643.44}{e^{\left(-0.60*I_p-0.89*w-0.00012*\psi+76.29\right)}+1} - \frac{4208.82}{e^{\left(-0.19*I_p+0.4*w+0.000019*\psi-8.14\right)}+1} + \frac{5050.58}{e^{\left(0.16*I_p-0.33*w+0.000013*\psi+7.05\right)}+1} + 4353.40 \tag{3.16}$$

$$P_s = \frac{9876.70}{e^{\left(0.025*\gamma_d-0.028*I_p+0.069*w+0.012*c+1.05*e_0-13.52*C_s-0.000037*\psi-5.48\right)}+1} + \frac{1843.86}{e^{\left(-1.15*\gamma_d+0.095*I_p-0.63*w+0.34*c+14.81*e_0-366.27*C_s+0.0001*\psi+9.40\right)}+1} + \frac{3731.82}{e^{\left(0.62*\gamma_d-0.064*I_p+0.71*w+0.043*c-0.92*e_0-109.31*C_s+0.000055*\psi-24.62\right)}+1} - 7579.61 \tag{3.17}$$

$$P_s = \frac{12104.57}{e^{\left(-0.29*I_p-0.085*c+0.00023*\psi+19.31\right)}+1} - \frac{14412.46}{e^{\left(0.09*I_p+0.0022*c-0.0026*\psi-7.60\right)}+1} + \frac{4243.54}{e^{\left(0.52*I_p+0.16*c-0.00034*\psi-32.34\right)}+1} - 18515.89 \tag{3.18}$$

$$P_s = \frac{11358.06}{e^{\left(-0.44*\gamma_d - 0.034*I_p + 0.11*w + 0.0032*c - 3.12*e_0 + 32.91*C_s - 0.005*\psi + 2.50\right)} + 1} + \frac{5422.18}{e^{\left(-8.12*\gamma_d + 0.46*I_p - 0.71*w - 0.34*c + 2.91*e_0 - 159.27*C_s + 0.0016*\psi + 149.88\right)} + 1} + \frac{5463.13}{e^{\left(-5.68*\gamma_d + 0.027*I_p - 0.19*w - 0.22*c - 5.85*e_0 - 22.75*C_s + 0.0016*\psi + 109.10\right)} + 1} - 11174.98 \quad (3.19)$$

where γ_d is dry unit weight, I_p is plasticity index, w is water content (%), C is clay fraction (%), e_0 is initial void ratio, C_s is swelling index, ψ is initial suction.

Table 3.11 Weights and biases of the MLP swelling pressure prediction models

Models	Inputs	Hidden layers	ω_{ij}^{IP}							ω_j^{OP}	b_j^{IP}	b^{OP}
1	γ_d, I_p, w%, c%, e_0, C_s, ψ	1	1.00	-0.61	0.96	0.19	1.01	-0.16	-0.68	-3.59	-1.2	
		2	-0.69	1.20	-0.56	-0.86	-1.76	0.31	-0.88	-5.53	-0.46	-3.81
		3	-0.69	-0.56	-0.36	1.02	1.59	-0.73	0.94	-4.98	-0.56	
3	I_p, w%, ψ	1	7.75			9.05		3.79		0.41	-10.82	
		2	2.51			-4.05		-0.57		-1.05	-0.17	-0.72
		3	-2.01			3.31		-0.40		-1.26	-0.88	
5	γ_d, I_p, w%, c%, e_0, C_s, ψ	1	6.39	-0.14	0.88	3.99	1.11	0.38	-2.73	16.14	1.79	
		2	9.14	-2.43	3.39	6.33	-0.55	2.63	-2.74	-16.02	5.52	-33.69
		3	0.50	0.18	-0.52	-0.06	0.59	-0.54	8.79	33.56	10.40	
9	I_p, c%, ψ	1	1.50			1.57		-0.58		35.77	-2.19	-19.86

2	-2.71	-2.92	0.85	12.54	2.35
3	-0.04	-0.04	6.38	42.59	8.39

3.5 Summary

In this chapter, three algorithms, MLP, SVM and ELM, are employed to establish multiple AI models to predict the swelling index and swelling pressure of expansive soils. Two equations were proposed in this study to predict the swelling index using only one easily accessible soil property, plasticity index, as input through regression analysis and AI modelling. In addition, multiple MLP models and equations for predicting swelling pressure are developed by comparing the results of evaluation index analysis and sensitivity analysis. The following conclusions are obtained:

(i) The empirical equation, AI models, and an MLP-based equation presented in this paper are all simple and reliable for estimating the swelling index of expansive soils with plasticity index values ranging from 25 to 100.

(ii) According to sensitivity analysis, swelling pressure is strongly influenced by initial suction, plasticity index, clay fraction and water content. Among them, initial suction is the key factor affecting the prediction of swelling pressure.

(iii) Among the three algorithms, MLP demonstrates the highest prediction accuracy, while ELM stands out for its efficiency, and SVM yields satisfactory results that can meet the requirements of engineering practice.

(iv) Four simplified empirical equations (Eqs. 3.16–3.19) based on the MLP model were developed to reliably predict swelling pressure using basic soil properties. These equations do not require the use of any AI software and be easily implemented with the aid of simple spreadsheets or hand calculator, making them practical tools that balance simplicity and accuracy.

(v) The AI models and empirical equations introduced in this study provide user-friendly tools for predicting both the swelling index and swelling pressure of expansive soils. These methods rely on conventional soil properties that can be easily determined in standard laboratories. By offering accessible and practical solutions, this study bridges the gap between AI prediction models and real-world applications in geotechnical engineering.

References

Abbas, M. F., Shaker, A. A., and Al-Shamrani, M. A., 2023. Hydraulic and volume change behaviors of compacted highly expansive soil under cyclic wetting and drying. Journal of Rock Mechanics and Geotechnical Engineering, 15(2), 486-499.

Abduljauwad, S., Al-Sulaimani, G., Basunbul, I., and Al-Buraim, I., 1998. Laboratory and field studies of response of structures to heave of expansive clay. Géotechnique, 48(1), 103-121.

Abdulkareem, A.H., and Aziz, D.O., 2020. Multiple regression and ANN (MLP) model for predicting swelling index of Ramadi cohesive soil. IOP Conference Series: Materials Science and Engineering, 737(1): 012034.

Abiodun, O. I., Jantan, A., Omolara, A. E., Dada, K. V., Umar, A. M., Linus, O. U., Arshad, H., Kazaure, A. A., Gana, U., and Kiru, M. U., 2019. Comprehensive review of artificial neural network applications to pattern recognition. IEEE Access, 7, 158820-158846.

Adem, H. H., and Vanapalli, S. K., 2016. Heave prediction in a natural unsaturated expansive soil deposit under a lightly loaded structure. Geotechnical and Geological Engineering, 34(4), 1181-1192.

Adoko, A. C., and Yagiz, S., 2019. Fuzzy inference system-based for TBM field penetration index estimation in rock mass. Geotechnical and Geological Engineering, 37(3), 1533-1553.

Al-Shamrani, M. A., and Dhowian, A. W., 2003. Experimental study of lateral restraint effects on the potential heave of expansive soils. Engineering Geology, 69(1-2), 63-81.

Alptekin, A., and Taga, H., 2019. Prediction of compression and swelling index parameters of quaternary sediments from index tests at Mersin District. Open Geosciences, 11(1), 482-491.

Amin Benbouras, M., and Petrisor, A.-I., 2021. Prediction of swelling index using advanced machine learning techniques for cohesive soils. Applied Sciences, 11(2), 536.

Azam, S., 2006. Study on the swelling behaviour of blended clay–sand soils. Geotechnical and Geological Engineering, 25(3), 369-381.

Azam, S., Shah, I., Raghunandan, M. E., and Ito, M., 2013. Study on swelling properties of an expansive soil deposit in Saskatchewan, Canada. Bulletin of Engineering

Geology and the Environment, 72(1), 25-35.

Azam, S., and Wilson, G.W., 2006. Volume change behavior of a fissured expansive clay containing anhydrous calcium sulfate. In Unsaturated Soils 2006, pp. 906-915.

Azmi, M., Ramli, M.H., Hezmi, M.A., Yusoff, S.M., and Alel, M.A. 2019. Estimation of Soil Water Characteristic Curves (SWCC) of mining sand using soil suction modelling. IOP Conference Series: Materials Science and Engineering, 527(1): 012016.

Bandara, T., Yapa, R., and Kodituwakku, S., 2011. Simulation of regression analysis by an automated system utilizing artificial neural networks. International Journal of Latest Trends in Computing, 2(3): 378.

Chen, F. H., 2012. Foundations on expansive soils (Vol. 12). Elsevier.

Chen, Y., Xu, Y., Jamhiri, B., Wang, L., and Li, T., 2022. Predicting uniaxial tensile strength of expansive soil with ensemble learning methods. Computers and Geotechnics, 150: 104904.

Ching, R.K.H., and Fredlund, D.G., 1984. A small Saskatchewan town copes with swelling clay problems. In Proceedings of the 5th International Conference on Expansive Soils, pp. 306-310.

Cho, S.E., 2009. Probabilistic stability analyses of slopes using the ANN-based response surface. Computers and Geotechnics, 36(5): 787-797.

Clifton, A.W., Yoshida, R.T., Fredlund, D.G., and Chursinoff, R.W., 1984. Performance of Dark Hall, Regina, Canada, constructed on a highly swelling clay. In Proceedings of the 5th International Conference on Expansive Soils, pp. 197-201.

Das, S.K., Samui, P., Sabat, A.K., and Sitharam, T., 2010. Prediction of swelling pressure of soil using artificial intelligence techniques. Environmental Earth Sciences, 61: 393-403.

Dave, V.S., and Dutta, K., 2014. Neural network based models for software effort estimation: a review. Artificial Intelligence Review, 42(2): 295-307.

Djellali, A., Houam, A., and Saghafi, B., 2017. Indirect estimation of swelling pressure of clayey subgrade under pavement structures. Arabian Journal for Science and Engineering, 42(9): 3991-3999.

Du, J., Zhou, A., Lin, X., Bu, Y., and Kodikara, J., 2021. Prediction of swelling pressure of expansive soil using an improved molecular dynamics approach combining diffuse double layer theory. Applied Clay Science, 203: 105998.

Elisha, A.T., 2012. Prediction of swell pressure of Black Cotton Soil of North-eastern Nigeria. Electronic Journal of Geotechnical Engineering, 17: 1731-1739.

Ermias, B., and Vishal, V., 2020. Application of artificial intelligence for prediction of swelling potential of clay-rich soils. Geotechnical and Geological Engineering, 38(6): 6189-6205.

Erzin, Y., and Güneş, N., 2011. The prediction of swell percent and swell pressure by using neural networks. Mathematical and Computational Applications, 16(2): 425-436.

Fityus, S., Smith, D., and Allman, M., 2004. Expansive soil test site near Newcastle. Journal of Geotechnical and Geoenvironmental Engineering, 130(7): 686-695.

Folorunso, T.A., Aibinu, A.M., Kolo, J.G., Sadiku, S.O., and Orire, A.M., 2018. Effects of data normalization on water quality model in a recirculatory aquaculture system using artificial neural network.

Fondjo, A.A., Theron, E., and Ray, R.P., 2021. Semi-empirical model for predicting the swelling stress of compacted, unsaturated expansive soils. Civil Engineering and Architecture, 9(1): 225-239.

Fredlund, D.G., 1969. Consolidometer test procedural factors affecting swell properties. In Proceedings of the Second International Conference on Expansive Clay Soils, Texas A & M Press, College Station, TX, pp. 435-456.

Fredlund, D.G., 1983. Prediction of ground movements in swelling clays. In 31st Annual Soil Mechanics and Foundation Engineering Conference.

Fredlund, D.G., and Rahardjo, H., 1993. Soil mechanics for unsaturated soils. John Wiley & Sons.

Gratchev, I., and Saeidi, S., 2020. Free swell of compacted plastic soils. International Journal of Geotechnical Engineering, 14(8): 956-961.

Han, Z., Zhang, P., Zou, W., Fan, K., Vanapalli, S.K., and Wan, L., 2024. At-rest lateral earth pressure of compacted expansive soils: Experimental investigations and prediction approach. Journal of Rock Mechanics and Geotechnical Engineering, 16(4): 1425-1435.

Hossain, I., Rasel, H., Imteaz, M.A., and Mekanik, F., 2020. Long-term seasonal rainfall forecasting using linear and non-linear modelling approaches: a case study for Western Australia. Meteorology and Atmospheric Physics, 132(1): 131-141.

Huang, G.-B., Zhu, Q.-Y., and Siew, C.-K., 2006. Extreme learning machine: theory and applications. Neurocomputing, 70(1-3): 489-501.

Ikechukwu, A.F., and Mostafa, M.M., 2022. Swelling pressure prediction of compacted unsaturated expansive soils. International Journal of Engineering Research in Africa, 59: 119-134.

Indiramma, P., Sudharani, C., and Needhidasan, S., 2020. Utilization of fly ash and lime to stabilize expansive soil and to sustain pollution-free environment – an experimental study. Materials Today: Proceedings, 22: 694-700.

Israr, J., Farooq, K., and Mujtaba, H., 2014. Modelling of swelling parameters and associated characteristics based on index properties of expansive soils. Pakistan Journal of Engineering and Applied Sciences.

ISRM. 1989. Suggested Methods for Laboratory Testing of Argillaceous Swelling Rocks. Int. J. Rock Mech., Mining Sciences and Geomechanics Abstracts, vol. 26 (5), pp. 415- 426.

Ito, M., and Azam, S., 2009. Engineering characteristics of a glacio-lacustrine clay deposit in a semi-arid climate. Bulletin of Engineering Geology and the Environment, 68(4): 551-557.

Jalal, F.E., Xu, Y., Iqbal, M., Javed, M.F., and Jamhiri, B., 2021. Predictive modeling of swell-strength of expansive soils using artificial intelligence approaches: ANN, ANFIS and GEP. Journal of Environmental Management, 289: 112420.

Jones Jr, D.E., and Holtz, W.G., 1973. Expansive soils—the hidden disaster. Civil Engineering, 43(8).

Jones, L. D., Jefferson, I., 2012. Expansive soils.

Khattab, S.A.A., Al-Mukhtar, M., and Fleureau, J.M., 2002. Effect of initial suction on the swelling pressure and porosity of lime stabilized clays. In Proceedings of the 3rd International Conference on Unsaturated Soils, UNSAT 2002, pp. 10-13.

Li, C., Wang, L., Li, J., and Chen, Y., 2024. Application of multi-algorithm ensemble methods in high-dimensional and small-sample data of geotechnical engineering: A case study of swelling pressure of expansive soils. Journal of Rock Mechanics and Geotechnical Engineering, 16(5): 1896-1917.

Li, T., Kong, L., and Guo, A., 2021. The deformation and microstructure characteristics of expansive soil under freeze–thaw cycles with loads. Cold Regions Science and Technology, 192: 103393.

Liang, X., Jiang, A., Li, T., Xue, Y., and Wang, G., 2020. LR-SMOTE—An improved unbalanced data set oversampling based on K-means and SVM. Knowledge-Based Systems, 196: 105845.

Lin, Z., Qian, J., and Shi, Z., 2022. Estimation of the unsaturated shear strength of expansive soils in relation to capillary water-retention curve. Computers and Geotechnics, 146: 104735.

Liu, Y., Mu, Y., Chen, K., Li, Y., and Guo, J., 2020. Daily activity feature selection in smart homes based on Pearson correlation coefficient. Neural Processing Letters, 51(2): 1771-1787.

Liu, Y., and Vanapalli, S.K., 2017. Influence of lateral swelling pressure on the geotechnical infrastructure in expansive soils. Journal of Geotechnical and Geoenvironmental Engineering, 143(6): 04017006.

Lyu, Y., Li, H., Sayagh, M., Jiang, Z.M., and Hassan, A.E., 2021. An empirical study of the impact of data splitting decisions on the performance of AIOps solutions. ACM Transactions on Software Engineering and Methodology (TOSEM), 30(4): 1-38.

Ma, G., Zhang, H., Ji, Z., and Tan, Y., 2021. Comparison of the swelling pressure of bentonite pellet-contained materials and powder. Construction and Building Materials, 281: 122531.

Ma, Y., Wu, L., Guan, Y., and Peng, Z., 2020. The capacity estimation and cycle life prediction of lithium-ion batteries using a new broad extreme learning machine approach. Journal of Power Sources, 476: 228581.

Mawlood, Y.I., and Hummadi, R.A., 2020. Large-scale model swelling potential of expansive soils in comparison with oedometer swelling methods. Iranian Journal of Science and Technology, Transactions of Civil Engineering, 44(4): 1283-1293.

Mir, B., 2015. Some studies on the effect of fly ash and lime on physical and mechanical properties of expansive clay. International Journal of Civil Engineering, 13(3): 203-212.

Mohamed, O.Z., Taha, Y.K., and El-Aziz, E.-S.M.A., 2014. Field study of the distribution of lateral swelling pressure of expansive soil on retaining structure. JES. Journal of Engineering Sciences, 42(2): 289-302.

Mokhtari, M., and Dehghani, M., 2012. Swell-shrink behavior of expansive soils, damage and control. Electronic Journal of Geotechnical Engineering, 17: 2673-2682.

Moreira, L.L., de Brito, M.M., and Kobiyama, M., 2021. Effects of different normalization, aggregation, and classification methods on the construction of flood vulnerability indexes. Water, 13(1): 98.

Nelson, J., and Miller, D.J., 1997. Expansive soils: problems and practice in foundation and pavement engineering. John Wiley & Sons.

Nelson, J.D., Chao, K.C., Overton, D.D., and Nelson, E.J., 2015. Foundation engineering for expansive soils. John Wiley & Sons.

Ng, C.W.W., Zhan, L.T., Bao, C.G., Fredlund, D.G., and Gong, B.W., 2003. Performance of an unsaturated expansive soil slope subjected to artificial rainfall infiltration. Géotechnique, 53(2): 143-157.

Pedarla, A., Puppala, A.J., Hoyos, L.R., Vanapalli, S.K., and Zapata, C., 2012. SWRC modelling framework for evaluating volume change behavior of expansive soils. In Unsaturated Soils: Research and Applications: Volume 1, Springer Berlin Heidelberg, pp. 221-228.

Phanikumar, B., Dembla, S., and Yatindra, A., 2021. Swelling behaviour of an expansive clay blended with fine sand and fly ash. Geotechnical and Geological Engineering, 39(1): 583-591.

Piepho, H.P., 2019. A coefficient of determination (R^2) for generalized linear mixed models. Biometrical Journal, 61(4): 860-872.

Puppala, A.J., and Cerato, A., 2009. Heave distress problems in chemically-treated sulfate-laden materials. Geo-Strata—Geo Institute of ASCE, 10(2): 28.

Roshan Joseph, V., 2022. Optimal ratio for data splitting. Statistical Analysis and Data Mining, 15(4): 531-538.

Sabat, A.K., 2015. Prediction of California bearing ratio of a stabilized expansive soil using artificial neural network and support vector machine. Electronic Journal of Geotechnical Engineering, 20(3): 981-991.

Shuai, F., 1998. Simulation of swelling pressure measurements on expansive soils. Ph.D thesis. University of Saskatchewan.

Singhal, S., 2010. Expansive soil behavior: property measurement techniques and heave prediction methods. Ph.D thesis. Arizona State University.

Soltani, A., Deng, A., Taheri, A., and Sridharan, A., 2019. Swell-shrink-consolidation behavior of rubber-reinforced expansive soils. Geotechnical Testing Journal, 42(3): 761-788.

Sun, Y., Zhu, J., Yu, X., Ye, C., and Fan, G., 2020. Research on early warning of power grid construction safety based on PSO-SVM model. Journal of Physics: Conference Series, IOP Publishing, 1449(1): 012037.

Taherdangkoo, R., Tyurin, V., Shehab, M., Ardejani, F.D., Tang, A.M., Narmandakh, D., and Butscher, C., 2023. An efficient neural network model to determine maximum swelling pressure of clayey soils. Computers and Geotechnics, 162: 105693.

Tao, P., Sun, Z., and Sun, Z., 2018. An improved intrusion detection algorithm based on GA and SVM. IEEE Access, 6: 13624-13631.

Tiwari, B., and Ajmera, B., 2011. Consolidation and swelling behavior of major clay minerals and their mixtures. Applied Clay Science, 54(3-4): 264-273.

Tiwari, N., and Satyam, N., 2021. Coupling effect of pond ash and polypropylene fiber on strength and durability of expansive soil subgrades: An integrated experimental and machine learning approach. Journal of Rock Mechanics and Geotechnical Engineering, 13(5): 1101-1112.

Tu, H., and Vanapalli, S.K., 2016. Prediction of the variation of swelling pressure and one-dimensional heave of expansive soils with respect to suction using the soil-water retention curve as a tool. Canadian Geotechnical Journal, 53(8): 1213-1234.

Uzair, M., and Jamil, N., 2020. Effects of hidden layers on the efficiency of neural networks. In 2020 IEEE 23rd International Multitopic Conference (INMIC), pp. 1-6. IEEE.

Vanapalli, S., and Lu, L., 2012. A state-of-the-art review of 1-D heave prediction methods for expansive soils. International Journal of Geotechnical Engineering, 6(1): 15-41.

Venkatesan, S., Droniou, J., Roy, I., Robert, D., and Zhou, A., 2021. Application of diffusion-advection equations to in-field monitoring of soil suction profiles. Computers and Geotechnics, 139: 104329.

Vrigazova, B., 2021. The proportion for splitting data into training and test set for the bootstrap in classification problems. Business Systems Research: International Journal of the Society for Advancing Innovation and Research in Economy, 12(1): 228-242.

Vu, H.Q., and Fredlund, D.G., 2004. The prediction of one-, two-, and three-dimensional heave in expansive soils. Canadian Geotechnical Journal, 41(4): 713-737.

Wang, G., Zhao, B., Wu, B., Zhang, C., and Liu, W. 2023. Intelligent prediction of slope stability based on visual exploratory data analysis of 77 in situ cases. Int. J. Min. Sci. Technol., 33(1): 47-59.

Wang, H., Zentar, R., and Wang, D. 2023. Predicting the compaction parameters of solidified dredged fine sediments with statistical approach. Mar. Georesour. Geotech., 41(2): 195-210.

Wang, J., and Vanapalli, S. 2024. A framework for estimating the matric suction in unsaturated soils using multiple artificial intelligence techniques. Int. J. Numer. Anal. Methods Geomech., 1–26.

Wang, Z., and Qu, Z., 2017. Research on Web text classification algorithm based on

improved CNN and SVM. In 2017 IEEE 17th International Conference on Communication Technology (ICCT).

Watanabe, Y., and Tanaka, Y., 2021. Swelling pressure of compacted bentonite acting on constraining material with deformability. Géotechnique, 1-10.

Wen, L., Li, Y., Zhao, W., Cao, W., and Zhang, H., 2023. Predicting the deformation behaviour of concrete face rockfill dams by combining support vector machine and AdaBoost ensemble algorithm. Computers and Geotechnics, 161: 105611.

Xu, Y., and Goodacre, R., 2018. On splitting training and validation set: a comparative study of cross-validation, bootstrap, and systematic sampling for estimating the generalization performance of supervised learning. Journal of Analytical Testing, 2(3): 249-262.

Yang, J., Cai, Y., Pan, C., and Mi, C., 2019. A novel resistor-inductor network-based equivalent circuit model of lithium-ion batteries under constant-voltage charging condition. Applied Energy, 254: 113726.

Yao, H.L., Cheng, P., and Wu, W.P., 2005. Prediction of ground heaves in expansive soils based on consolidation tests. Chinese Journal of Rock Mechanics and Engineering, 24(21): 3911-3915.

Ying, X., 2019. An overview of overfitting and its solutions. Journal of Physics: Conference Series, IOP Publishing, 1168: 022022.

Yoshida, R., Fredlund, D.G., and Hamilton, J., 1983. The prediction of total heave of a slab-on-grade floor on Regina clay. Canadian Geotechnical Journal, 20(1): 69-81.

Zareef, M., Chen, Q., Hassan, M.M., Arslan, M., Hashim, M.M., Ahmad, W., Kutsanedzie, F.Y., and Agyekum, A.A., 2020. An overview on the applications of typical non-linear algorithms coupled with NIR spectroscopy in food analysis. Food Engineering Reviews, 12(2): 173-190.

Zhan, L.T., Chen, P., and Ng, C., 2007. Effect of suction change on water content and total volume of an expansive clay. Journal of Zhejiang University-Science A, 8(5): 699-706.

Zhan, T.L., Ng, C.W., and Fredlund, D.G., 2007. Field study of rainfall infiltration into a grassed unsaturated expansive soil slope. Canadian Geotechnical Journal, 44(4): 392-408.

Zhang, F., Cui, Y.-J., Conil, N., and Talandier, J., 2020. Assessment of swelling pressure determination methods with intact Callovo-Oxfordian claystone. Rock Mechanics and Rock Engineering, 53(4): 1879-1888.

Zhang, L., Li, J., and Zhang, B., 2015. Evaluation and prediction of the swelling pressures of GMZ bentonites saturated with saline solution. Applied Clay Science, 105: 207-216.

Zumrawi, M.M., 2013. Pavement design for roads on expansive clay subgrades. University of Khartoum Engineering Journal (UOFKEJ), 3(1): 52-58.

CHAPTER 4

A PRACTICAL MACHINE LEARNING-BASED APPROACH FOR PREDICTING 1-D VERTICAL SWELLING POTENTIAL OF EXPANSIVE SOILS

4.1 Introduction[2]

Expansive soils are widely distributed in over 40 different countries from North America, Central and South America, Africa, Asia, Australia, and some parts of Europe (Fig. 1.1) (Shi et al., 2002; Nelson et al., 2015; Liu et al., 2024). They are highly plastic clays known for their ability to swell or shrink respectively under wetting and drying conditions due to the presence of swelling minerals like montmorillonite and illite (Hou et al., 2013; Jamsawang et al., 2023). Chemical weathering and hydrolysis of feldspar-rich rocks contribute to the formation of highly swelling clay minerals such as the montmorillonite in expansive soils (Wilson, 1999; Chen, 2012).

Expansive soils are highly sensitive to increases in moisture content triggered by factors such as rainfall, snowmelt, flooding, or pipeline leaks (Ene and Okagbue, 2009). The swelling mechanism of expansive soils typically involves two stages: crystalline swelling and osmotic swelling (Zou et al., 2018). Crystalline swelling is primarily driven by the hydration of exchangeable interlayer cations and surface interactions between clay particles and surrounding liquids, such as hydrogen bonding and surface-dipole attraction (Likos, 2004). Osmotic swelling, on the other hand, is caused by the repulsion between electric double layers formed by negatively charged mineral surfaces, which attract cations and polar water molecules. Unlike crystalline swelling, which is limited to short distances (1–

[2] The contents presented in this chapter are published as a journal article: **Zhang, A.**, & Vanapalli, S. K. (2025). A practical machine learning-based approach for predicting 1-D vertical swelling potential of expansive soils. *Transportation Geotechnics*, 101710.

1.5 nm), osmotic swelling can extend up to 40 nm (Taylor and Smith, 1986; Madsen and Müller-Vonmoos, 1989).

The hazardous swelling characteristics of expansive soils pose significant risks to geo-infrastructures (Mokhtari and Dehghani, 2012; Zumrawi, 2013; Mohamed et al., 2014; Djellali et al., 2017; Liu and Vanapalli, 2017; Li et al., 2021; Venkatesan et al., 2021), resulting in billions of dollars in economic losses annually (see Table 4.1) (Johnson, 1973; Charlie et al., 1984; Ruwaih, 1987; Al-Rawas et al., 1998; Osman et al., 2005; Azam et al., 2009; Zhang et al., 2015; Adem and Vanapalli, 2016; Gourley et al., 2020; Abden et al., 2024). Most residential structures, pipelines, pavements and railways, being lightly loaded, are particularly vulnerable to the swelling behavior of these soils. When expansive soils absorb water, they often undergo ground heave, leading to pavement cracking, uneven subgrades, and reduced structural stability (Pandey et al., 2021; Sarker and Wang, 2022). Reliable prediction of swelling potential, also widely referred to as heave (Singhal et al., 2015), is essential for providing rational design of geotechnical and transportation infrastructure.

Table 4.1 Annual cost associated with expansive soils worldwide

Country	Annual costs
France	€ 3.3 billion
Saudi Arabia	$ 300 million
Sudan	$ 6 million
China	$ 15 billion
Australia	$ 150 million
South Africa	$ 4 million
UK	£ 150 million
USA	$ 11 Billion

Conventional methods for measuring the swelling potential of expansive soils are based on oedometer tests (Gaspar et al., 2022), which require trained personnel, extensive equipment

and are time-consuming; they typically require 2 to 3 weeks or more in certain scenarios and cost between $2,500 to $3,000 per test (Alptekin and Taga, 2019; Fondjo et al., 2021; Tavakkoli et al., 2024). In addition, undisturbed samples that are required for testing from site investigations involve additional costs. Fig. 4.1 illustrates a free-swell oedometer test which is a commonly used method for measuring swelling potential. The procedures for conducting this test are described in Method A of ASTM-D4546 (2003) (ASTM, 2003). The method involves saturating the soil specimen allowing access to water such that it swells freely in the vertical direction under a minimal load of at least 1 kPa (Point A to B in Fig. 4.1). Once swelling stops, the swelling potential is measured. A vertical load is then applied in stages until the specimen is recompressed to its initial void ratio (Point B to C). The specimen may be compressed to void ratios lower than the initial value (Point D) in certain scenarios, as the exact vertical load required to achieve the initial void ratio is not precisely known.

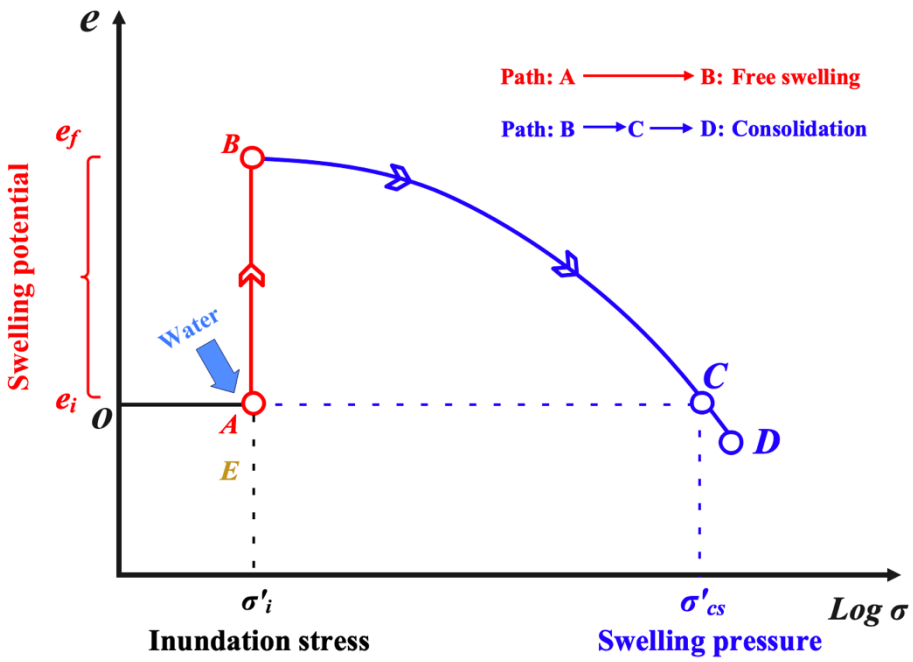


Fig. 4.1. Typical free-swell oedometer test

Numerous empirical relationships based on the information of simple soil properties have been developed over the past seven decades to predict swelling potential. These methods

are typically used in conventional practice to reduce project costs (Seed et al., 1962; Nayak and Christensen, 1971; Dhowian, 1990; Rao et al., 2004; Chen, 2012; Çimen et al., 2012). However, many of these empirical equations are based primarily on locally gathered soil samples, limiting their applicability to other regions or for universal use (Vanapalli and Lu, 2012; Tu and Vanapalli, 2016). Additionally, inherent variability of clay properties within a single site or across different locations further complicates the collection of representative soil samples and the generation of reliable laboratory data (Adem, 2015). This variability, combined with region-specific calibration of empirical models, significantly restricts the universal applicability of these methods, posing considerable challenges in the reliable prediction of the swelling potential of expansive soils.

Recently, several researchers have focused their efforts using machine learning techniques for predicting the swelling potential of expansive soils to enhance efficiency and reduce the dependence on extensive site investigations and laboratory experiments (Najjar et al., 2000; Kayadelen et al., 2009; Erzin and Güneş, 2011; Yilmaz and Kaynar, 2011; Çimen et al., 2012; Onyelowe et al., 2021; Eyo et al., 2022; Nguyen et al., 2022). In the early stages of machine learning model development, Najjar et al. (Najjar et al., 2000) pioneered the use of neural network-based (NNB) models to predict swelling potential, incorporating various combinations of soil parameters as inputs. Building on this approach, Erzin and Güneş (Erzin and Güneş, 2011) employed an artificial neural network (ANN) algorithm along with multiple regression methods to predict the swelling potential of a kaolin-bentonite mixture, employing a variety of soil properties such as clay fraction, cation exchange capacity, plasticity index, dry unit weight, and water content. Their findings demonstrated that the ANN algorithm outperformed traditional regression methods in prediction accuracy. Similarly, Onyelowe et al. applied adaptive neuro-fuzzy inference systems (ANFIS) to predict swelling potential, confirming the reliability of ANFIS as a tool for the design of infrastructures within expansive soils for addressing geo-environmental applications (Onyelowe et al., 2021). More recently, Nguyen et al. developed a suite of machine learning models, including Gaussian Process (GP), Multilayer Perceptron (MLP), and Bagging-MLP neural network models, for predicting soil swelling potential (Nguyen et al., 2022). They concluded that the Bagging-MLP model

exhibited the highest prediction accuracy, further showcasing the evolving capabilities of machine learning for applications in geotechnical engineering practice.

This study uses a comprehensive and diverse dataset of 173 expansive soils gathered from various regions of the world to develop novel machine learning models that are simple and yet reliable in predicting swelling potential, overcoming the limitations of currently available methods for use in practice applications with greater reliability. Three different models are proposed for predicting the swelling potential of expansive soils using two algorithms namely Multivariate Adaptive Regression Splines (MARS) and Multilayer Perceptron (MLP).

One key innovation of the developed models is their ability to predict a wide range of swelling potentials (0.5%–92.8%), achieving R^2 values of 0.887 or higher, which demonstrates their reliability and applicability to diverse expansive soils, enabling more confident decision-making in infrastructure design and maintenance. Additionally, the study enhances model transparency by providing an explicit MLP-based equation, that facilitates straightforward calculations using a simple spreadsheet, making it more practical compared to traditional machine learning models. Furthermore, the proposed equation has been validated for its effectiveness and accuracy on five case studies from different regions of the world, further supporting its practical applicability. The results of this study are encouraging and can be used in proposing rational design methods for lightly loaded transportation and geotechnical infrastructure.

4.2 Methodology

Selecting an appropriate machine learning algorithm prior to model construction is essential, as each algorithm has unique strengths and limitations that make them suitable for specific applications: Region-based Convolutional Neural Network (R-CNN) excels in prediction accuracy (Girshick, 2015). The Two-Stage Unsupervised Multiple Kernel Extreme Learning Machine (TUMK-ELM) prioritizes computational efficiency (Xiang et al., 2018). K-Nearest Neighbors (KNN) is suitable for small datasets (Cheamanunkul and Freund, 2014). Meanwhile, MARS and MLP provide interpretable fitting equations,

enhancing model transparency (De Veaux et al., 1993; Hakkoum et al., 2021; Fu and Peng, 2023). Notably, MLP has demonstrated its effectiveness in predicting the resilient modulus of compacted subgrade soils, showcasing its applicability in transportation engineering (Zou et al., 2021).

Machine learning algorithms that can provide interpretable equations not only enhance model usability but also facilitate their application in engineering practice. Considering these requirements, this study employs MARS and MLP, as they are particularly suited for addressing the challenges posed by expansive soils. More details are discussed in later paragraphs to highlight these details.

MARS is particularly effective in processing nonlinear data, creating adaptive basis functions to capture and model complex relationships across distinct data regions. This capability makes it well-suited for analyzing the intricate interactions between simple soil properties and the swelling potential of expansive soils. Additionally, MARS can automatically identify the most significant input parameters, simplifying the model and minimizing the risk of overfitting. These features are critical for handling the variability and complexity inherent in soil datasets, ensuring reliability of the model in diverse geotechnical applications.

MLP, a feedforward neural network algorithm, predicts target parameters by optimizing weights and biases through multiple hidden layers. Compared to MARS, MLP typically runs faster, completing predictions within one to two minutes, whereas MARS may take five to ten minutes depending on model complexity. Although MLP generally achieves higher prediction accuracy, its probabilistic nature introduces variability in results across different runs, requiring multiple iterations to identify an optimal model. Once established, the weights and biases of an MLP model can be extracted and incorporated into a mathematical equation, further enhancing its applicability in engineering design workflows.

In summary, MARS and MLP each offer distinct advantages and limitations that complement one another. By employing both algorithms independently, this study ensures

high prediction accuracy and practical applicability, providing a comprehensive approach for estimating the swelling potential of expansive soils in transportation geotechnics.

4.2.1. MLP algorithm

The MLP algorithm is a neural network that represents an advanced artificial intelligence model inspired by the biological processes of the human brain (Cho, 2009). It establishes a powerful computational network capable of mimicking information processing and decision-making. Unlike traditional regression and statistical models, ANNs like MLP have a significant advantage in accurately capturing and managing complex non-linear relationships among input variables (Bandara et al., 2011; Dave and Dutta, 2014; Abiodun et al., 2019; Hossain et al., 2020; Zareef et al., 2020). This ability makes MLP particularly well-suited for analyzing the non-linear variation in the swelling potential of expansive soils.

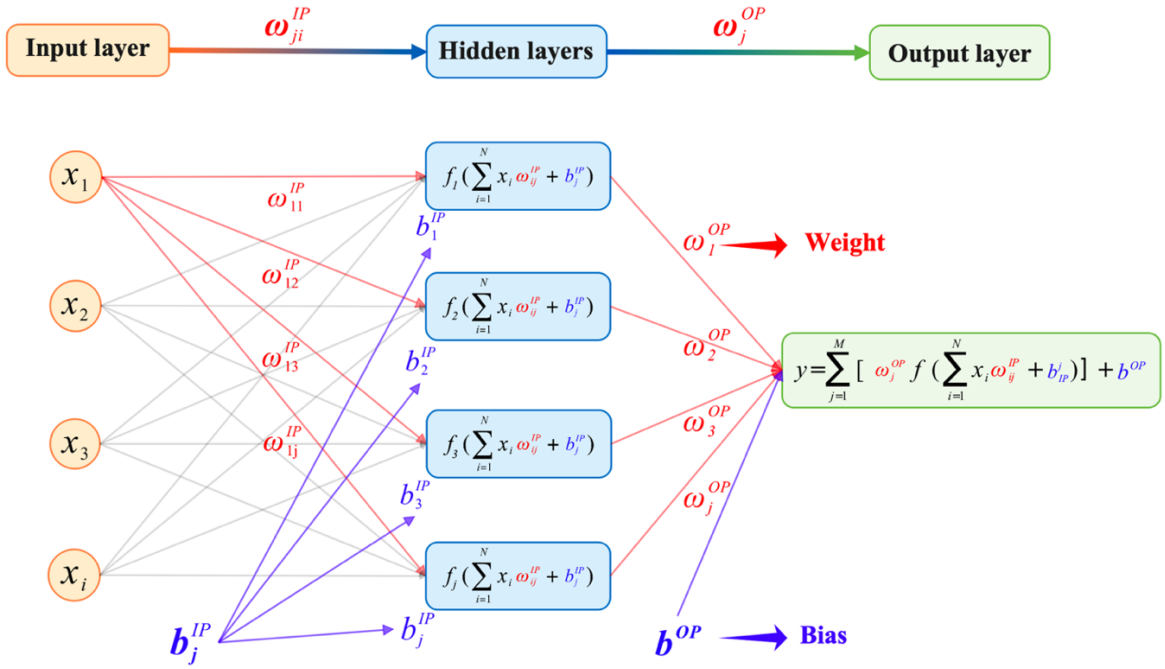


Fig. 4.2 The principle of the MLP algorithm.

Fig. 4.2 illustrates the architecture and functionality of the MLP algorithm, which consists of three main layers: the input layer, hidden layers, and the output layer. In the input layer,

each node represents an individual property of a soil specimen from the dataset, serving as the model's input variables. The hidden layers contain numerous neurons that simulate the functioning of biological neurons in the human brain. When signals are transmitted from the input layer to the hidden layer, weights are assigned to these connections and aggregated within the hidden neurons. Before the signal exits a neuron, it is processed through an activation function. If the weighted sum surpasses the threshold set by the activation function, the output value is transformed into a number typically ranging from 0 to 1. This processed value is then passed on to the next neuron, where further weight adjustments and learning occur. This iterative process continues through the network until the signal finally reaches the output layer, where the model generates its final prediction. The general equation of the MLP algorithm is presented in Eq. 4.1.

$$y = \sum_{j=1}^{M} \left[\omega_j^{OP} f\left(\sum_{i=1}^{N} x_i \, \omega_{ij}^{IP} + b_j^{IP} \right) \right] + b^{OP} \tag{4.1}$$

where, $\mathbf{x_i}$ is the $\boldsymbol{i}^{th}$ input parameter, $\boldsymbol{y}$ is the target parameter,$\boldsymbol{\omega}_{ij}^{IP}$ are the weights assigned to input parameters, $\boldsymbol{\omega}_j^{OP}$ are the weights assigned for the output layer, $\boldsymbol{b}_j^{IP}$ is the bias for the $\boldsymbol{j}^{th}$ hidden layer, $\boldsymbol{b}^{OP}$ is the bias for the output layer, $\boldsymbol{f}$ is the activation functions, $\boldsymbol{N}$ is the number of input parameters, $\boldsymbol{M}$ is the number of hidden layers.

4.2.2 MARS algorithm

The MARS algorithm, originally developed by Friedman (Friedman, 1991), is both a powerful and a flexible regression technique widely used in machine learning, that is particularly effective in modeling complex relationships and non-linearities in data. MARS works by partitioning the input space into smaller regions and fitting simple linear regression models within each region. The algorithm automatically identifies the optimal locations and shapes of these partitions, known as basis functions, while accounting for interactions between input variables. This adaptability enables MARS to handle both linear and non-linear relationships, making it well-suited for datasets with intricate structures. The MARS algorithm operates in two main steps: the forward pass and the backward pass.

During the forward pass, the model incrementally adds basis functions, gradually building a comprehensive model by considering possible interactions and changes in the input space. In the backward pass, the algorithm refines the model by pruning unnecessary or less significant basis functions, reducing model complexity. This iterative approach not only enhances the algorithm's ability to capture complex patterns within the data but also mitigates the risk of overfitting, ensuring a more robust and generalizable model. Fig. 4.3 illustrates the modelling process of the MARS algorithm.

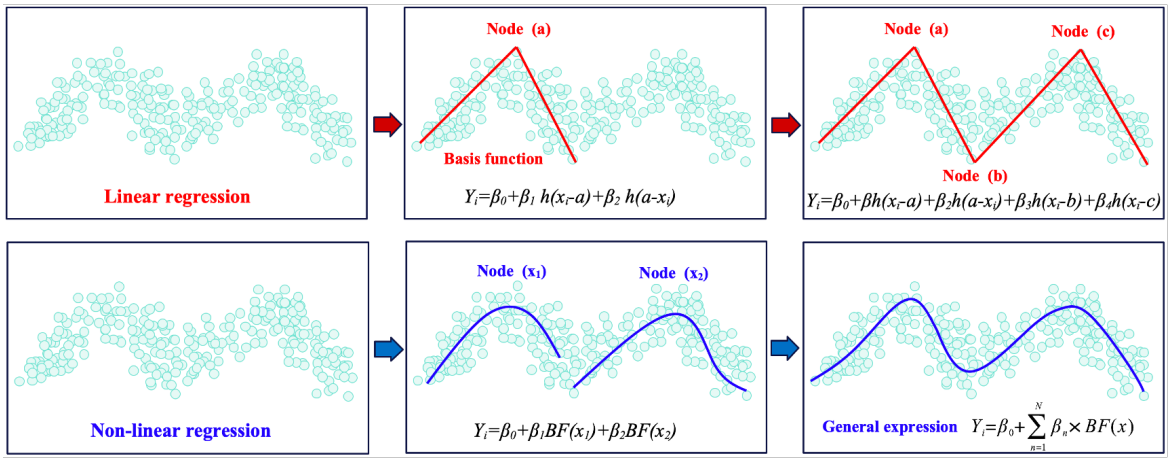


Fig. 4.3 The principle of the MARS algorithm.

Eq. (4.2) shows the general equation of MARS algorithm:

$$Y_i=\beta_0+\sum_{n=1}^{N}\beta_n\times BF(x) \tag{4.2}$$

where, Y is the target parameter, β_0 is the intercept, N is the total number of basis functions, β_n is the coefficient for each basis function, $BF(x)$ is the basis function.

4.2.3 Evaluation indexes

Eqs. (4.3)-(4.6) represent the evaluation metrics used to assess model performance. The Pearson correlation coefficient (r) quantifies the strength of the linear relationship between measured and predicted variables, where $r = 1$ signifies a perfect correlation. A value of $r >$ 0.8 indicates a fairly strong correlation between O_i (observed values) and P_i (predicted

values) (Liu et al., 2020). To assess the proportion of variance in one variable that can be predicted from another, the coefficient of determination (R^2) is employed. For instance, an R^2 of 0.8 implies that 80% of the total variation in the predicted values P_i can be explained by the measured values O_i (Piepho, 2019). Additionally, the Variance Accounted For (VAF) is a widely used statistical metric to verify model accuracy, with values closer to 100% indicating higher model accuracy (Adoko and Yagiz, 2019). The Root Mean Square Error (RMSE), representing the standard deviation of prediction errors, provides insight into how closely the data points cluster around the best-fit line. A lower RMSE value (closer to 0) suggests more accurate prediction results (Yang et al., 2019). In summary, higher values of r, R^2, and VAF, coupled with lower RMSE values, denote superior prediction accuracy.

$$r = \frac{\sum_{i=1}^{N}\left(O_i - \bar{O}_i\right)\cdot\left(P_i - \bar{P}_i\right)}{\sqrt{\sum_{i=1}^{N}\left(O_i - \bar{O}_i\right)^2 \cdot \sum_{i=1}^{N}\left(P_i - \bar{P}_i\right)^2}} \tag{4.3}$$

$$R^2 = \left(\frac{\sum_{i=1}^{N}\left(O_i - \bar{O}_i\right)\cdot\left(P_i - \bar{P}_i\right)}{\sqrt{\sum_{i=1}^{N}\left(O_i - O_i\right)^2 \cdot \sum_{i=1}^{N}\left(P_i - P_i\right)^2}}\right)^2 \tag{4.4}$$

$$VAF = \left(1 - \mathrm{var}\left(O_i - P_i\right)/\mathrm{var}\left(O_i\right)\right)\times 100 \tag{4.5}$$

$$RMSE = \sqrt{\frac{1}{N}\sum_{i=1}^{N}\left(O_i - P_i\right)^2} \tag{4.6}$$

where O_i is the i^{th} measured value and P_i is the i^{th} predicted value; $\overline{O}_i$ and $\overline{P}_i$ are the average values of the measured and predicted values, respectively, and N is the number of parameters.

In this study, the robustness of the prediction models is quantified by the robustness ratio Rr, whose expression is provided in Eq. (7). This metric, originally proposed by Wang and

Yin (2021), serves to further validate the feasibility of the proposed models. The reasonable prediction range is defined based on the measured minimum and maximum values of swelling potential, as shown in Table 4.2.

$$R_r = \frac{\text{Samples in the reasonable range}}{\text{Total testing samples}} \tag{4.7}$$

4.3 Database establishment

4.3.1 Selection of input parameters

The choice of input parameters is of importance in addition to selecting appropriate model algorithms. Reliable and effective input parameter selection is essential for the model to better capture the complex relationships between the input variables and the target parameter. In this study, three sets of parameters were employed as input values for predicting the swelling potential. The first set consists of basic soil properties, including plasticity index, clay content, dry density, and specific gravity. These are measured from relatively simple laboratory tests that strongly reflect the influence of expansive minerals and potential swelling trends (Kariuki and Van Der Meer, 2004). A higher clay fraction in expansive soils suggests a greater presence of swelling-active minerals, while a higher plasticity index reflects the soil's ability to remain plastic over a wider range of moisture contents. Together, these parameters suggest a stronger affinity for water and a higher potential for volume change upon wetting (Wagner, 2013). Although the proportion of expansive clay minerals (e.g., montmorillonite or illite) was not directly included due to data limitations and the high cost of X-ray diffraction (XRD) testing, both clay content and plasticity index were used as proxy indicators to account for the influence of swelling characteristics. In addition, higher dry density indicates denser particle packing, which tends to generate stronger internal swelling pressures upon wetting and results in more pronounced vertical expansion (Villar and Lloret, 2008). Specific gravity varies depending on the type and hydration capacity of the constituent clay minerals. Most natural clays are

mixtures of microscopic minerals such as carbonates, feldspars, micas, and quartz. Among these, feldspar weathering contributes to an easier and well-known pathway for the formation of swelling clay minerals such as montmorillonite. Therefore, variations in specific gravity may indirectly reflect the presence of expansive clay components (Uddin, 2008).

The second set of input parameters represents external factors, such as variation of water content and void ratio, and vertical loading conditions. This set reflects changes in the swelling behavior of expansive soils due to external environmental conditions, such as water infiltration or applied vertical load (e.g., surcharging or overburden pressure). These external factors are known to have a direct influence on the magnitude of soil swelling. An increase in water content typically leads to greater swelling due to the hydration and expansion of clay minerals. The influence of clay mineralogy on swelling is strongly related to the water content. Vertical loading, on the other hand, provides a mechanical constraint that limits the vertical expansion of the soil. The key environmental and mechanical factors that affect swelling behavior in real-world scenarios can be accounted by including these parameters into the model.

The third set comprises swelling characteristics, including the swelling index and swelling pressure. Compared to the other parameters, these directly represent the swelling behavior and potential of expansive soils. To build a strong and reliable prediction model, in this study a comprehensive dataset from literature, encompassing 173 soils is gathered from diverse regions worldwide. The collected dataset is presented in Table 4.2. This extensive dataset not only contributes towards enhancing the model's accuracy but also improves its generality, enabling reliable predictions of swelling potential across a wide range of soil types and environmental conditions.

Table 4.2 Summary of soil properties used for predicting the swelling potential of expansive soils

Soil property	C	I_p	ρ_d	G_s	q	Δw	Δe	C_s	P_s	ε

Max	82	92	1.98	2.84	400	25.5	0.293	0.038	1040	92.8
Min	8	21	1.26	1.97	1	2.7	0.041	0.187	7	0.5
Ave	39	49	1.64	2.67	7	9.6	0.119	0.149	261	11.2
Med	34	52	1.62	2.67	1	8.3	0.121	0.167	190	12.7
Qty	173	173	173	173	173	173	173	173	173	173

Note: C is clay fraction, I_p is plasticity index, ρ_d is dry unit weight, G_s is specific gravity, q is vertical stress, Δw is water content variation, Δe is void ratio variation, C_s is swelling index, P_s is the swelling pressure.

To ensure objective performance evaluation, the dataset was partitioned using simple random sampling into a training set (70%) and a testing set (30%). This 70/30 split is a commonly adopted strategy that provides a well-accepted balance between model training and testing effectiveness (Vrigazova, 2021). The use of simple random sampling is particularly advantageous as it tends to yield low bias in estimating model performance (Lohr, 2021). The training subset was used for model development and parameter optimization, while the testing subset was reserved exclusively for assessing the generalization performance of the final models on unseen data.

4.3.2 Correlation between selected inputs

Performing a correlation analysis between selected input variables prior to modeling offers several benefits and provides valuable insights for the modeling process. One primary advantage is the identification of inputs that exhibit high correlations with each other. Highly correlated input parameters can introduce redundant information into the model, leading to multicollinearity issues. Multicollinearity occurs when one or more independent variables in a multiple regression equation that are highly correlated with others, which can distort the prediction of regression coefficients and impair the model's interpretability (Allen, 1997).

Additionally, correlation analysis helps in mitigating overfitting, a situation where the model performs exceptionally well on training data but fails to generalize to new, unseen data. Overfitted models tend to memorize all the data, including noise and irrelevant patterns, instead of capturing the true underlying patterns in the dataset (Ying, 2019). By addressing multicollinearity, the model can become more robust and adaptable to different datasets, enhancing its prediction accuracy. Properly managing highly correlated variables not only streamlines the modeling process but also contributes to improved performance on test data, ensuring more reliable predictions. Fig. 4.4 illustrates the correlation relationships among the selected input parameters, highlighting key interactions that could impact the model's performance.

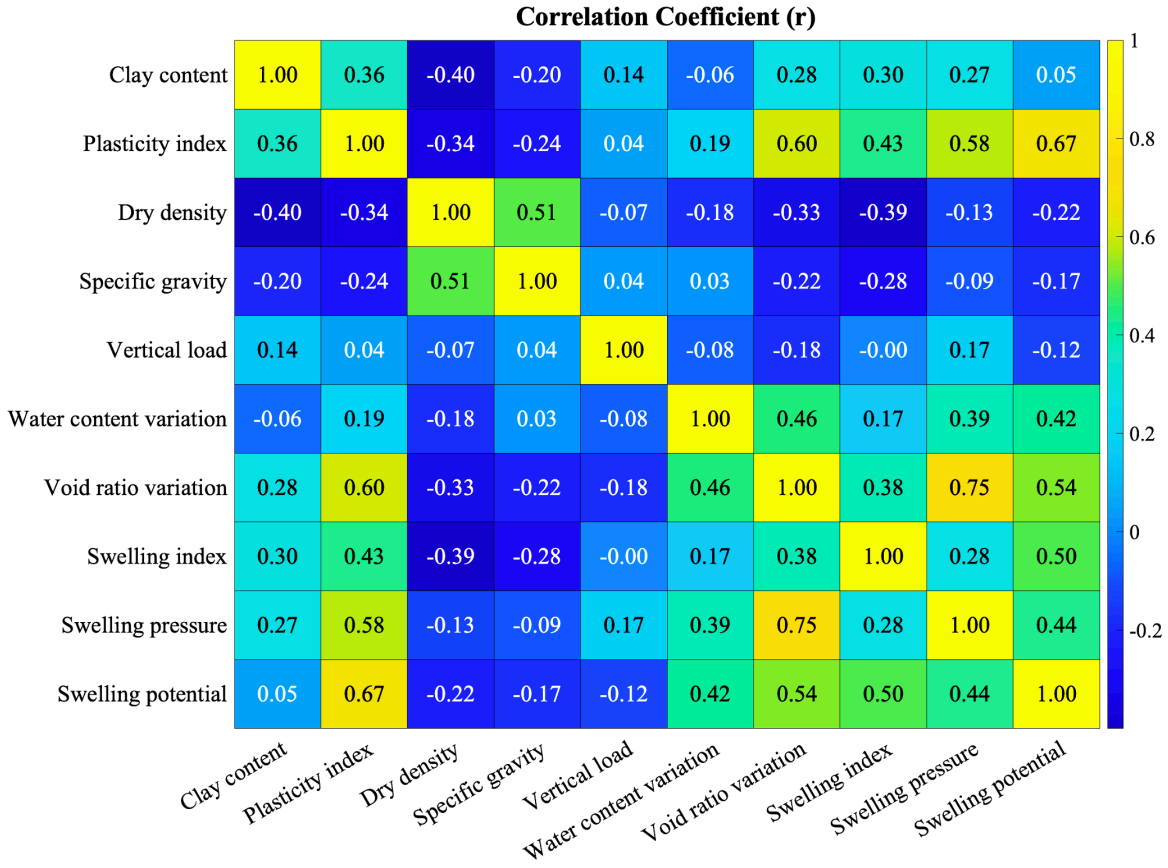


Fig. 4.4 Correlations between the selected inputs

According to the correlation analysis, the maximum correlation coefficient observed between the input parameters is 0.75. This indicates that there is no strong correlation among the input variables, as an r value exceeding 0.8 is typically regarded as indicative

of a strong relationship, where multicollinearity becomes a concern (Senaviratna and Cooray, 2019; Shrestha, 2020). Therefore, the selected input parameters in this study are well-suited for modeling, as they exhibit meaningful correlations with swelling potential without introducing redundancy. The influence of these parameters on swelling potential will be further explored and elaborated in the sensitivity analysis that is discussed later.

4.3.3 Outlier detection

Before establishing the model, it is also necessary to identify and remove outliers from the dataset to enhance the reliability of the analysis. An outlier is a data point that significantly deviates from the remainder of the observations, potentially skewing the results and affecting the model's performance (Singh and Upadhyaya, 2012). Removing outliers typically yields more representative and stable descriptive statistics that better reflect the characteristics of most of the data. In this study, outlier detection for the swelling potential of the 173 collected soil specimens was conducted using the "mean" method. This method involves calculating the mean and standard deviation of the dataset to identify values that deviate significantly from the average. A common threshold for detecting outliers is set at three standard deviations from the mean. Any values falling outside this range are considered outliers and are subsequently excluded from the analysis. Fig. 4.5 presents the results of the outlier detection process, highlighting the data points that were identified as outliers.

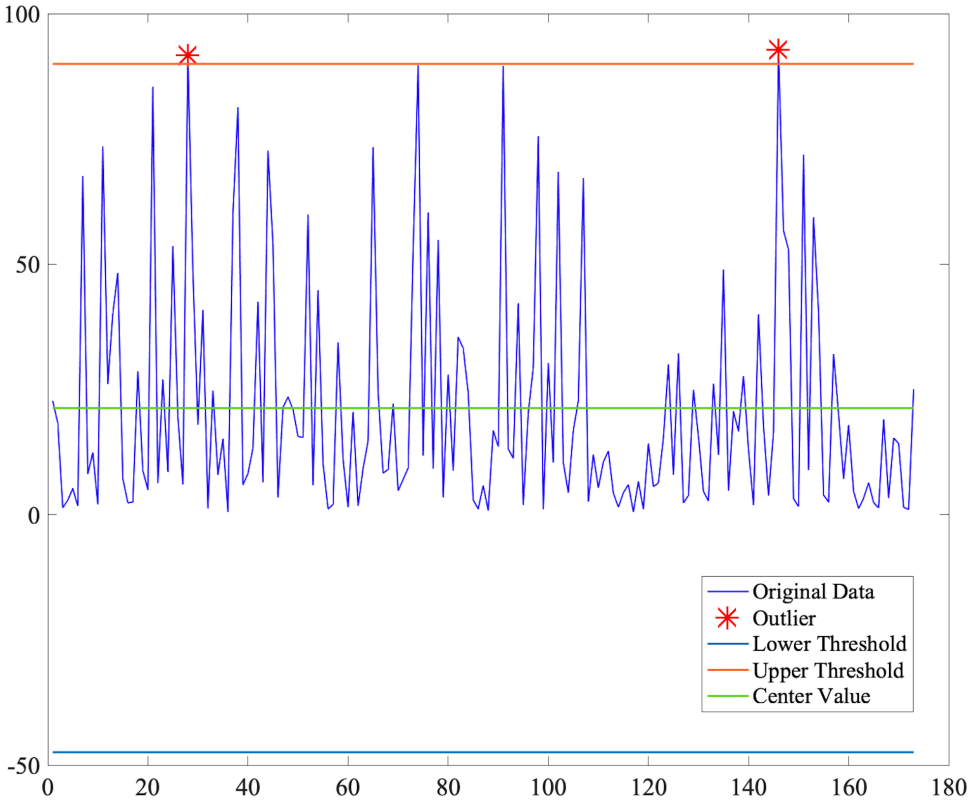


Fig. 4.5. Summary of results related to outlier detection

According to Fig. 4.5, two outliers have been identified in the established database. While the conventional approach for managing outliers involves pruning, it is essential not to remove these values indiscriminately. Instead, understanding the underlying reasons for their occurrence is crucial. Blindly eliminating outliers can inadvertently reduce the size and diversity of the dataset, potentially affecting the model's ability to generalize. In this case, the presence of these outliers may be closely related to the range of the collected data. The measured swelling potential values in this study predominantly lie within the 20% range. However, two specimens (Kaolin-bentonite mixture, both composed primarily of significant montmorillonite as the main mineral) exhibit significantly higher swelling potentials of 91.6% and 92.8%. Since these outliers merely exceed a predefined threshold, the decision has been made to retain them temporarily. They were identified as outliers using the "mean" method due to their position near the upper boundary of the dataset. Their retention is contingent on their impact on the prediction accuracy of model. If subsequent

analysis reveals that these outliers do not significantly compromise the model's performance, they will remain in the dataset. Conversely, if their presence adversely affects prediction accuracy, they will be removed, and efforts will be made to collect data with a more evenly distributed range to optimize the database.

4.4 Modelling results and analysis

4.4.1 Multivariate Adaptive Regression Splines (MARS)

In the MARS algorithm, increasing the number of basis functions can lead to overfitting, particularly when the count becomes excessive. Adding more basis functions increases the model's complexity by introducing additional parameters, enabling the model to closely fit the training data. However, this increased complexity may cause the model to capture variations influenced by noise rather than true underlying trends, leading to overfitting. Therefore, determining the optimal number of basis functions is a key step in fine-tuning the MARS algorithm to ensure robust and generalizable predictions. Fig. 4.6 depicts the relationship between the number of basis functions and the VAF values in both the training and testing sets. This trend analysis helps identify the point where the model achieves an appropriate balance between fitting the training data and maintaining prediction accuracy on the testing data, thereby avoiding overfitting.

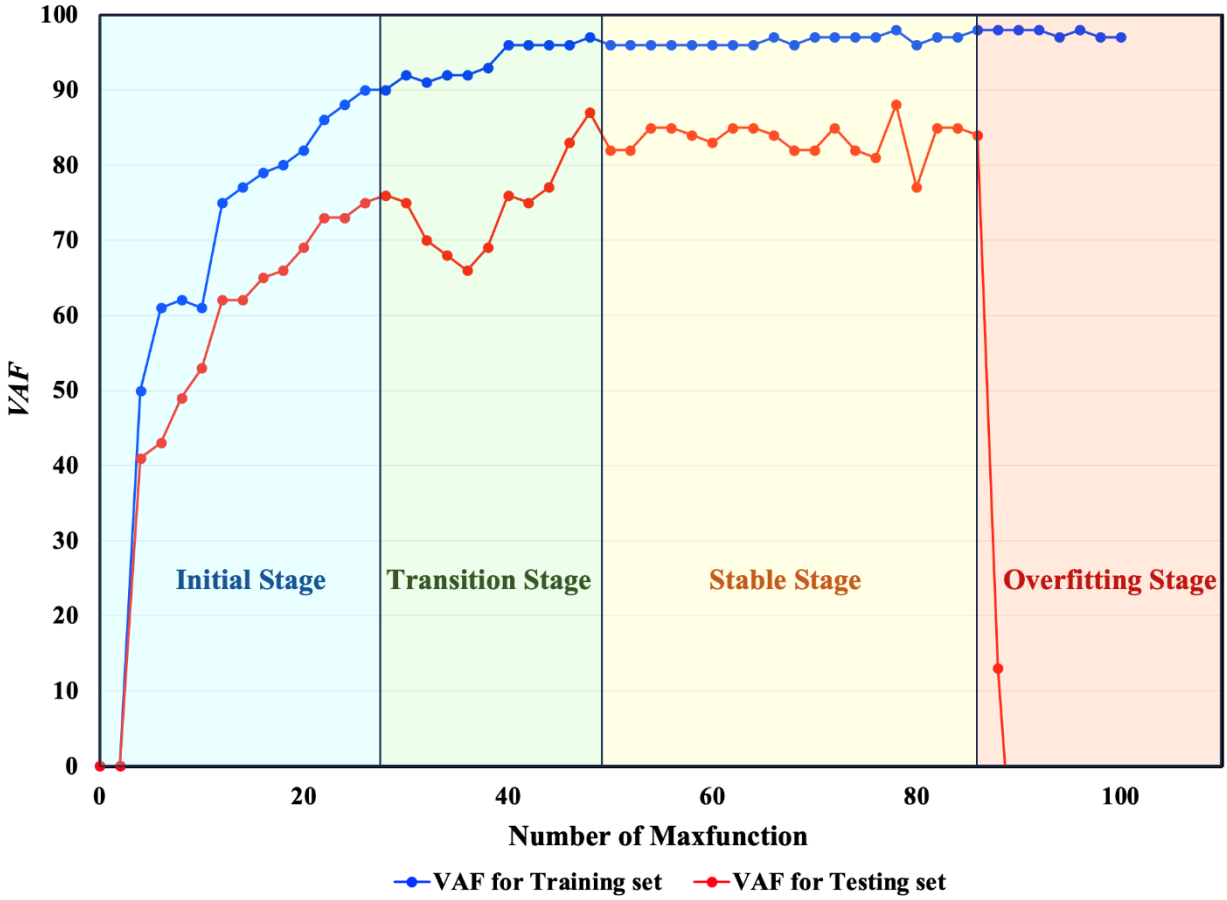


Fig. 4.6 The influence of Maxfunction on the performance of models.

Fig. 4.6 illustrates how the VAF values of the model change with the Maxfunction parameter across four distinct stages: the initial stage, transition stage, stable stage, and overfitting stage.

(i) Initial Stage (Maxfunction: 0 to 28): In this phase, the model's prediction accuracy (VAF) significantly improves as the number of Maxfunctions increases. During this period, numerous basis functions are generated, enabling the model to capture complex nonlinear relationships within the data. The average VAF values for both the training and testing sets can reach up to 80%, indicating that the model can predict a substantial portion of the data points. However, the overall prediction accuracy is not yet sufficiently high.

(ii) Transition Stage (Maxfunction: 28 to 48): During this stage, the training set's prediction accuracy continues to improve, but at a slower pace. In contrast, the prediction accuracy of

the test set exhibits noticeable fluctuations and even a significant drop. This fluctuation may result from the ongoing increase in the number of basis functions, which makes the model more complex but not yet stable. The model may begin to capture random variations and noise in the training data, rather than the true underlying patterns, leading to potential overfitting. Due to this reason, the trained model struggles to generalize the test set effectively.

(iii) Stable Stage (Maxfunction: 48 to 86): In this stage, the model achieves a higher level of sophistication, with slight fluctuations in prediction accuracy. Both the training and testing sets exhibit high prediction accuracy, with an average VAF of approximately 90%. Further increases in the number of basis functions during this phase do not lead to significant improvements in the VAF for the training set, suggesting that the model has reached an optimal balance between complexity and accuracy.

(iv) Overfitting Stage (Maxfunction > 86): Beyond this point, the VAF of the training set stabilizes, but the VAF of the test set experiences a severe decrease, indicating significant overfitting. In this stage, the excessive number of basis functions causes the model to become overly complex, attempting to fit every detail in the training data. As a result, the model becomes highly sensitive to the training set, making it unsuitable for generalization to new data and leading to poor performance on the test set.

To achieve optimal model performance, the number of Maxfunctions should be chosen within the stable stage, where the model demonstrates high prediction accuracy, reduced complexity, and minimal overfitting. Notably, at Maxfunction = 78, the VAF values for the training and test sets are 98.4% and 88.2%, respectively. This level of prediction accuracy surpasses the commonly accepted high-fit threshold of 80%, making it adequate for the prediction requirements in engineering practice applications. Therefore, 78 is selected as the optimal Maxfunction value for this study.

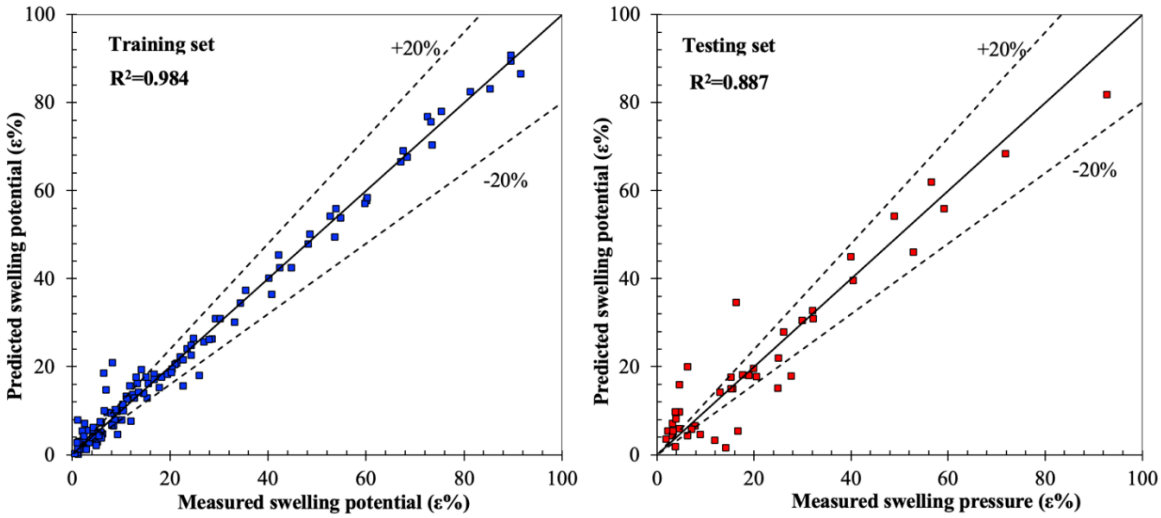


Fig. 4.7. Prediction results of the MARS model with 9 inputs (Model 1)

Fig. 4.7 illustrates relatively strong prediction performance of the MARS model with 9 input parameters, which is referred to as Model 1 in the present study. The model achieved R^2 values of 0.984 for the training set and 0.887 for the testing set, demonstrating performance accuracy across both datasets. These values indicate a strong positive correlation between the measured and predicted data points. Although the difference in R^2 values is approximately 9.7%, such a gap is still within an acceptable range and does not indicate severe overfitting. Prior studies on expansive soils using machine learning techniques have reported training–testing R^2 differences ranging from 6% to over 20%, which are generally considered acceptable in view of the inherent complexity of soil behavior and variability in geotechnical datasets (Chen et al., 2022; Rehman et al., 2022; Jalal et al., 2024). Additionally, the dashed line in the figure represents a 20% error threshold, and most data points fall within this range, clustering closely around the ideal prediction line. This pattern suggests that the model performs well in predicting soil swelling potential. However, in the testing set, a few predicted points deviate notably from the acceptable error range, indicating potential issues of overfitting. Upon closer examination, two possible underlying reasons for these deviations are identified. Firstly, approximately 90% of these outliers can be attributed to the limited database size, as only a few specimens are available for each specific soil. This limitation restricts the model's ability to adequately learn the unique properties of these soils, thereby affecting its

prediction accuracy. Secondly, the remainder 10% of outliers result from the similarity in basic soil properties among these specimens, despite significant differences in their swelling potential. This similarity complicates the model's ability to discern distinct patterns, making it challenging to accurately predict the swelling potential for these cases.

To address these challenges, potential solutions include expanding the sample size to provide a more comprehensive dataset, thereby improving the model's learning capacity. Additionally, incorporating new input parameters as additional features could enhance the model's ability to differentiate between soils with similar properties but varying swelling potentials, ultimately improving prediction accuracy.

4.4.2 Multilayer Perceptron (MLP)

The hidden layer is an important component of the MLP algorithm, as it directly impacts both the prediction accuracy and the convergence rate of the model. In theory, increasing the number of hidden layers can enhance prediction performance, as additional layers provide more opportunities to update and optimize the weights and biases originating from the input layer. These optimized weights and biases are key for interpreting the complex relationships between basic soil properties and the swelling potential. However, excessively increasing the number of hidden layers can lead to issues such as prolonged computational time and overfitting (Uzair and Jamil, 2020).

To prevent overfitting and ensure efficient model performance, it is essential to identify the optimal number of hidden layers for MLP modeling. Fig. 4.8 graphically illustrates the influence of varying the number of hidden layers on the model's performance, highlighting the need to balance model complexity with generalization capability.

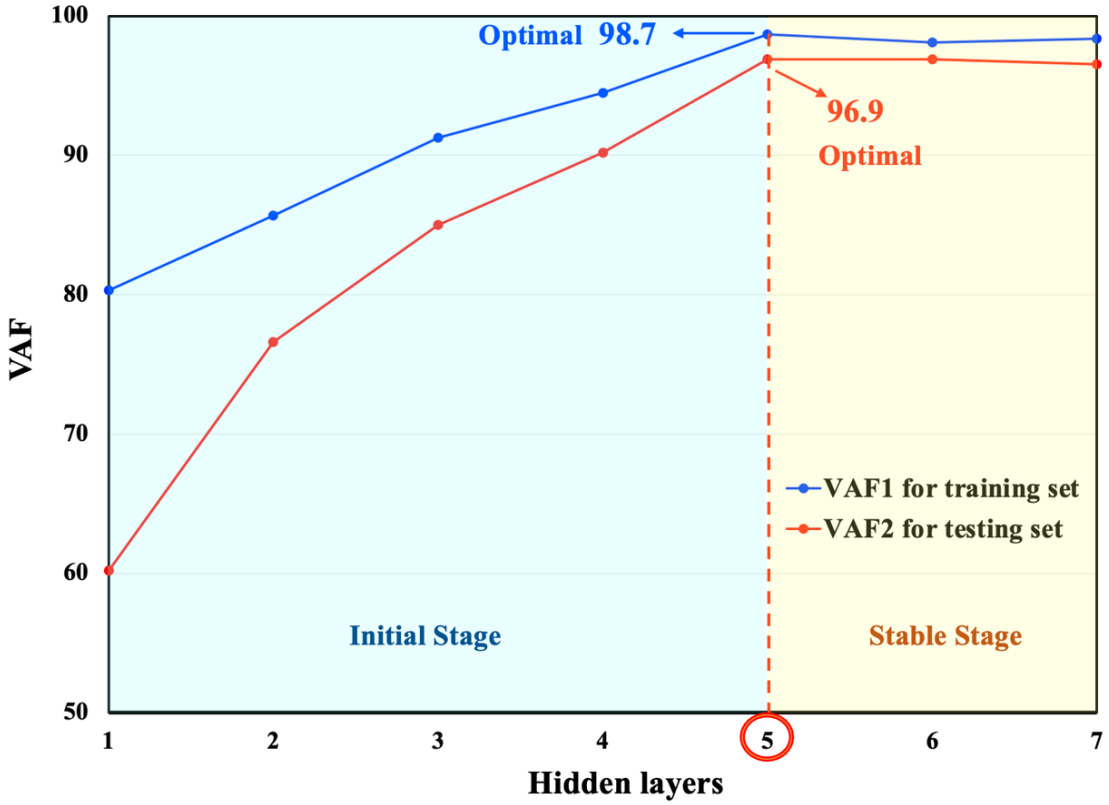


Fig. 4.8 Influence of hidden layer numbers on the prediction accuracy

Initially, the VAF value of the prediction results shows a positive correlation with the number of hidden layers. As the number of hidden layers increases, the VAF value experiences rapid growth, suggesting that the model's prediction accuracy is highly dependent on the quantity of hidden layers during the early stages. However, once the number of hidden layers exceeds 5, the improvement in prediction accuracy becomes negligible, fluctuating within a narrow range. Additionally, the model's runtime increases significantly at this point, disproportionate to the marginal gains in accuracy. This pattern indicates that the model has likely reached the upper limit of its prediction capability. Therefore, the optimal number of hidden layers is determined to be 5, with corresponding VAF values of 98.7 and 96.9 for the training and testing sets, respectively. This approach is consistent with the findings reported by Sheela and Deepa (2013), who noted that the appropriate number of hidden layers in a neural network should generally be identified through trial-and-error during training, as no fixed analytical method exists for determining it in advance.

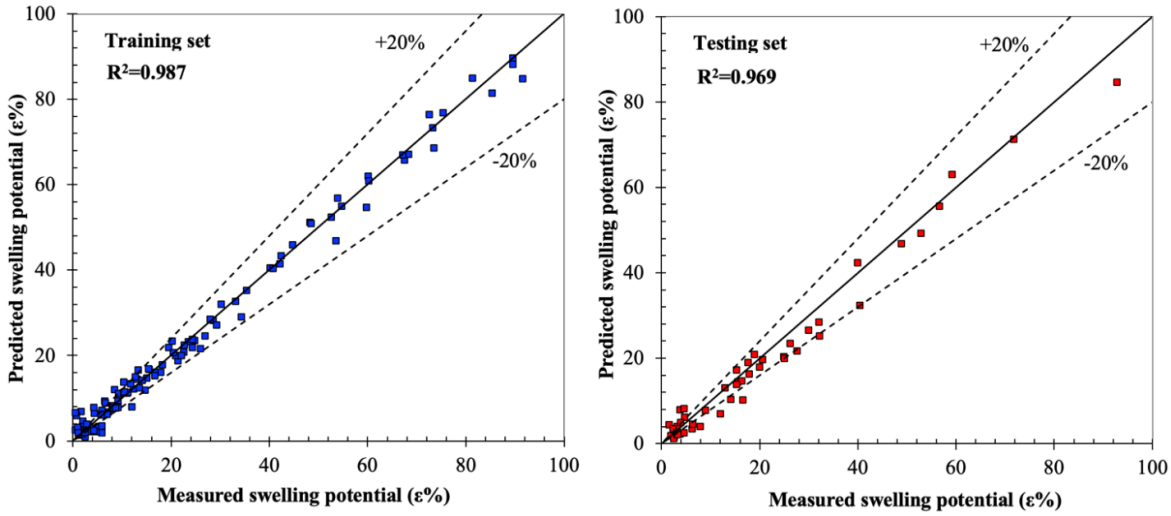
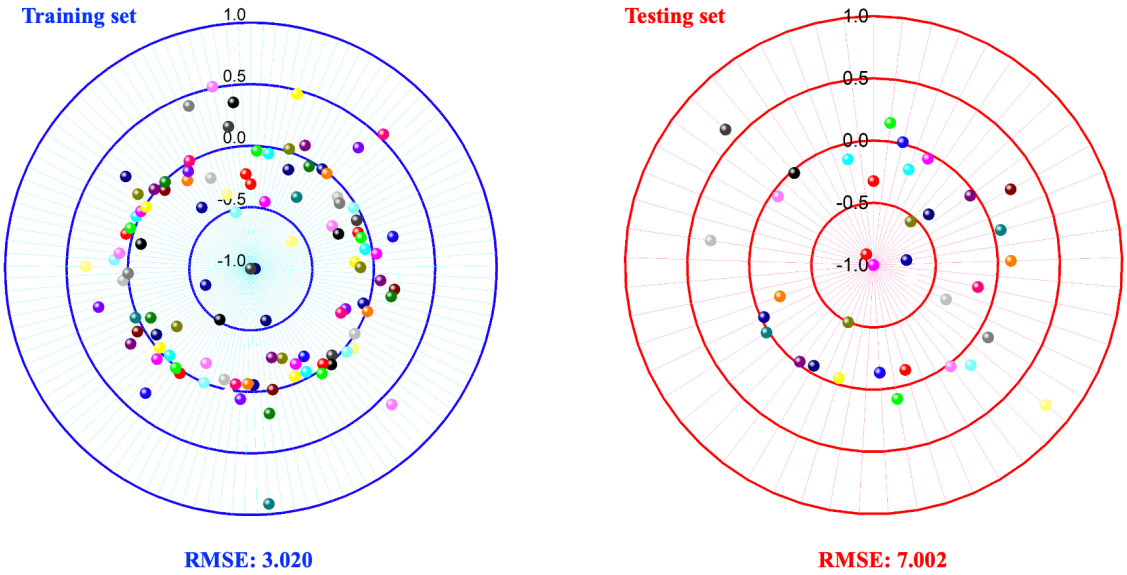


Fig. 4.9. Prediction results of the MLP model with 9 inputs (Model 2)

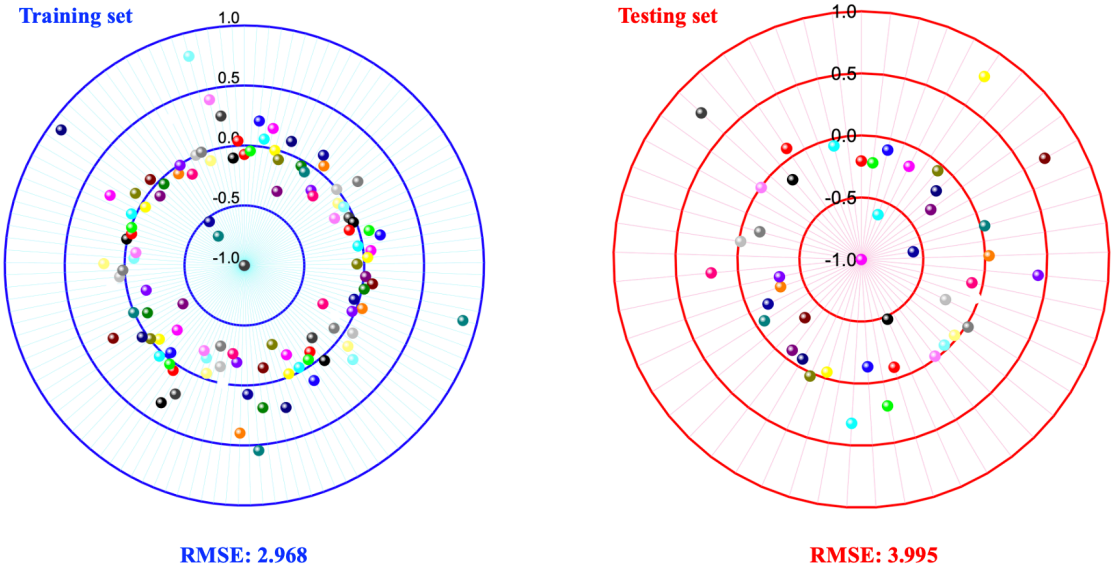
Fig. 4.9 clearly illustrates the excellent prediction performance of the MLP algorithm, with most data points accurately falling within a 20% error margin in both the training and testing sets. The R^2 value for the MLP model is 0.987 for the training set and 0.968 for the test set, which is referred to as Model 2. The percentage difference between the prediction accuracies of the training and test sets, often referred to as the degree of overfitting, is a critical metric, with a value below 5% typically indicating good generalization performance and minimal overfitting (Subramanian and Simon, 2013). In this study, the degree of overfitting for Model 2 is only 1.9%, indicating that overfitting is virtually nonexistent.

A comparative analysis between the MARS model and the MLP model reveals that both models perform similarly on the training set, with a marginal accuracy difference of just 0.2%. However, the MLP model exhibits superior performance on the test set, outperforming the MARS model by 8.6%. Therefore, in terms of prediction accuracy, the MLP model surpasses the MARS model, indicating its enhanced capability for generalization and prediction precision.

4.4.3 Error analysis



(a)



(b)

Fig. 4.10 Error distribution of the a) MARS and b) MLP model

The error associated with the prediction results is characterized by the ratio of the deviation between the predicted and measured values. Fig. 4.10a and Fig. 4.10b highlight the random distribution of errors in the MARS and MLP models on polar coordinates. Data points closer to the zero-error circle indicate lower prediction errors for those points. Overall, most error points for both models exhibit slight fluctuations within and around the zero-error circle, with only a few points showing significant deviations. The RMSE value for the Model 1 ranges from 3.020 to 7.002, indicating that the average difference between the measured and predicted swelling potential does not exceed 7%. In contrast, the RMSE value for the Model 2 ranges from 2.968 to 3.995, with a maximum average error of only 4%. This comparison suggests that the Model 2 provides higher accuracy, stronger generalization performance, and greater reliability than the Model 1.

4.4.4 Sensitivity analysis

After obtaining the Model 2, its connection weights were extracted for sensitivity analysis and summarized in Table 4.3. Garson's method (Garson, 1991) was employed for this analysis, as it is well-suited for weight-dependent algorithms such as MLP. This method interprets the connection weights between hidden layers to quantify the influence of each input variable. The relative importance of each input is calculated using the model's weights. For the MARS model (Model 1), the importance of each input variable is determined by the number of basis functions and their corresponding coefficients. The Model 1 developed in this study comprises 50 basis functions, each associated with a coefficient, as presented in Table 4.4. Typically, the absolute values of these coefficients indicate the relative contribution of each basis function to the target prediction. Each basis function may involve one or more input variables. By analyzing the expressions of all basis functions, the presence of a specific input variable is identified. For basis functions containing the input variable, the absolute values of their coefficients are summed to compute the total weight assigned to that variable, as shown in Table 4.5. The weights for all input variables are then normalized, ensuring their collective sum equals 1. The proportion of each input variable's weight relative to the total is used to represent its importance factor, providing valuable insight into the contribution of each variable within the prediction model.

Table 4.3 Weights and biases derived from the Model 2

Hidden Layers	ω_{ij}^{IP}									ω_j^{OP}	b_j^{IP}	b^{OP}
1	-0.48	-8.09	-0.74	0.27	2.75	5.67	4.62	0.01	-1.80	-4.02	-2.05	
2	-4.18	1.86	-2.85	-0.97	-1.28	1.78	-4.71	-0.81	-0.82	-0.44	2.21	
3	-8.04	5.01	-2.64	4.69	-0.80	-2.89	-6.81	4.00	5.35	-0.09	-1.29	1.35
4	0.17	7.37	0.70	-0.32	-2.35	-4.47	-4.72	0.48	1.75	-3.95	1.11	
5	-0.06	-0.33	0.23	0.45	-4.09	-0.04	0.17	0.82	-0.19	1.93	-5.92	

Table 4.4 Coefficients of basis functions derived from the Model 1

BF1	BF2	BF3	BF4	BF5	BF6	BF7	BF8	BF9	BF10
-44679.07	-18030.39	-5378.18	-241.59	515.69	11.41	16.58	-74.09	-17.44	862.92
BF11	BF12	BF13	BF14	BF15	BF16	BF17	BF18	BF19	BF20
-1174.92	2698.87	41.85	-73.94	-5.44	3.60	-0.07	-0.12	-20.29	11.12
BF21	BF22	BF23	BF24	BF25	BF26	BF27	BF28	BF29	BF30
-0.67	0.22	-307.27	330.98	1.38	12659.55	-1538.45	-0.09	-36.71	0.59
BF31	BF32	BF33	BF34	BF35	BF36	BF37	BF38	BF39	BF40
-0.84	-24.82	841.96	4.42	0.00	-0.03	0.38	-1.55	0.10	11.67
BF41	BF42	BF43	BF44	BF45	BF46	BF47	BF48	BF49	BF50
-8.78	0.56	0.00	0.00	-0.01	-0.24	-3.18	-0.01	0.67	0.26

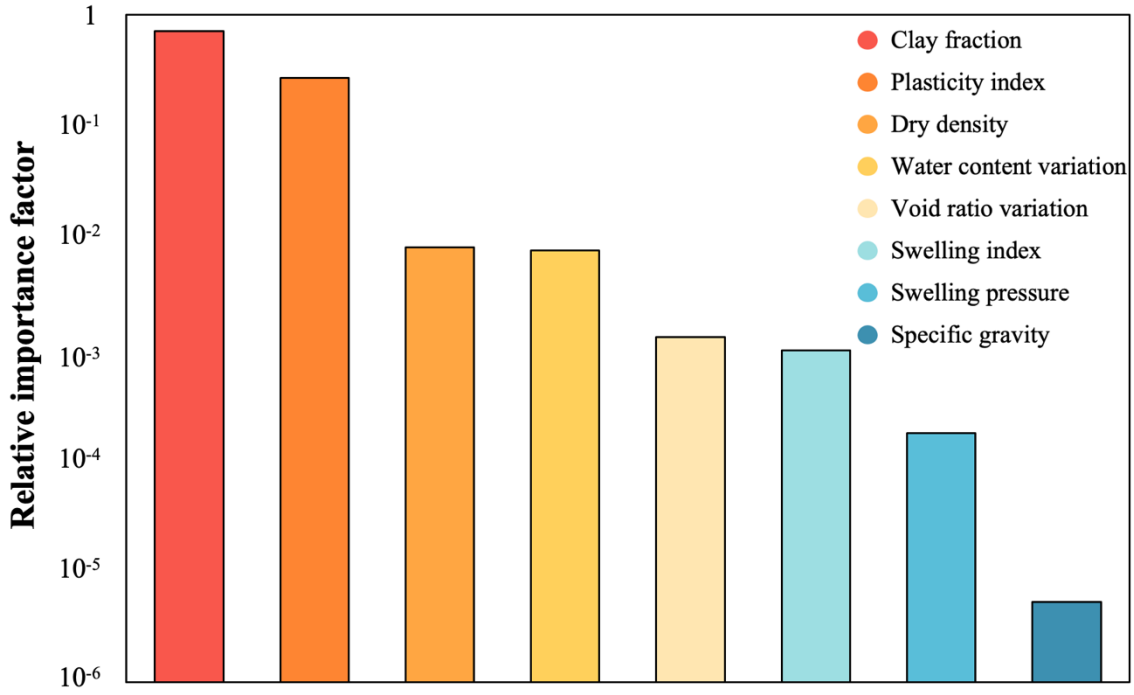
Table 4.5 Weights for each input variables in the Model 1

C	I_p	ρ_d	G_s	q	Δw	Δe	C_s	P_s
68142.00	5892.89	773.65	0.50	0.00	723.50	120.47	91.52	16.58

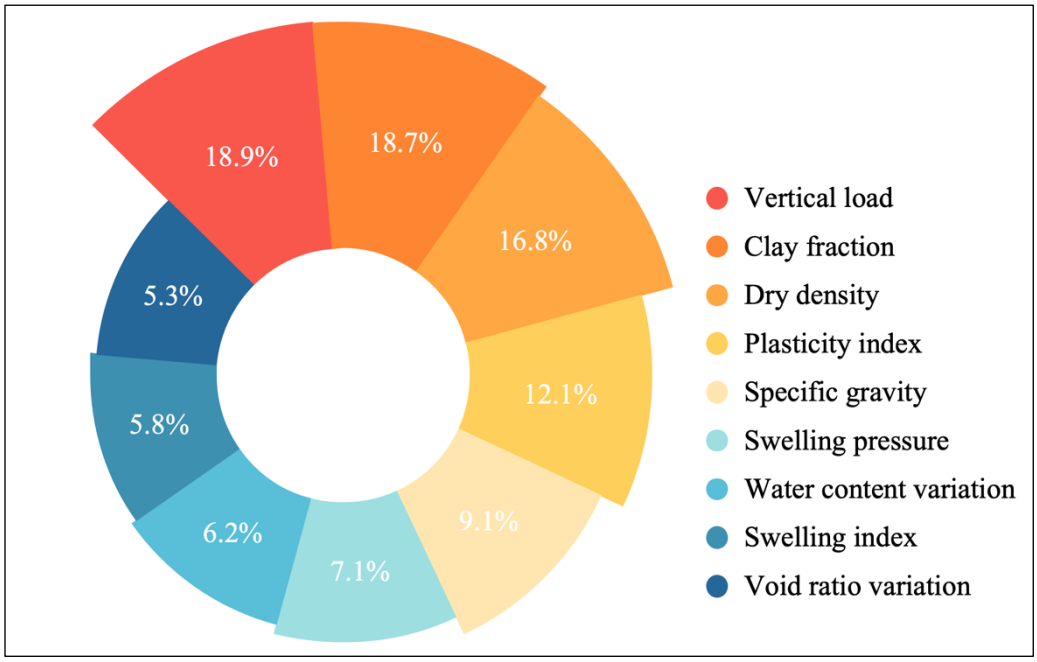
Note: C is clay fraction, I_p is plasticity index, ρ_d is dry unit weight, G_s is specific gravity, q is vertical load, Δw is water content variation, Δe is void ratio variation, C_s is swelling index, P_s is the swelling pressure.

Fig. 11a and Fig. 11b present the quantitative demonstration of the relative importance factor of each input parameter in predicting swelling potential. As shown, there are noticeable differences in the ranking of relative importance factors assigned to each input parameter by both models. These discrepancies may arise from the distinct prediction principles employed by the two algorithms. In the MLP algorithm, the weights between input parameters and the output target are directly derived from the model. Conversely, the MARS algorithm calculates the weight of each input parameter indirectly by summing the weighted absolute values of the coefficients of the basis functions that involve that parameter. Therefore, the weights produced by these two models are fundamentally different in their derivation. Despite variations in individual importance rankings, the overall trends remain consistent across both models. Both models identify dry density, clay fraction, and plasticity index as the most influential factors in determining the swelling potential of the analyzed expansive soils. While the rankings differ slightly between the models, parameters such as water content variation, void ratio variation, swelling pressure, and specific gravity show moderate influence, highlighting the combined effects of environmental and mechanical factors. Furthermore, the sensitivity analysis indicates that the relative importance of these parameters is model-dependent, with Model 2 assigning greater importance to specific gravity and swelling pressure compared to Model 1. The results of Model 2 suggest that vertical load has the greatest influence on swelling potential. In contrast, vertical load was not retained in Model 1 due to the automatic variable selection

mechanism of the MARS algorithm, which excludes parameters that contribute minimally to reducing prediction error. This does not imply that vertical load is not important; rather, it reflects differences in how MARS and MLP capture parameter interactions. The inclusion and high sensitivity of vertical load in Model 2 align with well-established engineering judgment that increasing vertical stress reduces soil swelling. Therefore, our conclusion is based on a combined interpretation of the two models and engineering judgment, indicating that swelling potential is strongly influenced by clay fraction, plasticity index, dry density, and vertical load.



(a)



(b)

Fig. 4.11 Relative importance factors given by a) Model 1 and b) Model 2

4.4.5 Model optimization

The discussions summarized in the earlier paragraph based on the sensitivity analysis highlight that the parameters, swelling pressure, swelling index, and void ratio have a lower influence on the prediction of swelling potential. The complexity and time-consuming nature of obtaining these parameters from oedometer tests suggest that it is more practical to optimize the models to achieve a close to similar prediction performance without relying on them. Model 2, developed using the MLP approach, demonstrates superior prediction accuracy, reduced overfitting, and a more straightforward formulation compared to Model 1. Therefore, it is selected and optimized into Model 3 by excluding swelling pressure, swelling index, and void ratio from the input parameters. The remaining six parameters that include clay fraction, plasticity index, vertical load, dry density, water content variation, and specific gravity are not only influential but also commonly gathered in routine

geotechnical investigations, making Model 3 both robust and simple for practical engineering application

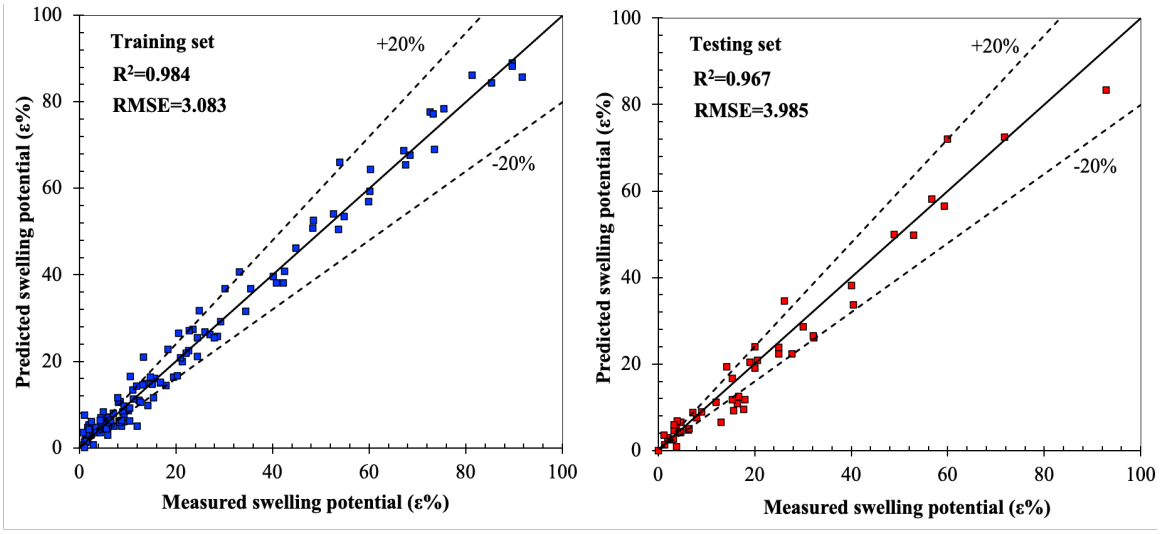


Fig. 4.12 Prediction results of the MLP model with 6 inputs (Model 3)

Fig. 4.12 presents the prediction results of Model 3 achieving R^2 values of 0.984 for the training set and 0.967 for the testing set, which are close to the values of 0.987 and 0.969 for Model 2. Additionally, the RMSE values of Model 3 are also comparable to those of Model 2. These results suggest that Model 3 is an optimized version of Model 2, requiring fewer input parameters while maintaining similar predictive accuracy. The R_r values for Model 2 and Model 3 range from 92.31% to 99.17%, exceeding the 90% threshold often used to indicate reliable robustness (Wang and Yin, 2021). The detailed statistical analysis for the three models is summarized in Table 4.6.

Table 4.6 Statistical analysis for the established swelling potential prediction models

Models	Algorithm	Inputs	Set	R^2	VAF	RMSE
Model 1	MARS	C, I_p, ρ_d, G_s, q, Δw, Δe, C_s, P_s	Train	0.984	98.4	3.020
			Test	0.887	88.2	7.002

Model 2	MLP	C, I_p, ρ_d, G_s, q, Δw, Δe C_s, P_s	Train	0.987	98.7	2.968
			Test	0.969	96.9	3.995
Model 3	MLP	C, I_p, ρ_d, G_s, q, Δw	Train	0.984	98.4	3.083
			Test	0.967	96.8	3.985

To facilitate the use of Model 3, its weights and biases are provided in Table 4.7. These values can be applied in Eq. (4.1) to generate an explicit equation, Eq. (4.8). This simplifies the prediction process while maintaining accuracy for easily predicting swelling potential in engineering practice.

Table 4.7 Weights and biases derived from the Model 3

Hidden Layers	ω_{ij}^{IP}						ω_j^{OP}	b_j^{IP}	b^{OP}
1	-0.89	36.59	11.36	53.56	-31.40	-3.04	-0.04	-3.68	
2	-41.19	-20.13	30.14	19.66	-14.87	-47.94	0.11	-4.92	
3	2.34	-8.50	-0.02	-0.09	1.37	-54.08	-68.88	27.72	-0.93
4	-2.32	8.34	0.01	0.07	68.17	52.86	-68.95	42.41	
5	0.23	0.15	1.64	-0.20	-0.41	0.81	0.30	0.88	

$$\begin{aligned}\varepsilon\% = {} & \left(-1.845 \cdot \text{tansig}\left(-0.012 \cdot C + 0.515 \cdot I_p + 0.445 \cdot \Delta\omega + 96.478 \cdot \rho_d - 0.079 \cdot q - 3.494 \cdot G_s - 142.476\right)\right. \\ & +5.073 \cdot \text{tansig}\left(-0.557 \cdot C - 0.284 \cdot I_p + 1.180 \cdot \Delta\omega + 35.441 \cdot \rho_d - 0.037 \cdot q - 55.103 \cdot G_s + 64.105\right) \\ & -3176.746 \cdot \text{tansig}\left(0.032 \cdot C - 0.120 \cdot I_p - 0.001 \cdot \Delta\omega - 0.162 \cdot \rho_d + 0.003 \cdot q - 62.149 \cdot G_s + 152.651\right) \\ & -3179.974 \cdot \text{tansig}\left(-0.031 \cdot C + 0.117 \cdot I_p + 0.0004 \cdot \Delta\omega + 0.126 \cdot \rho_d + 0.171 \cdot q + 60.828 \cdot G_s - 79.979\right) \\ & \left.+13.836 \cdot \text{tansig}\left(0.003 \cdot C + 0.002 \cdot I_p + 0.064 \cdot \Delta\omega - 0.360 \cdot \rho_d - 0.001 \cdot q + 0.931 \cdot G_s - 0.511\right)\right) + 3.768\end{aligned} \tag{4.8}$$

4.4.6 Model comparisons

In addition to statistical analysis comparisons, Fig. 4.13 presents a comprehensive comparison of swelling potential for 173 expansive soil specimens from various regions worldwide, evaluated using three different approaches: machine learning methods (Model 1, Model 2, and Model 3), experimental methods (measured data), and an empirical method proposed by Nayak and Christensen (Nayak and Christensen, 1971), which is a widely used relationship in the literature for estimating swelling potential. This comparison highlights the reliability and practical relevance of the machine learning models compared to both measured and empirical results, providing insights for their use in engineering practice. In Fig. 4.14, the measured values are represented by a blue line, while the predicted values of the MARS model (Model 1) are shown in yellow, the MLP models (Model 2 in red and Model 3 in green), and the predictions from the Nayak and Christensen method (NC) are depicted in light blue (Nayak and Christensen, 1971).

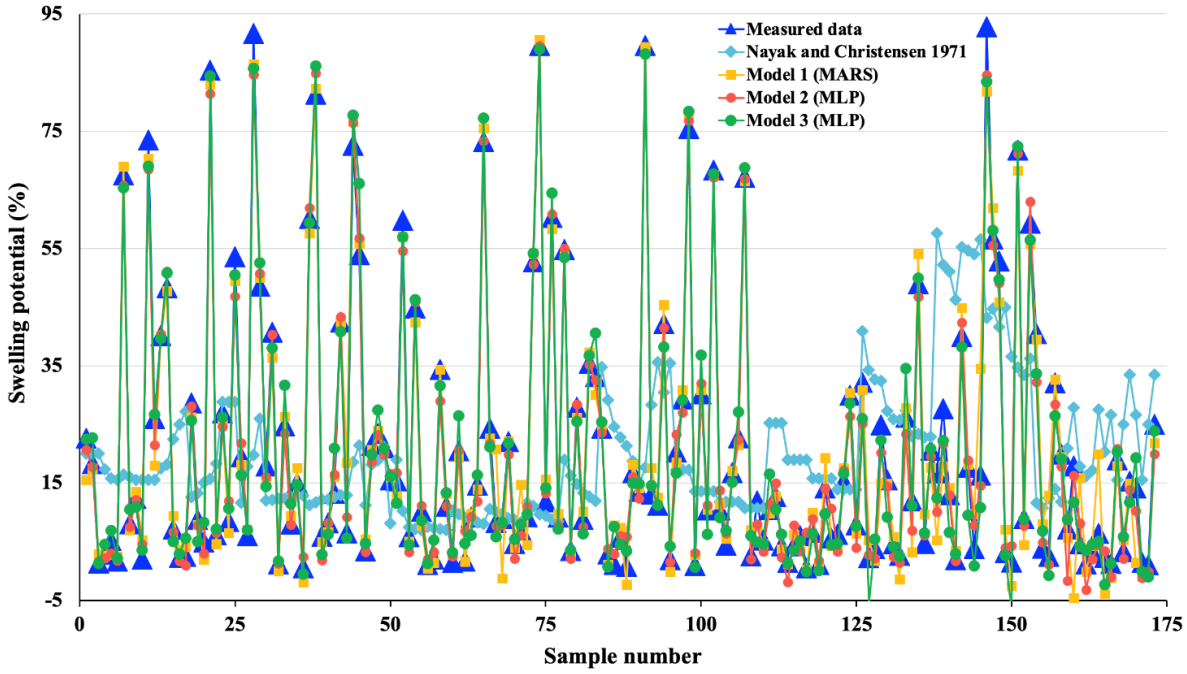


Fig. 4.13 Comparison of swelling potential prediction among experimental, AI, and empirical methods

The predicted values obtained using the NC method display a relatively uniform distribution, demonstrating strong prediction accuracy within the swelling potential range of 10% to 35%. However, the method's applicability is limited when addressing soils with very low or very high swelling potential. In contrast, the machine learning based models (Models 1–3) developed in this study exhibit superior prediction capabilities, as evidenced by their prediction lines closely aligning with experimental measurements and largely overlapping with one another.

These models effectively predict the swelling potential of expansive soils across a broader range, from 2% to 95%, making them more versatile for use particularly for pavements. Although minor deviations were observed for certain data, these variations did not result in significant errors that could compromise practical engineering applications. The comparison underscores the reliability and accuracy of the machine learning models, demonstrating their effectiveness in addressing challenges posed by expansive soils. Their superior performance in complex subgrade conditions provides engineers with critical insights for optimizing subgrade layer thickness, drainage systems, and pavement design.

4.5 Limitations

A limitation of this study is that certain intrinsic properties such as montmorillonite content, cation exchange capacity (CEC), and specific surface area (SSA) were not included because related information is not available for most of the expansive soils data gathered from the literature. Instead, proxy indicators (e.g., clay content and plasticity index) were used to ensure applicability with widely available parameters. Future studies incorporating these intrinsic factors, once larger datasets become available, may further improve prediction accuracy and provide deeper insights into mineralogical effects.

Another limitation lies in the complexity of in-situ expansive soils compared to laboratory conditions. The database used in this study was primarily derived from laboratory tests, where specimens are typically small, uniform, and subjected to a single wetting cycle. In contrast, field soils often display layered and fissured structures, experience long-term wetting–drying cycles and are influenced by non-uniform infiltration patterns. Although the proposed model has been validated against five independent case studies from different countries (see Chapter 6.3); some discrepancies between predicted and observed field behavior remain. Future studies should therefore focus on validating and refining the proposed model using large-scale field monitoring datasets under varied climatic and geological conditions to bridge the gap between laboratory and field environments.

4.6 Summary

Swelling potential is a critical parameter for assessing the performance and safety of lightly loaded geotechnical and transportation infrastructures constructed with or within expansive soils. Traditionally, this parameter is determined from oedometer test results, while accurate, they are time-intensive and costly. As a result, practicing engineers often turn to empirical methods for predicting swelling potential. However, these methods are typically derived from region-specific soil samples, limiting their applicability across diverse geotechnical scenarios. To overcome the limitations of both conventional oedometer tests and empirical approaches, this study employed two advanced machine learning algorithms, MARS and MLP, to develop three different models for reliably predicting swelling

potential in expansive soils. One of the three is an optimized model (Model 3; Eq. (4.8)) that has been simplified into an explicit equation for use in practical engineering. The key findings of this study are summarized as follows:

(i) Comprehensive validation using multiple evaluation indices demonstrated that both the MARS and MLP models achieve high accuracy and reliability in predicting swelling potential across a wide range of values. These models provide reliable tools for addressing the challenges associated with expansive soils in transportation geotechnics.

(ii) Sensitivity analysis identified vertical load, clay fraction, dry density, and plasticity index as the most influential factors affecting swelling potential. These insights were instrumental in refining the MLP-based Model 2, enhancing its predictive performance.

(iii) The optimized Model 3 is simpler and relies solely on six easily measurable soil properties: clay fraction, plasticity index, dry density, specific gravity, vertical load, and water content variation. Despite its simplicity, Model 3 achieves high prediction accuracy, making it a reliable alternative to existing empirical methods for engineering applications.

(iv) To facilitate the practical application of Model 3, its parameters have been integrated into a simplified equation. This approach enables straightforward calculations using a calculator or simple spreadsheet, providing engineers with a practical, efficient, and accessible tool for predicting swelling potential of expansive soils.

(v) While the current study focused on prediction accuracy and robustness, future work may incorporate monotonicity analysis to further improve model interpretability and consistency. This type of analysis examines whether predicted outputs follow expected trends with key inputs, as discussed by Wang and Yin (2020), and could enhance confidence in the practical use of data-driven models in geotechnical engineering.

References

Abden, A., Al-Shamrani, M., Dafalla, M., 2024. Evaluating the feasibility of inverted T foundation on expansive soils. Journal of Building Engineering, 97, 110788.

Abiodun, O. I., Jantan, A., Omolara, A. E., Dada, K. V., Umar, A. M., Linus, O. U., Arshad, H., Kazaure, A. A., Gana, U., Kiru, M. U., 2019. Comprehensive review of artificial neural network applications to pattern recognition. IEEE access, 7, 158820-158846.

Adem, H. H., 2015. Modulus of elasticity based method for estimating the vertical movement of natural unsaturated expansive soils Université d'Ottawa/University of Ottawa].

Adem, H. H., Vanapalli, S. K., 2016. Heave prediction in a natural unsaturated expansive soil deposit under a lightly loaded structure. Geotechnical and Geological Engineering, 34, 1181-1192.

Adoko, A. C., Yagiz, S., 2019. Fuzzy inference system-based for TBM field penetration index estimation in rock mass. Geotechnical and Geological Engineering, 37, 1533-1553.

Al-Rawas, A. A., Guba, I., McGown, A., 1998. Geological and engineering characteristics of expansive soils and rocks in northern Oman. Engineering Geology, 50(3-4), 267-281.

Al-Shamrani, M. A., Dhowian, A. W., 2003. Experimental study of lateral restraint effects on the potential heave of expansive soils. Engineering Geology, 69(1-2), 63-81.

Allen, M. P., 1997. The problem of multicollinearity. Understanding regression analysis, 176-180.

Alptekin, A., Taga, H., 2019. Prediction of compression and swelling index parameters of quaternary sediments from index tests at Mersin District. Open Geosciences, 11(1), 482-491.

ASTM, D., 2003. 4546. Standard Test Method for One-Dimensional Swell or Settlement Potential of Cohesive Soil.

Azam, S., Hu, Y., Chowdhury, R., 2009. Sensor installation for field monitoring in expansive soils. Proceedings of 62nd Canadian geotechnical conference, Halifax,

Bandara, T., Yapa, R., Kodituwakku, S., 2011. Simulation of regression analysis by an automated system utilizing artificial neural networks. Int. J Latest Trends Computing Vol, 2(3), 378.

Briaud, J.-L., Zhang, X., Moon, S., 2003. Shrink test–water content method for shrink and swell predictions. Journal of geotechnical and geoenvironmental engineering, 129(7), 590-600.

Charlie, W. A., Osman, M. A., Ali, E. M., 1984. Construction on expansive soils in Sudan. Journal of Construction Engineering and Management, 110(3), 359-374.

Cheamanunkul, S., Freund, Y., 2014. Improved kNN rule for small training sets. 2014 13th International Conference on Machine Learning and Applications,

Chen, F. H., 2012. Foundations on expansive soils (Vol. 12). Elsevier.

Chen, Y., Xu, Y., Jamhiri, B., Wang, L., Li, T., 2022. Predicting uniaxial tensile strength of expansive soil with ensemble learning methods. Computers and Geotechnics, 150, 104904.

Cho, S. E., 2009. Probabilistic stability analyses of slopes using the ANN-based response surface. Computers and Geotechnics, 36(5), 787-797.

Çimen, Ö., Keskin, S. N., Yıldırım, H., 2012. Prediction of swelling potential and pressure in compacted clay. Arabian Journal for Science and Engineering, 37, 1535-1546.

Dave, V. S., Dutta, K., 2014. Neural network based models for software effort estimation: a review. Artificial Intelligence Review, 42(2), 295-307.

De Veaux, R. D., Psichogios, D., Ungar, L., 1993. A comparison of two nonparametric estimation schemes: MARS and neural networks. Computers & chemical engineering, 17(8), 819-837.

Dhowian, A. W., 1990. Simplified heave prediction model for expansive shale. Geotechnical Testing Journal, 13(4), 323-333.

Djellali, A., Houam, A., Saghafi, B., 2017. Indirect estimation of swelling pressure of clayey subgrade under pavement structures. Arabian Journal for Science and Engineering, 42, 3991-3999.

Ene, E., Okagbue, C., 2009. Some basic geotechnical properties of expansive soil modified using pyroclastic dust. Engineering Geology, 107(1-2), 61-65.

Erzin, Y., Güneş, N., 2011. The prediction of swell percent and swell pressure by using neural networks. Mathematical and Computational Applications, 16(2), 425-436.

Eyo, E., Abbey, S., Lawrence, T., Tetteh, F., 2022. Improved prediction of clay soil expansion using machine learning algorithms and meta-heuristic dichotomous ensemble classifiers. Geoscience Frontiers, 13(1), 101296.

Fityus, S., Smith, D., Allman, M., 2004. Expansive soil test site near Newcastle. Journal of

Geotechnical and Geoenvironmental Engineering, 130(7), 686-695.

Fondjo, A. A., Theron, E., Ray, R. P., 2021. Semi-empirical model for predicting the swelling stress of compacted, unsaturated expansive soils. Civil Engineering and Architecture, 9(1), 225-239.

Friedman, J. H., 1991. Multivariate adaptive regression splines. The annals of statistics, 19(1), 1-67.

Fu, L., Peng, Z., 2023. An Improved Multivariate Adaptive Regression Splines (MARS) Method for Prediction of Compressive Strength of High-Strength (HS) Concrete. Arabian Journal for Science and Engineering, 48(4), 4511-4530.

Garson, D. G., 1991. Interpreting neural network connection weights.

Gaspar, T. A. V., Jacobsz, S. W., Heymann, G., Toll, D., Gens, A., Osman, A., 2022. The mechanical properties of a high plasticity expansive clay. Engineering Geology, 303, 106647.

Girshick, R., 2015. Fast r-cnn. arXiv preprint arXiv:1504.08083.

Gourley, C., Newill, D., Schreiner, H., 2020. Expansive soils: TRL's research strategy. In Engineering Characteristics of Arid Soils (pp. 247-260). CRC Press.

Hakkoum, H., Idri, A., Abnane, I., 2021. Assessing and comparing interpretability techniques for artificial neural networks breast cancer classification. Computer methods in biomechanics and biomedical engineering: imaging & visualization, 9(6), 587-599.

Hossain, I., Rasel, H., Imteaz, M. A., Mekanik, F., 2020. Long-term seasonal rainfall forecasting using linear and non-linear modelling approaches: a case study for Western Australia. Meteorology and Atmospheric Physics, 132, 131-141.

Hou, T.-s., Xu, G.-l., Shen, Y.-j., Wu, Z.-z., Zhang, N.-n., Wang, R., 2013. Formation mechanism and stability analysis of the Houba expansive soil landslide. Engineering Geology, 161, 34-43.

Jalal, F. E., Jamei, M., Hamaamin, Y. G., Mohammed, A. S., 2024. ANN-based swarm intelligence for predicting expansive soil swell pressure and compression strength. Scientific Reports, 14(1), 14597.

Jamsawang, P., Adulyamet, B., Voottipruex, P., Jongpradist, P., Likitlersuang, S., Tantayopin, K., 2023. The free swell potential of expansive clays stabilized with the shallow bottom ash mixing method. Engineering Geology, 315, 107027.

Johnson, L. D., 1973. Influence of suction on heave of expansive soils.

Kariuki, P. C., Van Der Meer, F., 2004. A unified swelling potential index for expansive soils. Engineering geology, 72(1-2), 1-8.

Kayadelen, C., Taşkıran, T., Günaydın, O., Fener, M., 2009. Adaptive neuro-fuzzy modeling for the swelling potential of compacted soils. Environmental Earth Sciences, 59, 109-115.

Li, T., Kong, L., Guo, A., 2021. The deformation and microstructure characteristics of expansive soil under freeze–thaw cycles with loads. Cold Regions Science and Technology, 192, 103393.

Likos, W. J., 2004. Measurement of crystalline swelling in expansive clay. Geotechnical Testing Journal, 27(6), 540-546.

Liu, Y., Mu, Y., Chen, K., Li, Y., Guo, J., 2020. Daily activity feature selection in smart homes based on pearson correlation coefficient. Neural processing letters, 51, 1771-1787.

Liu, Y., Vanapalli, S. K., 2017. Influence of lateral swelling pressure on the geotechnical infrastructure in expansive soils. Journal of Geotechnical and Geoenvironmental Engineering, 143(6), 04017006.

Liu, Y., Zhao, Y., Vanapalli, S. K., Mehmood, M., 2024. Soil-water characteristic curve of expansive soils considering cumulative damage effects of wetting and drying cycles. Engineering Geology, 339, 107642.

Lohr, S. L., 2021. Sampling: design and analysis. Chapman and Hall/CRC, Boca Raton.

Madsen, F. T., Müller-Vonmoos, M., 1989. The swelling behaviour of clays. Applied Clay Science, 4(2), 143-156.

Mohamed, O. Z., Taha, Y. K., El-Aziz, E.-S. M. A., 2014. Field study of the distribution of lateral swelling pressure of expansive soil on retaining structure. JES. Journal of Engineering Sciences, 42(2), 289-302.

Mokhtari, M., Dehghani, M., 2012. Swell-shrink behavior of expansive soils, damage and control. Electronic Journal of Geotechnical Engineering, 17, 2673-2682.

Najjar, Y. M., Basheer, I. A., Ali, H. E., McReynolds, R. L., 2000. Swelling potential of Kansas soils: Modeling and validation using artificial neural network reliability approach. Transportation research record, 1736(1), 141-147.

Nayak, N. V., Christensen, R., 1971. Swelling characteristics of compacted, expansive soils. Clays and clay minerals, 19, 251-261.

Nelson, J. D., Chao, K. C., Overton, D. D., Nelson, E. J., 2015. Foundation engineering for

expansive soils. John Wiley & Sons.

Ng, C. W. W., Zhan, L. T., Bao, C. G., Fredlund, D. G., Gong, B. W., 2003. Performance of an unsaturated expansive soil slope subjected to artificial rainfall infiltration. Geotechnique, 53(2), 143-157.

Nguyen, D. D., Roussis, P. C., Pham, B. T., Ferentinou, M., Mamou, A., Vu, D. Q., Bui, Q.-A. T., Trong, D. K., Asteris, P. G., 2022. Bagging and multilayer perceptron hybrid intelligence models predicting the swelling potential of soil. Transportation Geotechnics, 36, 100797.

Onyelowe, K. C., Fazal, E., Michael, E., Ifeanyichukwu, C., Alaneme, G. U., Chidozie, I., 2021. Artificial intelligence prediction model for swelling potential of soil and quicklime activated rice husk ash blend for sustainable construction. Jurnal Kejuruteraan, 33(4), 845-852.

Osman, N., McManus, K., Ng, A., 2005. Management and analysis of data for damage of light structures on expansive soils in Victoria, Australia.

Pandey, P., Hossain, M. S., Ahmed, A., 2021. Performance evaluation of modified moisture barrier in mitigating expansive soil associated pavement distresses. Transportation Geotechnics, 31, 100667.

Piepho, H. P., 2019. A coefficient of determination (R2) for generalized linear mixed models. Biometrical journal, 61(4), 860-872.

Puppala, A. J., Manosuthikij, T., Chittoori, B. C., 2013. Swell and shrinkage characterizations of unsaturated expansive clays from Texas. Engineering Geology, 164, 187-194.

Rao, A., Phanikumar, B., Sharma, R. S., 2004. Prediction of swelling characteristics of remoulded and compacted expansive soils using free swell index. Quarterly Journal of Engineering Geology and Hydrogeology, 37(3), 217-226.

Rehman, Z., Armaghani, D. J., Mohamad, E. T., Gharachorlou, A., Tahir, M. M., 2022. Machine learning-based intelligent modeling of hydraulic conductivity of sandy soils considering a wide range of grain sizes. Engineering Geology, 311, 106899.

Ruwaih, I., 1987. Experiences with expansive soils in Saudi Arabia. Proceedings of the 6th international conference on expansive soils, New Delhi, India.

Sarker, D., Wang, J. X., 2022. Moisture influence on structural responses of pavement on expansive soils. Transportation Geotechnics, 35, 100773.

Seed, H. B., Woodward Jr, R. J., Lundgren, R., 1962. Prediction of swelling potential for compacted clays. Journal of the soil mechanics and foundations division, 88(3), 53-

87.

Senaviratna, N., Cooray, T., 2019. Diagnosing multicollinearity of logistic regression model. Asian Journal of Probability and Statistics, 5(2), 1–9.

Sheela, K. G., Deepa, S. N., 2013. Review on methods to fix number of hidden neurons in neural networks. Mathematical Problems in Engineering, 2013(1), 425740.

Shi, B., Jiang, H., Liu, Z., Fang, H., 2002. Engineering geological characteristics of expansive soils in China. Engineering Geology, 67(1-2), 63-71.

Shrestha, N., 2020. Detecting multicollinearity in regression analysis. American Journal of Applied Mathematics and Statistics, 8(2), 39–42.

Singh, K., Upadhyaya, S., 2012. Outlier detection: applications and techniques. International Journal of Computer Science Issues (IJCSI), 9(1), 307.

Singhal, S., Houston, S. L., Houston, W. N., 2015. Swell pressure, matric suction, and matric suction equivalent for undisturbed expansive clays. Canadian Geotechnical Journal, 52(3), 356-366.

Subramanian, J., Simon, R., 2013. Overfitting in prediction models–is it a problem only in high dimensions? Contemporary clinical trials, 36(2), 636-641.

Tavakkoli, N. e., Oh, W. T., Vanapalli, S. K., 2024. Compilation of Consolidation Properties Data of Champlain Sea Clay from Ottawa Region. Geotechnical and Geological Engineering, 1-23.

Taylor, R., Smith, T., 1986. The engineering geology of clay minerals: swelling, shrinking and mudrock breakdown. Clay Minerals, 21(3), 235-260.

Tu, H., Vanapalli, S. K., 2016. Prediction of the variation of swelling pressure and one-dimensional heave of expansive soils with respect to suction using the soil-water retention curve as a tool. Canadian Geotechnical Journal, 53(8), 1213-1234.

Uddin, F., 2008. Clays, nanoclays, and montmorillonite minerals. Metallurgical and Materials Transactions A, 39(12), 2804–2814.

Uzair, M., Jamil, N., 2020. Effects of hidden layers on the efficiency of neural networks. 2020 IEEE 23rd international multitopic conference (INMIC),

Vanapalli, S., Lu, L., 2012. A state-of-the art review of 1-D heave prediction methods for expansive soils. International Journal of Geotechnical Engineering, 6(1), 15-41.

Venkatesan, S., Droniou, J., Roy, I., Robert, D., Zhou, A., 2021. Application of diffusion-advection equations to in-field monitoring of soil suction profiles. Computers and Geotechnics, 139, 104329.

Villar, M. V., Lloret, A., 2008. Influence of dry density and water content on the swelling of a compacted bentonite. Applied Clay Science, 39(1–2), 38–49.

Vrigazova, B., 2021. The proportion for splitting data into training and test set for the bootstrap in classification problems. Business Systems Research: International Journal of the Society for Advancing Innovation and Research in Economy, 12(1), 228–242.

Vu, H. Q., Fredlund, D. G., 2004. The prediction of one-, two-, and three-dimensional heave in expansive soils. Canadian Geotechnical Journal, 41(4), 713-737.

Wagner, J. F., 2013. Mechanical properties of clays and clay minerals. In: Developments in Clay Science. Elsevier, Amsterdam, pp. 347–381.

Wang, H. L., Yin, Z. Y., 2020. High performance prediction of soil compaction parameters using multi expression programming. Engineering Geology, 276, 105758.

Wang, H. L., Yin, Z. Y., 2021. Unconfined compressive strength of bio-cemented sand: state-of-the-art review and MEP-MC-based model development. Journal of Cleaner Production, 315, 128205.

Wilson, M., 1999. The origin and formation of clay minerals in soils: past, present and future perspectives. Clay minerals, 34(1), 7-25.

Xiang, L., Zhao, G., Li, Q., Hao, W., Li, F., 2018. TUMK-ELM: a fast unsupervised heterogeneous data learning approach. IEEE Access, 6, 35305-35315.

Yang, J., Cai, Y., Pan, C., Mi, C., 2019. A novel resistor-inductor network-based equivalent circuit model of lithium-ion batteries under constant-voltage charging condition. Applied Energy, 254, 113726.

Yilmaz, I., Kaynar, O., 2011. Multiple regression, ANN (RBF, MLP) and ANFIS models for prediction of swell potential of clayey soils. Expert systems with applications, 38(5), 5958-5966.

Ying, X., 2019. An overview of overfitting and its solutions. Journal of physics: Conference series,

Yoshida, R., Fredlund, D. G., Hamilton, J., 1983. The prediction of total heave of a slab-on-grade floor on Regina clay. Canadian Geotechnical Journal, 20(1), 69-81.

Zareef, M., Chen, Q., Hassan, M. M., Arslan, M., Hashim, M. M., Ahmad, W., Kutsanedzie, F. Y., Agyekum, A. A., 2020. An overview on the applications of typical non-linear algorithms coupled with NIR spectroscopy in food analysis. Food Engineering Reviews, 12, 173-190.

Zhan, T. L., Ng, C. W., Fredlund, D. G., 2007. Field study of rainfall infiltration into a grassed unsaturated expansive soil slope. Canadian Geotechnical Journal, 44(4), 392-408.

Zhang, J., Sun, D. a., Zhou, A., Jiang, T., 2015. Hydromechanical behaviour of expansive soils with different suctions and suction histories. Canadian Geotechnical Journal, 53(1), 1-13.

Zou, W.-l., Han, Z., Ding, L.-q., Wang, X.-q., 2021. Predicting resilient modulus of compacted subgrade soils under influences of freeze–thaw cycles and moisture using gene expression programming and artificial neural network approaches. Transportation Geotechnics, 28, 100520.

Zou, W.-l., Ye, J.-b., Han, Z., Vanapalli, S. K., Tu, H.-y., 2018. Effect of montmorillonite content and sodium chloride solution on the residual swelling pressure of an expansive clay. Environmental Earth Sciences, 77, 1-12.

Zumrawi, M. M., 2013. Pavement design for roads on expansive clay subgrades. University of Khartoum Engineering Journal, 3(1).

CHAPTER 5

PREDICTING THE COMPRESSION INDEX OF EXPANSIVE SOILS WITH HYBRID MACHINE LEARNING APPROACHES

5.1 Introduction[3]

Expansive soils are widely distributed over more than 40 countries worldwide posing significant challenges to the geotechnical engineers for the construction, design and maintenance of geo-infrastructures (Shi et al., 2003; Huang and Lizhou, 2007; Liu and Wang, 2023). These challenges primarily arise from the volume change behavior of expansive soils in response to moisture fluctuations which can lead to both swelling and shrinkage, resulting in ground heave and as well as settlement (Rao et al., 2001; Hou et al., 2013). Swelling upon water absorption causes ground heave, leading to distress of lightly loaded structures and pavements (Pandey et al., 2021), water supply network breakage (Azam et al., 2009), and instability of earth retaining structures (Han et al., 2024), while shrinkage during drying often results in desiccation cracks (Tang et al., 2021), leading to differential settlement in building foundations (Jones and Jefferson, 2012) and embankments (Zhang and Belmont, 2011). Although swelling-related issues have been widely documented, the settlement behavior of expansive soils under different loading conditions has received comparatively less attention, despite its crucial role in assessing the settlement of heavily loaded foundations and embankments in expansive soils.

[3] The contents presented in this chapter are published as a journal article: **Zhang, A.**, & Vanapalli, S. K. (2025). Predicting the compression index of expansive soils with hybrid machine learning approaches. *Engineering Application of Artificial Intelligence*, 162, 112579.

Table 5.1 Global annual expenditures related to expansive soils

Country	Annual costs (US Dollars)	References
China	$ 15 billion	(Abden et al., 2024)
USA	$ 11 billion	(Abden et al., 2024)
France	$ 3.5 billion	(Johnson, 1973)
Saudi Arabia	$ 300 million	(Ruwaih, 1987)
UK	$ 193 million	(Driscoll and Crilly, 2000)
Australia	$ 150 million	(Osman et al., 2005)
South Africa	$ 4 million	(Gourley et al., 2020)
Sudan	$ 6 million	(Charlie et al., 1984)

Table 5.1 presents an updated summary of estimated global economic losses associated with expansive soils, which amount to billions of dollars annually (Johnson, 1973; Charlie et al., 1984; Ruwaih, 1987; Al-Rawas et al., 1998; Driscoll and Crilly, 2000; Osman et al., 2005, Adem and Vanapalli, 2016; Gourley et al., 2020; Abden et al., 2024). These damages not only increase maintenance and repair costs but also likely compromise the long-term stability of geo-infrastructures constructed with or within expansive soils under many scenarios. Therefore, a reliable prediction of settlement and compressibility behavior is essential for improving the design and serviceability of various geo-infrastructures.

The compressibility behavior of expansive soils is influenced not only by external loading but also by their mineralogical composition and geological origin. The formation of expansive soils is predominantly by geological evolution that is influenced by long term climatic conditions (Wang et al., 2024). These soils predominantly constitute of clays minerals that include montmorillonite and illite. The depositional environment plays a critical role in the mineralogical characteristics and subsequent geotechnical behavior of expansive soils. Soils developed from lacustrine, marine, and alluvial deposits tend to

exhibit higher clay fractions and plasticity, which significantly affect their compressibility (Mitchell and Soga, 2005). In contrast, residual soils derived from the in-situ weathering of basalt, shale, or granite often demonstrate variable compressibility due to differences in mineral weathering stages (Blight, 1997; Al-Rawas and Goosen, 2006). The swelling properties of these soils, including swelling index, swelling pressure, and swelling potential, have been extensively studied (Fredlund, 1983; Dhowian, 1990; Vanapalli and Lu, 2012; Adem and Vanapalli, 2016; Tu and Vanapalli, 2016; Liu and Vanapalli, 2019; Dai et al., 2025). However, compared to their swelling characteristics, the compressibility of expansive soils has received limited attention, despite its critical role in settlement prediction information required for the design of foundations. The compressibility behavior of expansive soils is more complex than that of conventional clays, largely due to initiation and expansion of cracks (Dai et al., 2024). Over prolonged drying periods or repeated wetting-drying cycles, expansive soils tend to develop fissures, which, under loading, close before significant compression occurs, resulting in a high compressibility (Holtz et al., 1981; Mitchell and Soga, 2005; Zhou et al., 2024). Moreover, expansive soils from different geological periods exhibit varying consolidation behaviors. For instance, Quaternary lacustrine clays often show higher compressibility due to their relatively young depositional age and weaker diagenetic processes, while older Tertiary deposits may exhibit preconsolidation effects resulting from geological loading and cementation (Culshaw et al., 1991). These factors collectively suggest that expansive soils exhibit significantly variable compressibility patterns compared to conventional clays, underscoring the need for further investigation to improve prediction models and propose rational strategies for engineering design.

The compression index (C_c) is a key parameter for assessing soil compressibility, directly influencing settlement calculations and design of foundations. Conventionally, C_c is determined from consolidation test results (Zhou et al., 2024). However, due to the low coefficient of permeability of expansive soils, these tests are often time-consuming, require trained personnel and are costly, which is approximately US 2000 dollars per test, making them less practical for use in low to medium cost geotechnical engineering projects (Alptekin and Taga, 2019; Tavakkoli et al., 2024). In addition, there are additional costs

associated with gathering high quality undisturbed samples required from site investigations. As an alternative, researchers have developed empirical equations to estimate C_c based on soil properties such as void ratio, dry density, water content, liquid limit, and plasticity index (Terzaghi and Peck, 1967; Sridharan and Nagaraj, 2000; Yukselen-Aksoy et al., 2008; Vinod and Bindu, 2010; Tiwari and Ajmera, 2012; Akbarimehr et al., 2021). While these early empirical correlations represent important milestones for predicting compression index, C_c, they were predominantly developed for conventional clays. For this reason, they are not useful and have limitations when extended to expansive soils. As a result, despite their pioneering nature, these relationships are not capable of reliably predicting the C_c of expansive soils. This limitation has motivated recent research using advanced modeling techniques.

In recent years, machine learning (ML) has been increasingly applied to the prediction of the C_c for various types of clays. This approach can capture complex nonlinear relationships, reduce reliance on experimental testing, and achieve greater prediction accuracy compared to empirical correlations (Park and Lee, 2011; Shi and Gao, 2013; Benbouras et al., 2019; Mohammadzadeh S et al., 2019; Pham et al., 2019; Bardhan et al., 2022; Díaz and Spagnoli, 2024; Uzer, 2024; Yang et al., 2025). However, research applying ML approaches to predict the C_c of expansive soils remains scarce, with only a few studies in recent years exploring this direction. For instance, Alnmr et al. (2024) employed symbolic regression to predict the C_c of expansive soil-sand mixtures. However, only one expansive soil type was considered, limiting the diversity of soil types examined. Similarly, Vamsi Nagaraju et al. (2020) applied the Invasive Weed Optimization (IWO) and Particle Swarm Optimization (PSO) algorithms combined with multiple linear regression to predict the C_c of lime-treated expansive soils. Their approach relied on parameters such as I_p, free swell index, rate of heave, and swell potential which require input parameters that are not easily obtainable in practical applications. Current research on predicting the C_c of expansive soils has primarily focused on chemically treated samples, with less emphasis on natural, untreated expansive soils. Additionally, the limited diversity of soil types in existing databases and the challenges in achieving high predictive accuracy may affect the broader applicability of these models.

The statistical correlations for conventional clays may not reliably capture the compressibility characteristics of expansive soils. Most of the ML studies published in the literature focus on chemically treated expansive soil samples or with limited datasets; due to this reason, their general applicability across different types of expansive clays is not good.

To address these gaps, this study focuses on the relatively underexplored task of predicting the C_c of expansive soils and introduces four distinct innovations: (i) development of an advanced model using Newton-Raphson-Based Optimizer optimized Extreme Gradient Boosting (NRBO-XGBoost), (ii) development of a comprehensive database and modeling framework, (iii) proposal of a simplified prediction equation derived from the Multilayer Perceptron (MLP) model, and (iv) demonstration of the practical applicability of the proposed approaches through engineering case studies.

First, an advanced ML model was developed using NRBO-XGBoost, in which the XGBoost algorithm is optimized through the Newton-Raphson-Based Optimizer (NRBO). NRBO improves search efficiency and accelerates convergence using the Newton-Raphson Search Rule (NRSR). The Trap Avoidance Operator (TAO) helps prevent entrapment in local optima. These mechanisms enhance parameter tuning, resulting in improved model accuracy, stability, and generalization capability. Compared to conventional ML methods, NRBO-XGBoost (Model 2) demonstrates superior performance in capturing complex nonlinear relationships.

Second, a comprehensive modeling framework was established. Seven ML models based on five algorithms were trained and validated with a large-scale database of 238 expansive soil samples compiled from nearly 60 years of published studies. These include two models developed using NRBO-XGBoost (Model 1 and Model 2), two using the MLP algorithm (Model 3 and Model 4), and one model each using Support Vector Regression (SVR) (Model 5), Extreme Learning Machine (ELM) (Model 6), and Multivariate Adaptive Regression Splines (MARS) (Model 7). This diverse modeling setup facilitates comparative evaluation and highlights the relative effectiveness of different algorithms in predicting the C_c of expansive soils.

Third, a simplified prediction equation derived from the MLP algorithm (Model 4) is proposed. This equation enables convenient estimation of the compression index using basic soil properties, making it suitable for routine geotechnical engineering practice without the need to implement ML code.

Fourth, the practical applicability of the proposed approaches is validated through three engineering case studies, which demonstrate the applicability of the simplified equation in real-world conditions and provide an additional layer of verification. Unlike many ML studies that remain limited to presenting prediction outcomes through graphical comparisons, these case studies bridge the gap between model development and practical engineering applications.

5.2 Database establishment

5.2.1 Selection of input parameters

The selection of input parameters for the machine learning models was guided by two main considerations: (i) their well-established correlations with the compression index in the literature, (ii) their availability and ease of measurement using simple laboratory tests.

Previous studies in the literature have established a strong correlation between the compression index and fundamental soil properties, including liquid limit (LL), plasticity index (I_p), initial void ratio (e_0), dry density (ρ_d), clay content (C), water content (w), and specific gravity (G_s) (Mayne, 1980; Rendon-Herrero, 1980; Koppula, 1981; Terzaghi et al., 1996; Sridharan and Nagaraj, 2000; Tiwari and Ajmera, 2012; Kumar et al., 2016; Zaman et al., 2016; Gao et al., 2019). As key Atterberg limits, the liquid limit and plasticity index information can be valuable for providing reasonable relationships for estimating the soil compressibility. The liquid limit represents the water content at which soil begins to flow, affecting its moisture retention and compressibility (Al-Khafaji and Andersland, 1992). The plasticity index defines the range of plastic deformation in clay and exhibits a positive correlation with the compression index, indicating that highly plastic soils tend to undergo greater consolidation deformation (Ibrahim et al., 2012). Clay content and water content

jointly influence soil compressibility. Higher clay content indicates a finer particle size, larger specific surface area, and greater water absorption capacity, making the soil more susceptible to particle rearrangement and deformation under loading (Mitchell and Soga, 2005). Additionally, higher water content reduces interparticle friction, further facilitating deformation under stress, thereby increasing the compression index. Initial void ratio and dry density reflect soil compactness and have opposing effects on compressibility. A higher void ratio provides more pore space, allowing greater compression, while higher dry density indicates a tighter structure with less compressibility. Specific gravity represents particle density, with lower values, as seen in highly plastic expansive clays, corresponding to less dense structures that are susceptible to greater deformation, leading to a higher compression index.

Apart from these fundamental properties, other factors can influence the compression index. One such factor is the preconsolidation pressure, which reflects the stress history of the soil and has an impact on its compressibility (Mitchell and Soga, 2005). A higher preconsolidation pressure typically indicates that the soil has undergone greater historical loading, resulting in lower compressibility. However, similar to the compression index itself, preconsolidation pressure is generally obtained through consolidation tests, which are time-consuming, costly, and impractical for routine geotechnical investigations. Furthermore, its effect is partially represented by other soil parameters, such as the initial void ratio and dry density, which capture aspects of soil compactness and stress history (Imhoff et al., 2004; Kayabali and Demir, 2011). Therefore, preconsolidation pressure was excluded from the input parameters to enhance the practical applicability of the proposed machine learning models to enhance model generalizability and ensure that only parameters easily obtainable in simple laboratories and practice were used.

The basic soil properties, (i.e., LL, I_p, e_0, ρ_d, C, w, G_s) were selected as primary input parameters in the machine learning models based on the relationship between and compression index. In this study, a dataset of 238 expansive soil samples with these parameters available were gathered on expansive from around the world and compiled. More detailed information about the dataset is provided in Table 5.2.

Table 5.2 Summary of soil properties used for predicting the compression index of expansive soils

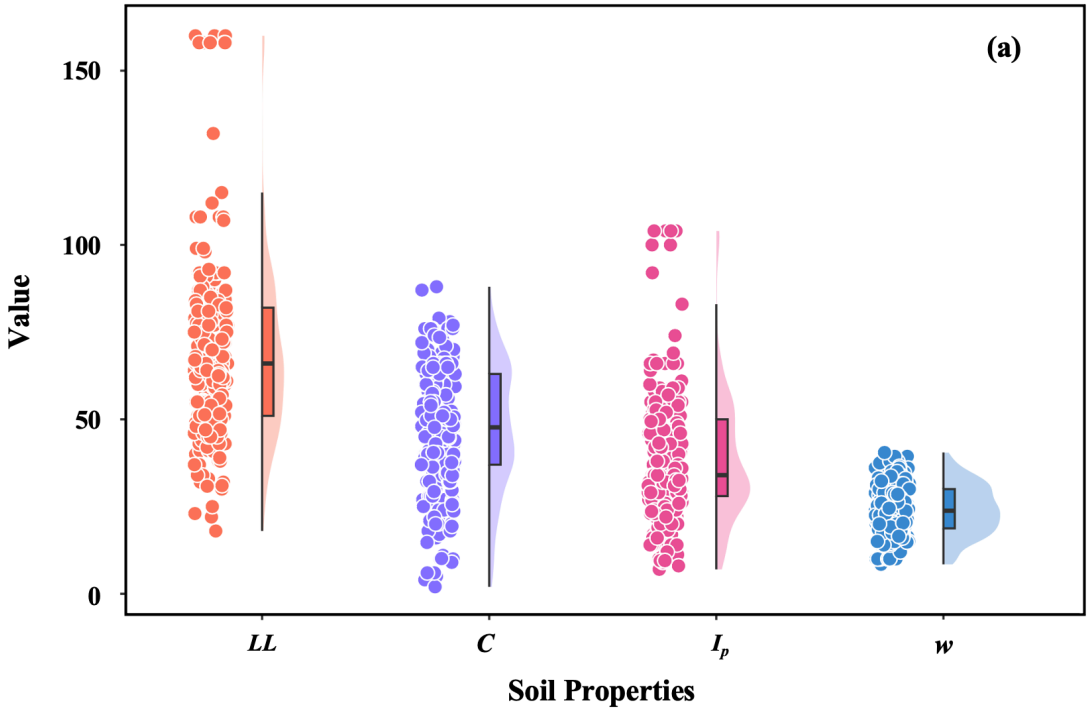
Soil property	LL	I_p	C	w	e_0	ρ_d	G_s	C_c
Max	160	107	88	50.2	1.61	2.00	2.88	0.590
Min	28	17	12	8.5	0.34	1.00	2.54	0.138
Ave	69	39	47	24.6	0.88	1.56	2.71	0.271
Med	66	35	48	23.9	0.88	1.59	2.70	0.260
SD	27	19	18	7.8	0.25	0.20	0.07	0.074
Q1(25%)	51	28	37	18.8	0.70	1.42	2.66	0.196
Q3(75%)	82	50	63	30.0	1.07	1.74	2.76	0.339
Qty	238	238	238	238	238	238	238	238

Note: LL is liquid limit, I_p is plasticity index, C is clay content, w is gravimetric water content, e_0 is initial void ratio, ρ_d is dry density, G_s is specific gravity, C_c is compression index

In summary, the expansive soil samples in the database originate from diverse geological settings. Lacustrine, marine, and residual formations are represented among the samples. Identified parent materials include shale, marl, basalt, and claystone. The dataset includes samples associated with Quaternary and Tertiary geological periods, as reported in the literature. The database incorporates data from Asia, North America, the Middle East, Africa, South America, and Australia, providing a geologically diverse and globally representative foundation for model development.

5.2.2 Outlier detection

Outlier detection is an essential step in data preprocessing, as extreme values can significantly affect the accuracy and reliability of models for prediction, potentially leading to misinterpretations of soil behavior. This study employs a modified violin plot (Fig. 1), referred to as a cloud-rain plot, to analyze the distribution of key soil properties, including liquid limit, plasticity index, clay content, water content, specific gravity, dry density, initial void ratio, and compression index. The cloud-rain plot integrates the strengths of scatter plots, violin plots, and box plots. Scatter points provide a direct visualization of raw data, facilitating the identification of potential outliers. The violin plot's density estimation reveals overall distribution trends, highlighting skewness or multimodal characteristics. Meanwhile, the box plot illustrates quartile ranges, median values, and potential outliers, offering insights into data variability.



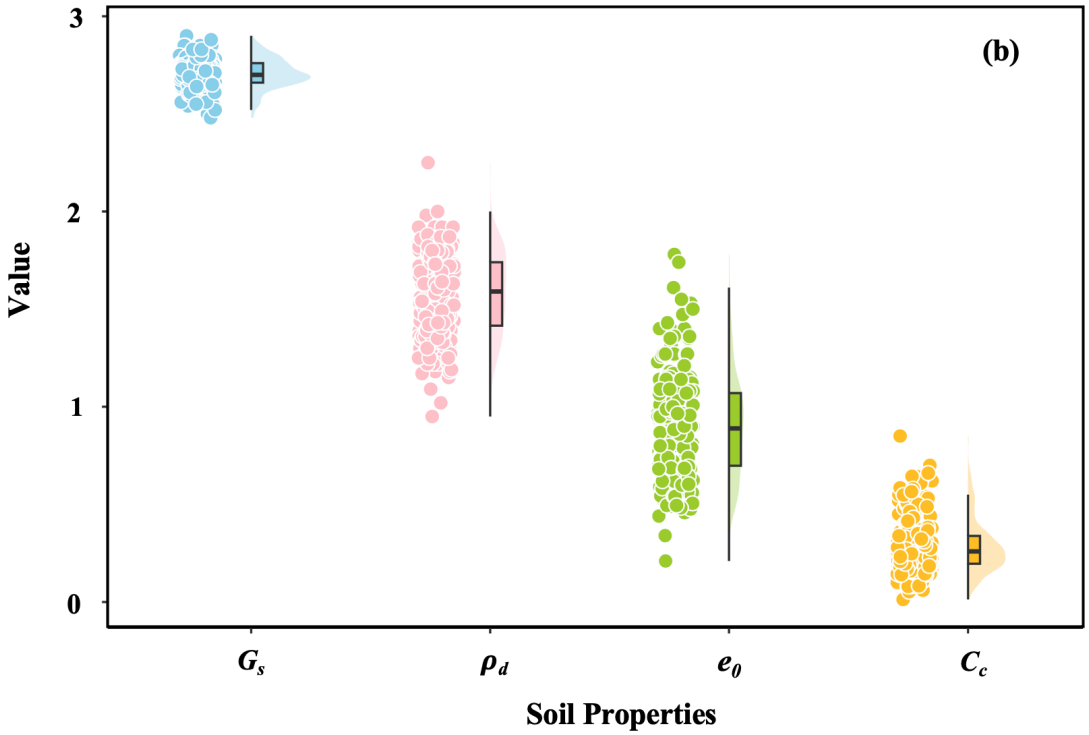


Fig. 5.1 Cloud-rain plot for outlier detection (a) Liquid limit (*LL*), clay content (*C*), plasticity index (I_p), and water content (w); (b) Specific gravity (G_s), dry density (ρ_d), initial void ratio (e_o), and compression index (C_c)

The results show that liquid limit and plasticity index exhibit a wide distribution, with some high-value samples corresponding to highly plastic soils, such as Al-Qatif expansive soil in Saudi Arabia, which naturally exhibit distinct consolidation and swelling characteristics (Al-Mahbashi et al., 2021). Similarly, water content and compression index contain a few extreme values, reflecting the inherent variability in the compressibility of expansive soils (Azam, 2003). However, these values remain within an expected range and align with the anticipated behavior of such soils. In contrast, specific gravity, clay content, initial void ratio, and dry density display more compact distributions with no significant outliers. A few extreme values exist; however, they fall within the expected variability of expansive soils and are unlikely to compromise the reliability of the proposed prediction models.

5.2.3 Correlation analysis of input soil properties

To develop reliable prediction models while maintaining computational efficiency, it is essential to select input parameters that provide meaningful information about soil compressibility. Retaining weakly correlated variables can introduce noise and increase model complexity, making it more challenging to capture the fundamental relationships between compression index and other soil properties. Conversely, removing key parameters that are strongly related to compression index may lead to information loss and reduced model performance. Thus, a rational approach is required to determine the most relevant parameters for modeling. Correlation analysis was conducted to determine the key parameters influencing soil compressibility. A correlation matrix, visualized using a pairwise correlation plot (Fig. 5.2), was used to examine the relationships among the selected soil properties. This visualization integrates scatter plots to illustrate pairwise trends, histograms to provide an overview of data distribution, and a heatmap to quantify the strength and direction of correlations.

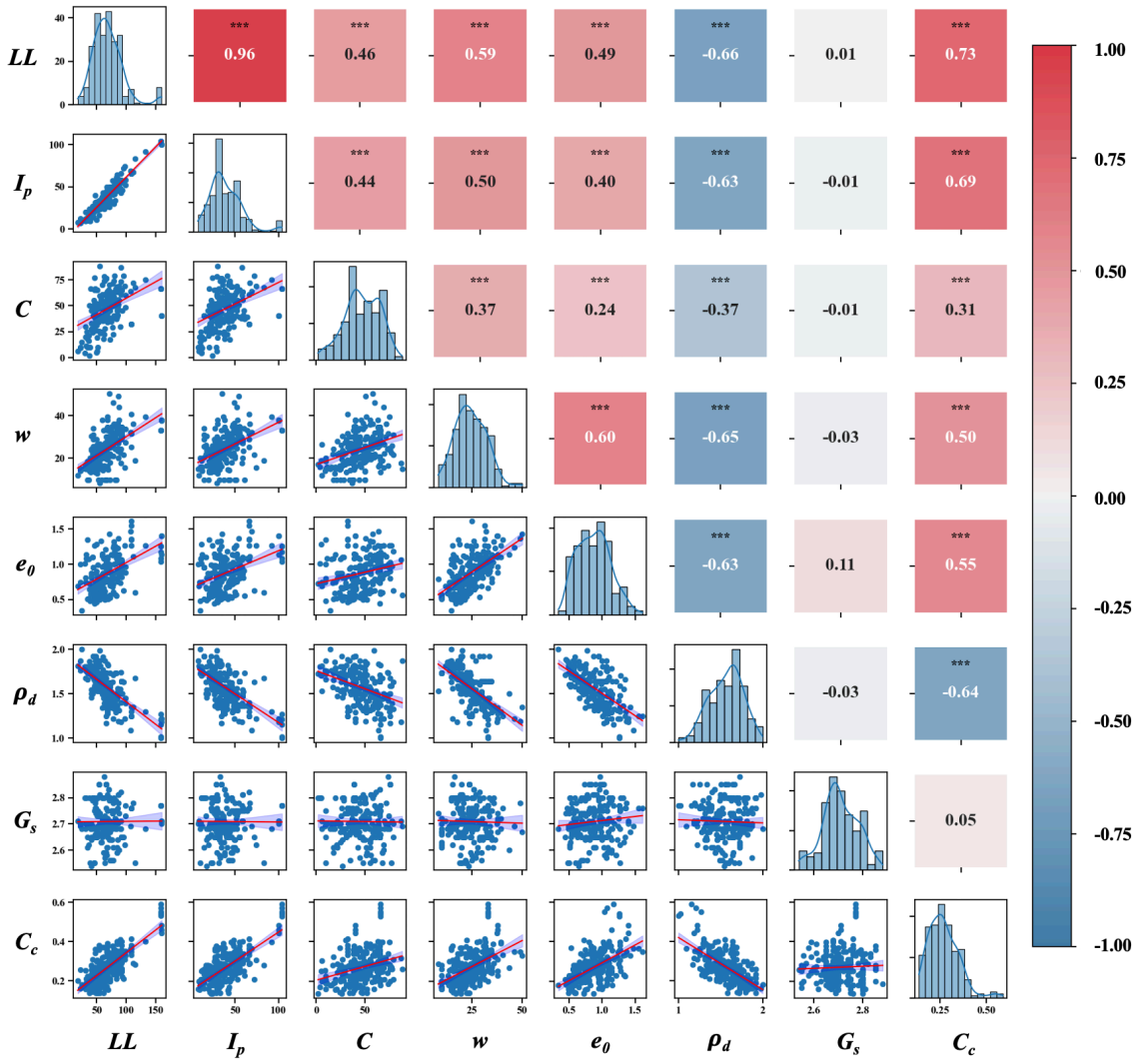


Fig. 5.2 Correlation matrix and pairwise scatter plots among soil variables and compression index

The results reveal a strong correlation between the liquid limit (r = 0.73), plasticity index (r = 0.69), and compression index, highlighting their significant influence on soil compressibility. Additionally, the initial void ratio (r = 0.55) exhibits a moderate positive correlation with the compression index, underscoring the role of soil structure in consolidation behavior. Conversely, dry density (r = -0.64) shows a notable negative correlation, suggesting that higher soil compactness generally leads to lower compressibility. Other soil properties exhibit relatively weaker correlations (|r|< 0.5), which suggests that they are less influential in predicting the C_c. This classification of

correlation strength follows the guidelines suggested by Chen (2022), where $|r| \geq 0.8$ indicates a very strong correlation, $0.6 \leq |r| < 0.8$ moderately strong, and $|r| < 0.5$ weak to fair. The interpretation of Pearson's correlation coefficient (r), along with other evaluation metrics, is further detailed in Section 5.3.4.

To evaluate the effect of parameter selection, machine learning models were developed using two input sets: one with all seven selected soil properties and another with the four most influential parameters; namely, liquid limit, plasticity index, initial void ratio, and dry density. This comparison provides insights into how parameter selection impacts model performance while maintaining a balance between the prediction accuracy and their interpretability.

5.2.4 Data splitting

To ensure both robust model training and reliable performance evaluation, the dataset of 238 expansive soil samples was randomly divided into training and testing subsets in an 80%–20% ratio, a commonly followed and well accepted practice in machine learning. This partitioning strategy ensured sufficient data for model training while preserving an adequate portion for independent testing.

5.3 Methodology

Recent studies have shown that advanced AI-based methods, such as gene expression programming (Krzywanski et al., 2025) and fuzzy logic-based models (Krzywanski et al., 2024), can effectively capture nonlinear and complex behaviors. These behaviors are typically encountered in engineering practice applications, where conventional empirical approaches are not suitable. For alleviating such limitations in geotechnical applications, Ding and El-Zein (2024) demonstrated that deeper neural network architectures can significantly improve the prediction of soil water retention curves, highlighting the importance of model design and input selection. Similarly, Wang and Vanapalli (2025) developed a hybrid ML framework integrating PSO-SVR and MGGP to estimate matric suction in compacted fine-grained soils, introducing the novel parameter "effective degree

of aggregation" to better represent soil structure. Collectively, these studies illustrate the growing role of advanced ML in soil behavior modeling. Building on these advances, this study investigates hybrid machine learning approaches for predicting the compression index of expansive soils.

To this end, the methodology adopted in this study involves developing seven models with five different algorithms, aiming to balance complexity, prediction capability, and interpretability in predicting the C_c of expansive soils. The algorithms include the (i) Newton-Raphson-Based Optimizer optimized Extreme Gradient Boosting (NRBO-XGBoost), (ii) Multilayer Perceptron (MLP), (iii) Support Vector Machine (SVM), (iv) Extreme Learning Machine (ELM), and (v) Multivariate Adaptive Regression Splines (MARS). NRBO-XGBoost and MLP were selected as the primary models due to their advanced learning capabilities, while SVM, ELM, and MARS were used as baseline models to provide comparative analysis.

5.3.1 Newton-Raphson-Based Optimizer Enhanced Extreme Gradient Boosting

Extreme Gradient Boosting (XGBoost) is a widely used machine learning algorithm known for its efficiency and predictive power. It is based on gradient boosting, where decision trees are sequentially constructed to minimize the residual error from previous iterations. The model optimization process involves minimizing a loss function while incorporating regularization terms to control model complexity and prevent overfitting.

At each boosting iteration, XGBoost constructs a new tree to fit the negative gradient of the loss function with respect to the model's predictions. The optimization process relies on the second-order Taylor expansion of the loss function, enabling the model to utilize both first-order gradients and second-order Hessians for more stable and accurate updates. The tree structure is determined by splitting rules that maximize the gain in objective reduction, while leaf weights are optimized to minimize the loss.

During the optimization process, XGBoost essentially seeks to minimize the loss function. In the t th iteration, its objective function can be written as:

$$\text{Obj}^{(t)} = \sum_{i=1}^{n} \ell\left(y_i, \hat{y}_i^{(t-1)} + f_t(x_i)\right) + \Omega(f_t) \tag{5.1}$$

where y_i the true label of sample, $\hat{y}_i^{(t-1)}$ is the accumulated prediction of the model up to iteration t-1, $f_t(x_i)$ is the prediction contribution from the t th tree for sample xi, ℓ is the loss function, and $\Omega(f_t)$ is the regularization term that controls the complexity of the tree.

To efficiently optimize the objective function, XGBoost employs a second-order Taylor expansion. This approximation allows the model to incorporate both the first-order gradient (representing the direction of improvement) and the second-order Hessian (capturing curvature information), leading to more stable and accurate updates. The expanded objective function is given by:

$$\text{Obj}^{(t)} \approx \sum_{i=1}^{n} \left[\ell\left(y_i, \hat{y}_i^{(t-1)}\right) + g_i f_t(x_i) + \frac{1}{2} h_i f_t(x_i)^2\right] + \Omega(f_t) \tag{5.2}$$

where g_i is first derivative (gradient) and h_i is the second derivative (Hessian).

In each iteration, XGBoost optimizes the structure of decision trees by aggregating the first-order gradient G_j and the second-order Hessian H_j for each leaf node j. The regularization term is defined as:

$$\Omega(f_t) = \gamma T + \frac{1}{2}\lambda \sum_{j=1}^{T} w_j^2 \tag{5.3}$$

where T is the total number of leaf nodes, λ is the regularization parameter, and w_j represents the weight of leaf j.

The objective function over all leaves is then approximated as:

$$\text{Obj}^{(t)} \approx \sum_{j=1}^{T} \left[w_j + \frac{1}{2}(H_j + \lambda) w_j^2 \right] + \gamma T \tag{5.4}$$

To determine the optimal leaf weights, the derivative with respect to w_j is set to zero:

$$G_j + (H_j + \lambda) w_j = 0 \Longrightarrow w_j^* = -\frac{G_j}{H_j + \lambda} \tag{5.5}$$

where w_j^* is the optimal weight for leaf j. Substituting w_j^* back into the objective function, we obtain the minimized objective:

$$\text{Obj}^{(t)}(w^*) = -\frac{1}{2} \sum_{j=1}^{T} \frac{G_j^2}{H_j + \lambda} + \gamma T \tag{5.6}$$

This optimization process ensures that XGBoost efficiently determines the best leaf values while maintaining model regularization, improving both predictive accuracy and generalization ability.

While XGBoost efficiently optimizes its structure, its predictive performance is highly dependent on hyperparameter selection. The compression index of expansive soils is influenced by multiple physical parameters with complex, nonlinear relationships. Traditional hyperparameter optimization methods, such as grid search and Bayesian optimization, struggle with high-dimensional search spaces and often suffer from computational inefficiency and local optima entrapment.

In this study, the emerging and powerful Newton-Raphson-Based Optimizer (NRBO), proposed by Sowmya et al. (2024), was employed to fine-tune the hyperparameters of the XGBoost model for predicting the compression index of expansive soils. NRBO was selected for its efficient global search capability and its effectiveness in handling high-dimensional, nonlinear optimization problems commonly encountered in geotechnical and geological engineering applications. Compared to conventional methods, such as grid

search and Bayesian optimization, NRBO achieves faster convergence and reduces the likelihood of selecting hyperparameters that result in unreasonable or physically inconsistent predictions.

The algorithm incorporates several key mechanisms, including population initialization, the Newton-Raphson Search Rule (NRSR), adaptive step size adjustment, position updating strategies, and the Trap Avoidance Operator (TAO). These components work in combination to balance global exploration and local exploitation during the optimization process, improving the robustness, accuracy, and stability of the hyperparameter tuning. By integrating NRBO with XGBoost, the resulting NRBO-XGBoost model demonstrates superior predictive performance and enhanced generalization capability in modeling the complex relationships between the compression index and the properties of expansive soils.

Initially, the algorithm generates a population of candidate solutions uniformly distributed within the feasible design space. This step ensures a diverse distribution of solutions in the search space. The position of each candidate in the population is determined using the following expression:

$$x_n^j = lb_j + \text{rand}\,(0,1) \times \left(ub_j - lb_j\right) \tag{5.7}$$

where lb_j and ub_j are the lower and upper bounds for the j-th decision variable, and rand(0,1) represents a random number between 0 and 1.

The core mechanism of NRBO is the NRSR, which guides the search direction and magnitude based on the positions of the best and worst individuals in the population. Instead of relying on exact derivatives, NRSR estimates the search step using the following equation:

$$NRSR = randn \times \frac{(X_w - X_b) \cdot \Delta x}{2(X_w + X_b - 2X_n)} \tag{5.8}$$

where $randn$ is a random number drawn from a standard normal distribution; X_w and X_b are the positions of the worst and best individuals in the population, respectively; X_n is the position of the current individual; and Δx is the step size vector that controls the extent of the search.

The step size Δx, which determines the scale of exploration, is computed by:

$$\Delta x = rand(1, dim) \times |X_b - X_n| \tag{5.9}$$

where $rand(1, dim)$ is a vector of uniformly distributed random values between 0 and 1, with a length equal to the problem dimension; and $|X_b - X_n|$ represents the absolute difference between the best solution and the current individual.

The updated position of individual is calculated by incorporating both the influence of the best solution and the differences between two randomly selected individuals from the population:

$$X_n^{new} = X_n - NRSR + a(X_b - X_n) + b(X_{r1} - X_{r2}) \tag{5.10}$$

where *a* and *b* are uniformly distributed random scalars within [0, 1]; X_{r1} and X_{r2} are two randomly selected individuals from the population, distinct from X_n.

To avoid stagnation in local optima, NRBO employs a TAO. When a randomly generated number is less than a predefined threshold, the individual's position is further perturbed according to the following equation:

$$X_{TAO}^{IT} = X_n^{IT+1} + \theta_1(\mu_1 X_b - \mu_2 X_n^{IT}) + \theta_2 \delta(\mu_1 \text{Mean}\,(X^{IT}) - \mu_2 X_n^{IT}) \tag{5.11}$$

where θ_1 and θ_2 are random weights in the range [0, 1]; μ_1 and μ_2 are control parameters, typically set to 0 or 1; Mean (X^{IT}) represents the average position of all individuals in the population at iteration IT; and δ is an adaptive factor controlling the perturbation amplitude.

The adaptive factor δ decreases over time to balance exploration and exploitation, and is calculated as:

$$\delta = \left(1 - \frac{2 \cdot IT}{MaxIT}\right)^5 \tag{5.12}$$

where IT is the current iteration number; and $MaxIT$ is the maximum number of iterations.

The overall modelling framework of the NRBO-XGBoost algorithm is illustrated in Fig. 5.3. It consists of three main stages: data collection, data preprocessing, and model development. In the first stage, basic soil properties are collected as input parameters, with the compression index defined as the prediction target. During data preprocessing, outlier detection, feature selection, normalization, and data splitting are performed to ensure data quality and consistency. The modelling process begins with training an initial XGBoost model, followed by hyperparameter optimization using the NRBO. The optimized model is validated through K-fold cross-validation. If the predefined performance criteria ($R^2 > 0.9$ and RMSE < 0.04) are satisfied, the final NRBO-XGBoost model is established; otherwise, the optimization continues. This iterative framework ensures that the model achieves both high prediction accuracy and good generalization in estimating the compression index of expansive soils.

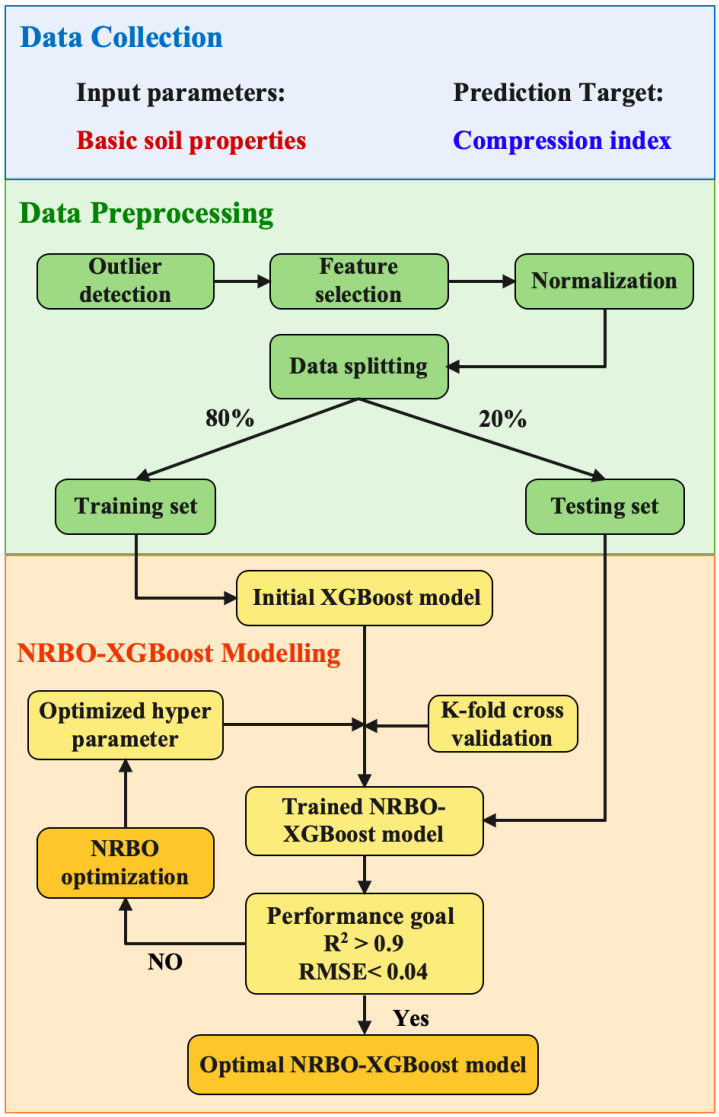


Fig. 5.3 Flowchart of NRBO-XGBoost modelling process

5.3.2 Multilayer Perceptron

In this study, in addition to employing the NRBO-XGBoost algorithm to develop the primary prediction model, a Multilayer Perceptron (MLP) model was introduced as a supplementary tool to derive a simplified prediction formula for practical engineering applications. As a type of feedforward Artificial Neural Network (ANN), the MLP has been widely applied in geotechnical engineering due to its ability to capture complex nonlinear relationships. It is particularly effective in predicting the engineering properties

of expansive soils, which exhibit highly nonlinear hydro-mechanical behavior. The adoption of the MLP provides a reliable and efficient approach for developing stable prediction models suited to such complex geomaterials.

The MLP network consists of three main components: an input layer, one or more hidden layers, and an output layer. The input layer receives the initial variables required by the model, typically including basic physical and mechanical properties of the soil. These inputs are transmitted to the hidden layers, where neurons perform weighted summations and process signals through nonlinear activation functions, such as the hyperbolic tangent (tansig) or rectified linear unit (ReLU) (Ding and El-Zein, 2024). This process enables the extraction of complex feature interactions among variables. After multiple transformations, the data reaches the output layer, which produces the final predicted value.

The relationship between the input and output variables can be mathematically expressed by the standard forward propagation equation of the MLP, as shown in Eq. (5.13).

$$y = \sum_{j=1}^{M} \left[\omega_j^P f\left(\sum_{i=1}^{N} x_i \omega_{ij}^I + b_j^I \right) \right] + b^P \tag{5.13}$$

where, x_i is the i^{th} input parameter, y is the target parameter,ω_{ij}^I are the weights assigned to input parameters, ω_j^P are the weights assigned for the output layer, b_j^P is the bias for the j^{th} hidden layer, b^P is the bias for the output layer, f is the activation functions, N is the number of input parameters, M is the number of hidden layers.

This formulation illustrates the nonlinear mapping mechanism, where input data undergoes weighted summation, bias adjustment, and nonlinear activation before being aggregated to generate the output prediction.

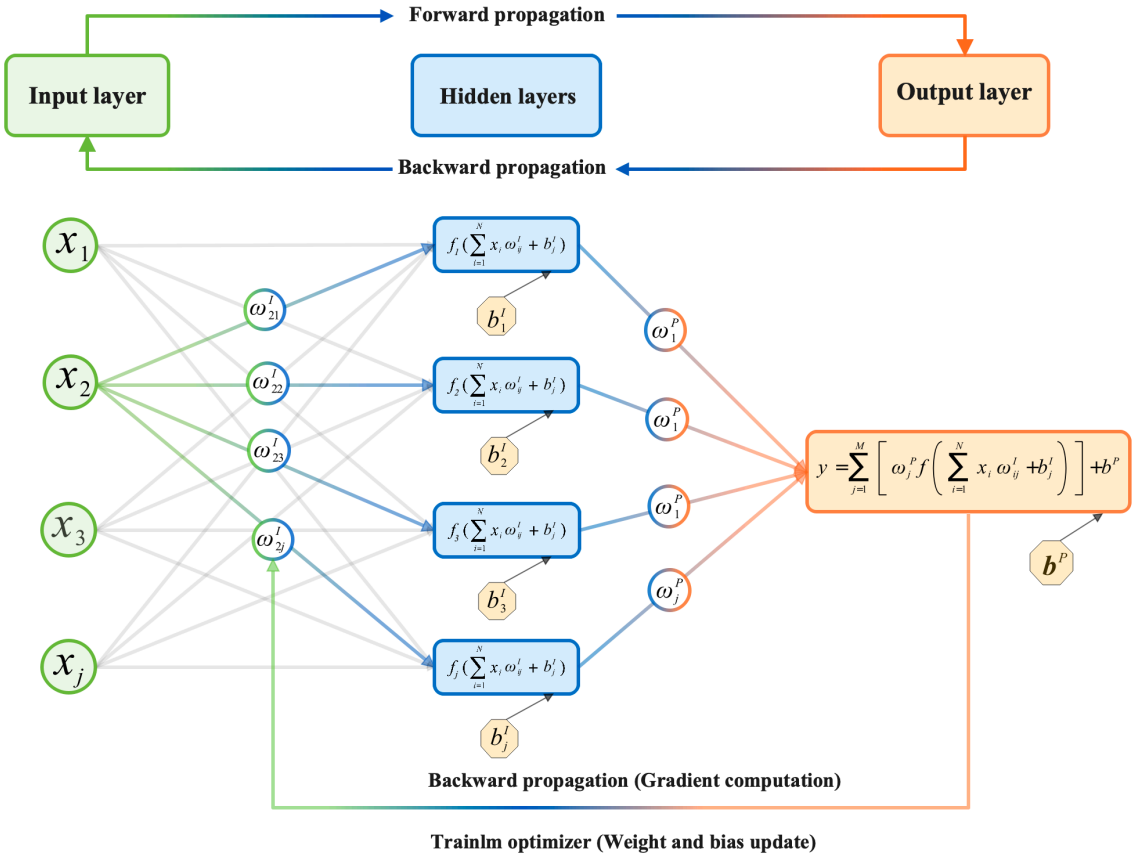


Fig. 5.4 The principle and flowchart of MLP algorithm

As illustrated in Fig. 5.4, the training of the MLP involves two main stages: forward propagation and backward propagation. During forward propagation, data flows sequentially through the network layers to compute the predicted output. The prediction error, typically measured by the mean squared error (MSE), is then calculated by comparing the predicted and observed values. In the backward propagation stage, gradients of the loss function are computed via the chain rule and propagated backward through the network to iteratively update the connection weights and biases, aiming to minimize prediction errors and improve model performance.

To enhance the optimization process, the Levenberg-Marquardt (trainlm) algorithm was employed in this study. Combining the advantages of gradient descent and the Gauss-Newton method, trainlm significantly improves convergence speed and helps avoid entrapment in local minima. Compared with traditional first-order optimization algorithms,

it leverages an approximate Hessian matrix to increase the precision and efficiency of parameter updates. This makes the MLP model particularly suitable for geotechnical applications where experimental data is limited due to the high cost and complexity of testing.

5.3.3 Other conventional algorithms

In addition to the two primary models (NRBO-XGBoost and MLP), three conventional machine learning algorithms—Support Vector Machine (SVM), Extreme Learning Machine (ELM), and Multivariate Adaptive Regression Splines (MARS)—were employed in this study. These algorithms were selected to provide benchmark models for comparative analysis. Given the moderate sample size of the dataset (238 samples), they are well-suited for evaluating the relative performance of the proposed advanced models.

Support Vector Regression (SVR), derived from SVM, is a supervised learning algorithm based on statistical learning theory. It is specifically designed for regression tasks and operates by mapping input data into a high-dimensional feature space through kernel functions. SVR constructs an optimal regression function by minimizing prediction errors within a specified margin of tolerance, known as the ε-insensitive loss function. By following the principle of structural risk minimization, SVR effectively balances model complexity and prediction accuracy, enhancing its generalization capability on unseen data (Basak et al., 2007; Awad et al., 2015).

Extreme Learning Machine (ELM) is a single hidden layer feedforward neural network that differs from traditional neural networks in its training process. In ELM, the input weights and biases of the hidden layer neurons are randomly assigned and remain fixed, while only the output weights are determined through a simple analytical solution, typically using least squares. This process significantly reduces training time and simplifies the learning algorithm, making it efficient for regression tasks on moderate-sized datasets (Huang et al., 2004; Henríquez and Ruz, 2017).

Multivariate Adaptive Regression Splines (MARS) is a non-parametric regression technique that models complex nonlinear relationships using piecewise linear basis

functions. MARS automatically partitions the input space by identifying optimal knots and fits separate linear regressions within each region. The algorithm uses a two-step process consisting of forward selection, which adds basis functions to improve model fit, and backward elimination, which prunes the model to avoid overfitting. This method provides a flexible framework for capturing variable interactions and nonlinearities in the data (Friedman, 1991; España et al., 2024).

A comprehensive summary of the advantages and limitations of each algorithm employed in this study is presented in Table 5.3.

Table 5.3 Summary of the advantages and limitations of the employed machine learning algorithms

Algorithms	Models	Advantage	Limitation
NRBO-XGBoost	Model 1 Model 2	Superior predictive accuracy Enhanced global optimization capability Mitigates local optima and overfitting	Relatively time-consuming
MLP	Model 3 Model 4	Captures complex nonlinear relationships Efficient for practical applications	Prone to overfitting and requires tuning
SVR	Model 5	Good generalization on small datasets	Kernel and parameter sensitivity
ELM	Model 6	Extremely fast training	Unstable predictions
MARS	Model 7	Automatic feature selection	Discontinuous and non-smooth predictions

5.3.4 Evaluation indexes

The prediction performance of the developed models was evaluated using four commonly applied statistical indicators, as shown in Eqs. (5.14) - (5.17): the Pearson correlation coefficient (r), the coefficient of determination (R^2), the root mean square error (RMSE), and the normalized root mean square error (NRMSE). The parameters r and R^2 assess the

correlation and goodness of fit between the predicted and measured values, respectively (Gong et al., 2024), while RMSE and NRMSE quantify the magnitude of prediction errors. Among them, NRMSE provides a relative measure of error by normalizing RMSE with respect to the mean of the observed data, enabling comparison across different datasets or units.

$$r = \frac{\sum_{i=1}^{N} (O_i - \bar{O}_i) \cdot (P_i - \bar{P}_i)}{\sqrt{\sum_{i=1}^{N} (O_i - \bar{O}_i)^2 \cdot \sum_{i=1}^{N} (P_i - \bar{P}_i)^2}} \tag{5.14}$$

$$R^2 = \left(\frac{\sum_{i=1}^{N} (O_i - \bar{O}_i) \cdot (P_i - \bar{P}_i)}{\sqrt{\sum_{i=1}^{N} (O_i - \bar{O}_i)^2 \cdot \sum_{i=1}^{N} \left(P_i - \bar{P}_i\right)^2}} \right)^2 \tag{5.15}$$

$$RMSE = \sqrt{\frac{1}{N} \sum_{i=1}^{N} (O_i - P_i)^2} \tag{5.16}$$

$$NRMSE = \frac{\sqrt{\frac{1}{N} \sum_{i=1}^{N} (O_i - P_i)^2}}{\bar{O}} \tag{5.17}$$

where O_i and P_i refer to the individual measured and predicted values, respectively; $\overline{O}_i$ and $\overline{P}_i$ represent the average values of the measured and predicted datasets and N is the total number of samples considered in the analysis.

5.4 Modelling results and analysis

This section presents the modelling results and performance analysis of five predictive models for estimating the compression index of expansive soils. The models include NRBO-XGBoost, MLP, SVR, ELM, and MARS. Two different input combinations were considered to evaluate the influence of feature selection on model performance. The

analysis focuses on prediction accuracy, generalization capability, and model simplicity. In addition, a detailed residual analysis is provided to further assess the predictive reliability of each model.

5.4.1 NRBO-XGBoost models

The prediction performance of the NRBO-XGBoost model for estimating the compression index is shown in Fig. 5.5 and Fig. 5.6. Two sets of input parameters were considered in this study to explore the impact of feature selection on model performance. One model was developed using all seven selected soil properties, while the other used only the four most influential parameters, consistent with the earlier summarized discussion (i.e., liquid limit, plasticity index, initial void ratio, and dry density). This comparison helps to evaluate the balance between prediction accuracy, model simplicity, and practical engineering application.

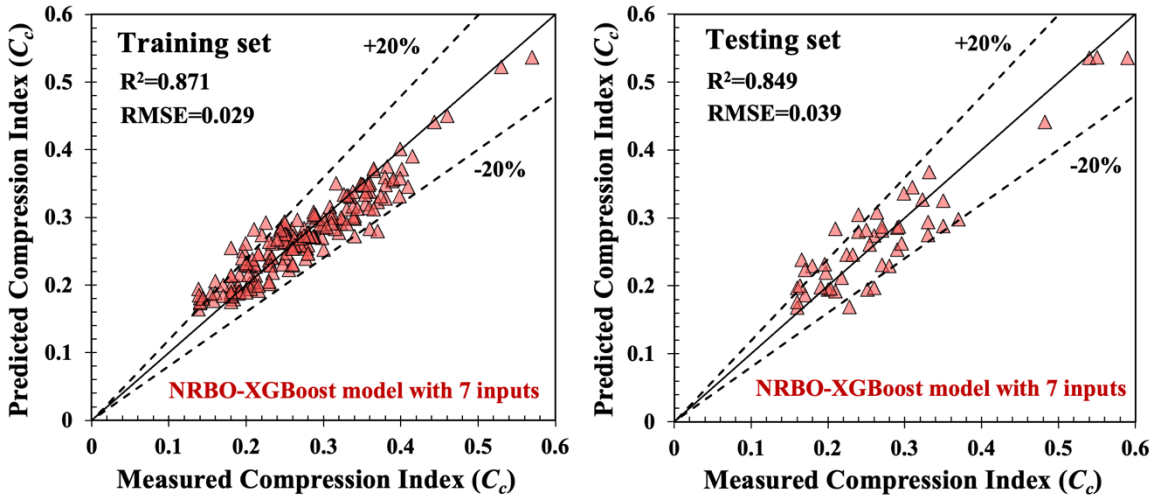


Fig. 5.5 Prediction results of NRBO-XGBoost model with 7 inputs (Model 1)

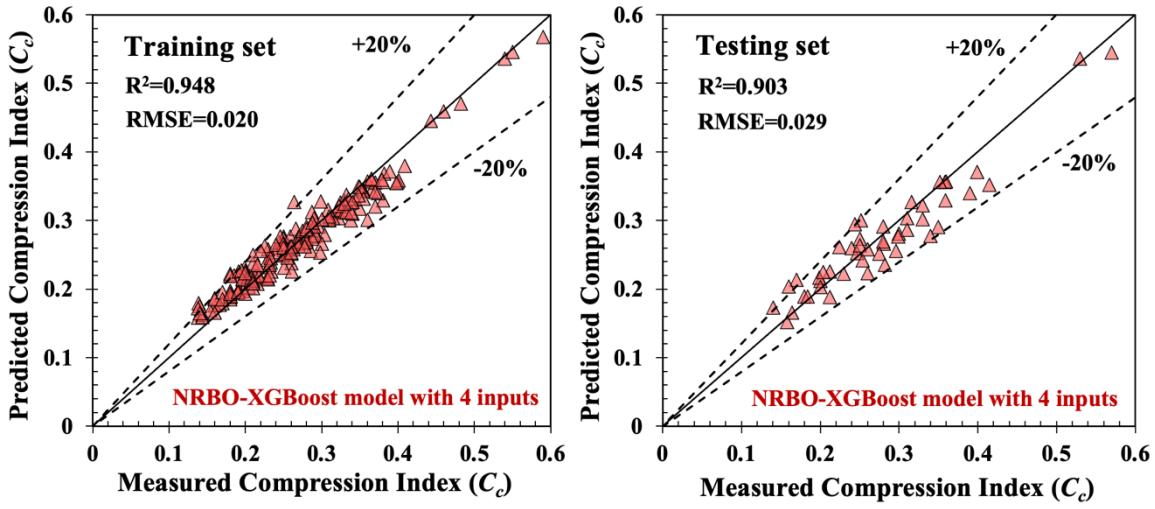


Fig. 5.6 Prediction results of NRBO-XGBoost model with 4 inputs (Model 2)

As shown in Fig. 5.5, the NRBO-XGBoost model with seven input parameters produced accurate and reliable results. In the training dataset, the model achieved an R^2 value of 0.871 and an RMSE of 0.029, while in the testing dataset, it obtained an R^2 of 0.849 and an RMSE of 0.039. The predicted values generally follow the 1:1 line, and a substantial proportion of predictions fall within the ±20% deviation range. These results confirm that the model, even when using a comprehensive set of input parameters, is capable of effectively capturing the nonlinear relationships between soil properties and the compression index. However, some degree of variability is observed in the prediction outcomes, which may be attributed to the inclusion of less influential variables in the model.

In comparison, the NRBO-XGBoost model trained with the four key input parameters (Fig. 5.6) demonstrated even better performance. In the training dataset, the model achieved an R^2 value of 0.948 and an RMSE of 0.020. The testing dataset also showed a higher prediction accuracy, with an R^2 of 0.903 and an RMSE of 0.029. Most of the predicted values are tightly clustered along the 1:1 line, and nearly all data points fall within the ±20% bounds. These results indicate that reducing the input parameters not only simplified the model but also enhanced its ability to capture the underlying relationship between soil properties and the compression index. By eliminating less relevant inputs, the reduced-parameter model avoids potential noise and improves generalization.

The main parameters of the established NRBO-XGBoost models (Model 1 and Model 2) are summarized in Table 5.4 to support reproducibility and potential practical application.

Table 5.4 Main parameters of the NRBO-XGBoost models established in this study.

Models	Number of trees	Maximum depth	Learning rate	Loss function
Model 1	528	5	0.015	Squared error
Model 2	414	4	0.038	Squared error

5.4.2 MLP models

The prediction performance of the MLP model for estimating the compression index is shown in Fig. 5.7 and Fig. 5.8. As with the NRBO-XGBoost model, two input sets were used to evaluate the effect of input parameter selection on model performance.

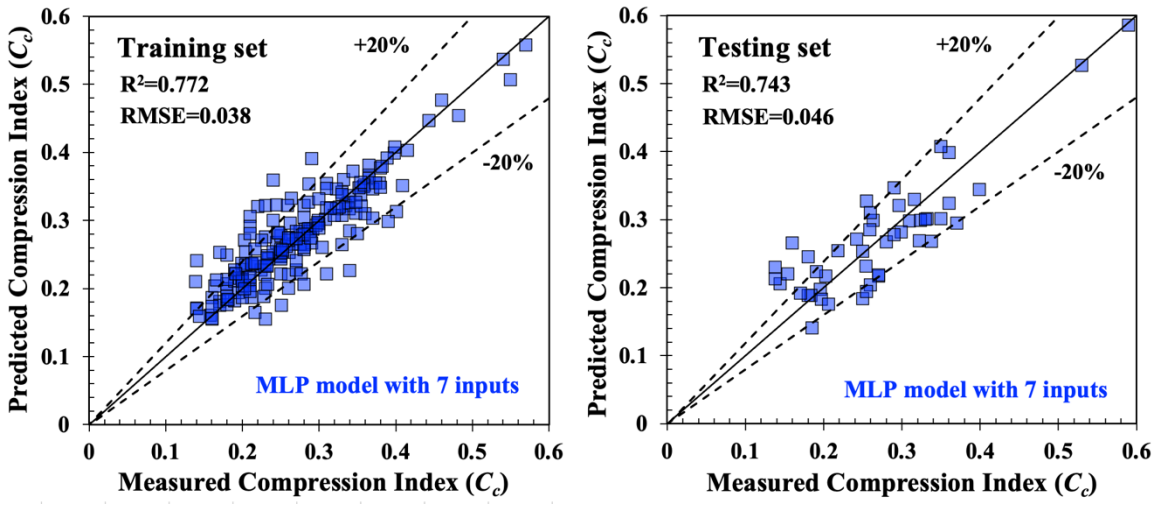


Fig. 5.7 Prediction results of MLP model with 7 inputs (Model 3)

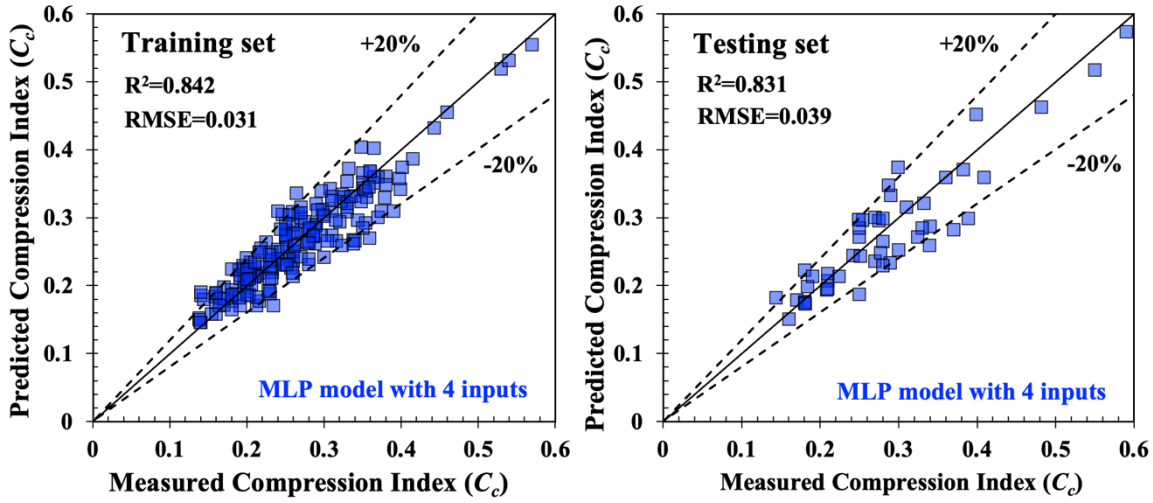


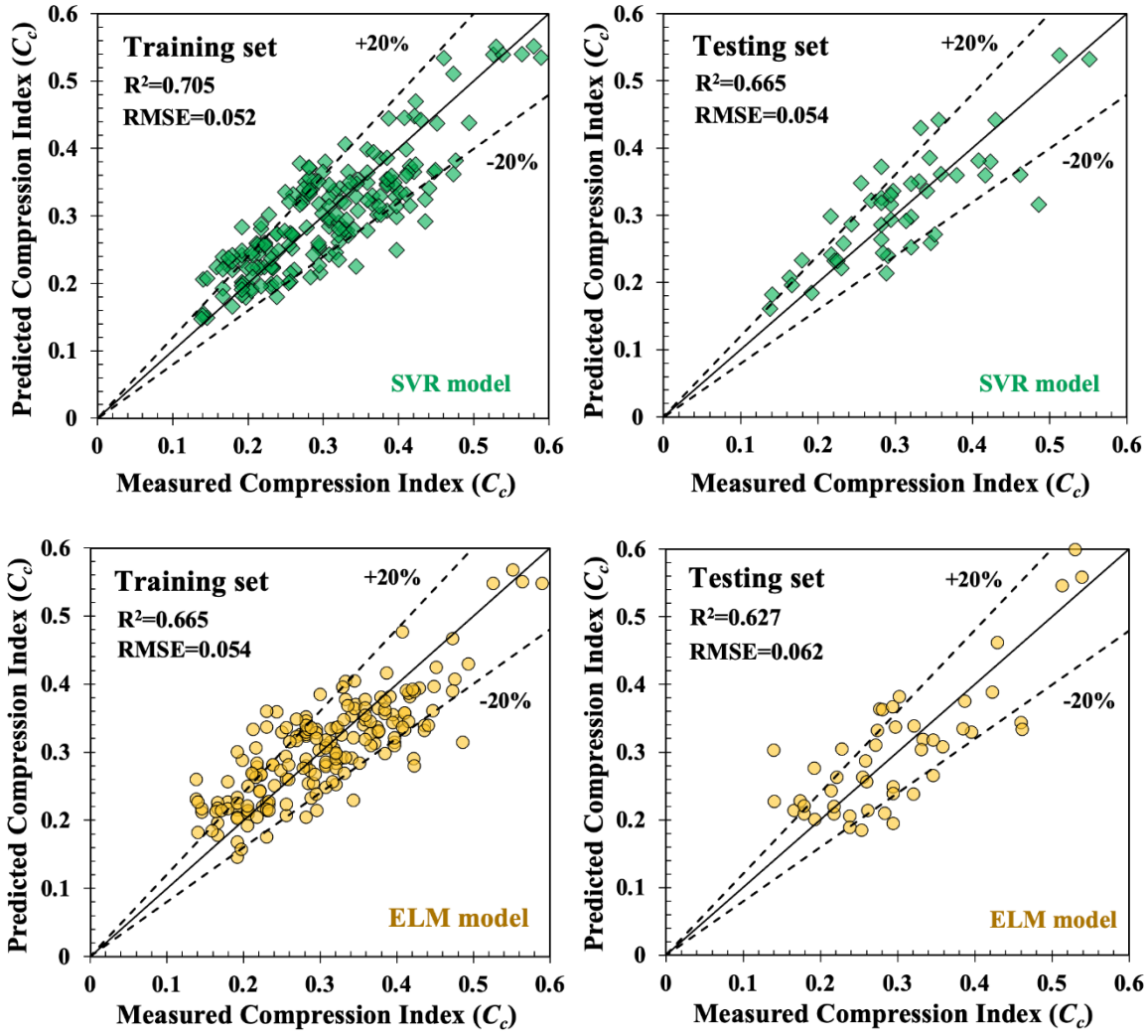
Fig. 5.8 Prediction results of MLP model with 4 inputs (Model 4)

As illustrated in Fig. 5.7, the MLP model trained with seven input parameters achieved an R^2 value of 0.772 and an RMSE of 0.038 for the training dataset. For the testing dataset, the model reached an R^2 of 0.743 and an RMSE of 0.046. The predicted values generally follow the 1:1 line, although the scatter is more pronounced compared to the NRBO-XGBoost model. While a considerable portion of the predicted values falls within the ±20% error margin, some data points deviate beyond this range, indicating that the inclusion of less relevant parameters may have reduced the model's ability to generalize.

Fig. 5.8 presents the prediction results of the MLP model developed with the reduced set of four input parameters. In this case, the model's performance improved. The R^2 value increased to 0.842 in the training dataset, with a corresponding RMSE of 0.031. In the testing dataset, the model produced an R^2 of 0.831 and an RMSE of 0.039. The predicted values are more concentrated along the 1:1 line, and most points fall within the ±20% deviation bounds. This improvement highlights the advantage of reducing input variables by focusing on the most influential factors, which enhances both the accuracy and the generalization of the model.

5.4.3 Other conventional machine learning models

Considering that both the NRBO-XGBoost and MLP models demonstrated good performance using four key input parameters, the remaining conventional machine learning algorithms; namely, SVR, ELM, and MARS were also developed and evaluated using the same reduced input set. This ensures consistency in the comparison and minimizes the potential interference from less relevant parameters.



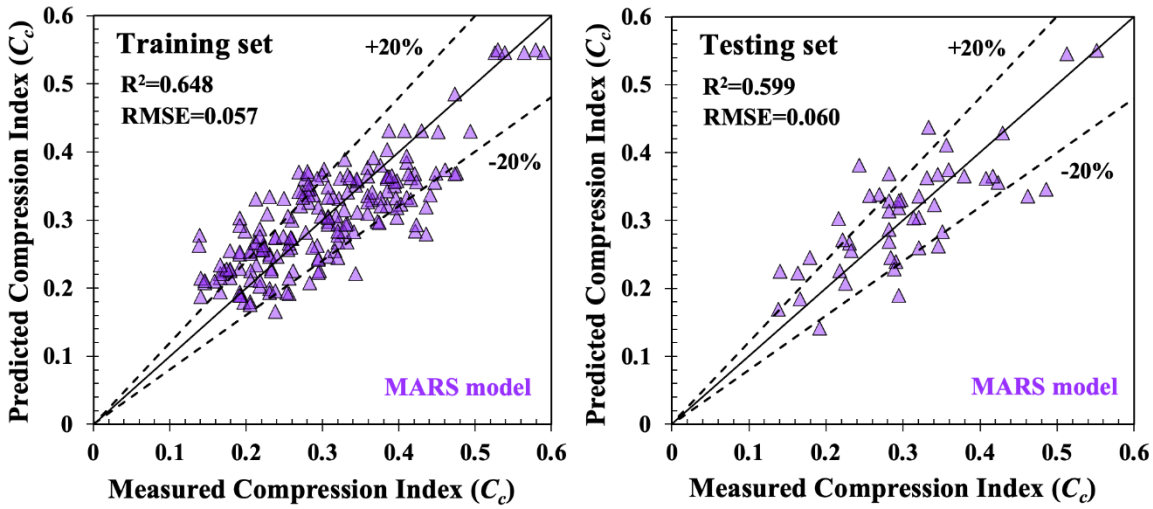


Fig. 5.9 Prediction results of SVM (Model 5), ELM (Model 6), and MARS (Model 7) models with 4 inputs

As shown in Fig. 5.9, the SVR model achieved an R^2 of 0.705 with an RMSE of 0.052 for the training dataset, and an R^2 of 0.665 with an RMSE of 0.054 for the testing dataset. The predicted values generally follow the 1:1 line, but there is noticeable scatter, and a few points lie outside the ±20% deviation bounds, particularly in the testing set.

The ELM model yielded R^2 values of 0.665 for the training set and 0.627 for the testing set, with corresponding RMSE values of 0.054 and 0.062. The predictions show a broader spread compared to SVR, and a significant portion of data points fall beyond the ±20% range, indicating relatively lower accuracy and stability.

Similarly, the MARS model produced R^2 values of 0.648 (training) and 0.599 (testing), with RMSE values of 0.057 and 0.060. The distribution of predicted values demonstrates a consistent trend but with substantial scatter, and many predictions deviate from the ideal line, especially in the testing dataset.

Overall, while these conventional machine learning models captured the general relationship between soil properties and the compression index, their predictive accuracy and generalization ability were relatively limited compared to the NRBO-XGBoost and MLP models.

In summary, the prediction performance of the five machine learning models demonstrated varying degrees of accuracy and generalization capability. The NRBO-XGBoost model consistently outperformed the others, achieving the highest R^2 values and the lowest RMSE values across both training and testing datasets. The MLP model also provided reliable results with good generalization ability, particularly when using the reduced set of four key input parameters. In contrast, the conventional models; namely, SVR, ELM, and MARS provided lower prediction accuracy and greater scatter in their results, although they were still capable of capturing the general trend between the input parameters and the compression index. These findings highlight the advantages of using advanced machine learning algorithms, such as NRBO-XGBoost and MLP, for predicting the compression index of expansive soils. A more detailed error analysis is presented in the following section.

5.4.4 Error analysis and model comparisons

In this study, the plasticity index (I_p) was selected as the independent variable for evaluating the prediction performance of different models. Given its strong correlation with the compression index (C_c), I_p serves as an effective indicator for assessing model accuracy across varying soil plasticity conditions. The comparison results are shown in Fig. 5.10 to Fig. 5.12 and summarized in Table 5.5.

In Fig. 5.10(a) and Fig. 5.10(b), the soil samples were arranged in ascending order of their I_p values (ranging from 7 to 107 in the database) to clearly illustrate the variation trend. As illustrated in Fig. 5.10(a), both the NRBO-XGBoost model and the MLP model demonstrated superior prediction performance. Among them, the NRBO-XGBoost model consistently achieved the best results, with predicted C_c values closely matching the measured data across the entire I_p range. Fig. 5.10(b) further shows that the residuals of the NRBO-XGBoost model were tightly concentrated, primarily within ±0.05, and NRMSE was only 8.1%. This indicates its good prediction accuracy and generalization ability, particularly valuable in practical applications. Even in the high plasticity range (I_p > 85), where prediction complexity typically increases, the NRBO-XGBoost maintained stable and reliable outputs with minimal deviation. The MLP model also exhibited good

predictive capability, achieving an NRMSE of 12.2%. Its residuals were mainly within ±0.08, showing slightly larger dispersion compared to NRBO-XGBoost. The MLP model performed well in low to medium I_p ranges but demonstrated minor fluctuations when I_p ranged between 40 and 60, indicating some sensitivity in this interval.

As illustrated in Fig. 5.11(a), the SVR, ELM, and MARS models exhibit generally consistent trends between predicted and measured C_c, but with noticeably larger fluctuations compared to the NRBO-XGBoost and MLP models. Their predictions become less stable, particularly in the medium plasticity range (I_p =30–50), where significant deviations are observed. Fig. 5.11(b) further highlights these limitations: although most residuals fall within ±0.15, their distribution is considerably wider than in Fig. 5.10, indicating reduced accuracy and robustness. The relatively high NRMSE values (19.2%–21.0%) suggest that these models are less capable of capturing the nonlinear relationships inherent in expansive soils, leading to weaker generalization ability and higher sensitivity to variability in soil plasticity characteristics.

As shown in Fig. 5.12(a), the NRBO-XGBoost model is compared with the widely used empirical equation proposed by Terzaghi and Peck (1967). This classical equation has been extensively applied in geotechnical engineering practice; however, for expansive soils examined in this study, its predictions tend to increasingly overestimate C_c with rising I_p. Fig. 5.12(b) further illustrates this behavior: the residuals of the Terzaghi and Peck (1967) equation expand with higher I_p, frequently exceeding 1.0 when I_p >80, resulting in an NRMSE of 117.0%. By contrast, the NRBO-XGBoost model maintains stable accuracy across the entire I_p spectrum, with tightly distributed residuals (NRMSE = 8.1%). These findings indicate that while the Terzaghi and Peck (1967) equation provides a conservative estimation and remains valuable in practice, it may not fully capture the nonlinear behavior of highly plastic expansive soils, whereas the NRBO-XGBoost model demonstrates improved adaptability and predictive capability for such conditions.

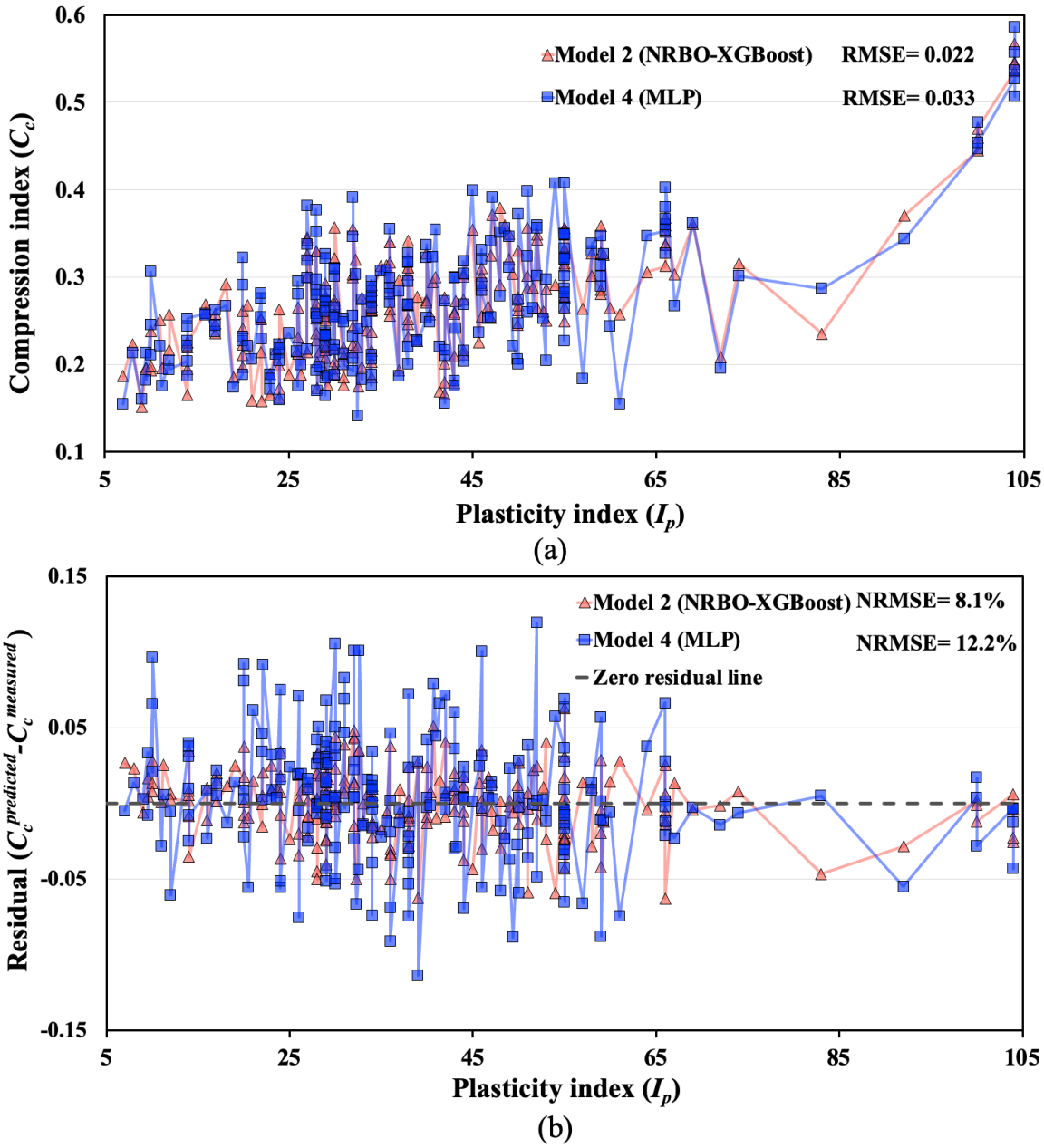


Fig. 5.10 (a) Predicted compression index C_c versus I_p using NRBO-XGBoost and MLP models; (b) Residuals of predicted versus measured C_c across I_p for NRBO-XGBoost and MLP models.

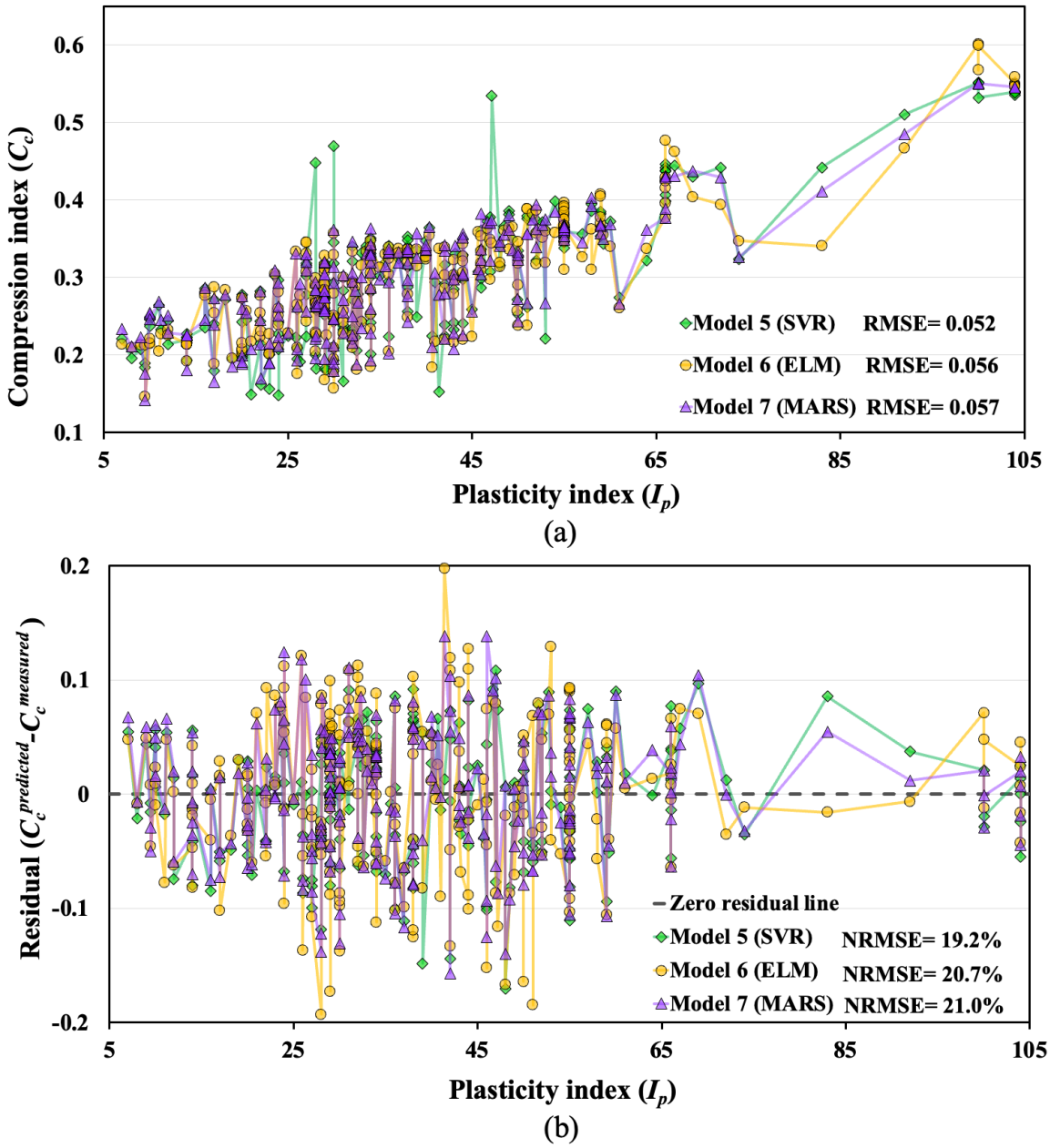


Fig. 5.11 (a) Predicted compression index C_c versus I_p using SVR, ELM and MARS models; (b) Residuals of predicted versus measured C_c across I_p for SVR, ELM and MARS models.

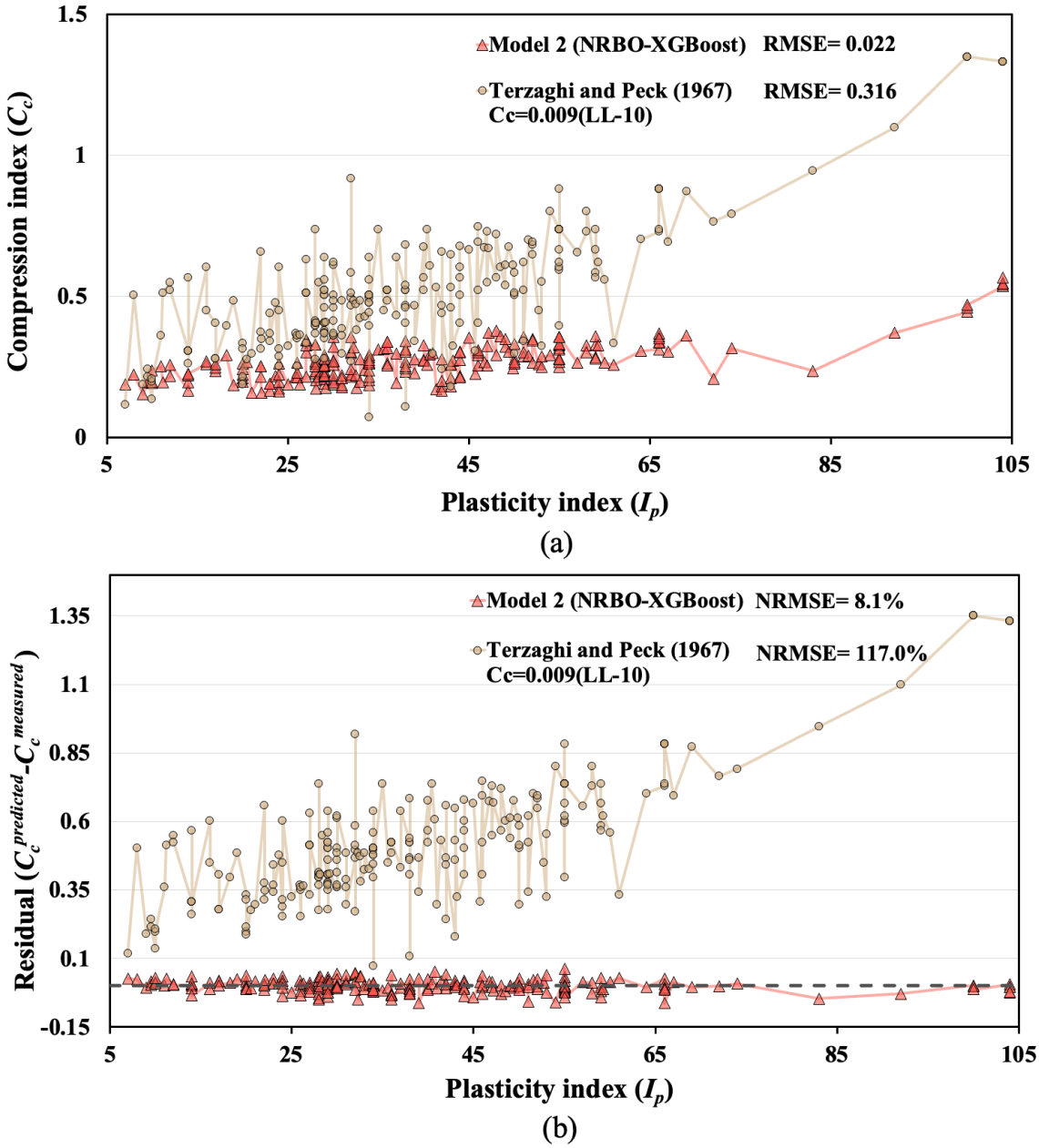


Fig. 5.12 (a) Predicted compression index C_c versus I_p using the NRBO-XGBoost model and Terzaghi and Peck (1967) equation; (b) Residuals of predicted versus measured C_c across I_p for the NRBO-XGBoost model and Terzaghi and Peck (1967) equation.

Table 5.5 Summary of prediction performance (R^2, RMSE, and NRMSE) of the employed models

Models	Description	R^2 (Train)	R^2 (Test)	$RMSE_{(All)}$	$NRMSE_{(All)}$
Model 1	NRBO-XGBoost (7 inputs)	0.871	0.849	0.031	11.4
Model 2	NRBO-XGBoost (4 inputs)	0.948	0.903	0.022	8.1
Model 3	MLP (7 inputs)	0.772	0.743	0.040	14.8
Model 4	MLP (4 inputs)	0.842	0.831	0.033	12.2
Model 5	SVM (4 inputs)	0.705	0.665	0.054	19.9
Model 6	ELM (4 inputs)	0.665	0.627	0.062	22.9
Model 7	MARS (4 inputs)	0.648	0.599	0.060	22.1
Terzaghi and Peck (1967)	$C_c = 0.009\,(LL - 10)$	0.538		0.316	117.0

In summary, the NRBO-XGBoost model outperformed all other methods, offering the highest prediction accuracy, the smallest residuals, and consistent performance across different plasticity index intervals. The MLP model provided reliable predictions with slightly reduced accuracy. In contrast, SVR, ELM, and MARS showed comparable but limited capabilities.

5.4.5 Sensitivity analysis

To enhance the interpretability of the best-performing NRBO-XGBoost model (Model 2), the SHAP (SHapley Additive exPlanations) method proposed by Lundberg and Lee (2017) was adopted. The SHAP framework facilitates a transparent interpretation of model behavior, highlighting the relative importance of different soil parameters. Owing to its

proven efficiency and suitability for ensemble tree-based algorithms, SHAP is particularly appropriate for interpreting the predictions of the NRBO-XGBoost model.

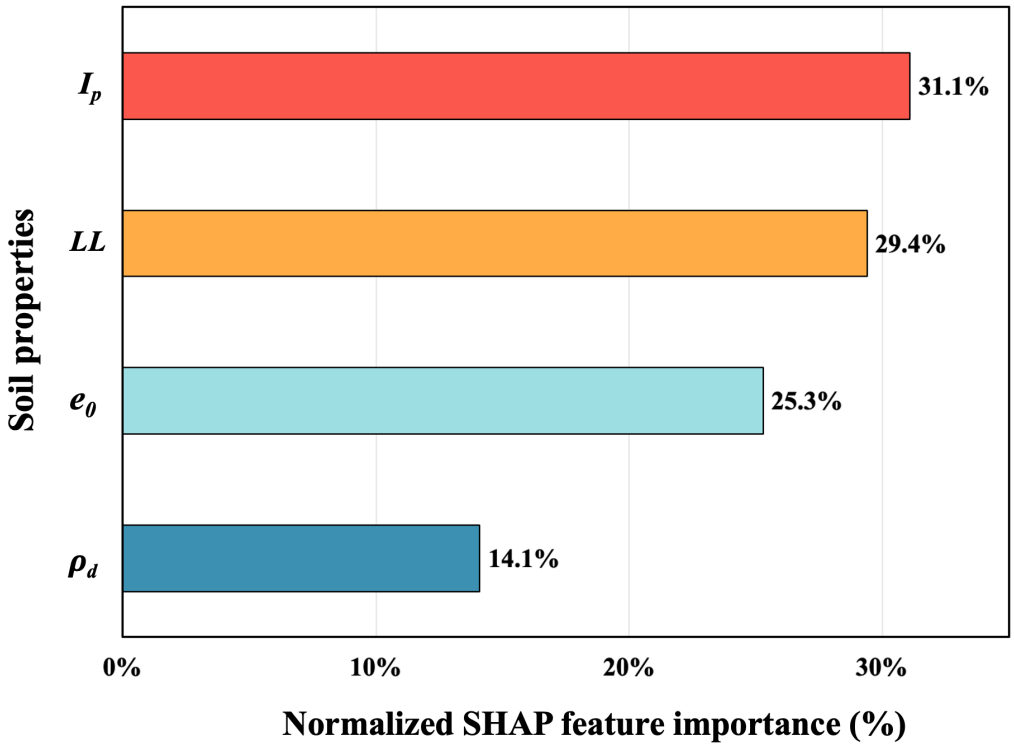


Fig. 5.13. Normalized SHAP feature importance of the input soil properties for the best-performing NRBO-XGBoost model (Model 2).

Fig. 5.13 shows the normalized SHAP feature importance for the NRBO-XGBoost model (Model 2). The ranking is I_p (31.1%) > LL (29.4%) > e_o (25.3%) > ρ_d (14.1%). The first three parameters together account for about 86% of the total contribution, indicating that the model predictions are mainly governed by I_p, LL, and e_o. The I_p is the most influential factor, underscoring its critical role in determining soil compressibility. In contrast, the influence of ρ_d is relatively smaller, although it still provides useful information. This outcome is consistent with geotechnical understanding: higher plasticity and larger initial void ratio generally lead to greater compressibility, whereas higher dry density tends to reduce compressibility.

5.4.6 Simplified MLP-based equation for predicting compression index

To encourage the use of the proposed models in engineering practice applications, the MLP-based Model 4 was further simplified into an explicit empirical equation, as presented in Eq. (5.18). This simplified formulation allows practitioners to efficiently estimate the compression index using basic soil parameters without relying on complex computational tools or machine learning platforms. By offering a direct calculation method, this approach facilitates the application of the model in routine practice applications.

Before applying Eq. (5.18), all input variables should be normalized using the min-max normalization method defined in Eq. (5.20), which scales the data to a range of [-1, 1]. This ensures consistency with the model's development process and maintains prediction accuracy.

$$\begin{aligned} y = {} & -0.64799 * \text{tansig}\,(-4.94 * x_1' + 2.93 * x_2' + 3.13 * x_3' + 1.93 * x_4' + 1.85) \\ & -1.65773 * \text{tansig}\,(-0.19 * x_1' + 0.10 * x_2' - 0.51 * x_3' - 0.13 * x_4' - 0.52) \\ & -0.25684 * \text{tansig}\,(9.30 * x_1' - 10.97 * x_2' + 5.66 * x_3' + 4.88 * x_4' - 4.09) \\ & -0.71 \end{aligned} \tag{5.18}$$

$$\text{tansig}(h) = \frac{2}{1 + e^{-2h}} - 1 \tag{5.19}$$

$$x' = -1 + \frac{2 \times (x - x_{min})}{x_{max} - x_{min}} \tag{5.20}$$

Where x is original variables, y is compression index, x' is normalized variables (x_1' is liquid limit, x_2' is plasticity index, x_3' is initial void ratio, and x_4' is dry density), x_{max} and x_{min} are the maximum and minimum of each input variable.

The applicability and reliability of Eq. (5.18) will be further validated through case studies in Chapter 6.4.

5.5 Limitations and future works

While this study focused on widely available physical properties for predicting the C_c of expansive soils and demonstrated reasonable model performance, several limitations remain that suggest the need for further investigation to improve the applicability and robustness of the proposed approach.

The database covers a broad range of soil types; however, it includes relatively few samples with I_p values between 70 and 107, which may limit model performance for highly plastic expansive clays. In addition, extreme cases with I_p values beyond 107 are not fully captured; due to this reason, the models may show reduced accuracy when applied to such conditions.

Second, the dataset consists of both compacted and undisturbed samples, which could introduce variability due to differences in sample preparation and testing conditions. This is because the current dataset is not large enough to support separate model development for each sample type.

Third, although a simplified equation was proposed for practical use, its applicability requires further validation through site-specific applications. This study includes three case analyses (see Chapter 6.4) as an initial demonstration but given the limited field research on settlement behavior of expansive soils, more real-world validation studies are necessary to support wider application in practice. The simplified MLP equation (Eq. 5.18) is considered applicable when the input parameters fall within the range of the database used in this study, whereas caution should be exercised for conditions beyond this range.

In addition, since the models rely on a complete set of measured basic soil parameters, their accuracy may decrease if key inputs (e.g., I_p, LL, or e_o) are unavailable or estimated indirectly using empirical correlations or simplified assumptions.

Future research could focus on expanding the dataset, enabling the inclusion of other informative variables such as cation exchange capacity (CEC), and specific surface area (SSA). As the database grows, incorporating stress history indicators such as

preconsolidation pressure or overconsolidation ratio may also be feasible to further enhance the predictive accuracy of the proposed models.

5.6 Summary

This study presents a simple and effective approach for predicting the compression index of expansive soils, aiming to overcome the limitations of conventional empirical methods. Seven models based on five different machine learning algorithms were developed using a large and diverse dataset. Specifically, two models were constructed using NRBO-XGBoost (Model 1 and Model 2), two using MLP (Model 3 and Model 4), and one each using SVR (Model 5), ELM (Model 6), and MARS (Model 7). The main conclusions are summarized as follows:

(i) An extensive database comprising 238 expansive soil samples was compiled using published data gathered from 40 countries during the last 60 years from the published literature. The dataset covers a broad range of expansive soils and geological conditions, providing a solid foundation for developing reliable prediction methods.

(ii) An optimized prediction model (Model 2) was developed by integrating NRBO with the XGBoost algorithm. The NRBO-XGBoost model achieved high prediction accuracy, with an R^2 value of 0.903 and an RMSE of 0.029 on the test dataset, demonstrating good stability and generalization capability.

(iii) To facilitate practical engineering applications, a simplified empirical equation was proposed based on the MLP-derived Model 4 (i.e., Eq. 5.18), which can be used without relying on any machine learning tools or models. This equation enables direct estimation of the compression index based on four fundamental soil parameters: liquid limit, plasticity index, initial void ratio, and dry density.

(iv) Comparative analysis demonstrated that the NRBO-XGBoost model and the simplified MLP-based Model 4 equation outperformed conventional machine learning algorithms (SVR, ELM, and MARS) and the widely used empirical equation by Terzaghi and Peck

(1967). The proposed methods consistently provided higher prediction accuracy and better generalization across different soil plasticity conditions.

(v) The methods developed in this study offer reliable and efficient tools for estimating the compression index of expansive soils. They provide a practical alternative to time-consuming laboratory consolidation tests and can assist in the prediction of settlement in geo-infrastructure projects involving expansive soils.

References

Abden, A., Al-Shamrani, M., Dafalla, M., 2024. Evaluating the feasibility of inverted T foundation on expansive soils. J. Build. Eng. 97, 110788.

Adem, H.H., Vanapalli, S.K., 2016. Heave prediction in a natural unsaturated expansive soil deposit under a lightly loaded structure. Geotech. Geol. Eng. 34, 1181–1192.

Akbarimehr, D., Eslami, A., Imam, R., 2021. Correlations between compression index and index properties of undisturbed and disturbed Tehran clay. Geotech. Geol. Eng. 39(7), 5387–5393.

Al-Mahbashi, A.M., Al-Shamrani, M.A., Abbas, M.F., 2021. Hydromechanical behavior of unsaturated expansive clay under repetitive loading. J. Rock Mech. Geotech. Eng. 13(5), 1136–1146.

Al-Khafaji, A., Andersland, O., 1992. Equations for compression index approximation. J. Geotech. Eng. 118(1), 148–153.

Al-Rawas, A.A., Goosen, M.F., 2006. Expansive Soils: Recent Advances in Characterization and Treatment. 1st edn. CRC Press, Boca Raton.

Al-Rawas, A.A., Guba, I., McGown, A., 1998. Geological and engineering characteristics of expansive soils and rocks in northern Oman. Eng. Geol. 50(3–4), 267–281.

Alnmr, A., Alsirawan, R., Ray, R., Alzawi, M.O., 2024. Compressibility of expansive soil mixed with sand and its correlation to index properties. Heliyon. 10(15).

Alptekin, A., Taga, H., 2019. Prediction of compression and swelling index parameters of Quaternary sediments from index tests at Mersin District. Open Geosci. 11(1), 482–491.

Awad, M., Khanna, R., 2015. Support vector regression. In: Efficient Learning Machines, Springer, New York, pp. 67–80.

Azam, S., 2003. Influence of mineralogy on swelling and consolidation of soils in eastern Saudi Arabia. Can. Geotech. J. 40(5), 964–975.

Azam, S., Hu, Y., Chowdhury, R., 2009. Sensor installation for field monitoring in expansive soils. In: Proc 62nd Can. Geotech. Conf., Halifax, pp. 917–922.

Bardhan, A., Kardani, N., Alzo'ubi, A.K., Samui, P., Gandomi, A.H., Gokceoglu, C., 2022. A comparative analysis of hybrid computational models constructed with swarm intelligence algorithms for estimating soil compression index. Arch. Comput. Methods Eng. 29(7), 4735–4773.

Basak, D., Pal, S., Patranabis, D.C., 2007. Support vector regression. Neural Inf. Process. Lett. Rev. 11(10), 203–224.

Benbouras, M.A., Kettab Mitiche, R., Zedira, H., Petrisor, A.I., Mezouar, N., Debiche, F., 2019. A new approach to predict the compression index using artificial intelligence methods. Mar. Georesour. Geotechnol. 37(6), 704–720.

Blight, G., 1997. Origin and formation of residual soils. Mech. Residual Soil 1, 15.

Charlie, W.A., Osman, M.A., Ali, E.M., 1984. Construction on expansive soils in Sudan. J. Constr. Eng. Manag. 110(3), 359–374.

Chen, Y., Xu, Y., Jamhiri, B., Wang, L., Li, T., 2022. Predicting uniaxial tensile strength of expansive soil with ensemble learning methods. Comput. Geotech. 150, 104904.

Culshaw, M., Cripps, J., Bell, F., Moon, C., 1991. Engineering geology of Quaternary soils: I. Processes and properties. Geol. Soc. London Eng. Geol. Spec. Publ. 7(1), 3–38.

Dai, Z., Guo, J., Zhong, K., Tong, K., Li, S., Huang, K., Chen, S., 2024. Dynamic evolution of three-dimensional cracks in expansive soil under wet-dry cycles: insights from resistivity monitoring. Bull. Eng. Geol. Environ. 83(8), 305.

Dai, Z.J., Liu, Z.H., Chi, Z.C., Wang, W., Huang, K., Chen, S.X., 2025. Lateral residual stress effect on the swelling pressure of compacted expansive soil and microscopic mechanism. Bull. Eng. Geol. Environ. 84(3), 128.

Dhowian, A.W., 1990. Simplified heave prediction model for expansive shale. Geotech. Test. J. 13(4), 323–333.

Díaz, E., Spagnoli, G., 2024. A super-learner machine learning model for a global prediction of compression index in clays. Appl. Clay Sci. 249, 107239.

Ding, X., El-Zein, A., 2024. Predicting soil water retention curves using machine learning: A study of model architecture and input variables. Eng. Appl. Artif. Intell. 133, 108122.

Driscoll, R., Crilly, M., 2000. Subsidence damage to domestic buildings: lessons learned and questions asked. Build. Res. Estab., London.

Ejjaaouani, H., 2008. Interactions des fondations et des sols gonflants: pathologie, calculs et études expérimentales. Thèse de doctorat, École Nationale des Ponts et Chaussées, Spécialité Géotechnique.

España, V.J., Aparicio, J., Barber, X., Esteve, M., 2024. Estimating production functions through additive models based on regression splines. Eur. J. Oper. Res. 312(2), 684–699.

Fredlund, D.G., 1983. Prediction of ground movements in swelling clays. In: Proc 31st

Annu. Soil Mech. Found. Eng. Conf., Univ. of Minnesota, Minneapolis, MN.

Friedman, J.H., 1991. Multivariate adaptive regression splines. Ann. Stat. 19(1), 1–67.

Gao, Y., Chen, Z., Airey, D., 2019. Compression index versus natural water content relationships for China's coastal soft clays. KSCE J. Civ. Eng. 23, 4611–4620.

Gong, H., Li, Y., Zhang, J., Zhang, B., Wang, X., 2024. A new filter feature selection algorithm for classification task by ensembling Pearson correlation coefficient and mutual information. Eng. Appl. Artif. Intell. 131, 107865.

Gourley, C.S., Newill, D., Schreiner, H.D., 2020. Expansive soils: TRL's research strategy. In: Engineering Characteristics of Arid Soils. CRC Press, 247–260.

Han, Z., Zhang, P., Zou, W., Fan, K., Vanapalli, S.K., Wan, L., 2024. At-rest lateral earth pressure of compacted expansive soils: experimental investigations and prediction approach. J. Rock Mech. Geotech. Eng. 16(4), 1425–1435.

Henríquez, P.A., Ruz, G.A., 2017. Extreme learning machine with a deterministic assignment of hidden weights in two parallel layers. Neurocomputing 226, 109–116.

Holtz, R.D., Kovacs, W.D., Sheahan, T.C., 1981. An Introduction to Geotechnical Engineering. Prentice-Hall, Englewood Cliffs, NJ.

Hou, T.S., Xu, B., Jiang, Q., Liu, G., Zhao, X., 2013. Formation mechanism and stability analysis of the Houba expansive soil landslide. Eng. Geol. 161, 34–43.

Huang, G.B., Zhu, Q.Y., Siew, C.K., 2004. Extreme learning machine: a new learning scheme of feedforward neural networks. In: Proc IEEE Int. Joint Conf. Neural Netw., Vol. 2, pp. 985–990.

Huang, R., Lizhou, W., 2007. Stability analysis of unsaturated expansive soil slope. Earth Sci. Front. 14(6), 129–133.

Ibrahim, N.M., Rahim, N.L., Amat, R.C., Salehuddin, S., Ariffin, N.A., 2012. Determination of plasticity index and compression index of soil at Perlis. APCBEE Procedia 4, 94–98.

Imhoff, S., Da Silva, A.P., Fallow, D., 2004. Susceptibility to compaction, load support capacity, and soil compressibility of Hapludox. Soil Sci. Soc. Am. J. 68(1), 17–24.

Jeevanantham, V., Jayashree, J., Roja, S.Y., 2023. Experimental analysis on swelling, shrinkage and consolidation behavior of expansive soils under wetting–drying cycles. IOP Conf. Ser. Earth Environ. Sci. 1258(1), 012006.

Jiang, G., Chen, W., Liu, X., Yuan, S., Wu, L., Zhang, C., 2018. Field study on swelling–shrinkage response of an expansive soil foundation under high-speed railway

embankment loads. Soils Found. 58(6), 1538–1552.

Johnson, L.D., 1973. Influence of suction on heave of expansive soils. Miscellaneous Paper S-73-17, US Army Engineers Waterways Experiment Station, Vicksburg, MS.

Jones, L.D., Jefferson, I., 2012. Expansive soils. In: Geotechnical Engineering Principles, Problematic Soils and Site Investigation, vol. 1, ICE Publishing, London, pp. 413–441.

Kayabali, K., Demir, S., 2011. Measurement of swelling pressure: direct method versus indirect methods. Can. Geotech. J. 48(3), 354–364.

Koppula, S., 1981. Statistical estimation of compression index. Geotech. Test. J. 4(2), 68–73.

Krzywanski, J., Czakiert, T., Nowak, W., Shimizu, T., Ashraf, W.M., Zylka, A., Iliev, I., 2024. Towards cleaner energy: an innovative model to minimize NOx emissions in chemical looping and CO2 capture technologies. Energy 312, 133397.

Krzywanski, J., Nowak, W., Skrobek, D., Zylka, A., Ashraf, W.M., Grabowska, K., Sosnowski, M., Kulakowska, A., Czakiert, T., Gao, Y., 2025. Modeling of bed-to-wall heat transfer coefficient in fluidized adsorption bed by gene expression programming approach. Powder Technol. 449, 120392.

Kumar, R., Jain, P., Dwivedi, P., 2016. Prediction of compression index (Cc) of fine grained remolded soils from basic soil properties. Int. J. Appl. Eng. Res. 11(1), 592–598.

Liu, Q., Wang, M., 2023. Numerical investigation of water migration in a closed unsaturated expansive clay system. Bull. Eng. Geol. Environ. 82(6), 202.

Liu, Y., Vanapalli, S.K., 2019. Prediction of lateral swelling pressure behind retaining structure with expansive soil as backfill. Soils Found. 59(1), 176–195.

Lundberg, S.M., Lee, S.I., 2017. A unified approach to interpreting model predictions. Adv. Neural Inf. Process. Syst. 30, 4768–4777.

Mayne, P.W., 1980. Cam-clay predictions of undrained strength. J. Geotech. Eng. Div. 106(11), 1219–1242.

Mitchell, J.K., Soga, K., 2005. Fundamentals of Soil Behavior. 3rd edn. John Wiley & Sons, New York.

Mohammadzadeh, S.D., Kazemi, S.F., Mosavi, A., Nasseralshariati, E., Tah, J.H., 2019. Prediction of compression index of fine-grained soils using a gene expression programming model. Infrastructures 4(2), 26.

Osman, N.Y., McManus, K., Ng, A.W.M., 2005. Management and analysis of data for damage of light structures on expansive soils in Victoria, Australia. In: Proceedings

of the First International Conference on Structural Condition Assessment, Monitoring and Improvement, Perth, Australia. CI-Premier, Singapore, 283–290.

Pandey, P., Hossain, M.S., Ahmed, A., 2021. Performance evaluation of modified moisture barrier in mitigating expansive soil associated pavement distresses. Transp. Geotech. 31, 100667.

Park, H.I., Lee, S.R., 2011. Evaluation of the compression index of soils using an artificial neural network. Comput. Geotech. 38(4), 472–481.

Pham, B.T., Nguyen, M.D., Van Dao, D., Prakash, I., Ly, H.B., Le, T.T., Ho, L.S., Nguyen, K.T., Ngo, T.Q., Hoang, V., 2019. Development of artificial intelligence models for the prediction of compression coefficient of soil: an application of Monte Carlo sensitivity analysis. Sci. Total Environ. 679, 172–184.

Rao, S.M., Reddy, B.V.V., Muttharam, M., 2001. The impact of cyclic wetting and drying on the swelling behaviour of stabilized expansive soils. Eng. Geol. 60(1–4), 223–233.

Rendon-Herrero, O., 1980. Universal compression index equation. J. Geotech. Eng. Div. 106(11), 1179–1200.

Ruwaih, I., 1987. Experiences with expansive soils in Saudi Arabia. In: Proc 6th Int. Conf. Expansive Soils, New Delhi, India.

Shi, B., Jiang, H., Liu, Z., Fang, H., 2002. Engineering geological characteristics of expansive soils in China. Eng. Geol. 67, 63–71.

Shi, X.C., Gao, Y.F., 2013. Application of genetic arithmetic and support vector machine in prediction of compression index of clay. Appl. Mech. Mater. 438, 1167–1170.

Sowmya, R., Premkumar, M., Jangir, P., 2024. Newton-Raphson-based optimizer: a new population-based metaheuristic algorithm for continuous optimization problems. Eng. Appl. Artif. Intell. 128, 107532.

Sridharan, A., Nagaraj, H., 2000. Compressibility behaviour of remoulded, fine-grained soils and correlation with index properties. Can. Geotech. J. 37(3), 712–722.

Tang, C.S., Zhu, C., Cheng, Q., Zeng, H., Xu, J.J., Tian, B.G., Shi, B., 2021. Desiccation cracking of soils: a review of investigation approaches, underlying mechanisms, and influencing factors. Earth Sci. Rev. 216, 103586.

Tavakkoli, N.E., Oh, W.T., Vanapalli, S.K., 2024. Compilation of consolidation properties data of Champlain Sea Clay from Ottawa Region. Geotech. Geol. Eng., 1–23.

Terzaghi, K., Peck, R.B., 1967. Soil Mechanics in Engineering Practice. John Wiley & Sons, New York.

Tiwari, B., Ajmera, B., 2012. New correlation equations for compression index of remolded clays. J. Geotech. Geoenviron. Eng. 138(6), 757–762.

Tu, H., Vanapalli, S.K., 2016. Prediction of the variation of swelling pressure and one-dimensional heave of expansive soils with respect to suction using the soil-water retention curve as a tool. Can. Geotech. J. 53(8), 1213–1234.

Uzer, A.U., 2024. Accurate prediction of compression index of normally consolidated soils using artificial neural networks. Buildings 14(9), 2688.

Vamsi Nagaraju, T., Durga Prasad, C., Murthy, N., 2020. Invasive weed optimization algorithm for prediction of compression index of lime-treated expansive clays. In: Soft Computing for Problem Solving: SocProS 2018, Volume 2.

Vanapalli, S., Lu, L., 2012. A state-of-the-art review of 1-D heave prediction methods for expansive soils. Int. J. Geotech. Eng. 6(1), 15–41.

Vinod, P., Bindu, J., 2010. Compression index of highly plastic clays—an empirical correlation. Indian Geotech. J. 40(3), 174–180.

Wang, H., Zhang, R., Zheng, J., Song, X., Yang, T., Wu, G., 2024. Numerical analysis of an enhanced flexible reinforcement system for expansive soil slopes based on on-site validation. Bull. Eng. Geol. Environ. 83(8), 337.

Wang, J., Vanapalli, S., 2025. A framework for estimating matric suction in compacted fine-grained soils based on a machine learning-assisted conceptual model. Int. J. Numer. Anal. Methods Geomech. 49, 2177–2199.

Yang, F., Zhang, J., Xie, M., Cui, W., Dong, X., 2025. Evaluation of compression index of red mud by machine learning interpretability methods. Comput. Geotech. 181, 107130.

Yukselen-Aksoy, Y., Kaya, A., Ören, A.H., 2008. Seawater effect on consistency limits and compressibility characteristics of clays. Eng. Geol. 102(1–2), 54–61.

Zaman, M.W., Hossain, M.R., Shahin, H., Alam, A., 2016. A study on correlation between consolidation properties of soil with liquid limit, in situ water content, void ratio and plasticity index. In: Geotechnics for Sustainable Infrastructure Development, pp. 899–902.

Zhang, X., Belmont, N., 2011. Use of wicking fabric to help prevent differential settlements in expansive soil embankments. In: Geo-Frontiers 2011: Advances in Geotechnical Engineering, pp. 3915–3924.

Zhou, R., Wang, B.T., Han, S.Y., Wang, D.Y., Zhang, F.H., 2024. Mechanisms of crack development and strength deterioration in compacted expansive soils under

controlled wetting-drying conditions. Eng. Fail. Anal. 159, 108133

CHAPTER 6

VALIDATION AND APPLICATION OF THE PROPOSED METHODS IN THIS STUDY ON PUBLISHED CASE STUDIES

This chapter presents the validation and practical application of the predictive models developed in the previous chapters. In Chapter 3, machine learning algorithms were used to predict two fundamental parameters describing the expansive behavior of soils: the swelling index (C_s) and the swelling pressure (P_s). Chapter 4 further developed models to predict the swelling potential ($\varepsilon\%$), while Chapter 5 focused on predicting the compression index (C_c), which governs the compressibility and settlement behavior of expansive clays under loading.

Section 6.1 focuses on validating the swelling index prediction models. The predicted C_s values are incorporated into a physically-based semi-empirical equation to estimate the swelling potential of expansive soils. This approach enables indirect validation by comparing the calculated swelling potential with measured values, thereby assessing the practical reliability of the swelling index predictions.

Section 6.2 presents the validation of the swelling pressure prediction models. The predicted P_s values are directly compared with laboratory test data from a variety of expansive soils. The comparison evaluates the ability of the models to capture the variability of swelling pressure across different soil types and conditions.

Section 6.3 addresses the validation and application of the swelling potential prediction models in field conditions. While the database used for model development is primarily derived from laboratory testing on idealized samples, in-situ expansive soils are typically more complex due to layered and fissured structures, climate variations, and repeated dry-wet cycles. To evaluate the practical applicability of the proposed predictive equation (Eq.

4.8), it has been applied to five published case studies covering a range of engineering scenarios, such as natural heave caused by rainfall, pipeline leakage-induced heave beneath concrete slabs, and ground heave under spread footings. These case studies are from Australia, Canada, China, Saudi Arabia, and the United States, providing a diverse set of validation conditions. The results confirm that the proposed model provides reasonable predictions of field-scale swelling potential in various geotechnical contexts.

Section 6.4 presents the validation of the compression index prediction models. The predicted C_c values are incorporated into a consolidation settlement equation with clear physical significance to estimate settlement in expansive soils. These calculated settlements are then compared with measured field data to assess the accuracy of the predictions. This section demonstrates the applicability of the proposed models for evaluating settlement behavior, which is essential for the design and long-term performance assessment of foundations and other geo-structures on expansive soils.

The validation results confirm that the proposed models and equations are reliable, practical, and applicable to a wide range of expansive soil conditions in both laboratory and field settings.

6.1 Case studies of the proposed methods for estimating swelling index

In this section, the effectiveness and reliability of the proposed predictive models for estimating the swelling index (C_s) are systematically evaluated. The swelling index plays a fundamental role in characterizing the expansive behavior of soils and serves as a critical input parameter in various predictive frameworks for estimating the deformation and stability of geo-infrastructure founded on expansive soils. Although C_s can be directly measured through laboratory testing, such procedures are often labor-intensive, time-consuming, and prone to variability due to differences in testing protocols, equipment calibration, and operator expertise. Therefore, the development of reliable and accurate predictive models for C_s is of both theoretical significance and practical value in geotechnical engineering applications.

To verify the validity and practical applicability of the C_s prediction equations proposed in Chapter 3—namely the empirical regression equation (Eq. 3.4), the multilayer perceptron (MLP)-based equation (Eq. 3.15), and the extreme learning machine (ELM)-based equation (Eq. 3.16)—a comprehensive validation was undertaken. In addition to a direct comparison between the predicted C_s values and those obtained from laboratory testing, an indirect validation approach was adopted. This involved incorporating the predicted C_s values into a physically-based semi-empirical equation to estimate the swelling potential (S%) of expansive soils. This additional step was designed to demonstrate not only the consistency of the predicted C_s values with the known swelling behavior of expansive soils but also to highlight the practical utility of the proposed models within geotechnical design contexts.

The semi-empirical equation employed for this validation was originally proposed by Fredlund (1983) and is expressed as:

$$\Delta h = h \frac{C_s}{1 + e_0} \log\left(\frac{P_f}{P_s'}\right)$$

where Δh is the vertical deformation of the soil layer, h is the initial thickness of the soil layer, e_o is the initial void ratio, P_s' is the corrected swelling pressure, and P_f is the final stress state, calculated as the sum of the total overburden pressure (σ_y) and the change in total stress ($\Delta\sigma_y$), minus the pore-water pressure (u_{wf}).

The validation dataset used in this study comprises 14 expansive soil samples collected from geographically diverse regions, including the United States, Canada, China, India, Turkey, and Australia (Yoshida et al., 1983; Sridharan and Gurtug, 2004; Vu and Fredlund, 2004; Zhan et al., 2007; Kayabali and Demir, 2011; Pedarla, 2013; Liu et al., 2016; Yuan et al., 2016; Puppala et al., 2017; Kumar et al., 2020). These soils were carefully selected to ensure that the proposed predictive models for the swelling index were tested against a representative range of expansive soil types commonly encountered in varying climatic zones and geological settings worldwide. The diversity in sample origins enhances the

comprehensiveness of the validation process and demonstrates the potential applicability of the models under different environmental and engineering conditions.

The expansive soils included in the dataset exhibit substantial variation in their geotechnical properties, reflecting differences in mineralogical composition, depositional environments, and degrees of weathering. Specifically, the plasticity index of the selected soils ranges from 27% to 62%, encompassing both low-plasticity and highly plastic clays. This range effectively captures the influence of different clay minerals, such as kaolinite, illite, and montmorillonite, which significantly affect swelling behavior. The specific gravity values vary from 2.60 to 2.82, indicating differences in mineral density and composition, including the presence of lighter clay minerals and heavier iron-rich materials. Furthermore, the dry density of the soils ranges from 1.27 g/cm³ to 1.92 g/cm³, representing both loose natural deposits and densely compacted soils, often found in engineered or treated ground conditions. In addition to these basic soil properties, the dataset includes expansive soils exhibiting a wide range of swelling pressures, from 50.5 kPa to 679.0 kPa, and final stress states, from 1.0 kPa to 400.0 kPa. This variation reflects the inclusion of soils subjected to differing overburden stresses thereby improving the representativeness and generalizability of the dataset.

By substituting the predicted C_s values into the semi-empirical equation, the corresponding swelling potential was calculated and compared against the experimentally measured values. This indirect validation approach provides an additional layer of evidence supporting the accuracy and reliability of the proposed C_s prediction models, confirming that the predicted swelling indexes are not only consistent with theoretical expectations but also produce reliable outcomes when applied in practical engineering analyses.

The results presented in Table 6.1 indicate that both machine learning-based models achieved superior predictive performance relative to the empirical regression model. The MLP-based equation achieved an R^2 value of 0.869 in estimating swelling potential, while the ELM-based equation produced a slightly higher R^2 of 0.870. However, a closer examination of the predicted S% values reveal notable differences in the behavior of the two machine learning approaches. Although the ELM model attained the highest

coefficient of determination, its predictions exhibit a tendency to slightly overfit the data, particularly by closely matching individual data points rather than accurately capturing broader trends. This localized sensitivity is most apparent in soils with intermediate plasticity indices ranging from 35% to 50% and may reduce the generalization ability of the ELM model in practice.

In contrast, the MLP-based model demonstrated superior generalization performance, providing stable and consistent predictions across a wide range of soil types and geotechnical conditions. This robustness makes the MLP model particularly advantageous for engineering applications, where reliable predictions are essential for design and risk assessment in expansive soil environments.

In summary, the validation results confirm the effectiveness of coupling machine learning-predicted swelling indices with a physically-based semi-empirical equation to estimate swelling potential. Among the three methods evaluated, the MLP-coupled approach offers the most balanced solution, combining predictive accuracy, generalization ability, and model interpretability. These attributes make the MLP-based model an attractive option for practical geotechnical engineering applications involving expansive soils.

Table 6.1 Detailed comparisons of three methods for estimating swelling index and swelling potential.

Soils	I_p (%)	G_s	γ_d (g cm^{-3})	C_s (Emp)	C_s (MLP)	C_s (ELM)	P_s (kPa)	P_f (kPa)	S % (Measured)	S % (Emp)	S % (MLP)	S % (ELM)
Anthem	27	2.72	1.63	0.055	0.011	0.054	94.2	7	4.5	3.7	2.8	2.7
Burleson	37	2.72	1.52	0.066	0.042	0.072	112.8	7	5.5	4.5	4.2	4.9
Colorado	42	2.70	1.57	0.078	0.064	0.095	137.7	7	8.2	5.9	5.7	6.1
Grayson	49	2.73	1.39	0.102	0.099	0.125	156.4	7	9.8	7.0	6.9	6.6
San Antonio	43	2.79	1.53	0.081	0.069	0.095	137.7	7	7.3	5.7	5.6	5.9
San Diego	28	2.72	1.65	0.055	0.013	0.048	50.5	7	3.4	2.9	2.3	2.3
Regina clay	44	2.82	1.92	0.084	0.074	0.094	679.0	1	16.7	16.2	16.0	16.4
Ankara clay	31.0	2.62	1.56	0.058	0.021	0.025	80	7	1.6	3.6	3.0	3.6
Padianallur soil	31.0	2.68	1.62	0.058	0.021	0.025	190	6.25	4.7	5.2	4.3	5.2
Trichy Soil	62.0	2.70	1.41	0.150	0.155	0.171	418	6.25	12.4	14.3	13.6	13.5
Waranagal soil	53.0	2.72	1.65	0.118	0.119	0.092	260	6.25	8.3	11.6	11.3	10.7
Turkey soil	58.0	2.60	1.27	0.137	0.141	0.134	467	7	10.7	12.2	11.7	11.3

Maryland clay	45.7	2.62	1.42	0.090	0.141	0.134	675	400	1.5	1.1	1.6	1.1
Mansfield clay	38.0	2.75	1.49	0.068	0.046	0.080	147.4	7	4.1	4.9	4.6	5.3
R^2	/			0.870	0.876	0.888	/		1	0.856	0.869	0.870

6.2 Case studies of the proposed methods for estimating swelling pressure

This section presents the validation and application of the proposed empirical equations, namely Eqs. (3.16) to (3.19), developed in Chapter 3 for predicting the swelling pressure of expansive soils. These equations were established based on the Multilayer Perceptron (MLP) algorithm and subsequently expressed in an empirical form to enhance their practicality and usability in geotechnical engineering applications. To evaluate the capability of reliability of the proposed prediction equations, eight case studies information on expansive soils from the literature were gathered from various regions worldwide. The selected expansive soils encompass a broad spectrum of geotechnical characteristics and expansive behaviors, ensuring a comprehensive assessment of the performance of the proposed models under different conditions.

The validation of the constant volume swelling pressure (P_{scv}) equations focused on four representative expansive soils: French clay from France, Guabirotuba Formation from Brazil, Oklahoma clay from the United States, and Regina clay from Canada. Fig. 6.1 presents the comparison between the measured swelling pressures and the predictions obtained using Eqs. (3.16) and (3.17). As shown in Fig. 6.1a, both equations capture the positive correlation between the initial suction and the swelling pressure for French clay. However, Eq. (3.17), which incorporates seven input parameters, provides higher prediction accuracy across the entire suction range, particularly at higher suction levels. In contrast, Eq. (3.16), which requires only three input parameters, tends to underpredict the swelling pressure when the suction exceeds 3000 kPa. A similar trend can be observed in Guabirotuba Formation (Fig. 6.1b). In this case, Eq. (3.16) produces an almost constant prediction of the swelling pressure, whereas Eq. (3.17) successfully captures the nonlinear increase associated with changes in suction. For Oklahoma clay (Fig. 6.1c), both equations offer reasonable estimates at lower suction levels; however, Eq. (3.17) consistently outperforms Eq. (3.16) as suction increases. In the case of Regina clay (Fig. 6.1d), the predictive accuracy of Eq. (3.16) is noticeably reduced. This reduction is likely due to the limited input data available for this particular soil type. Nevertheless, Eq. (3.17) demonstrates relatively reliable predictions across the entire suction range.

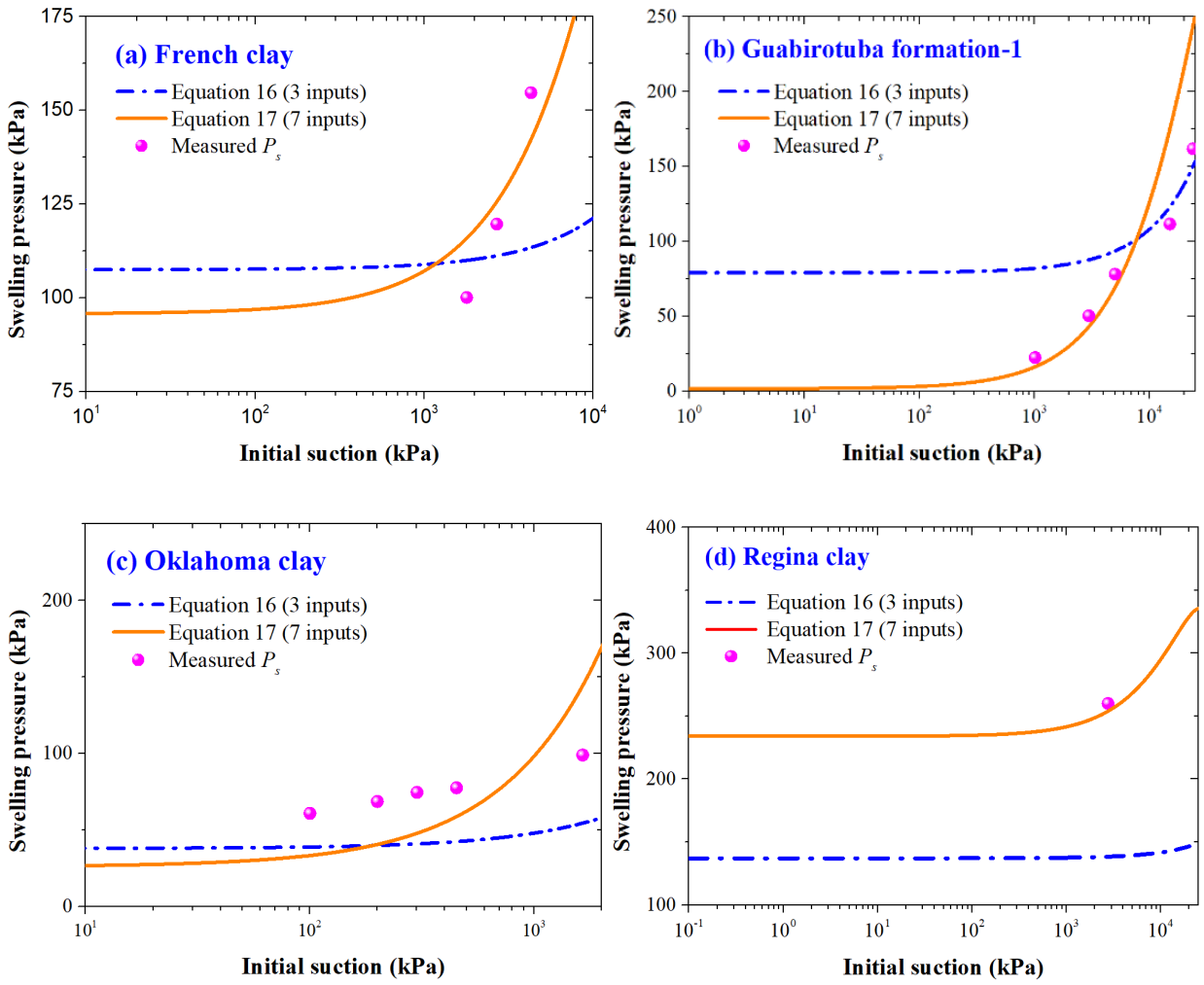
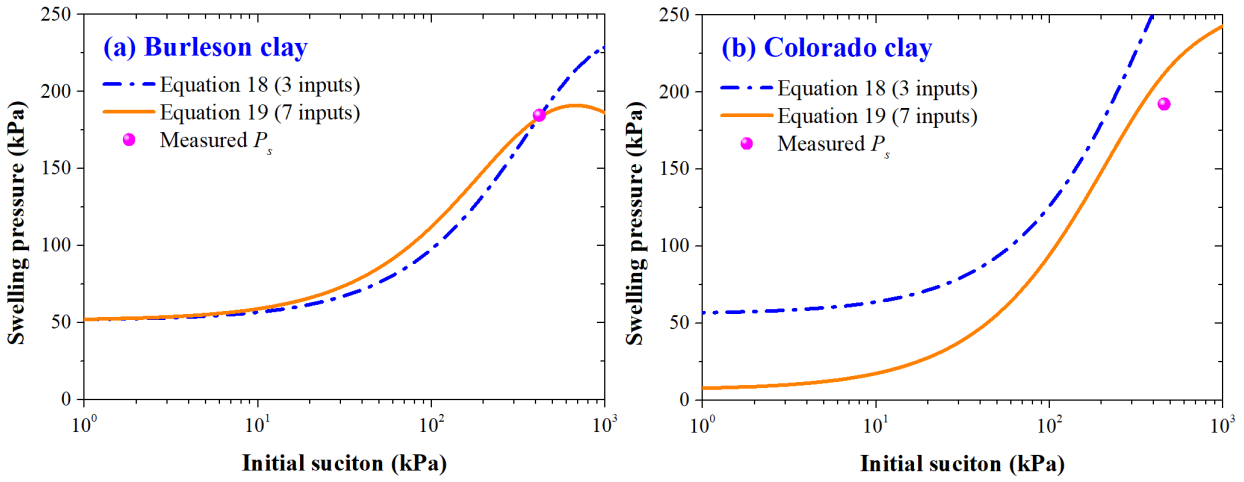


Fig. 6.1 Comparison among Eq. (3.16), (3.17) and measured P_{scv}: (a) French clay; (b) Guabirotuba Formation-1; (c) Oklahoma clay; (d) Regina clay.

The statistical evaluation results corresponding to these predictions are summarized in Table 6.2. The mean absolute percentage error (MAPE) values indicate that Eq. (3.17) substantially improves prediction accuracy compared to Eq. (3.16). For example, the MAPE for French clay decreases from 14.6% with Eq. (3.16) to 9.6% with Eq. (3.17). In the case of Guabirotuba Formation, although the overall prediction error remains relatively high due to the complex behavior and heterogeneity of this soil, Eq. (3.17) still reduces the MAPE from 75.8% to 32.1%. A similar improvement is observed for Oklahoma clay, where the MAPE is reduced from 40.7% to 37.4%. Regina clay exhibits the most significant improvement, with the MAPE reduced from 46.9% with

Eq. (3.16) to just 3.8% with Eq. (3.17). These results underscore the effectiveness of Eq. (3.17), particularly when more comprehensive input data are available.

For the consolidation-swell swelling pressure (P_{scs}), four classic expansive soils from the United States were analyzed: Burleson clay, Colorado clay, Grayson clay, and San Diego clay. The comparison between the predicted and measured P_{scs} values is presented in Fig. 6.2. As shown in Fig. 6.2a, both Eqs. (3.18) and (3.19) provide accurate predictions for Burleson clay, with Eq. (3.19) yielding nearly perfect agreement with the measured data. The MAPE for Eq. (3.19) is as low as 0.3%, compared to 0.7% for Eq. (3.18). In the case of Colorado clay (Fig. 6.2b), Eq. (3.19) also demonstrates superior performance by reducing the MAPE from 39.1% with Eq. (3.18) to 10.4%. For Grayson clay (Fig. 6.2c), both equations produce acceptable predictions; however, Eq. (3.19) achieves a lower MAPE of 1.6%, compared to 9.7% for Eq. (3.18). In San Diego clay (Fig. 6.2d), Eq. (3.19) provides more stable and consistent predictions, resulting in a MAPE of 3.9%, whereas Eq. (3.18) tends to overpredict the swelling pressure at higher suction values, leading to a higher MAPE of 26.3%. The detailed validation results for these soils are summarized in Table 6.3.



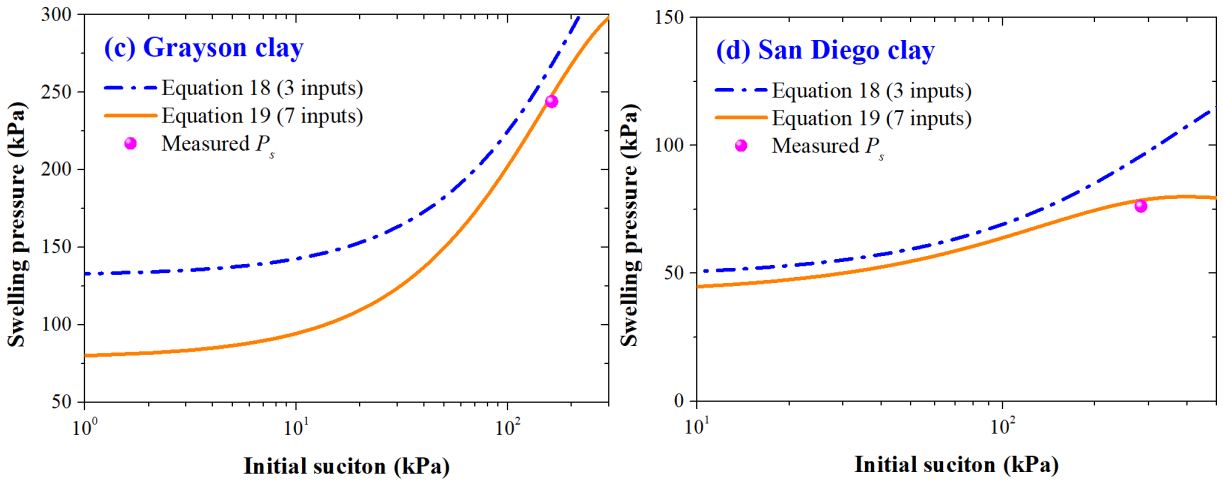


Fig. 6.2 Comparison among Eq. (3.18), (3.19) and measured P_{scs}: (a) Burleson clay; (b) Colorado clay; (c) Grayson clay; (d) San Diego clay.

Overall, the validation results clearly indicate that Eqs. (3.17) and (3.19), which incorporate seven input parameters, offer superior prediction accuracy when compared to the simpler Eqs. (3.16) and (3.18). The inclusion of additional variables such as clay content, swelling index, and initial void ratio allows these equations to better capture the complex interactions between soil properties and swelling pressure. This advantage is particularly significant for expansive soils exhibiting high plasticity indices or substantial variations in initial suction, where more simplified models may not be sufficient.

Nevertheless, despite the advantages of the comprehensive equations (Eqs. 3.17 and 3.19), the simplified equations (Eqs. 3.16 and 3.18) still provide reasonable predictions, particularly in cases where limited soil property data are available. These simplified models require only three input parameters—plasticity index, initial suction, and either clay content or gravimetric water content—making them practical and efficient tools for preliminary assessments and early-stage design in geotechnical engineering projects. Their ease of use and lower data requirements can significantly expedite the decision-making process in the early phases of project planning.

The validated models effectively capture the nonlinear relationship between initial suction and swelling pressure across various soil types and suction conditions. While the validation results are encouraging, some areas may benefit from additional data collection and further refinement,

particularly for complex soils such as Guabirotuba Formation. In addition, since the current equations are primarily developed from laboratory datasets, further validation using field data would be valuable in enhancing their applicability to real-world geotechnical engineering practice.

The proposed prediction equations offer a reliable tool for use in geotechnical engineering practice in the design and analysis of foundations and structures on expansive soils. The simplified equations (Eqs. 3.16 and 3.18) are particularly useful for rapid assessments during preliminary feasibility studies, while the comprehensive equations (Eqs. 3.17 and 3.19) are recommended for more detailed geotechnical investigations and design stages, where higher prediction accuracy is required. The adoption of these equations in practice has the potential to reduce reliance on time-consuming and costly laboratory testing, thereby improving the efficiency of expansive soil characterization and contributing to more effective risk assessment and management of engineering projects that deal with expansive soils.

Table 6.2 Validation results of swelling pressure prediction equations (P_{scv}) based on Eqs. (3.16) and (3.17)

Soil	ψ (kPa)	Measured P_{scv} (kPa)	Predicted P_s (kPa) Eq.(3.16)	RE (%)	MAPE (%)	Predicted P_{scv} (kPa) Eq.(3.17)	RE (%)	MAPE (%)
French clay	1790	100	110	9.9	14.6	115.9	15.8	9.6
	2695	120	111	7.1		125.6	5.0	
	4300	155	113	26.7		142.2	8.1	
Guabirotuba Formation	0	22	79	267.2	75.8	2	27.5	32.1
	1014	50	82	74.4		16	14.4	
	2973	78	88	19.8		43	11.2	
	5032	112	93	10.2		69	56.9	
	15074	162	123	7.4		175	50.5	
Okalahoma Clay	1	55	38	30.9	40.7	26	52.7	37.4
	100	61	39	36.1		33	45.9	
	200	69	40	42.0		40	42.0	

	300	74	41	44.6		48	35.1	
	450	77	42	45.5		59	23.4	
	1650	99	54	45.5		124	25.3	
Regina Clay	2767	260	138	46.9	46.9	250	3.8	3.8

Table 6.3 Validation results of swelling pressure prediction equations (P_{scs}) based on Eqs. (3.18) and (3.19)

Soil	**ψ (kPa)**	**Measured P_{scs} (kPa)**	**Predicted P_s (kPa) Eq.(3.18)**	**RE (%)**	**MAPE (%)**	**Predicted P_{scs} (kPa) Eq.(3.19)**	**RE (%)**	**MAPE (%)**
Burleson clay	419	184	183	0.7	0.7	184	0.3	0.3
Colorado clay	459	192	267	39.1	39.1	125.6	10.4	10.4
Grayson clay	161	244	268	9.7	9.7	248	1.6	1.6
San Diego clay	283	76	96	26.3	26.3	115.9	3.9	3.9

6.3 Case studies of the proposed methods for estimating swelling potential

The database established in this study is primarily based on test results performed on laboratory samples. These samples have the characteristics of small size, uniform texture, and exposure to a single wetting and swelling cycle making their swelling behavior relatively idealized. However, in engineering practice, the volumetric behavior of in-situ expansive soils is often far more complex and is influenced by various factors. Typical expansive soils exhibit layered and fissured structures and are significantly influenced by climate variations and long-term dry-wet cycles. These factors make it challenging for laboratory results to fully represent the actual swelling behavior observed in the field. To evaluate the practical applicability of Eq. (4.8), it has been applied to five different published case studies from the literature: (i) natural heave in open ground due to rainfall; (ii) pipeline leakage-induced heave under building concrete slab; (iii) heave of excavated slope with rooted vegetation; (iv) ground heave under spread footing; and (v) ground heave induced by excavation and artificial rainfall.

6.3.1 Natural heave in open ground due to rainfall

The case study site selected for this research is located in the Maryland suburb, approximately 10 kilometers west of Newcastle, New South Wales, Australia (Fityus et al., 2004). This region lies along Australia's eastern seaboard and is extensively underlain by expansive clay soils, known for their problematic shrink-swell behavior. The Maryland area has a long history of ground movement-induced damage to residential developments, making it an ideal location for evaluating the predictive capabilities of Eq. (4.8) in estimating the swelling potential of expansive soils. The site forms part of a dedicated research facility established to monitor the long-term behavior of expansive soils under natural climatic conditions and various surface treatments. Data collected from this site over several decades have been instrumental in advancing the understanding of expansive soil mechanics and informing geotechnical design practices in eastern Australia.

The climate of the region is temperate and coastal, with annual rainfall typically ranging between 1,000 and 1,200 millimeters. Seasonal variations in rainfall and temperature drive fluctuations in soil moisture content, particularly in the upper layers of the soil profile. These moisture variations are the principal factors controlling the cyclic shrink-swell behavior observed in the Maryland

clays. Evapotranspiration rates are highest during the summer months, contributing to substantial drying of the upper soil horizons. The site itself is relatively flat, with a gentle slope of 2.5 degrees toward the south-southeast. Surface runoff serves as the primary drainage mechanism, directing water toward an alluvium-filled floodplain approximately 300 meters from the site. Vegetative cover is predominantly kikuyu grass, with a large eucalyptus tree on the western boundary influencing localized soil suction profiles.

Geologically, the site is underlain by the Dempsey Formation of the Permian Tomago Coal Measures. The soils are residual in nature, having developed in situ through the weathering of underlying shales, mudstones, and siltstones. The soil profile consists of a surficial dark brown silty clay layer (CL) extending to a depth of 0.5 meters, underlain by an orange-brown high plasticity clay (CH) to a depth of 1.0 meter. Below this, a mottled pale brown to grey silty clay with ironstone gravels extends to 1.5 meters, followed by a pale grey-brown silty clay of medium to high plasticity. At depths beyond 2.0 meters, the profile comprises brown-grey silty clay interbedded with extremely weathered siltstones, transitioning into laminated light and dark grey clay layers mixed with highly weathered siltstones at 3.0 meters.

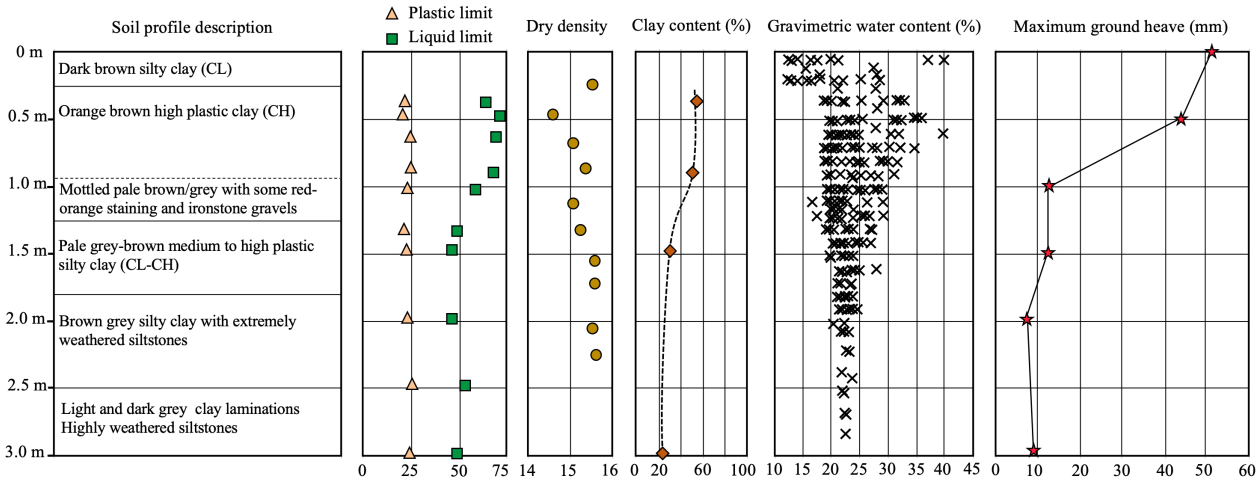


Fig. 6.3 Geotechnical properties of the Maryland clay site (Modified after Fityus et al., 2004)

The geotechnical properties of these soil layers are summarized in Fig. 6.3. The figure presents the stratigraphic description alongside key soil indices, including Atterberg limits (plastic and liquid

limits), dry density, clay content, gravimetric water content, and maximum ground heave. The plasticity characteristics indicate a progressive increase in plasticity index with depth, peaking within the orange-brown high plasticity clay horizon. Dry density measurements reveal a relatively consistent profile, while clay content is notably high within the upper 1.0 meter of the soil column, which aligns with observed high plasticity. Gravimetric water content shows significant scatter, reflective of seasonal moisture fluctuations and localized variability. The final column of Fig. 6.3 illustrates the distribution of maximum ground heave with depth, with peak heave values concentrated within the upper 1.0 meter of the profile.

Based on these observations, the depth of the active zone at the Maryland site has been identified as extending from 0.5 meters to 1.0 meter. This zone experiences the most pronounced moisture variations and, consequently, the greatest volume change, resulting in surface ground movements ranging between 40 and 70 millimeters. The expansive behavior of the soils within this depth range is directly responsible for the seasonal ground heave observed across the site. Therefore, the case study focuses on predicting the swelling potential specifically within this topsoil layer, as it represents the critical zone impacting shallow foundations and surface structures.

To quantify the swelling potential of this active zone, Eq. (4.8) was applied using site-specific input parameters derived from field and laboratory investigations. These parameters include the plasticity index, clay fraction, initial gravimetric water content, dry density, and the range of seasonal suction variation measured within the top 0.5m-1.0 meter of soil. The application of Eq. (4.8) yielded a predicted average swelling potential of 7.2% for the upper 0.5-1.0 meter of soil.

The predicted swelling potential was compared with measured values obtained from field monitoring and laboratory oedometer tests on undisturbed samples. The average measured swelling potential for the same soil horizon was 6.4%, suggesting a reasonably close agreement with the prediction. This slight overestimation of swelling potential by the model has been consistently observed across other case studies conducted in this research. The reasons for this discrepancy are analyzed in Section 6.3.6 and are attributed to factors such as spatial variability in soil properties, heterogeneity of residual soil profiles, and the limitations inherent in empirical modeling approaches when applied to complex unsaturated soil behavior.

Nevertheless, the Maryland case study demonstrates the practical applicability of Eq. (4.8) in predicting the swelling potential of expansive soils under field conditions. The model successfully captures the magnitude of volume change associated with seasonal moisture variations, particularly within the most active portion of the soil profile. The results from this case support the broader conclusion that Eq. (4.8) provides a reliable and efficient tool for preliminary assessment of swelling potential in expansive soils, informing geotechnical design strategies aimed at mitigating the risks posed by cyclic ground movement.

6.3.2 Pipeline leakage-induced heave under building concrete slab

Regina clay is widely recognized as one of the most problematic expansive soils in Canada, particularly in southern Saskatchewan. Due to its high montmorillonite content, this clay exhibits significant shrink-swell behavior in response to changes in moisture content. Seasonal climatic variations, in combination with human activities such as vegetation removal and water leakage, often lead to dramatic volume changes in these soils. Widespread structural damages to residential and light industrial buildings over the past several decades in Regina region expansive soils.

This case study summarized focuses on a light industrial building located in north-central Regina, Saskatchewan, which was constructed in 1961 on an expansive Regina clay deposit. The building became a focal point of a comprehensive field investigation after experiencing significant heaving and cracking within one year of completion. The distress was attributed to a leak in a hot-water line beneath the slab, which released approximately 35,000 liters of water into the underlying soil (Yoshida et al., 1983). This leakage dramatically altered the soil moisture regime, reducing matric suction in the expansive clay and triggering substantial heave of the floor slab. Fig. 6.4 shows the floor plan of the study site and the contours of the measured ground heave, illustrating the spatial extent of ground movement across the slab area.

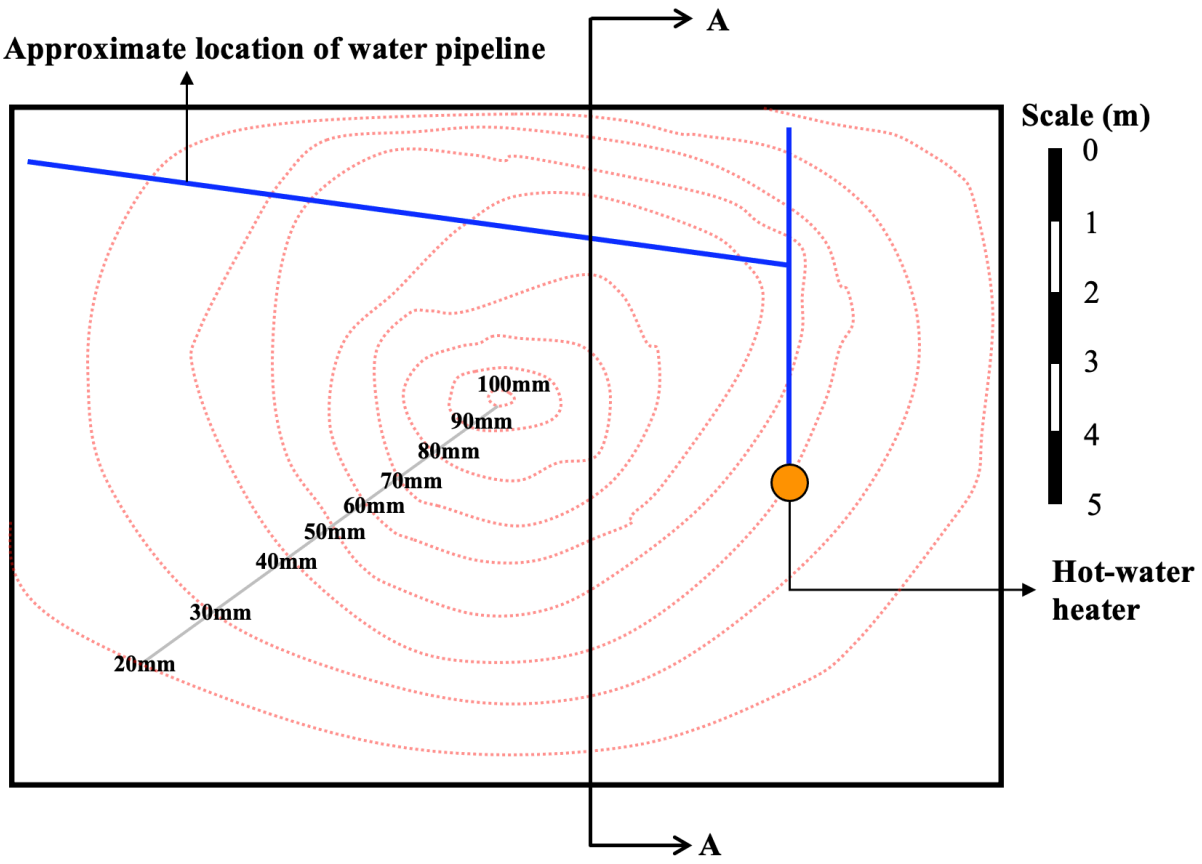


Fig. 6.4 Floor plan of study site and contours of measured heave (Modified after Yoshida et al., 1983)

To better understand the mechanisms of heave at this site, Vu and Fredlund (2004) conducted a detailed numerical analysis considering a 2.3-m thick deposit of Regina clay beneath the slab. The concrete slab was 100 mm thick and subjected to a uniform surface load of 5.76 kPa. Water infiltrated from the damaged hot-water line beneath the slab, migrating downward and laterally. Over a 150-day infiltration period, the soil suction near the surface decreased from -888 kPa to near zero, resulting in near-saturation conditions and corresponding volume expansion within the clay layer. Fig. 6.5 presents the geometry and boundary conditions used in the seepage analysis, showing the imposed suction boundaries and the location of the water source. This boundary condition setup replicates the conditions under which heave occurred and allows for accurate simulation of the infiltration and swelling processes.

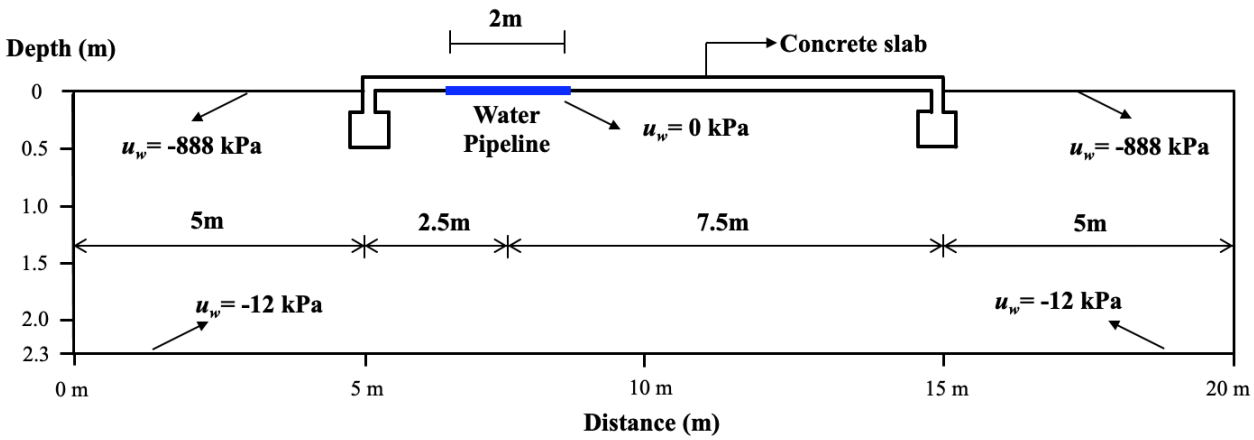


Fig. 6.5 Seepage analysis boundary setup (Modified after Vu and Fredlund 2004)

The soil-water characteristic behavior of the Regina clay was established through laboratory testing, providing essential data for the prediction model inputs. The relationship between volumetric water content, degree of saturation, and matric suction is shown in Fig. 6.6, which presents the estimated soil-water characteristic curve (SWCC) for Regina clay.

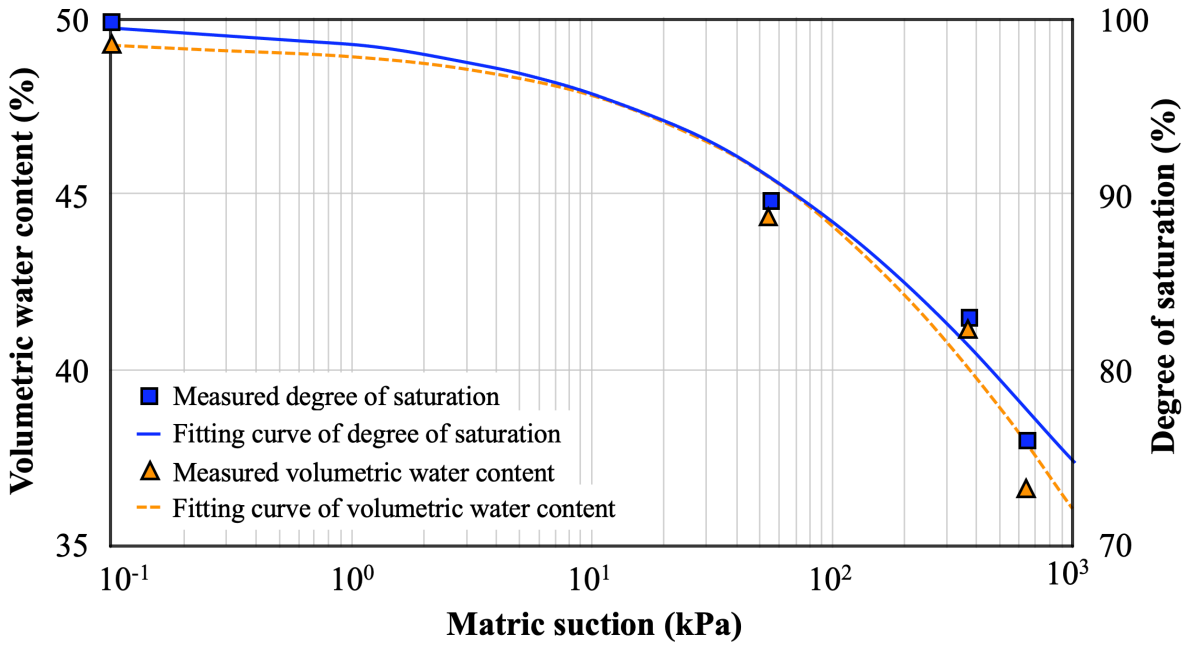


Fig. 6.6 Soil-water characteristic curve of Regina clay (Modified after Vu and Fredlund 2004)

Field monitoring at the site recorded a maximum ground heave of 106 mm beneath the slab after the infiltration event. Vu and Fredlund (2004) reported this vertical displacement, which corresponded to a swelling potential of approximately 4.6%. The measured vertical displacements over time and depth, as well as the predicted values from the numerical model, are summarized in Fig. 6.7. The figure illustrates how swelling progressed with time and depth, with close agreement between predicted and measured values in the near-surface zone, though some differences were noted at greater depths.

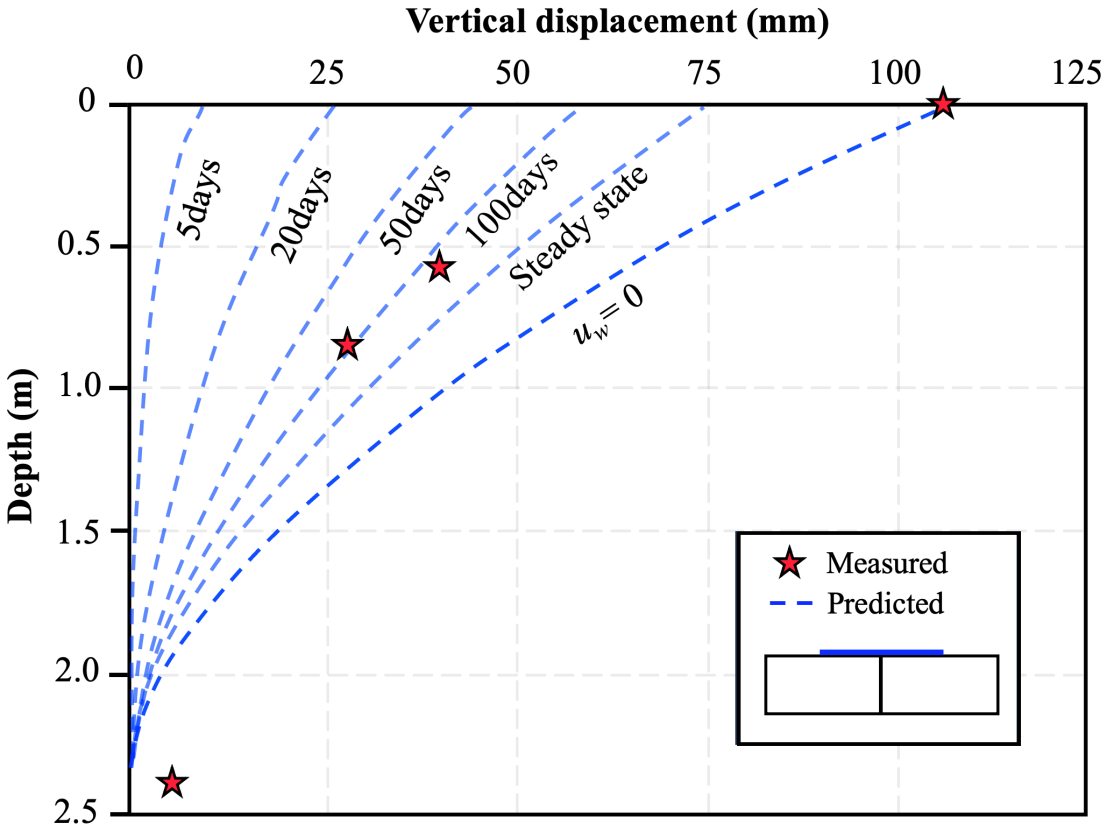


Fig. 6.7 Measured vs predicted displacements reported by Vu and Fredlund (2004)

For the purposes of validating Eq. (4.8), this case study focused on predicting the swelling potential of the upper portion of the Regina clay deposit that experienced the most significant moisture variation. The input parameters—plasticity index, clay content, initial water content, dry density, and suction variation—were derived from the laboratory and field data. The liquid limit of the Regina clay was recorded at 77%, with a plastic limit of 33%, and the natural gravimetric water

content was approximately 29%. The clay fraction was notably high, contributing to its high swelling capacity, while the dry density was measured at 18.88 kN/m³.

Using Eq. (4.8), the predicted swelling potential for the affected clay layer was 7.1%. This prediction was compared with the measured swelling potential of 4.6%, derived from the maximum heave recorded at the site. Although the predicted value slightly overestimated the observed swelling potential, the magnitude was consistent with the behavior expected of expansive soils under such conditions. The reasons for this discrepancy are discussed in Section 6.3.6 and include potential factors such as heterogeneity within the Regina clay, uncertainties in suction measurement, and simplifications inherent in empirical predictive models.

6.3.3 Heave of excavated slope with rooted vegetation

A field study conducted by Ng et al. (2003) was also selected to validate Eq. (4.8) for predicting the swelling potential of Zao-Yang expansive soil in an excavated slope subjected to artificial rainfall. This study provides valuable insight into the interaction between climatic conditions, vegetation, desiccation cracks, and the volumetric behavior of expansive soils. The test site is situated along the intake canal of the Dagangpo second-level pumping station in Zaoyang, Hubei Province, China, approximately 230 km northwest of Wuhan and 100 km south of the South-to-North Water Transfer Project's intake canal in Nanyang, Henan Province. The site lies in a semi-arid region characterized by an average annual rainfall of about 800 mm, with over two-thirds occurring between May and September.

The canal, excavated in 1970, features an average cut slope height of 13 meters and a slope angle of 22°. Over several decades, shallow slope failures have frequently occurred, primarily during the rainy season. The slope material consists of yellow-brown stiff fissured clay, locally interbedded with grey clay layers and iron concretions. The surficial soils exhibit extensive desiccation cracking, with crack depths commonly exceeding 1.0 meter. The primary vegetation includes couch grass and weeds, with root depths observed to range from 0.1 m to 0.3 m on the excavated surfaces (Zhan et al., 2007). This vegetation cover exerts minor suction variation control on the soil profile but does not significantly mitigate seasonal moisture fluctuations.

The slope stratigraphy and monitoring layout are illustrated in Fig. 6.8. The soil profile mainly consists of yellow-brown clay with mottled grey zones and varying amounts of iron concretions. Instrumentation includes tensiometers, thermal conductivity sensors, ThetaProbes for water content monitoring, and earth pressure cells installed along multiple sections of the slope. The R1 section, located at the crest of the slope, was selected for this study due to its high susceptibility to infiltration and swelling. Prior to artificial rainfall, the upper soil layers exhibited high suction conditions, with values greater than 200 kPa, indicative of a desiccated state.

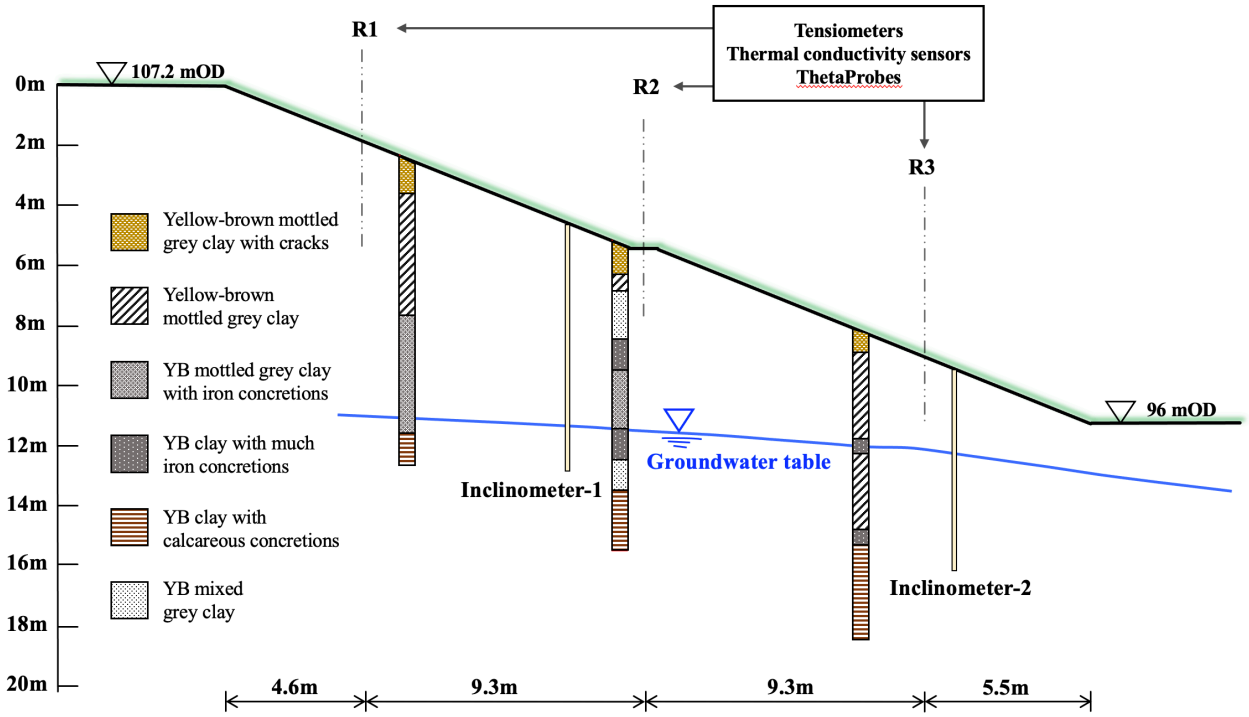


Fig. 6.8 Cross-section of the instrumented slope at Zaoyang site (modified after Ng et al. (2003))

Artificial rainfall experiments were carried out over a period of approximately one month, simulating extended wet conditions on the slope surface. During and after rainfall infiltration, substantial reductions in suction were observed within the upper 1.5 meters of soil, with the most pronounced changes occurring within the top 0.5 meters. Fig. 6.9 shows the variation of gravimetric water content with depth at different times during the rainfall period. These data demonstrate progressive wetting of the near-surface soils and deeper infiltration over time. The

decrease in suction and increase in water content triggered swelling in the expansive clay layers, which was closely monitored through surface displacement measurements.

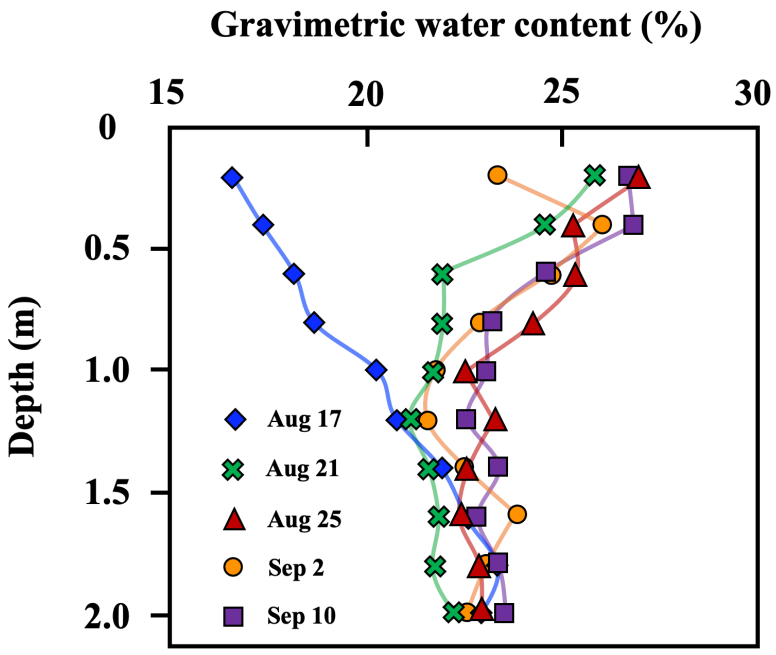


Fig. 6.9 Gravimetric water content profiles during artificial rainfall infiltration (modified after Ng et al. (2003))

Swelling measurements collected from the R1 monitoring points are presented in Fig. 6.10. The figure shows time-dependent vertical swelling displacements at various depths (0.1 m, 0.5 m, and 1.0 m) during and after the rainfall period. The results indicate a clear correlation between rainfall infiltration and volumetric expansion of the soil, with the largest swelling observed at 0.1 m depth, reaching up to 30 mm by the end of the observation period.

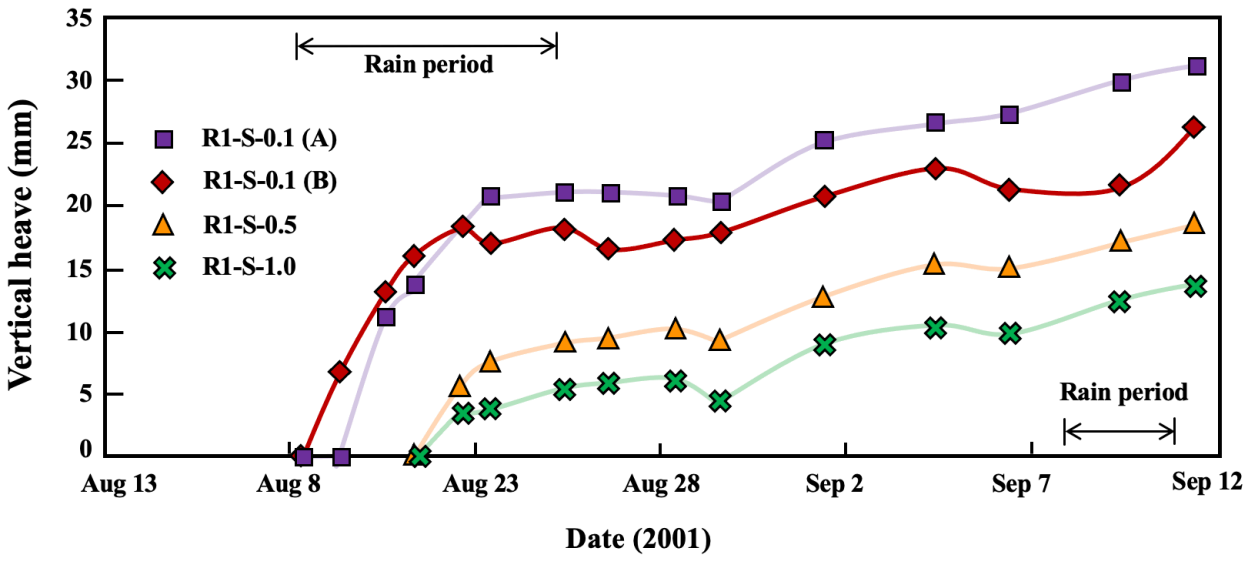


Fig. 6.10 Swelling of Zaoyang expansive soil at different depths (modified after Ng et al. (2003))

For the purpose of validating Eq. (4.8), this case study focused on the upper 0.1m -0.4 m of soil near point R1, where the most significant changes in moisture content and suction were recorded. This shallow layer is highly relevant in assessing the swelling potential in infrastructure applications, especially for light-loaded structures and road subgrades adjacent to cut slopes. Following one month of artificial rainfall infiltration, the in situ swelling potential of the upper soil layer was measured as 4.3%. Laboratory oedometer tests conducted on undisturbed samples from the same depth indicated swelling potentials ranging from 6% to 8%. Using Eq. (4.8), and based on input soil properties including plasticity index, clay content, initial water content, dry density, and seasonal suction variation, the predicted swelling potential was 6.7%.

Although the predicted value slightly exceeded the field-measured swelling potential, it closely aligned with laboratory results. This minor discrepancy is attributed to natural field heterogeneities, crack healing, and the differences between controlled laboratory conditions and actual field environments.

6.3.4 Ground heave under spread footing

In addition, a comprehensive field experiment conducted by Briaud et al. (2003) was selected to validate the performance of Eq. (4.8) in estimating the swelling potential of expansive soils under spread footing. The study site was in Arlington, Texas, USA, where expansive soils are a major concern for shallow foundation design due to significant seasonal fluctuations in moisture content. The region is characterized by a humid subtropical climate with hot, dry summers and mild, wet winters, contributing to cyclic changes in soil suction and water content. These environmental factors make Arlington an ideal location to study the behavior of expansive soils in field settings.

The experimental program was part of a broader investigation into the shrink-swell behavior of expansive clays beneath spread footings. Four isolated spread footings, each measuring 2.0 m × 2.0 m in plan and 0.6 m thick, were constructed for long-term monitoring of ground movements caused by seasonal moisture variations. Among these, the RF1 footing was specifically selected for analysis in this study due to its relatively undisturbed natural infiltration conditions and absence of artificial wetting or controlled watering, making it most representative of practical field conditions. Fig. 6.11 illustrates the layout of the RF1 footing and the surrounding monitoring points, along with the boring schedule for subsoil investigations. A total of nine boreholes were drilled at different times between June 1999 and July 2001 to collect soil samples for laboratory testing and to monitor in-situ soil properties. These boreholes provided critical data for developing a comprehensive understanding of the soil profile and its response to climatic influences over time.

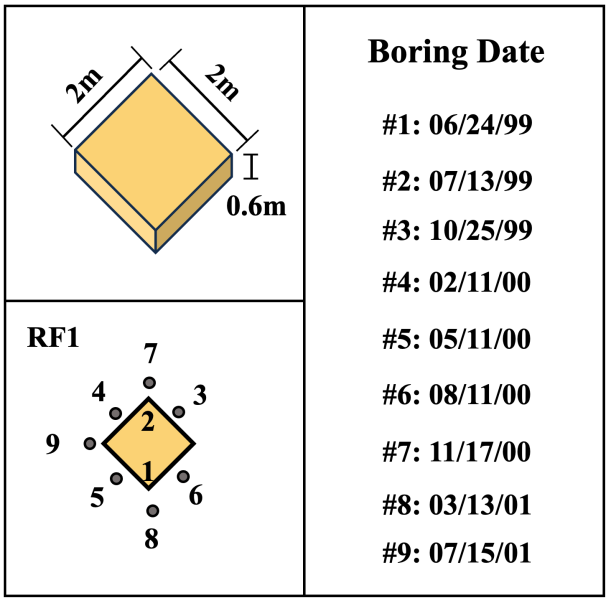


Fig. 6.11 Layout of spread footing if RF1 area and boring program (modified after Briaud et al. (2003))

The subsurface conditions at the RF1 site consist of two primary soil layers, each exhibiting distinct physical and mechanical characteristics that contribute to the overall swelling behavior of the site. The upper layer, extending from the ground surface to a depth of 1.8 m, comprises dark gray silty clay with trace amounts of fine sand. The second layer, from 1.8 m to 3.0 m, consists of brown silty clay, also containing fine sand and calcareous materials. Both soils are classified between CL and CH according to the Unified Soil Classification System (USCS), indicating moderate to high plasticity and potential for volume change. A summary of key geotechnical properties for these layers is presented in Fig. 6.12. The dark gray silty clay has an average undrained shear strength of 151.5 kPa, a total unit weight of 20.3 kN/m³, a fine particle content (% < 0.002 mm) of 47.7% and a mean water content of 20.73%. Its liquid limit and plastic limit are 51.3% and 22.3%, respectively, resulting in a plasticity index of 29.0%. The underlying brown silty clay has a slightly higher undrained shear strength of 179.8 kPa and a marginally higher total unit weight of 20.4 kN/m³, but its plasticity is slightly lower, calculated at 23.3%, with a liquid limit of 40.4% and a plastic limit of 17.1%. These soil parameters are the inputs for Eq. (4.8) in estimating the swelling potential.

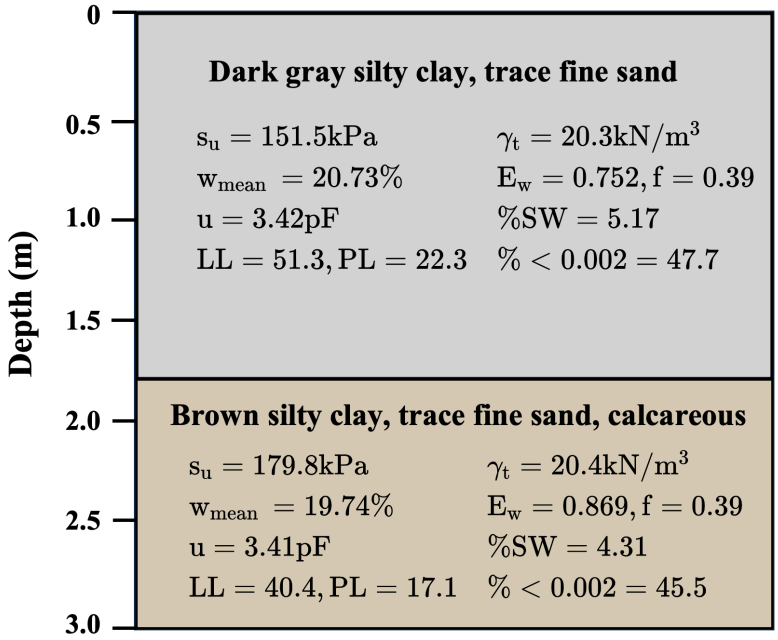


Fig. 6.12 Soil stratigraphy and geotechnical properties in RF1 (modified after Briaud et al. (2003))

The monitoring of vertical ground movements beneath RF1 was carried out over an extended period of more than two years, from August 1, 1999, to October 1, 2001. Displacement measurements were recorded monthly, providing valuable insights into the seasonal shrink-swell behavior of the expansive clay subgrade. Fig. 6.13 presents the recorded vertical displacement history of RF1 during the monitoring period. The figure clearly illustrates the cyclic nature of ground movement, with heave observed during wet seasons (fall and winter) and settlement during dry periods (spring and summer). The data indicate that ground movement at RF1 was strongly correlated with changes in soil water content, which varied between 10.9% and 27.5% during the observation period. These fluctuations in moisture content were identified as the primary driver of the shrink-swell behavior observed at the site.

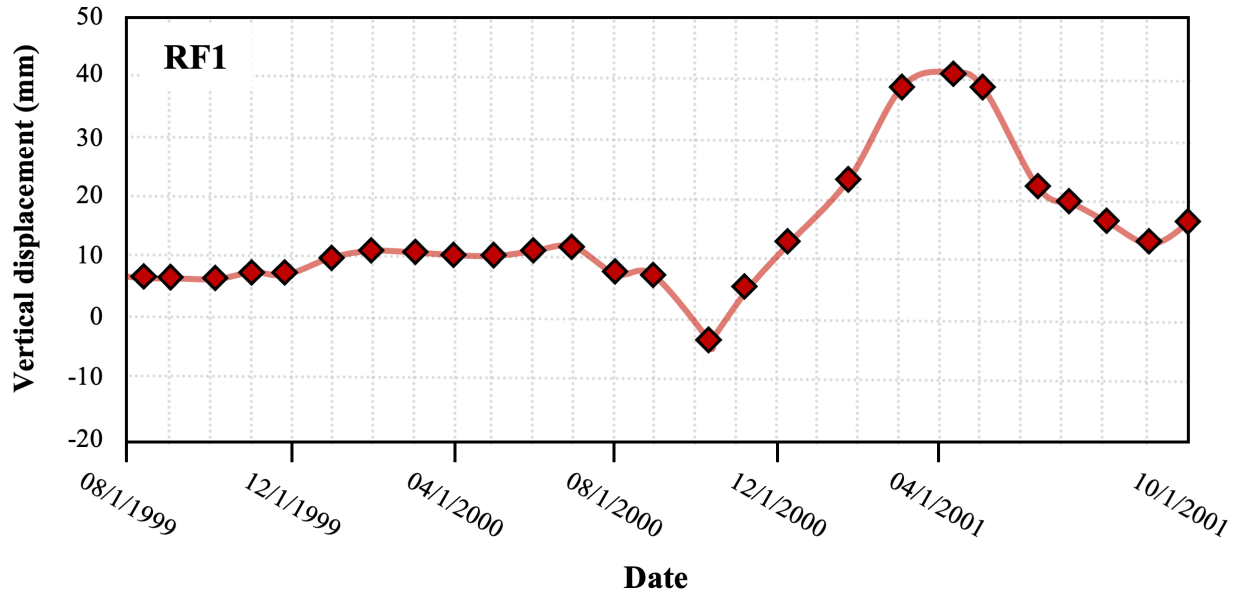


Fig. 6.13 Measured vertical displacement at the footing in RF1 (modified after Briaud et al. (2003))

For the purpose of validating Eq. (4.8), the displacement data collected between October 1, 2000, and April 1, 2001, were selected as the focus of the analysis. This six-month period was chosen because it included both a dry season, during which the soil underwent significant shrinkage, and a subsequent wet season, which induced noticeable heave. During the dry season, the soil experienced a maximum vertical shrinkage of 14 mm, while the wet season resulted in a vertical heave of 32 mm. The total vertical movement of 46 mm over the monitoring period was interpreted as representative of the full seasonal cycle of soil volume change. Considering the total soil thickness of 3.0 m beneath the footing, the field-derived average vertical swelling potential was calculated to be 1.5%. Complementary laboratory oedometer tests were performed on undisturbed samples extracted from the RF1 site during the same period. These tests indicated a swelling potential of 4.8% under controlled laboratory conditions. Using Eq. (4.8), and applying site-specific input parameters such as plasticity index, clay fraction, initial water content, dry density, and seasonal suction variation, the predicted swelling potential for the RF1 site was calculated to be 2%. This value falls between the field-derived potential of 1.5% and the laboratory-measured potential of 4.8%, demonstrating that Eq. (4.8) offers a balanced and reliable estimation of swelling potential that more closely reflects field conditions. The model's ability to capture the magnitude

of swelling behavior under variable environmental conditions reinforces its suitability for preliminary design assessments and risk evaluations for structures built on expansive soils.

6.3.5 Ground heave induced by excavation and artificial rainfall

The final case study for swelling potential is based on the research conducted by Al-Shamrani and Dhowian (2003), which investigated the swelling behavior of expansive shale deposits under controlled field conditions in Al-Ghatt, Saudi Arabia. The town of Al-Ghatt, located approximately 270 km northwest of Riyadh, has long suffered from differential heave problems, with widespread structural damage reported in residential buildings, pavements, and sidewalks. Diagonal cracking in beams and walls, door and window misalignments, and severe tilting of structures have been commonly observed due to the swelling and shrinkage behavior of the underlying expansive soils in this region.

In response to these geotechnical challenges, a dedicated field experimental station was established at a site where severe heave-related damage had previously been documented. The test area, measuring 20 m by 20 m, was prepared by removing approximately 1.5 m of overburden soil to expose the highly expansive shale formation beneath. This shale deposit, extending to depths of 8 to 10 m, consists predominantly of clay-sized particles and is classified as CH soil. Despite the absence of montmorillonite, mineralogical analysis using X-ray diffraction (XRD) confirmed kaolinite as the predominant clay mineral, along with smaller amounts of illite. The high swelling potential of this shale was attributed to its high plasticity, intense weathering, and low in-situ moisture content relative to its plastic limit.

To evaluate the heave potential under controlled saturation, an artificial wetting system was installed. The system comprised 19 sand drains, spaced evenly across the test site, and extended 4 m deep into the shale. These drains facilitated uniform infiltration, allowing water to percolate into the shale mass. Six monitoring stations were equipped with thermocouple psychrometers to measure soil suction, moisture probes for water content tracking, and surface and deep-seated heave plates to measure vertical displacements.

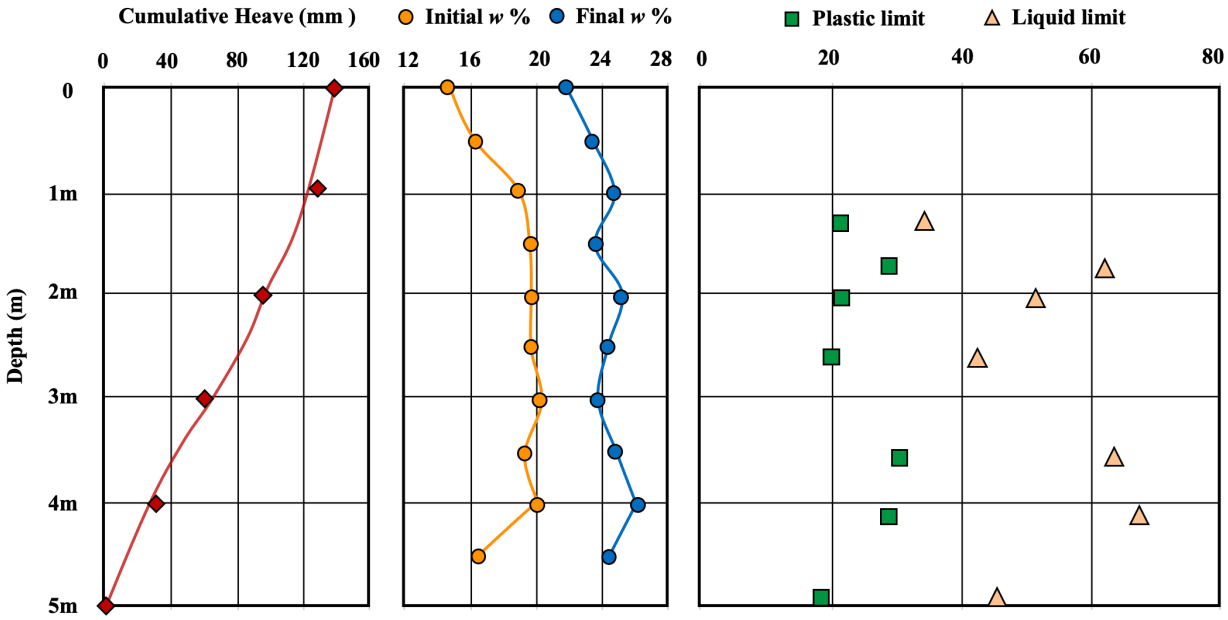


Fig. 6.14 Ground heave, moisture variation, and Atterberg limits of Al-Ghatt shale (modified after Briaud et al. (2003))

Over a 54-week monitoring period, the site was subjected to artificial saturation to simulate extreme wetting conditions. The measured cumulative heave within the top 5 m of the shale reached approximately 140 mm, corresponding to an average vertical swelling potential of 2.8%. The heave profile with depth is shown in Fig. 6.14 (left panel), indicating the distribution of vertical displacement throughout the active zone. The greatest heave occurred in the uppermost layers, tapering off with depth as the swelling potential diminished beyond 5 m. This distribution reflects the decreasing moisture penetration and reduced suction variation at greater depths.

The middle panel of Fig. 6.14 illustrates the changes in gravimetric water content before and after saturation. The initial water content ranged between 14% and 18%, increasing to as much as 26% following saturation. This significant increase in moisture content, particularly within the upper 2 m of soil, resulted in a marked reduction in matric suction from initial values of 4500–5500 kPa to 800–1500 kPa. This reduction in suction was the primary driver for volumetric expansion and the corresponding ground heave.

The third panel of Fig. 6.14 shows the spatial distribution of plastic and liquid limits with depth. The liquid limit values ranged from 55% to 68%, while the plastic limit values ranged from 27%

to 35%. The plasticity index was consistently high, confirming the expansive potential of the shale formation. The high clay fraction, with over 70% of particles finer than 0.002 mm, further reinforced the classification of this deposit as highly expansive.

In addition to field measurements, three types of oedometer tests were conducted to evaluate the swelling potential under laboratory conditions. These included the free swell oedometer test, the constant volume swell test, and the swell under overburden pressure test. Laboratory results indicated an average swelling potential of 6.8%, substantially higher than the field-observed 2.8%.

For this case study, Eq. (4.8) was applied to predict the swelling potential of the expansive shale deposit at the Al-Ghatt field site. The predicted swelling potential for the top 5 m of soil was 2.3%. Although this value is slightly lower than the field-measured swelling potential of 2.8%, it demonstrates significantly closer agreement with the actual field observations compared to the laboratory-derived swelling potential of 6.8%.

6.3.6 Discussion and summary of case study results

The proposed equation has demonstrated suitability for predicting the field swelling potential of expansive soils, as evidenced by the comprehensive case studies conducted across five countries on three continents. These case studies encompass a wide range of expansive soil types and diverse site conditions (see Table 6.4). Although the equation tends to slightly overestimate the measured swelling potential in some instances, it has consistently shown strong applicability in various geo-infrastructure scenarios. The results confirm the reliability of Eq. (4.8) as a practical tool for preliminary assessment of swelling potential in expansive soils. Nevertheless, discrepancies between predicted and measured values were observed in certain cases. The potential reasons for these differences are analyzed as follows:

(i) Differences in soil characteristics and scale

The database used for developing Eq. (4.8) is primarily derived from laboratory tests on small-scale specimens. These specimens are typically uniform in texture, carefully prepared to minimize variability, and are often only 25.4 mm (1 inch) thick. Such controlled conditions provide highly representative swelling potential measurements at the specimen scale. In contrast, the field case studies involve soil layers ranging from 0.3 m to 5.0 m in thickness, frequently consisting of

multiple layers with varying degrees of heterogeneity, fissures, and localized variations in water content and density. This represents a scale difference of nearly one to two orders of magnitude, introducing complexities that are not captured in laboratory conditions. Despite this, Eq. (4.8) maintained a reasonable level of predictive accuracy, with deviations from field measurements typically within 0.5-fold. This demonstrates the model's robustness in extrapolating laboratory-based predictions to field-scale applications. Fig. 6.15 presents a comparison of Eq. (4.8) predictions with both field and laboratory measurements, illustrating its performance across different scales.

(ii) Differences in boundary conditions

Another significant source of discrepancy lies in the difference between laboratory and field boundary conditions. Oedometer tests, which form the basis for much of the input data in this study, primarily measure vertical swelling deformation while strictly limiting radial expansion due to the lateral confinement provided by rigid steel rings. This setup often results in higher measured vertical swell strains, as the energy of the swelling process is focused in the vertical direction. In contrast, expansive soils in field conditions typically exhibit both vertical and lateral deformation. Surface soils in situ, particularly those with lower stiffness, tend to expand laterally, thereby reducing the magnitude of vertical swelling observed at the ground surface. This difference in deformation behavior between constrained laboratory conditions and less-restricted field environments can partially explain the tendency for Eq. (4.8) to overpredict swelling potential when compared to field measurements.

(iii) Impact of dry–wet cycles

In the laboratory, specimens are commonly subjected to a single wetting cycle, during which they absorb water until saturation, reaching their maximum swelling potential. Field soils, however, are continuously exposed to multiple natural dry–wet cycles. Repeated drying can lead to shrinkage and the development of desiccation cracks, while successive wetting may not fully restore the swelling potential due to structural degradation and the partial closure of these cracks. Over time, these cycles can result in a reduced effective swelling potential compared to the theoretical maximum observed under controlled laboratory conditions. Therefore, the cumulative effects of

these environmental factors tend to lower the field swelling potential, contributing to the difference between laboratory-derived values and field measurements.

(iv) Non-uniform infiltration conditions

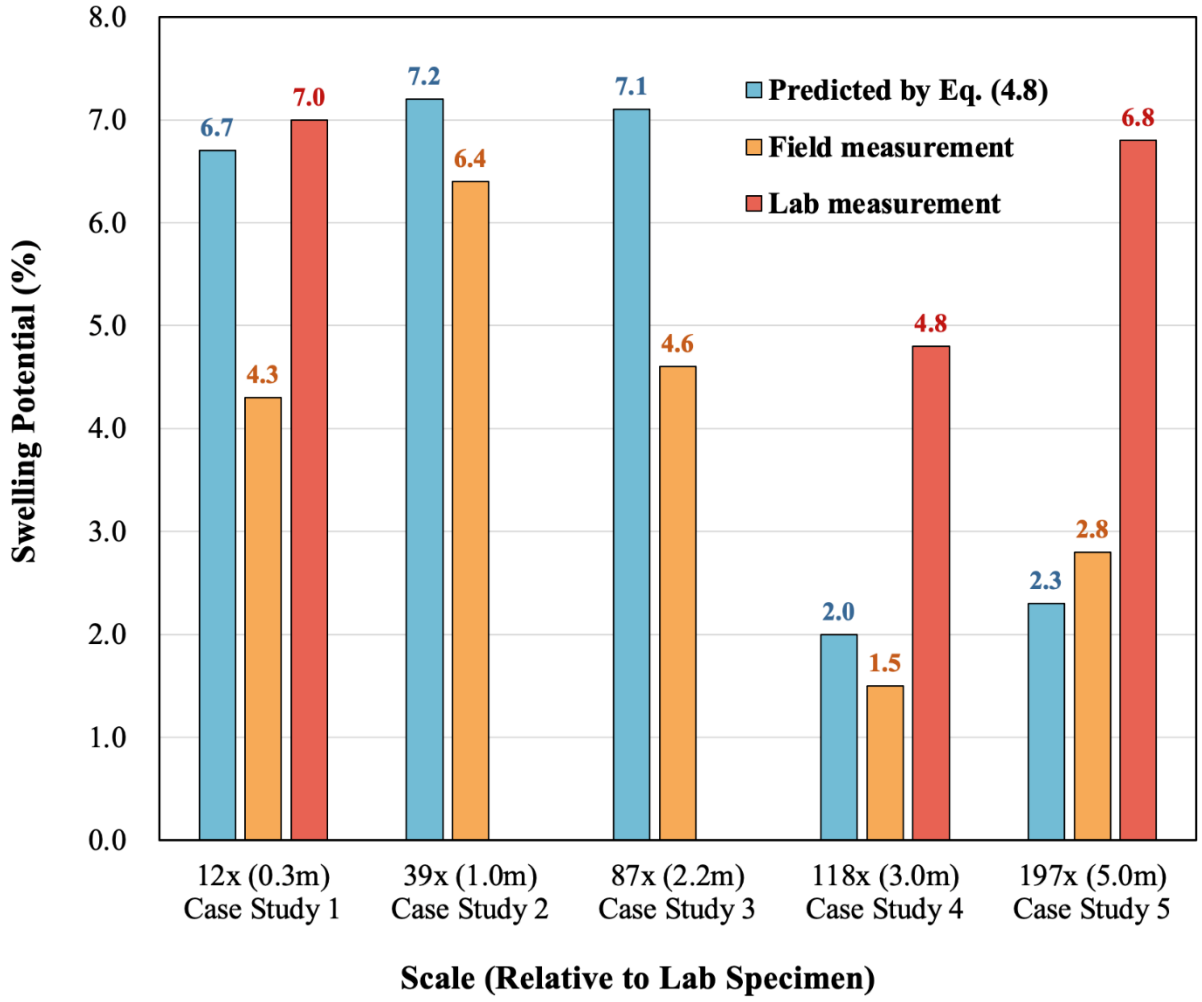
Uniform infiltration is typically assumed in laboratory tests, where water ingress is carefully controlled and applied evenly across the specimen. In the field, however, water infiltration is often highly non-uniform due to surface runoff patterns, vegetation cover, and the presence of cracks and fissures within the soil. Cracked soils can exhibit preferential flow paths, leading to rapid and localized water ingress, which may cause uneven swelling within different sections of the soil profile. This spatial variability in infiltration and moisture distribution is difficult to replicate in laboratory settings and is another factor that can contribute to discrepancies between field and laboratory observations.

Despite these inherent differences between laboratory testing and field conditions, the proposed Model 3 in Chapter 4 and its associated equation, Eq. (4.8), have demonstrated reliable performance. The validation results from five distinct case studies, representing a wide range of climatic zones, soil types, and engineering conditions, confirm the equation's ability to provide realistic predictions of swelling potential. Detailed comparisons between Eq. (4.8) predictions and both field and laboratory measurements are provided in Table 6.4. These results highlight the model's potential as a valuable tool for geotechnical engineers in the preliminary evaluation of expansive soil behavior.

Nevertheless, it is acknowledged that additional research is necessary to further assess the predictive capabilities of Eq. (4.8) under a broader range of field scenarios, including complex geological environments and long-term moisture variation conditions. Future studies that integrate more comprehensive field data, including long-term monitoring of dry–wet cycles and varying infiltration regimes, will be essential for refining the model and enhancing its applicability. Such investigations will also contribute to bridging the gap between idealized laboratory conditions and the complex realities of expansive soil behavior in the field.

Notably, for Case Studies 4 and 5, the predicted values are closer to the field measurements in comparison to the laboratory results. This may be attributed to two main reasons. First, these two

cases were not included in the model development dataset as the associated laboratory specimens may differ in soil properties or test methods from those represented in our database. Second, the model was trained on a diverse set of laboratory tests data collected from various regions worldwide, which is likely contributing to better capturing general trends. These trends in turn are reasonably capturing the integrated response of expansive soils under field-scale conditions.



Note: The scale values represent relative thickness compared to lab specimens (1x = 25.4 mm).

Fig. 6.15 Comparative evaluation of swelling potential across scales

Table 6.4 Summary of case study results for swelling potential

Case study	Soil	Country	Depth	C	I_p	Δw	ρ_d	q	G_s	$\varepsilon\%$ (Predicted)	$\varepsilon\%$ (Field)	$\varepsilon\%$ (Measured)
Natural heave in open ground due to rainfall	Maryland Clay	Australia	0.5m ~1.0 m	55.5	45.6	14	1.54	0	2.65	7.2	6.4	-
Pipeline leakage-induced heave under building concrete slab	Regina Clay	Canada	0m ~ 2.3 m	46	44	6.2	1.44	5.76	2.82	7.1	4.6	-
Heave of excavated slope with rooted vegetation	Zao-Yang expansive Clay	China	0.1m ~ 0.5m	39	31	3.8	1.62	0	2.67	6.7	4.3	6%-8%
Ground heave under spread footing	Arlington Clay	USA	0 m ~3.0 m	46.8	26.7	4.4	1.71	0	2.65	2.0	1.5	4.8%
Ground heave induced by excavation and artificial rainfall	Al-Ghatt Shale	Saudi Arabia	0 m ~5.0 m	72	35	6	1.88	0	2.78	2.3	2.8	6.8%

6.4 Case studies of the proposed methods for estimating compression index

The compression index is a key parameter in evaluating the consolidation settlement behavior of compressible soils. To verify the effectiveness of Eq. (5.18) in predicting this parameter, a case study on settlement prediction was conducted.

6.4.1 Case study A: Consolidation settlement of an untreated expansive soil site

The compression index is a key parameter in evaluating the consolidation settlement behavior of compressible soils. To verify the effectiveness of Eq. (5.18) as a parameter in the settlement predictions, a case study results summarized by Jeevanantham et al., 2023 on a normally consolidated Black Cotton Soil (BCS) were used for validation purposes. BCS is an expansive clayey soil predominantly found in Australia, India, and Sudan. It derives its name from its characteristic dark color and its traditional suitability for cotton cultivation. BCS is classified as a highly plastic and expansive soil, with significant swelling and shrinkage potential due to its high montmorillonite clay content. These soils typically exhibit a high liquid limit, wide plasticity index, low permeability, and are prone to substantial volume changes in response to fluctuations in moisture content. These characteristics make BCS particularly challenging for foundation design and ground improvement in geotechnical engineering.

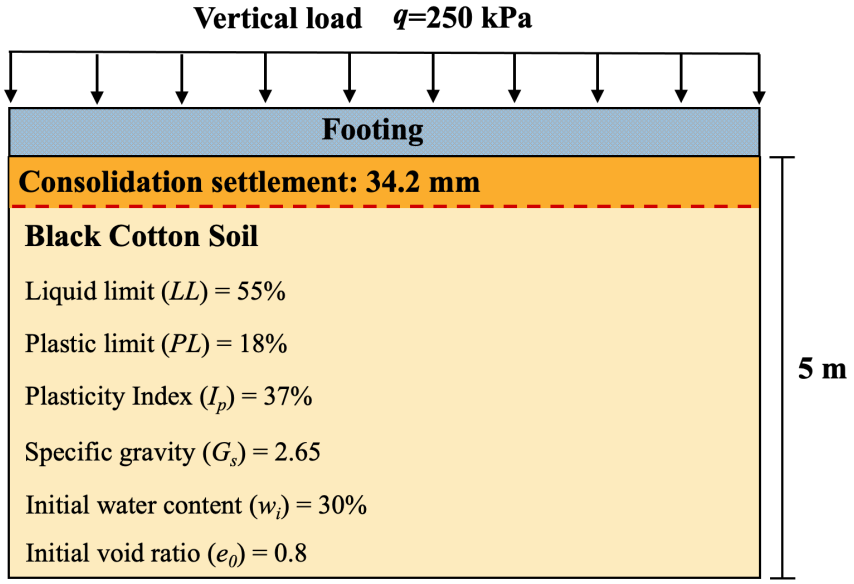


Fig. 6.16 Consolidation settlement of footing on Black Cotton Soil (Case study A)

In this case study, the soil properties of the BCS layer were reported as follows: liquid limit (55%), plasticity index (37%), initial void ratio of (0.8), and dry density (1.47 g/cm³). The compressible soil layer had a thickness of 5 m, with an initial effective vertical stress of 100 kPa. An additional uniform surface load of 250 kPa was applied to simulate the stress imposed by a typical shallow foundation. Field monitoring indicated a final consolidation settlement of 34.2 mm under the applied load, as illustrated in Fig. 6.16. Using Eq. (18), the predicted compression index is 0.212. This predicted value was subsequently incorporated into the classical consolidation settlement equation for normally consolidated clays summarized as Eq. (6.1):

$$\Delta s = \frac{C_c}{1 + e_0} \times H \times \log\left(\frac{\sigma_f'}{\sigma_0'}\right) \tag{6.1}$$

where Δs is the consolidation settlement of normally consolidated clay, H is the thickness of the compressible layer, σ_0' and σ_f' represent the initial and final effective stresses, respectively.

By substituting the predicted C_c value into this equation, the calculated consolidation settlement was determined to be 32.04 mm. The relative error between the calculated and observed settlements was 6.4%, which demonstrates a close agreement between the predicted and measured values. This result verifies the reliability and accuracy of Eq. (5.18) for predicting the compression index and highlights its practical applicability in routine geotechnical engineering projects involving expansive soils.

6.4.2 Case study B: Settlement behavior of expansive soil under a square footing

To further assess the applicability of Eq. (5.18) for predicting the compression index, a second case study was conducted using in-situ data obtain by Ejjaaouani (2008) from Ouarzazate, a city in the northwestern region of Morocco. This site has a well-documented history of structural damage resulting from an overconsolidated expansive soils. Mineralogical analysis of the clay fraction revealed a composition of 10–15% illite, 25–40% kaolinite, and a dominant presence of montmorillonite ranging from 45–55%. This composition suggests a high potential for volume change, particularly due to the substantial montmorillonite content. A thickness of 1.7 m,

corresponding to the active zone thickness, was adopted for the soil layer in the analysis. The analyzed 1 m × 1 m square footing, denoted as SF1 and shown in Fig. 6.17, was subjected to a uniformly distributed load of 400 kPa to simulate structural loading conditions.

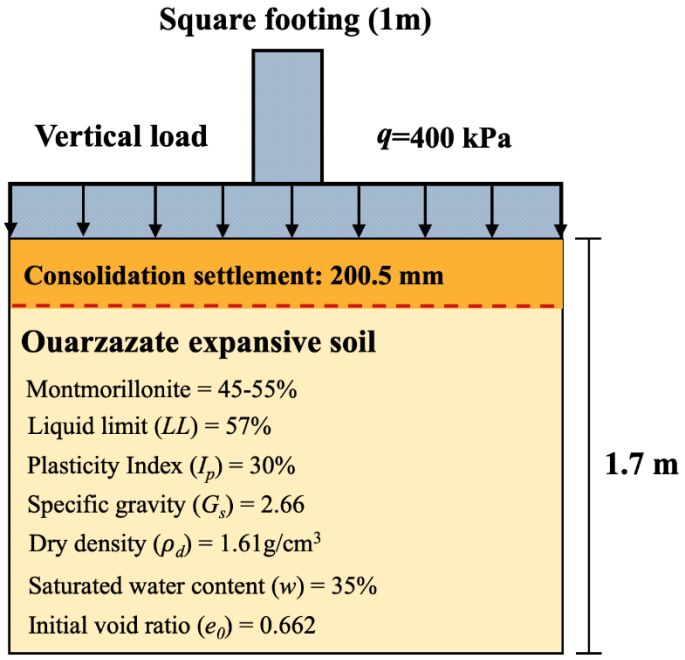


Fig. 6.17 Consolidation settlement of a square footing on Ouarzazate expansive soil (Case study B)

The properties of the tested clay include liquid limit (57%), plasticity index (30%), initial void ratio (0.662), dry density (1.61 g/cm³), and saturated water content (35%). Field monitoring under these conditions recorded a final consolidation settlement of 201 mm. Using Eq. (5.18), the predicted compression index was calculated to be 0.155. This value was subsequently incorporated into Eq. (6.2), a commonly used equation for estimating primary consolidation settlement for overconsolidated clays.

$$\Delta s = \frac{C_s}{1+e_0} \times H \times \log\left(\frac{\sigma_c'}{\sigma_0'}\right) + \frac{C_c}{1+e_0} \times H \times \log\left(\frac{\sigma_f'}{\sigma_c'}\right) \tag{6.2}$$

where C_s represents swelling index and σ_c' represent the preconsolidation pressure.

The swelling index was not reported in this case study but was estimated using the method proposed by Tu and Vanapalli (2016), as follows:

$$C_s = 0.188/\left[1 + e^{(44.526 - I_p)/15.636}\right] \tag{6.3}$$

The preconsolidation pressure was approximately 50 kPa, and the estimated swelling index from Eq. 6.3 was 0.053. Based on these values, the computed consolidation settlement was 190.3 mm, resulting in a relative error of 5.1% compared to the measured value (200.5 mm). This close agreement confirms the effectiveness of Eq. (5.18) in predicting compression index in expansive soils.

6.4.3 Case study C: Settlement prediction for expansive soil under embankment loading

To further validate the applicability of Eq. (5.18) for predicting the compression index of expansive clays, a third case study was conducted on settlement behavior beneath embankment loading, as shown in Fig. 6.18, using field data obtained by Jiang et al. (2018) from a test site located in the Mile Basin, Yunnan Province, China. The site lies near the Kunming–Nanning high-speed railway, which extends over 715.8 km. According to the borehole investigations, the upper 5 m of the subgrade consists of yellow-brown organic clay and red-brown clay with calcareous concretions, both of which are heavily overconsolidated, with a preconsolidation pressure of approximately 200 kPa. These soils are weathered products of Tertiary mudstone, marl, and claystone, and are characterized by medium to high swelling potential due to their mineralogical composition, particularly the montmorillonite content, which ranges from 12.7% to 27.7%.

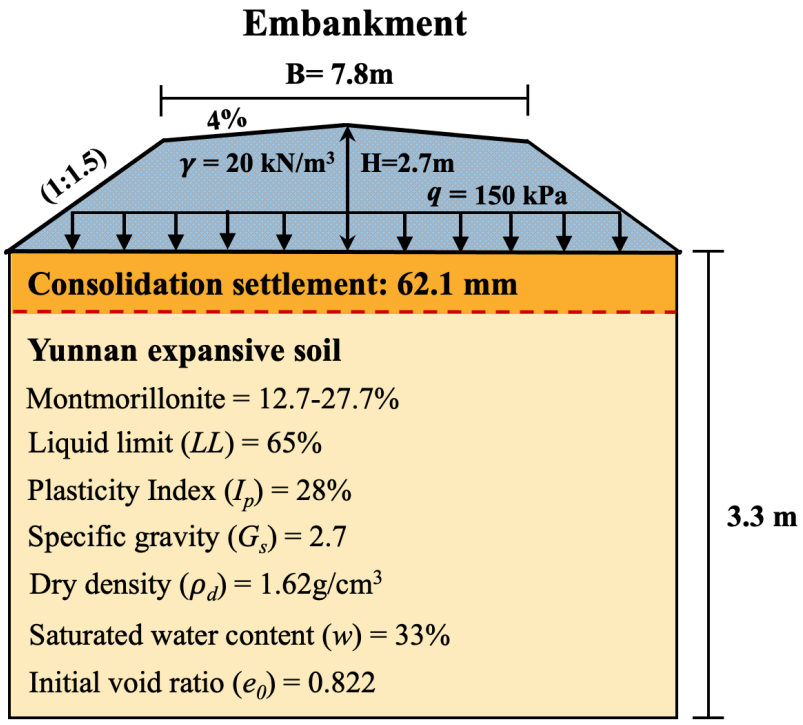


Fig. 6.18 Consolidation settlement of Yunnan expansive soil under embankment (Case study C)

This case study focuses on a 3.3 m thick expansive clay stratum at sampling point JS3 within the T1 plate loading zone. Laboratory testing revealed the following average geotechnical properties: a liquid limit of 65%, plasticity index of 28%, initial void ratio of 0.822, and dry density of 1.62 g/cm³. The degree of saturation was measured at 87.1%. During field testing under fully saturated conditions, the swelling pressure was determined to be 21.5 kPa. A stress increment of 150 kPa was applied to simulate structural loading. Using Eqs. (5.18) and (6.3), the predicted compression index and swelling index were 0.207 and 0.048, respectively. These values were then incorporated into Eq. (6.2) to compute the primary consolidation settlement. The calculated settlement was 70.8 mm, which closely matched the field-measured settlement of 62.1 mm, with a relative error of approximately 14.0%. These findings indicate that Eq. (5.18) provides a reasonable estimation of the compression index in expansive soils, leading to settlement predictions that are consistent with field observations.

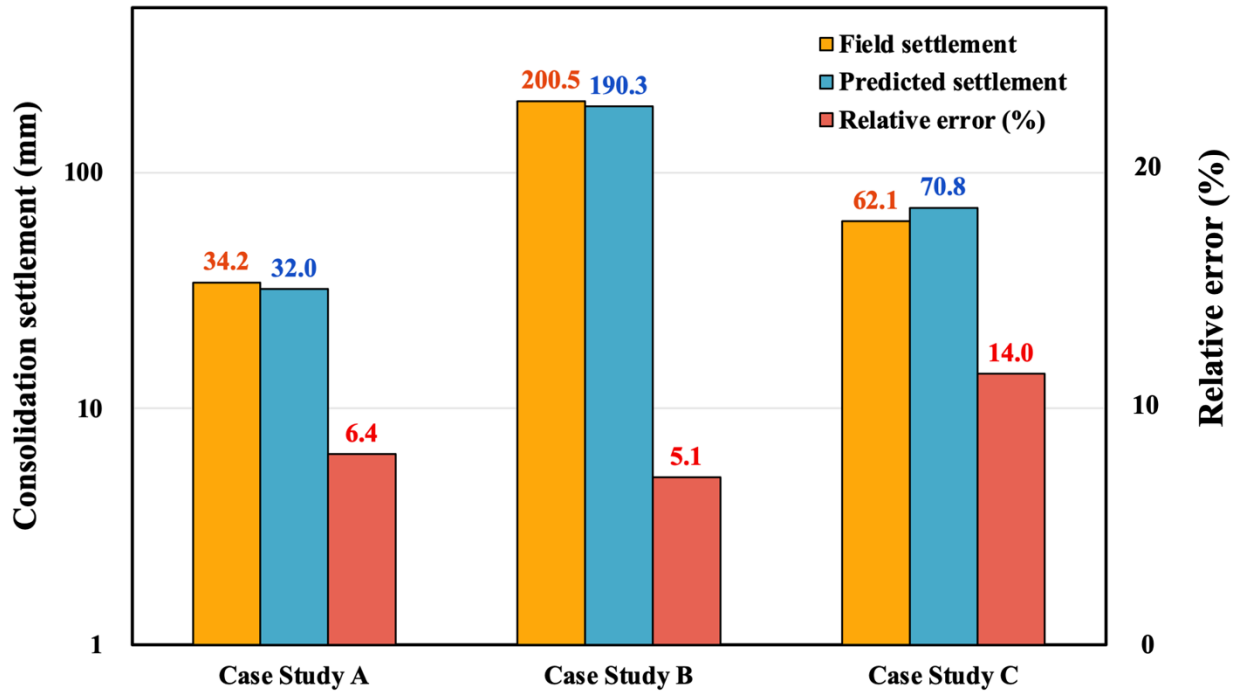


Fig. 6.19 Comparison of field and predicted consolidation settlements for the three case studies

In summary, the three case studies collectively illustrate that Eq. (5.18) performs well in estimating the compression index of expansive soils under varying site conditions and loading scenarios. When the predicted C_c values were applied within the framework of classical consolidation theory, the resulting settlement estimates showed good agreement with field measurements, with relative errors ranging between 5.1% and 14.0%, as shown in Fig. 6.19. These outcomes highlight the practical value of Eq. (5.18) in consistently and reliably capturing the compressibility behavior of expansive clays and support its use in preliminary design and settlement assessment in geotechnical and geological engineering applications.

6.5 Summary

Chapter 6 presents the validation and practical application of the predictive models proposed in this study, focusing on expansive soils. The chapter systematically evaluates the reliability, generalization ability, and engineering applicability of the models developed in previous chapters,

covering four key parameters: the swelling index (C_s), swelling pressure (P_s), swelling potential ($S\%$), and compression index (C_c).

Section 6.1 validates the C_s prediction models by integrating predicted swelling index values into a semi-empirical equation for estimating swelling potential. This indirect validation demonstrates that the predicted C_s values align with measured swelling behavior, confirming their practical utility in geotechnical applications.

Section 6.2 focuses on the validation of the P_s prediction models. Eight case studies of typical expansive soils from various countries were conducted to assess the accuracy of the proposed empirical equations derived from the MLP algorithm. The results show that the comprehensive equations (Eqs. 3.17 and 3.19), which incorporate seven input parameters, offer higher predictive accuracy than the simplified versions (Eqs. 3.16 and 3.18), especially for soils with complex behaviors.

Section 6.3 evaluates the field application of the $S\%$ prediction model (Eq. 4.8) across five diverse case studies from Australia, Canada, China, Saudi Arabia, and the United States. Despite the complexity and heterogeneity of field conditions, the model consistently provides reasonable estimates of field-scale swelling potential, supporting its suitability for practical engineering use.

Section 6.4 validates the C_c prediction model by incorporating the predicted values into consolidation settlement equations. Comparisons between predicted and measured settlements confirm the model's accuracy and demonstrate its applicability in assessing the settlement behavior of expansive soils under loading.

In conclusion, the validation results confirm that the proposed predictive models are reliable and practical tools for estimating the swelling and compressibility characteristics of expansive soils. They offer valuable support for geotechnical design and analysis, enabling more efficient risk assessment and decision-making in expansive soil engineering.

References

Al-Shamrani, M. A., Dhowian, A. W., 2003. Experimental study of lateral restraint effects on the potential heave of expansive soils. Engineering Geology, 69(1-2), 63-81.

Briaud, J.-L., Zhang, X., Moon, S., 2003. Shrink test–water content method for shrink and swell predictions. Journal of geotechnical and geoenvironmental engineering, 129(7), 590-600.

Ejjaaouani, H., 2008. Interactions des fondations et des sols gonflants: pathologie, calculs et études expérimentales. Thèse de doctorat, École Nationale des Ponts et Chaussées, Spécialité Géotechnique.

Fityus, S., Smith, D., Allman, M., 2004. Expansive soil test site near Newcastle. Journal of Geotechnical and Geoenvironmental Engineering, 130(7), 686-695.

Jeevanantham, V., Jayashree, J., and Roja, S.Y. 2023. Experimental analysis on swelling, shrinkage and consolidation behavior of expansive soils under wetting–drying cycles. IOP Conference Series: Earth and Environmental Science, 1258(1): 012006.

Jiang, G., Chen, W., Liu, X., Yuan, S., Wu, L., Zhang, C., 2018. Field study on swelling–shrinkage response of an expansive soil foundation under high-speed railway embankment loads. Soils Found. 58(6), 1538–1552.

Kumar, T. A., Raheena, M., Robinson, R., Thyagaraj, T., 2020. A rapid method of determination of swell potential and swell pressure of expansive soils using constant rate of strain apparatus. Geotechnical Testing Journal, 43(6), 1368-1378.

Liu, X., Buzzi, O., Yuan, S., Mendes, J., Fityus, S., 2016. Multi-scale characterization of retention and shrinkage behaviour of four Australian clayey soils. Canadian Geotechnical Journal, 53(5), 854-870.

Ng, C. W. W., Zhan, L. T., Bao, C. G., Fredlund, D. G., Gong, B. W., 2003. Performance of an unsaturated expansive soil slope subjected to artificial rainfall infiltration. Geotechnique, 53(2), 143-157.

Pedarla, A., 2013. SWCC and clay mineralogy based models for realistic simulation of swell behavior of expansive soils.

Puppala, A. J., Pedarla, A., Pino, A., Hoyos, L. R., 2017. Diffused double-layer swell prediction model to better characterize natural expansive clays. Journal of Engineering Mechanics, 143(9), 04017069.

Sridharan, A., Gurtug, Y., 2004. Swelling behaviour of compacted fine-grained soils. Engineering geology, 72(1-2), 9-18.

Vu, H. Q., Fredlund, D. G., 2004. The prediction of one-, two-, and three-dimensional heave in expansive soils. Canadian Geotechnical Journal, 41(4), 713-737.

Yoshida, R., Fredlund, D. G., Hamilton, J., 1983. The prediction of total heave of a slab-on-grade floor on Regina clay. Canadian Geotechnical Journal, 20(1), 69-81.

Yuan, S., Liu, X., Sloan, S. W., Buzzi, O. P., 2016. Multi-scale characterization of swelling behaviour of compacted Maryland clay. Acta Geotechnica, 11, 789-804.

Zhan, L.-t., Chen, P., Ng, C., 2007. Effect of suction change on water content and total volume of an expansive clay. Journal of Zhejiang University-SCIENCE A, 8(5), 699-706.

Zhan, T. L., Ng, C. W., Fredlund, D. G., 2007. Field study of rainfall infiltration into a grassed unsaturated expansive soil slope. Canadian Geotechnical Journal, 44(4), 392-408.

CHAPTER 7

INTEGRATED APPLICATION OF MODELS FOR PREDICTING CONSTANT VOLUME AND CONSOLIDATION-SWELL OEDOMETER TEST CURVES

7.1 Introduction[4]

In the preceding chapters, a series of prediction models were developed and validated to estimate key geotechnical parameters of expansive soils. Specifically, Chapter 3 proposed models for predicting the swelling index, C_s (Eq. 3.15) and swelling pressure, P_s (Eq. 3.16 and Eq. 3.18) based on easily measurable soil properties. Chapter 4 introduced a model (Eq. 4.8) for estimating the swelling potential, $\varepsilon\%$ (Eq. 4.7) while Chapter 5 focused on the prediction of the compression index, C_c (Eq. 5.18). Each model targeted a specific deformation characteristic and was constructed using distinct datasets of input parameters. To ensure reliability and generalizability, these models were independently validated in Chapter 6 through separate case studies using different soil datasets. This approach enabled separate predictions for each parameter but made it difficult to interpret the models together in an integrated way.

This chapter aims to address this limitation by bringing together all previously developed models and applying them to the same set of soils, enabling a unified analysis of the deformation behavior of expansive soils. This chapter links the predicted indices to their corresponding CVT and CST curves, where CVT captures C_s, P_{scv}, and C_c, and CST reflects C_s, P_{scs}, ε %,C_c. This approach not

[4] Work is under progress to summarize the contents in this chapter for submission to an international journal for peer review by **Zhang, A**., & Vanapalli, S. K.

only verifies the reliability of each model in an integrated setting but also enhances the overall understanding of soil behavior through the joint interpretation of all predicted parameters.

The structure of the predictive framework and its evolution across Chapters 3 to 7 is illustrated in Fig. 7.1, with Chapter 7 representing the final stage in which all models are jointly applied and compared using oedometer test curves from the same set of soil samples.

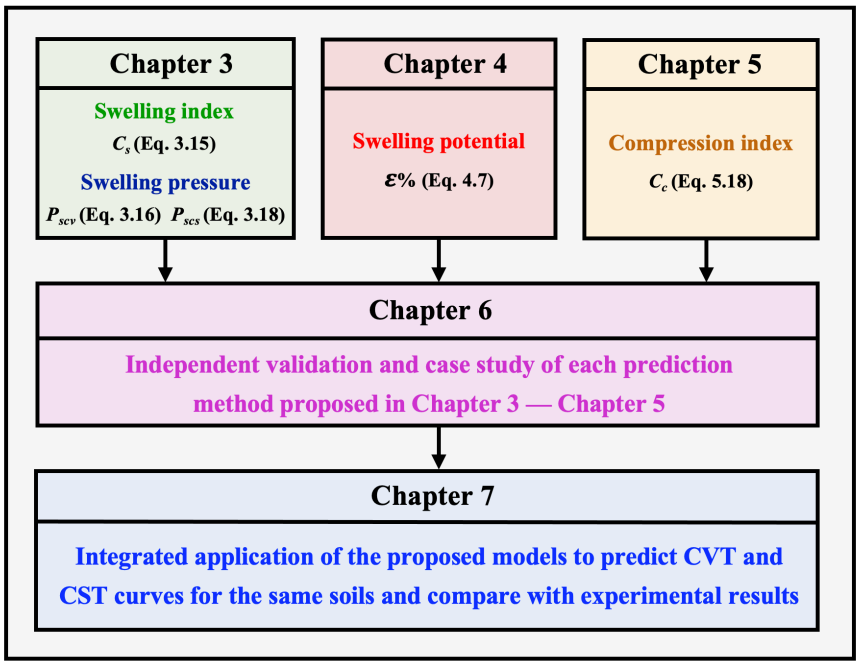


Fig. 7.1 Framework for model development, validation, and integrated application

7.2 Integrated validation of the proposed models using constant-volume test curves

This section presents an integrated validation of the proposed models using constant-volume test (CVT) curves from three distinct expansive soils: Regina Clay (Canada), Al-Qatif Clay (Saudi Arabia), and Dallas Soil (USA). The CVT provides a useful framework for validating the predicted swelling index (C_s), swelling pressure (P_{scv}), and compression index (C_c), enabling a comprehensive evaluation of the predictive capability of the models developed in Chapters 3 and 5.

For each soil, predicted values of C_s, P_{scv}, and C_c were used to reconstruct the CVT curves and compared with laboratory measurements. The comparison results are illustrated in Fig. 7.2 to Fig. 7.4.

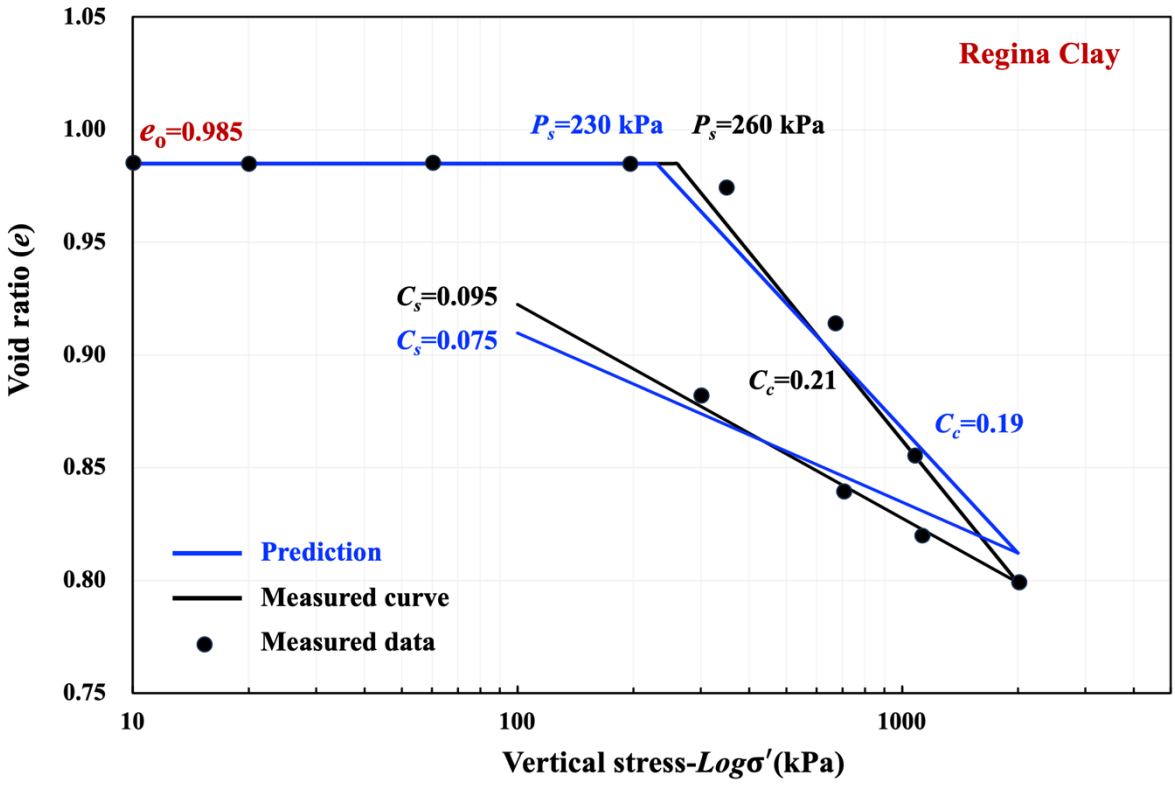


Fig. 7.2 Integrated model validation using CVT results for Regina Clay

As shown in Fig. 7.2, the predicted constant-volume test (CVT) curve (blue) for Regina Clay shows good agreement with the experimental results (black). Regina Clay is one of the most representative expansive soils in Saskatchewan, Canada, and has been widely studied due to its high swelling potential and the challenges it poses to light structures and transportation infrastructure. The test data used in this study were originally reported by Yoshida et al. (1983) and Vu and Fredlund (2004).

In the present analysis, the predicted swelling pressure is 230 kPa, compared to the measured value of 260 kPa, indicating that the model provides a satisfactory approximation of the swelling behavior under constant-volume conditions. The predicted compression index (C_c = 0.19) closely matches the measured value of 0.21, showing good consistency in the compression phase. The

swelling index (C_s) is slightly lower than the experimental result (0.075 vs. 0.095). Overall, the general shape of the e–logσ′ curve, including its key features, is well reproduced.

These results suggest that, although each model was developed independently, their combined application yields a coherent representation of the deformation response observed in constant-volume test curves. This highlights the potential of the integrated modeling approach to capture the coupled behavior of expansive soils based on simple soil properties, and to support the interpretation of their volume change behavior under constrained conditions.

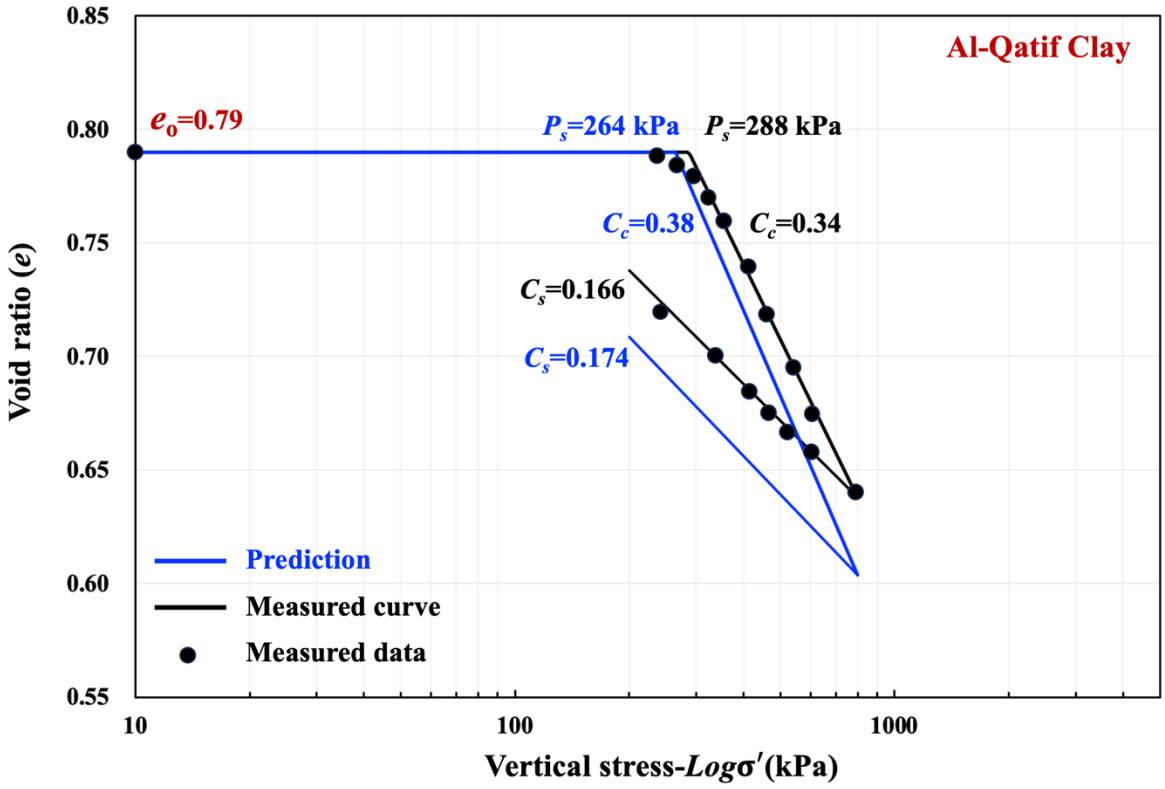


Fig. 7.3 Integrated model validation using CVT results for Al-Qatif Clay

Fig. 7.3 presents the comparison between the predicted and experimental CVT curves for Al-Qatif Clay. This soil, originating from the Eastern Province of Saudi Arabia, is notable for its high plasticity and salinity, which contribute to its strong swelling tendency under arid climatic

conditions. The test data used for model validation were sourced from earlier laboratory investigations (Abduljauwad et al., 1998).

The model predicts a P_{scv} of 264 kPa, which compares well with the measured value of 288 kPa. The predicted compression index (C_c = 0.38) is slightly higher than the experimental result (0.34), while the swelling index (C_s = 0.174) closely matches the measured value of 0.166. The general form of the CVT curve is effectively captured, lending further support to the applicability of the integrated modeling framework to expansive soils from other regions.

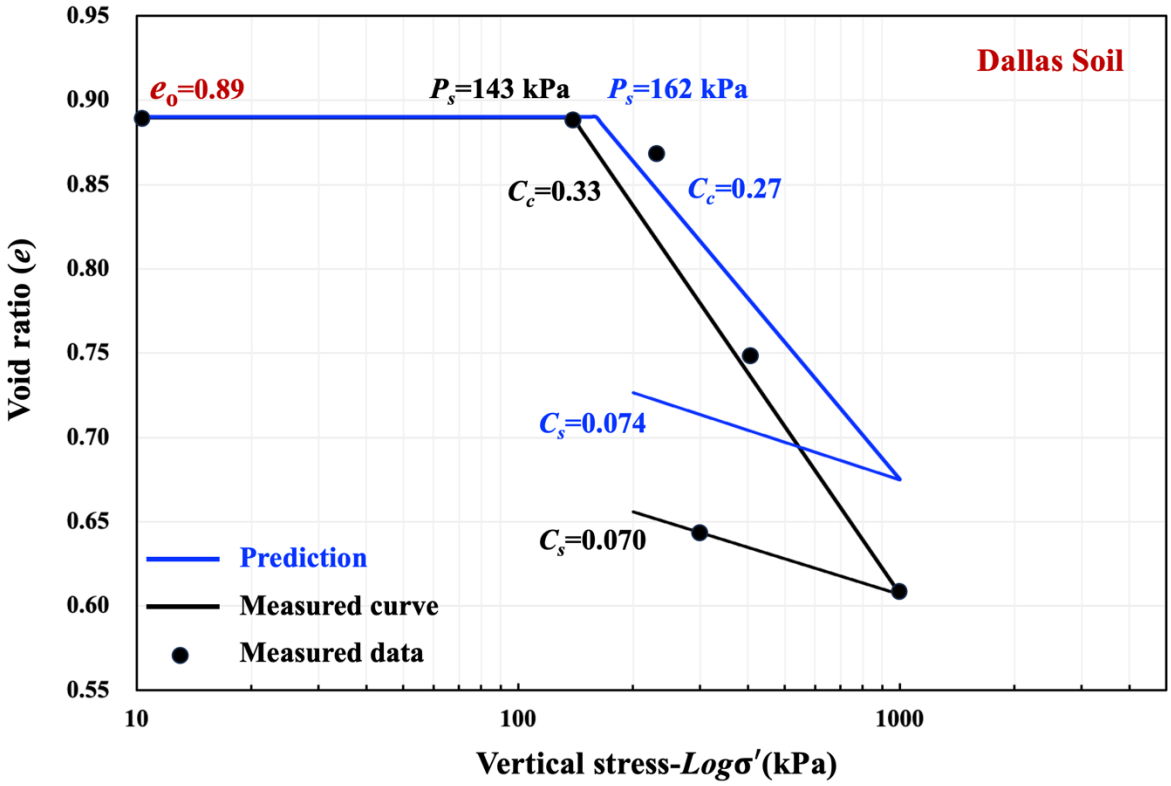


Fig. 7.4 Integrated model validation using CVT results for Dallas Soil

The comparison shown in Fig. 7.4 indicates that the predicted CVT curve for Dallas Soil agrees well with the corresponding experimental data. The validation dataset was drawn from earlier laboratory studies (Singhal 2010).

The predicted P_{scv} reaches 162 kPa, which is reasonably close to the measured 143 kPa. For the C_c, the model yields a value of 0.27, slightly lower than the observed 0.33. The predicted C_s is nearly

identical to the measured value of 0.070. These results provide further support for the reliability of the integrated approach across different soil conditions.

Table 7.1 summarizes the key results of the combined application of the developed predictive models using constant-volume test data for three representative expansive soils. For each soil, the table includes fundamental physical properties such as initial void ratio, liquid limit, plasticity index, initial water content, dry density, and initial suction. It also presents a comparison between the measured and predicted values of swelling pressure, compression index, and swelling index, with the predictions derived from the equations proposed in earlier chapters.

Across all three soils, the predicted values show good agreement with laboratory measurements. The predicted swelling pressure differs from the measured values by no more than 10–15%, while the predicted compression and swelling indices generally fall within acceptable engineering ranges. These results demonstrate that the coordinated use of the individual models enables a reliable estimation of the volume change behavior of expansive soils based on commonly available properties. The consistency observed across soils with varying plasticity, initial suction, and dry density suggests that this approach may be practically reliable and reasonably generalizable for different types of expansive soils.

Table 7.1 Summary of integrated model validation using CVT results

Soil	Country	e_o	LL	I_p	w_o	ρ_d	Ψ_i	P_{scv} (Measured)	P_{scv} (Eq. 3.16)	C_c (Measured)	C_c (Eq. 5.18)	C_s (Measured)	C_s (Eq. 3.15)
Regina Clay	Canada	0.985	77	47	25	1.44	800	260	230	0.21	0.19	0.095	0.075
Al-Qatif Clay	Saudi Arabia	0.79	130	70	35	1.18	2100	288	264	0.34	0.38	0.166	0.174
Dallas Clay	USA	0.890	67	45	24	1.47	182	143	162	0.33	0.27	0.070	0.074

7.3 Integrated validation of the proposed models using consolidation-swell test curves

This section presents an integrated validation of the proposed models using consolidation-swell test (CST) curves from three expansive soils: Regina Clay (Canada), Medinah White Clay (Saudi Arabia), and Black Cotton Soil (India). The CST curves provide a basis for validating the predicted maximum swelling potential (ε %), consolidation swell swelling pressure (P_{scs}), compression index (C_c), swelling index (C_s),enabling a comprehensive evaluation of the predictive capability of the models developed in Chapters 3,4 and 5.

For each soil, predicted values of these parameters were used to reconstruct the CST curves and compared with laboratory measurements. The comparison results are illustrated in Fig. 7.5 to Fig. 7.7.

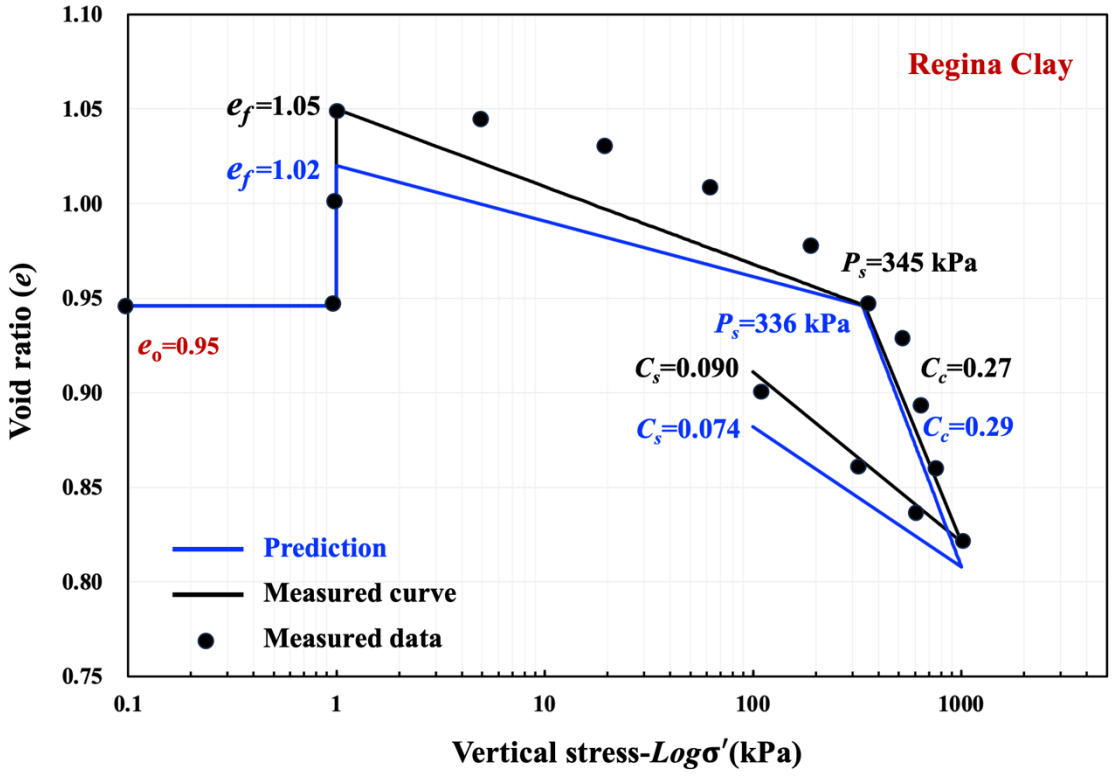


Fig. 7.5 Integrated model validation using CST results for Regina Clay

Fig. 7.5 shows the comparison between the predicted and measured consolidation-swell test (CST) curve for Regina Clay. The experimental data were obtained from Fredlund and Rahardjo (1993) and Vu and Fredlund (2004), who reported detailed laboratory measurements on the swelling behavior of Regina Clay in Saskatchewan, Canada. In this test, the initial void ratio was 0.95, and the measured final void ratio after swelling reached 1.05, corresponding to a maximum swelling potential of approximately 10.3%. In comparison, the predicted final void ratio was 1.02, yielding a swelling potential of 7.3%. Although the predicted swelling is slightly lower than the measured value, the overall swelling trend is reasonably well captured. The predicted swelling pressure is 336 kPa, which compares well with the measured value of 345 kPa. The swelling index is slightly underestimated (C_s = 0.074 vs. 0.090), while the predicted compression index (C_c = 0.29) closely matches the measured value (0.27). Overall, the predicted CST curve reproduces the shape and key features of the experimental curve, suggesting that the combined application of the models can provide a reasonable approximation of the deformation behavior observed in consolidation-swell tests.

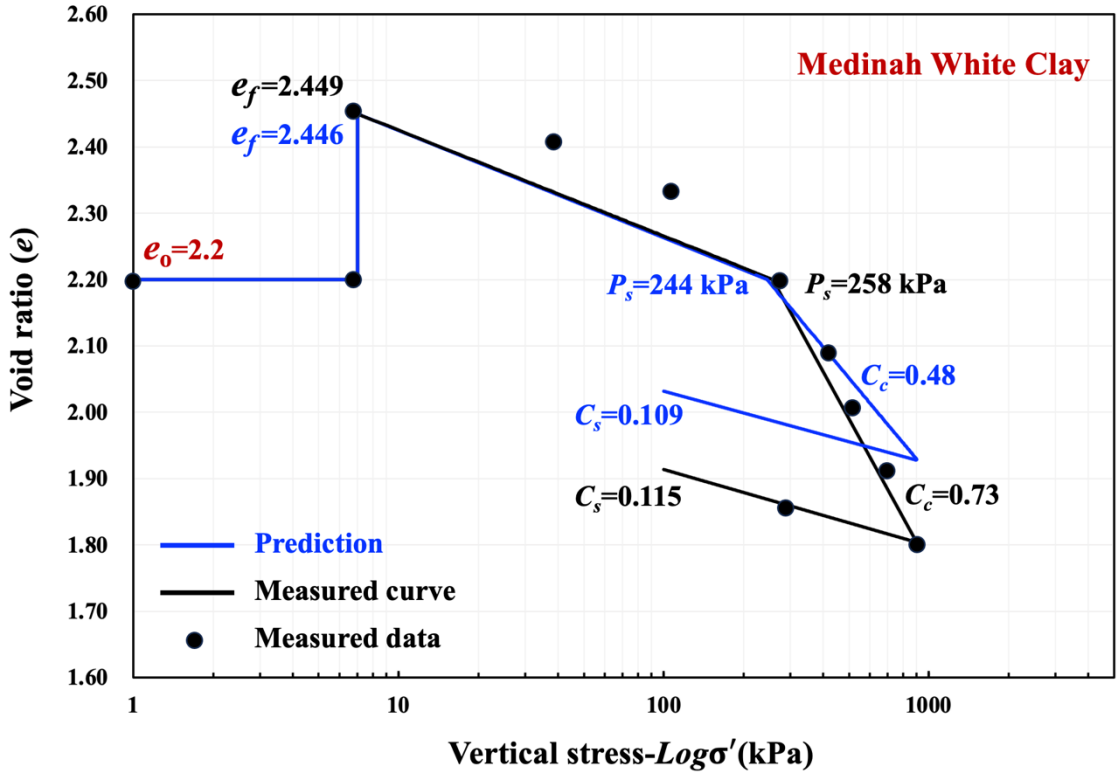


Fig. 7.6 Integrated model validation using CST results for Medinah White Clay

Fig. 7.6 presents the comparison between the predicted and measured CST curve for Medinah White Clay. The experimental data were obtained from Dhowian et al. (1988), based on laboratory tests conducted in Saudi Arabia. In this test, the initial void ratio was 2.20, and the measured final void ratio after swelling reached 2.449, corresponding to a maximum swelling potential of approximately 11.3%. The predicted final void ratio was 2.446, yielding a swelling potential of 11.2%, which shows excellent agreement with the experimental result. The predicted swelling pressure is 244 kPa, slightly lower than the measured value of 258 kPa. The swelling index also closely matches the experimental result (0.109 predicted vs. 0.115 measured). In contrast, the predicted compression index (C_c = 0.48) is notably lower than the measured value of 0.73. This difference is largely due to the fact that the C_c prediction model was trained on data with an upper bound of approximately 0.59, and thus tends to underpredict when the actual value exceeds this range. Nevertheless, the predicted C_c still falls within a commonly observed range for high-plasticity clays, and can provide a reasonable approximation for practical engineering applications.

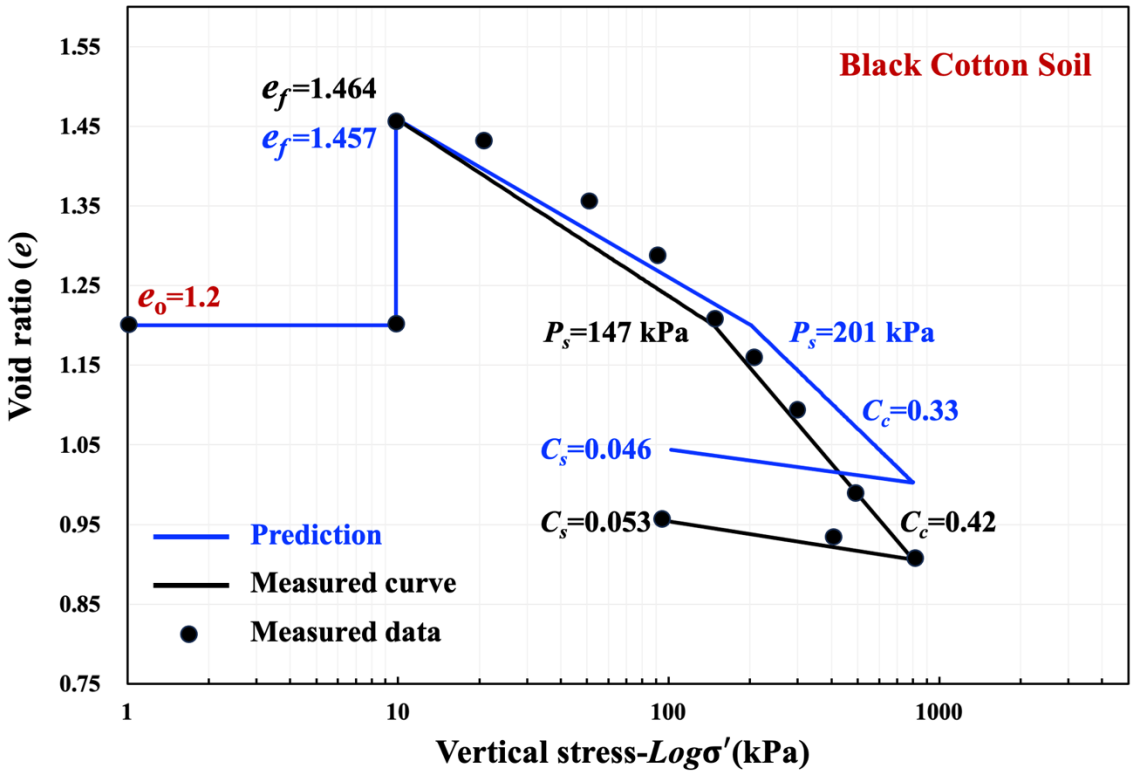


Fig. 7.7 Integrated model validation using CST results for Black Cotton Soil

Fig. 7.7 illustrates the predicted and measured CST curve for Black Cotton Soil. The original test data were reported by Katti (1978), based on laboratory tests conducted on Black Cotton Soil from India. The initial void ratio was 1.20, and the measured final void ratio after swelling reached 1.464, giving a maximum swelling potential of approximately 22.0%. The predicted final void ratio was 1.457, corresponding to a swelling potential of 21.4%, showing a very close match with the experimental result. The predicted swelling pressure is 201 kPa, moderately higher than the measured 147 kPa. The swelling index is slightly underestimated (0.046 vs. 0.053), while the predicted compression index (0.33) underestimates the measured value of 0.42. The CST curve is reasonably well captured, with predicted values falling within typical engineering ranges.

Table 7.2 summarizes the results of model validation based on consolidation-swell test data for three expansive soils. The table presents both measured and predicted values of maximum swelling potential, swelling pressure under CST conditions, swelling index, and compression index, alongside relevant soil parameters including initial void ratio, Atterberg limits, specific gravity, Initial water content, dry density, and initial suction. The predictions were generated using the models introduced in Chapters 3, 4, and 5, and applied collectively to simulate the swelling and consolidation for each soil.

Overall, the predicted values align well with experimental observations. The maximum swelling potential is reproduced with reasonable precision, and the predicted swelling pressures remain close to the measured values across all three soils. Although some variation is observed in the predicted compression and swelling indices, the majority of the values are within typical bounds encountered in engineering applications. Taken together, these outcomes demonstrate the feasibility of using the developed models in combination to estimate the volume change behavior of expansive soils based on commonly available soil properties.

Table 7.2 Summary of integrated model validation using CST results

Soil	Country	e_o	LL	I_p	G_s	C	w_o	ρ_d	Ψ_i	$\varepsilon\%$ (Measured)	$\varepsilon\%$ (Eq. 4.8)	P_{scs} (Measured)	P_{scs} (Eq. 3.18)	C_c (Measured)	C_c (Eq. 5.18)	C_s (Measured)	C_s (Eq. 3.15)
Regina Clay	Canada	0.946	77	44	2.82	52	25	1.44	800	10.5	7.3	345	336	0.27	0.29	0.090	0.074
Medinah Clay	Saudi Arabia	2.250	88	51	2.74	68	38	1.28	1000	11.3	11.2	258	244	0.73	0.48	0.115	0.109
Black Cotton Soil	India	1.200	85	38	2.72	56	42	1.38	225	22.0	21.3	147	201	0.42	0.33	0.053	0.046

7.4 Summary

This chapter demonstrated the joint application of the models proposed in Chapters 3 to 5 to predict the volume change behavior of expansive soils. Three soils were examined under each of the two oedometer test conditions, constant-volume and consolidation-swell, allowing for a unified evaluation of the models' performance.

As shown in Tables 7.1 and 7.2, the maximum swelling potential was predicted with high accuracy, with differences from measured values generally within 1–3%. The predicted swelling pressure also aligned well with experimental results, showing deviations typically between 2% and 13%. The swelling index was predicted using only the plasticity index and a limited dataset of 12 expansive soils. Given these constraints, the results—with errors below 20%—are considered acceptable. Relatively larger deviations were observed in the prediction of the compression index, with errors reaching up to 34% when the measured values exceeded the upper range of the training data. However, for the other five soils, the deviations ranged from 6% to 21%, indicating that the model performs reasonably well within its trained domain.

In this chapter, all models were applied in an integrated manner to reconstruct the full deformation response of expansive soils under oedometer test conditions. Using only fundamental soil properties, the proposed models successfully reproduced the shapes and magnitudes of both constant-volume and consolidation-swell curves. These curves incorporate key deformation parameters including swelling potential ($\varepsilon\%$), swelling pressure (P_s), swelling index (C_s), and compression index (C_c), and the reasonable agreement between predicted and measured values confirms the compatibility and reliability of the models when used in combination.

The integrated framework presented here offers not only a practical alternative to conventional experimental methods, but also a more comprehensive understanding of expansive soil behavior. By eliminating the need for complex testing procedures, it enables geotechnical engineers to assess the deformation characteristics of expansive soils during preliminary site investigations and early design stages. Moreover, the framework demonstrates applicability across a wide range of expansive soil types and environmental conditions, supporting its broader use in engineering practice. In summary, this chapter highlights the value of integrating multiple models in a

coordinated framework and demonstrates its potential to enhance prediction efficiency and support informed decision-making in geotechnical engineering.

References

Abduljauwad, S. N., Al-Sulaimani, G. J., Basunbul, I. A., and Al-Buraim, I., 1998. Laboratory and field studies of response of structures to heave of expansive clay. Geotechnique, 48(1), 103-121.

Dhowian, A., Youssef, A., and Orhan, A.E., 1988. Swelling soil problems in Saudi Arabia. Engineering Geology, 25(3): 241–255.

Fredlund, D.G., and Rahardjo, H., 1993. Soil mechanics for unsaturated soils. John Wiley & Sons.

Katti, R.K., 1978. Search for solutions to problems in black cotton soils. Indian Institute of Technology, Bombay.

Singhal, S., 2010. Expansive Soil Behavior: Property Measurement Techniques and Heave Prediction Methods. Ph.D. thesis, Arizona State University.

Vu, H.Q., and Fredlund, D.G., 2004. The prediction of one-, two-, and three-dimensional heave in expansive soils. Canadian Geotechnical Journal, 41(4): 713-737.

Yoshida, R., Fredlund, D.G., and Hamilton, J., 1983. The prediction of total heave of a slab-on-grade floor on Regina clay. Canadian Geotechnical Journal, 20(1): 69-81.

CHAPTER 8

CONCLUSIONS AND SUGGESTIONS FOR FUTURE RESEARCH

8.1 Major conclusions

This research focused on developing reliable and practical machine learning based methods for predicting the swelling and compression behavior of expansive soils. The main contributions of the study include the development of several prediction models and explicit equations for estimating swelling index, swelling pressure, swelling potential and compression index, validated through comprehensive statistical analyses and case studies. These findings offer significant value for improving the efficiency and accuracy of geotechnical design in areas underlain by expansive soils. The major conclusions of this research are summarized as follows:

8.1.1 Predicting swelling index and swelling pressure of expansive soils using multiple artificial intelligence techniques

Three machine learning techniques, namely, Multilayer Perceptron (MLP), Support Vector Machine (SVM), and Extreme Learning Machine (ELM), were employed to develop predictive models for estimating the swelling index (C_s) and swelling pressure, (P_s) of expansive soils based on fundamental soil properties. Among these, the MLP model demonstrated the best prediction performance in terms of accuracy and generalization capability.

Four explicit prediction equations were proposed based on the optimized MLP model to enhance the transparency and practical applicability of the models. These equations allow for straightforward application in geotechnical practice without the need for complex computational tools. The proposed models and equations were validated using a comprehensive dataset of expansive soils collected from different geographic regions, and they exhibited strong predictive capability across a wide range of soil types and conditions.

8.1.2 A practical machine learning-based approach for predicting 1-D vertical swelling potential of expansive soils

A machine learning-based approach was developed for predicting the one-dimensional vertical swelling potential of expansive soils under unsaturated conditions. Two machine learning techniques; namely, Multivariate Adaptive Regression Splines (MARS) and Multilayer Perceptron (MLP) were applied to construct prediction models based on a comprehensive database of 173 soil samples from different regions.

An explicit equation was derived from the optimized MLP model to improve interpretability and facilitate practical engineering applications. The prediction performance of the equation was evaluated through statistical analyses and verified using five published case studies. The results demonstrated that the proposed model provides reliable and accurate predictions of swelling potential under various soil and environmental conditions, offering a practical tool for geotechnical engineers.

8.1.3 Advanced machine learning models for predicting the compression index of expansive soils

Advanced machine learning models were developed to predict the compression index of expansive soils using fundamental soil properties. A hybrid Newton-Raphson-Based Optimizer Enhanced Extreme Gradient Boosting (NRBO-XGBoost) model and an optimized Multilayer Perceptron (MLP) model were proposed and trained using a comprehensive global database of expansive soil data.

An explicit equation was derived from the optimized MLP model to provide a simplified prediction tool suitable for practical geotechnical engineering applications. Validation results showed that both the NRBO-XGBoost and MLP models outperformed traditional empirical methods in terms of accuracy and generalization ability. The predictive performance of the models was further confirmed through a case study, demonstrating their effectiveness in estimating the compression behavior of expansive soils.

8.1.4 Validation and application: Case studies of the proposed methods in this study

The prediction models and equations proposed in this study were validated through multiple case studies to assess their reliability and applicability. These case studies included the prediction of swelling index, swelling pressure, swelling potential and compression index for expansive soils under various environmental and geotechnical conditions.

The validation results demonstrated that the proposed methods provide accurate and consistent predictions, confirming their practical value for use in geotechnical engineering practice. The successful application of the developed models in different case studies highlights their potential for improving the efficiency of geotechnical investigations and reducing the dependence on time-consuming laboratory testing procedures.

8.1.5 Integrated application of models for predicting constant volume and consolidation-swell oedometer test curves

The developed models for predicting swelling index, swelling pressure, swelling potential, and compression index were combinedly applied to simulate the volume change behavior of expansive soils under both constant-volume and consolidation-swell oedometer test conditions. Validation was performed using six representative soils from Canada, Saudi Arabia, India, and the United States.

For the constant-volume test curves, the predicted deformation behavior closely matched the experimental results. The predicted swelling pressure and compression index generally deviated by less than 15% from the measured values, and the swelling index values remained within a reasonable engineering range. In the consolidation-swell tests, the predicted maximum swelling potential showed good agreement with the measured results, with differences mostly within 1–3%. The predicted swelling pressures were also consistent with laboratory data. While the compression index was underestimated in one case where the measured value exceeded the model's training range, the predictions for other cases remained within typical bounds.

These results demonstrate that the proposed models, though developed separately, can be effectively applied together to predict complete oedometer test curves using only basic soil

properties. The integrated approach enhances the practical value of the models by enabling the prediction of soil deformation behavior under different loading and boundary conditions, offering a reliable alternative to time-consuming laboratory testing.

8.2 Recommendation for future research studies

While this study has developed practical and reliable machine learning-based models for predicting the swelling and compressive properties of expansive soils, there remain opportunities to further enhance and extend the current research. The following recommendations are proposed to support future work in this area:

(i) Expansion of the database for model development: The database used in this study was compiled from published experimental results, primarily conducted in accordance with ASTM standards. A few datasets following other national standards, such as GB in China and IS in India, were also included. These standards are mostly consistent with ASTM standards; hence, the overall impact on data consistency and reliability is considered minimal. While this database has provided a solid foundation for developing the proposed prediction models, further expansion through the inclusion of more recent and high-quality data may help improve the accuracy, robustness, and general applicability of the models.

(ii) Field validation of the proposed models: In this study, validation of the proposed models for swelling index and swelling pressure was primarily conducted using laboratory-based datasets. To further assess the reliability and practical value of these models, future research is encouraged to incorporate field-based validation under actual site conditions. In addition, expanding the field validation of the proposed models for swelling potential and compression index would offer valuable insights and strengthen their applicability in geotechnical engineering practice.

(iii) Consideration of cyclic drying-wetting conditions: The prediction models developed in this study were based on data corresponding to single wetting scenario. However, expansive soils in the field are often subjected to long-term cyclic seasonal variations involving repeated drying and wetting cycles. Considering the influence of these cyclic environmental conditions on the swelling

and compression behavior of expansive soils in future model development may enhance the relevance and reliability of the predictive methods.

(iv) Exploration of physics-informed neural networks (PINNs): The predictive models presented in this study are based on data-driven machine learning approaches. Future studies may explore the potential of physics-informed neural networks (PINNs), which incorporate physical laws and governing equations into the learning process. Integrating PINNs into the model framework could enhance the interpretability and physical consistency of machine learning-based predictions, thereby providing a more comprehensive tool for assessing the deformation behavior of expansive soils.